BEILSTEIN JOURNAL OF NANOTECHNOLOGY

Nanomaterial-based sensors for water remediation, healthcare and food monitoring applications

Edited by Akeem Adeyemi Oladipo, Yap Wing Fen, Abdur Rahim, Pramod K Gupta and Amin Mousavi Khaneghah

Generated on 12 November 2026, 11:31

Imprint

Beilstein Journal of Nanotechnology
www.bjnano.org
ISSN 2190-4286
Email: journals-support@beilstein-institut.de

The *Beilstein Journal of Nanotechnology* is published by the Beilstein-Institut zur Förderung der Chemischen Wissenschaften.

Beilstein-Institut zur Förderung der Chemischen Wissenschaften
Trakehner Straße 7–9
60487 Frankfurt am Main
Germany
www.beilstein-institut.de

The copyright to this document as a whole, which is published in the *Beilstein Journal of Nanotechnology*, is held by the Beilstein-Institut zur Förderung der Chemischen Wissenschaften. The copyright to the individual articles in this document is held by the respective authors, subject to a Creative Commons Attribution license.

BEILSTEIN JOURNAL OF NANOTECHNOLOGY

A photonic crystal material for the online detection of nonpolar hydrocarbon vapors

Evgenii S. Bolshakov*[1], Aleksander V. Ivanov[1,2], Andrei A. Kozlov[3], Anton S. Aksenov[3], Elena V. Isanbaeva[1], Sergei E. Kushnir[1,4], Aleksei D. Yapryntsev[2], Aleksander E. Baranchikov[2] and Yury A. Zolotov[1,2]

Full Research Paper

Open Access

Address:
[1]Department of Chemistry, Lomonosov Moscow State University, Moscow, 119991, Russia, [2]Kurnakov Institute of General and Inorganic Chemistry, Russian Academy of Sciences, Moscow, 119991, Russia, [3]Institute of Fine Chemical Technologies, Russian Technological University Moscow, 119454, Russia and [4]Department of Materials Science, Lomonosov Moscow State University, Moscow, 119991, Russia

Email:
Evgenii S. Bolshakov* - esbolshakov@yahoo.com

* Corresponding author

Keywords:
diffuse reflectance spectroscopy; photonic crystal sensor; stimuli-responsive materials

Beilstein J. Nanotechnol. **2022,** *13,* 127–136.
https://doi.org/10.3762/bjnano.13.9

Received: 23 October 2021
Accepted: 03 January 2022
Published: 25 January 2022

This article is part of the thematic issue "Nanomaterial-based sensors for water remediation, healthcare and food monitoring applications".

Guest Editor: A. A. Oladipo

© 2022 Bolshakov et al.; licensee Beilstein-Institut.
License and terms: see end of document.

Abstract

A modern level of nanotechnology allows us to create conceptually new test systems for chemical analyses and to develop sensitive and compact sensors for various types of substances. However, at present, there are very few commercially available compact sensors for the determination of toxic and carcinogenic substances, such as organic solvents that are used in some construction materials. This article contains an overview of how 3D photonic crystals are used for the creation of a new test system for nonpolar organic solvents. The morphology and structural parameters of the photonic crystals, based upon a crystalline colloidal array with a sensing matrix of polydimethylsiloxane, have been determined by using scanning electron microscopy and by the results of specular reflectance spectroscopy based on the Bragg–Snell law. A new approach has been proposed for the application of this sensor in chemical analysis for the qualitative detection of saturated vapors of volatile organic compounds due to configuration changes of the photonic bandgap, recorded by diffuse reflectance spectroscopy. The exposure of the sensor to aromatic (benzene, toluene and *p*-xylene) and aliphatic (*n*-pentane, *n*-heptane, *n*-octane and *n*-decane) hydrocarbons has been analyzed. The reconstitution of spectral parameters of the sensor during the periodic detection of saturated vapors of toluene has been evaluated.

Introduction

Photonic crystals (PhCs) used for chemical sensors can be divided into three groups depending upon their structure, that is, one-dimensional (1D), two-dimensional (2D), and three-dimensional (3D) [1-10]. 2D and 3D structures used as chemical sensors are studied in most projects. 2D structures consist of a monolayer of spherical particles placed on a substrate. 3D struc-

tures, which appear in the form of a crystalline colloidal array (CCA), are called opal structures (spherical particles close-packed in an ordered structure). If the structure has been placed in a matrix and the particles have been removed, then it is an inverse opal structure [11-13]. A photonic bandgap (PBG) appears in colloidal crystals due to the periodic modulation of the refractive index. At the bandgap, selective reflection of light is observed, which is connected to a low photon density of states within the materials [14]. Most of the configuration changes of the photonic bandgap in opal and inverse opal structures occur due to swelling or compression of the polymer matrix or gel.

To date, four main methods for the modification of photonic crystals are used for the creation of stimuli-responsive materials: (a) formation of a sensitive polymer matrix, (b) impregnation of the reagent, (c) immobilization of the reagent and (d) preparation of the sensor elements from molecularly imprinted polymers.

Organic solvents are usually detected by using polymer matrix sensors (Table 1) through matrix interaction [7-9,15,16]. The impregnation and immobilization methods are rather close; they are used for the determination of inorganic ions (Cu^{2+}, Pb^{2+}, Hg^{2+}, Ni^{2+} and Cd^{2+}) [2,11,17-19] and organic molecules of simple and complex structure (glucose, organophosphates, urea, creatinine, ciprofloxacin and sarin) [5,6,20-27]. The development of a sensor device with molecularly imprinted polymers allows for the determination of organic compounds (nicotinamide, sulfonamides, bisphenol A and diethylstilbestrol) with a more complex structure [12,13,28,29].

The color shift (blueshift or redshift) or the color intensity of the sensor serves as an analytical signal for such sensors. The standard method for measuring an analytical signal is specular reflectance spectroscopy within the visible range; however, the interaction of a 2D PhC with the analyte is also analyzed by changing the diameter of the Debye diffraction ring [2,5,6,10].

Currently, very few works are devoted to the study of the mechanism that leads to the shift of the PBG in 2D and 3D photonic crystals. This is caused by the variety of flow processes in the structure, which are significantly influenced by the filling of the structure, the structural heterogeneity within a volume, the presence of foreign chemical substances and the size variation of the matrix and particles during the chemical analysis process. However, one cannot ignore sensors based on molecularly imprinted polymers for the selective detection of volatile organic compounds [30-32]. In most cases, the response of such sensors is a change in mass recorded using a quartz microbalance. A simpler design and research method made it possible to investigate in more detail the processes occurring during the absorption of solvents. The ability to control selectivity in molecularly imprinted sensors and the simple visual response in photonic crystal sensors make it promising and even mandatory to combine these two approaches.

In our previous study, the optimal parameters of polystyrene (PS) particles for sensor matrices for saturated vapors of volatile organic compounds have been determined [33]. In this work, we determined the parameters of the sensor structure and examined online the detection of high concentrations of aromatic and aliphatic hydrocarbon vapors in air. The detection was

Table 1: Some photonic crystal structures for chemical sensing of organic solvents.

Geometry	Material	Response	Analyte	Limit of detection	Ref.
3D PhC (CCA)	polystyrene	redshift (<50 nm)	methanol vapors	5% ($V_{methane}/V_0$)	[7]
3D PhC (PCCA)[a]	polystyrene-Ag/ polydimethylsiloxane	redshift (<50 nm)	chloroform, chlorobenzene, tetrahydrofuran, dichloromethane and dimethoxyethane liquids	5 µL (5 nm)	[8]
3D PhC (CCA)	polystyrene	redshift (<40 nm)	methanol, ethanol, isopropanol, 1-propanol and *n*-butanol vapors	2% (V_{ethane}/V)	[9]
3D PhC (PCCA)	polymethylmethacrylate/ methyl cellulose	redshift (<80 nm)	ethanol, *n*-propanol, isopropanol and *n*-butanol liquids and vapors	NA	[15]
3D PhC (CCA)	polystyrene	redshift	methanol and ethanol	NA	[16]
3D PhC (PCCA)	polystyrene/ polydimethylsiloxane	redshift (<150 nm)	benzene, toluene, *p*-xylene, *n*-pentane, *n*-heptane, *n*-octane and *n*-decane vapors	0.3 mg/m^3 (toluene)	this work

[a]Polymerized crystalline colloidal array.

performed by using 3D PhC-based sensors, which are a CCA of polystyrene submicrometer particles embedded in a polydimethylsiloxane (PDMS) layer. The matrix interaction was responsible for the main mechanism, which was monitored by configuration changes of the photonic bandgap using diffuse reflectance spectroscopy.

Results and Discussion

Determination of the morphology and the structural parameters of the sensor

A comparison between the specular reflectance and the diffuse reflectance spectra tested in the "specular component included (SCI)" and "specular component excluded (SCE)" modes has shown (Figure 1a) that the maximum of the diffuse reflectance spectra of the PhC sensor in the SCI mode coincides with the maximum of the specular reflection spectra resulting from flat (111) surfaces at an 8° angle. This applies regardless whether the sensor has a PDMS layer or not. However, the diffuse reflectance spectra of the sample without a polydimethylsiloxane layer, measured in the SCE mode, had a significant intensity decrease at the assumed maximum point of the reflection. For a sensor with a PDMS layer, the spectrum intensity of the specular reflectance component, regarding the diffuse reflectance spectrum, decreases. This is expressed in the smaller influence of the viewing angle on the color of the sensor and a simpler visual registration of the color due to a decrease of the iridescence effect, which is an important requirement for the testing system.

A reflection peak was approximated by a quadratic function ($y = ax^2 + bx + c$) to determine the PBG position. The fitted coefficients of the quadratic function of spectral maxima were used to determine the dependence of the photonic bandgap position on the exposure time and the incident angle by the analysis of the diffuse and specular reflectance spectra.

According to the literature data, the structure has a face-centered cubic lattice (FCC), therefore, it can be assumed that the structure is filled by 74% with PS and that the remaining volume is filled with air or polydimethylsiloxane [34,35]. Figure 2 shows the surface of a crystalline colloidal array obtained by using scanning electron microscopy.

The investigated samples have an ordered lattice structure similar to crystals; therefore, the Bragg equation has been applied for the analysis. Since the diameter of particles in the lattice is in the submicrometer region, diffraction occurs in the visible spectrum, and it becomes necessary to consider the refraction of light during propagation through materials with different refractive indices. In the case of the CCA with FCC lattice, the Bragg–Snell law can be written as follows:

$$m\lambda = 2d_{111}\sqrt{n_{\text{eff}}^2 - n_{\text{air}}^2 \sin^2\theta}, \quad (1)$$

where m is the order of a diffraction maximum, λ is the wavelength of the reflectance maximum, d_{111} is the interplanar distance between crystallographic (111) planes, n_{eff} is the effec-

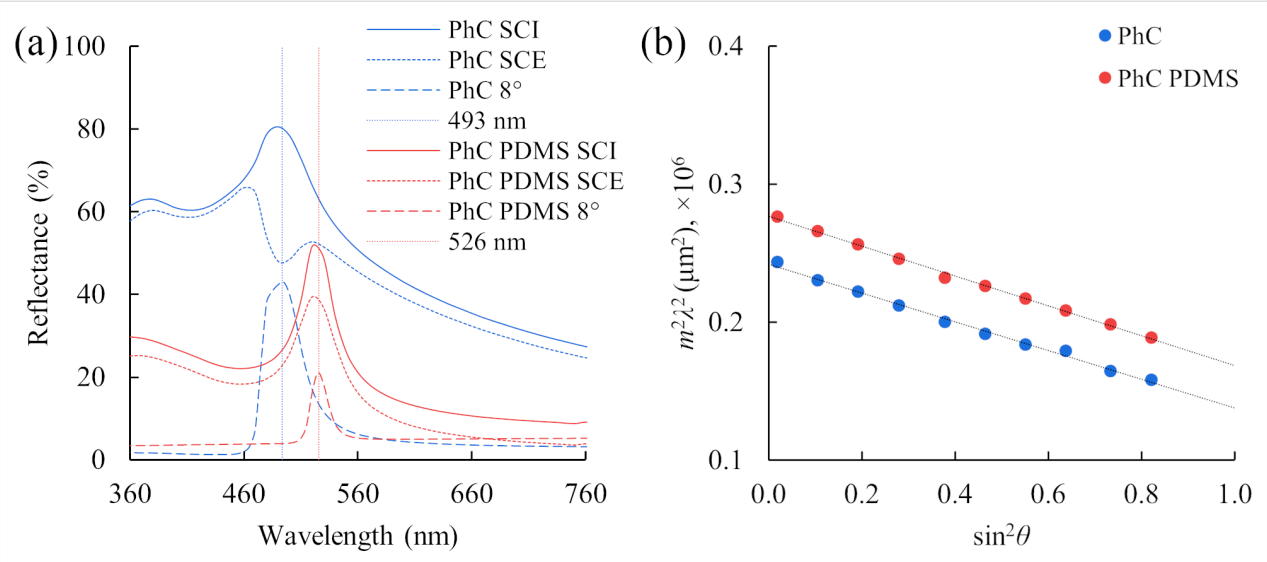


Figure 1: Optical characteristics of sensors based on 3D PhC (matrix thickness ≈ 90 μm): (a) diffuse reflectance and specular (8°) reflectance spectra of the sensor before and after the PDMS layer formation (the difference in reflection intensity is caused by different apertures and the area of samples) and (b) dependence of $m^2\lambda^2$ on $\sin^2\theta$ for the sensor with the PDMS layer (red circles) and without (blue circles), where m is the order of the photonic bandgap, λ is the wavelength of the photonic bandgap, θ is the incident angle. Black lines show the linear correspondence of the experimental data.

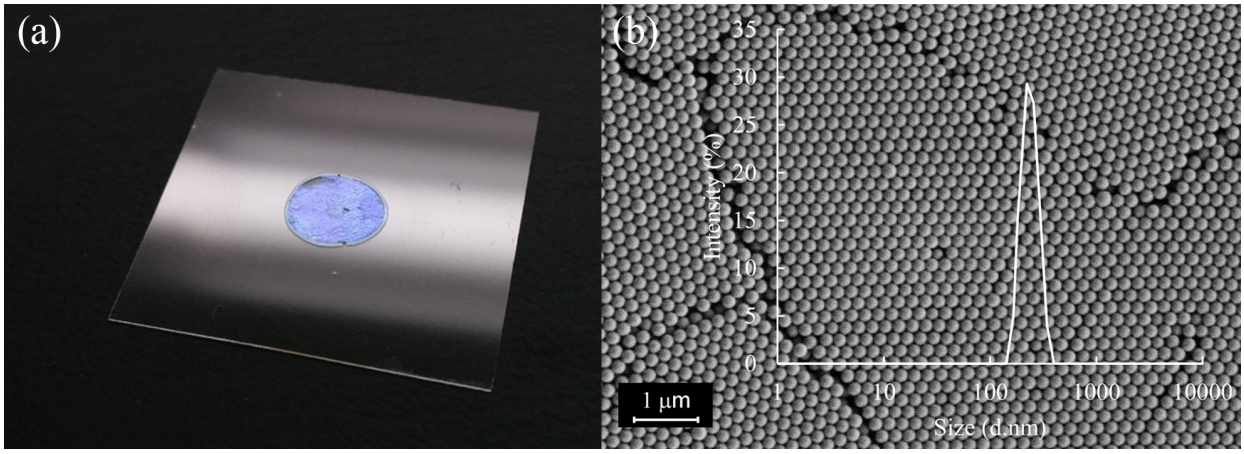


Figure 2: (a) Photo of the sensor and (b) electron microscopy image of a CCA of polystyrene particles without a PDMS layer on a glass substrate (effective particle size = 201 nm). The data obtained with dynamic light scattering slightly overestimates the diameter in comparison with the data obtained from microphotographs. This may be related to the specificity of the dynamic light scattering (DLS) method (hydrodynamic diameter measurement).

tive refractive index of the CCA, n_{air} is the refractive index of the medium (in our case air) from which light falls in and θ is the incidence angle [8,9,36]. The incidence angle was varied from 8° to 65° in the experiments.

Knowing the volume fraction of particles in the CCA (f_p) and their refractive index (n_p), as well as the volume fraction of air or other substances (f_f) that fill the spaces between the particles and the corresponding refractive index (n_f), an effective refractive index of the CCA can be calculated by using the following formula:

$$n_{eff}^2 = \sqrt{f_p n_p^2 + f_f n_f^2}. \quad (2)$$

The interplanar distance between crystallographic planes (111) in a FCC lattice is related to the effective particle diameter D by the following equation:

$$d_{111} = \sqrt{2/3} D. \quad (3)$$

From the linear dependence (Figure 1b) and Equations 1–3, an average diameter of spherical particles and the effective refractive index of the photonic crystal can be obtained [37,38]. The effective refractive index of the structure without PDMS is 1.525, with PDMS it is 1.599, and the average diameter of the particles is 197.5 nm and 201.5 nm, respectively. The obtained average diameters of the polystyrene particles are consistent with the SEM results, and the effective refractive indices are slightly overestimated in comparison with the theoretically calculated values (without PDMS: 1.477, with PDMS: 1.568) [39,40]. This may be due to the presence of surfactants in the interparticle space, defects of the crystal lattice, and a different ratio of volume fractions.

The use of diffuse reflectance spectrometry in further experiments is necessary to obtain integrated optical characteristics of the stimuli-responsive matrix as an analogue of visual recordings. This allows one to optimize the development of sensors with a visual recording of analysis results.

Kinetics of interaction between the sensor and solvent vapors

Of interest is the use of a 3D PhC-based sensor for online measurements of the concentration of nonpolar solvents and their vapors. Exposure to saturated solvent vapors allows the analyte to be delivered more evenly to the surface of the stimuli-responsive matrix than applying a liquid sample to the surface of the sensitive layer, which is an important feature in studying the mechanism of interaction. The following analytes were studied: benzene, toluene, *p*-xylene (the BTX aromatics), *n*-pentane, *n*-heptane, *n*-octane and *n*-decane, which have a high vapor pressure under normal conditions.

As a result of exposure to aromatic and aliphatic nonpolar solvents, a redshift in the PBG is observed using diffuse reflectance spectroscopy. The diffusion of vapors of organic solvents into the PDMS layer and the CCA leads to their swelling and, to a lesser extent, to a change in the effective refractive index of the structure (Figure 3). Since the experimental observation of the photonic bandgap shift was more than 100 nm, this would require a very large change in the effective refractive index. Consequently, the degree of swelling of polydimethylsiloxane

predominantly affects the formation of a response when exposed to hydrocarbons. In this regard, it can be assumed that the sensor will be able to detect other hydrocarbons leading to a swelling of PDMS, such as diethyl ether, tetrahydrofuran and chlorobenzene [41]. Therefore, the main factor can be considered the affinity of solvents to PDMS, namely the polarity and rate of diffusion of the solvent through the matrix. In addition, the polydimethylsiloxane matrix protects the polystyrene CCA from the effects of high concentrations of hydrocarbons, thus, it acts as a "conductor" and "dispenser" of the analyte.

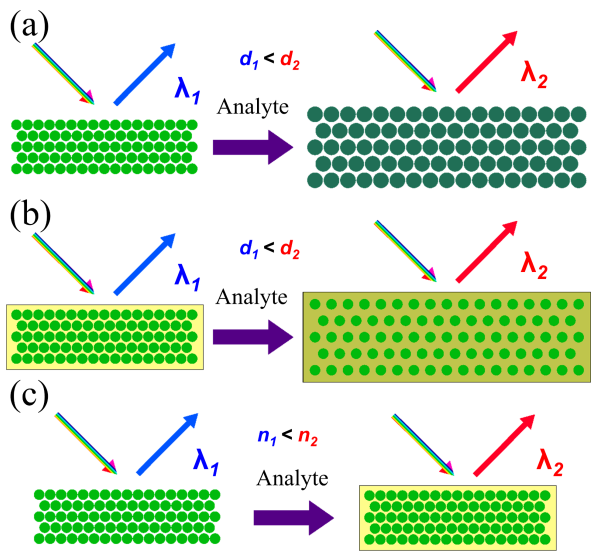


Figure 3: A mechanism of detecting hydrocarbons with a sensor based on a 3D PhC: (a, b) swelling of colloidal particles or polymer matrix, leading to a change in the lattice period *d*; (c) change in the average refractive index of a periodic structure *n*.

An analysis of the vapor effects of the analytes was performed through studying kinetic curves (Figure 4a). It was found that nonpolar aromatic compounds have some response delay, but a steeper rise of the S-curve, which is visually expressed as a more contrasting color change of the sensor matrix. The effect of vapors of nonpolar aliphatic organic solvents, in contrast, leads to an instantaneous photonic bandgap shift, but there is no sharp jump in the kinetic curve. The response time means the moment when the PBG shift rate is maximum; this parameter is well determined by the first derivative of the curves from Figure 4b. This feature allows one to distinguish qualitatively the analytes. This behavior can be explained by the rapid dissolution of the necks ("bridges") between neighboring particles that occur during CCA assembly and hold this array, preventing it from moving apart due to the swelling of the polydimethylsiloxane layer, whereas when exposed to the test alkanes, this does not happen so quickly, and the shift of the lower layers is delayed, resulting in broadening of the photonic bandgap and a less pronounced color.

Qualitative detection of nonpolar low-molecular-weight organic compounds

It was found that the response rate increases exponentially among *n*-pentane, *n*-heptane, *n*-octane and *n*-decane. This is

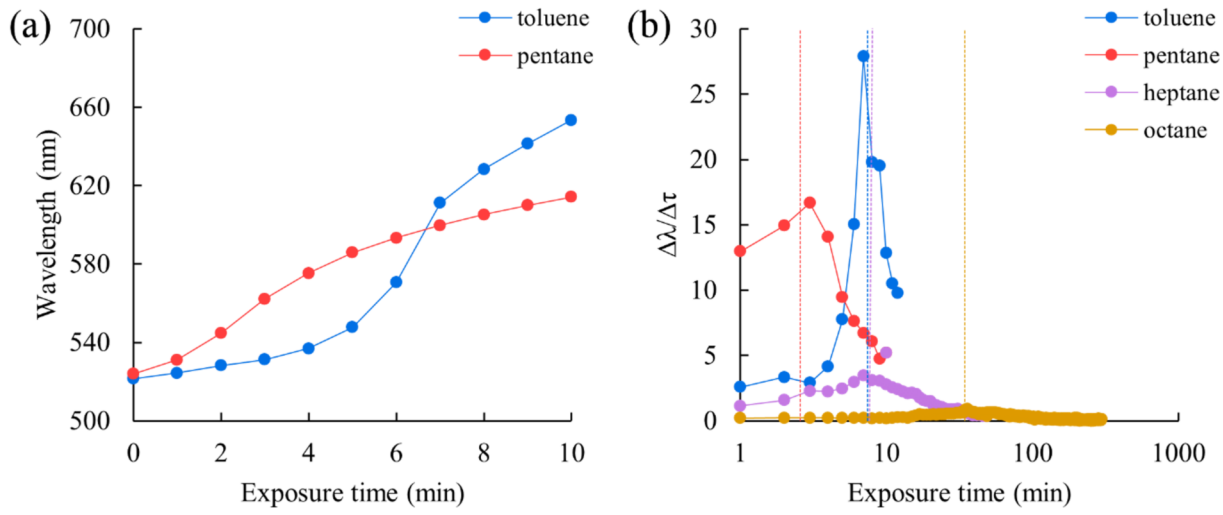


Figure 4: Comparison of the PBG shift rate exposed to toluene and *n*-pentane vapors (matrix thickness about 90 μm): (a) an example of kinetic curves (the experimental temperature was maintained at 23.1–23.6 °C) and (b) differential curves plotted from the average experimental data (additional curves are given for *n*-heptane and *n*-octane).

consistent with an exponential decrease in vapor pressure and a decrease in the rate of diffusion of the compounds into the polymer matrix (Figure 5). The effect of *n*-decane vapor does not lead to a significant change in the sensor color, but only shifts the PBG by just ≈10 nm, nevertheless, the approach proposed here allows one to detect slight changes in the sensor color.

Aromatic and aliphatic hydrocarbons were screened for the color change time of the sensor. For the series benzene, toluene, *p*-xylene and *n*-pentane, *n*-heptane, *n*-octane and *n*-decane, an increase in the response time is observed that is close to exponential. This allows for the detection of the total toxic effect considering the different analytical response rates and the toxicity of the detected compounds.

Since the absorption of hydrocarbon vapors is responsible for the delivery of the analyte to the photonic crystal, a change in the sensor sensitivity is possible by varying the thickness of the sensitive PDMS layer. In the experiments, sensors with a polydimethylsiloxane layer thickness from 10 µm to 2 mm were investigated for detecting low concentrations of vapors and liquid hydrocarbons. As the limit of detection depends on the matrix thickness, the main obstacle to its reduction is the development of a technique for uniform application of polydimethylsiloxane. In some experiments, it was possible to detect toluene vapors with a concentration of ca. 0.3 mg/m^3 using a sensor with a sensitive layer thickness about 20 µm.

Effects of organic solvent mixtures on the sensor

Of particular interest is the detection of analytes in complex objects. An example is the detection of toluene in the presence of xylenes. We discovered that the response rate of the composite sensor is affected by the *p*-xylene/toluene ratio in the analyzed mixture. The relationship shown in Figure 6, corre-

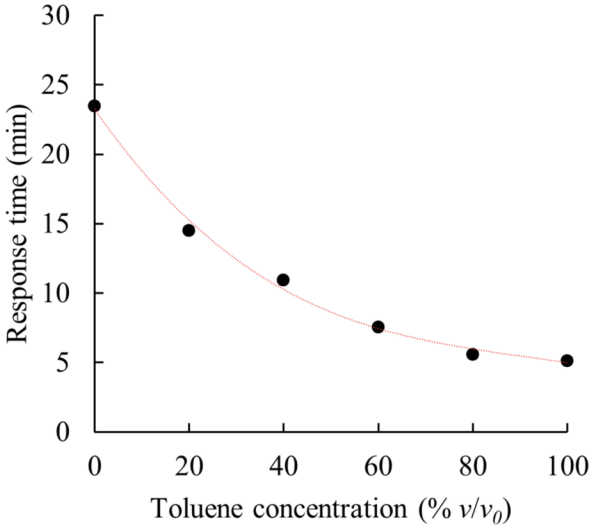


Figure 6: The dependence of the sensor response rate on the content of toluene in *p*-xylene (matrix thickness about 100 µm).

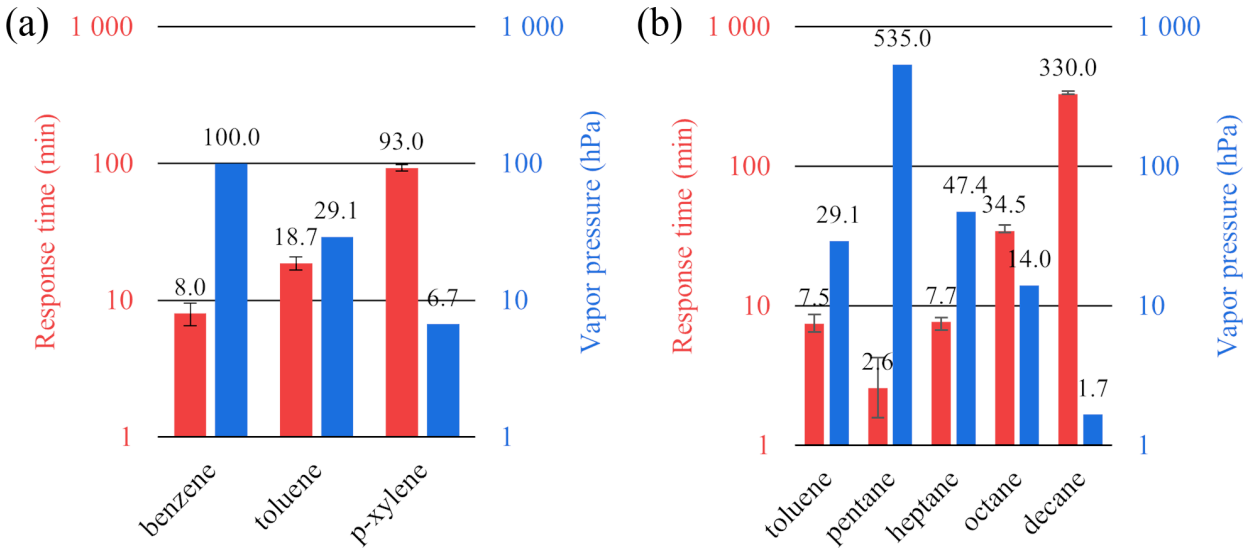


Figure 5: Response rates of sensor matrices (red) and vapor pressure (blue): (a) response time for aromatic hydrocarbons (matrix thickness about 280 µm) and (b) response time for normal alkanes (matrix thickness about 90 µm).

lates well (R^2 = 0.995) with a 3rd-degree polynomial curve: $t = -2.0 \times 10^{-5} C_{PhMe}{}^3 + 4.8 \times 10^{-3} C_{PhMe}{}^2 - 0.49 C_{PhMe} + 23$.

The rate of sensor response to the mixture increases sharply even with a low content of toluene. This factor indicates the possibility of detecting small concentrations of volatile organic compounds with a higher vapor pressure in complex objects. The experimental results also show the possibility of using a sensor to assess the total toxic effect of BTX vapors.

This approach shows that this sensor can be used for the qualitative analysis of complex matrices such as fossil fuel due to the different types of kinetic curves, for example, as shown for aliphatic and aromatic hydrocarbons, according to the criteria obtained after processing the kinetic curves using chemometric methods of analysis.

Reversibility of optical characteristics of the sensor during cyclic exposure to toluene

After the first cycle of exposure to both aromatic and aliphatic solvents, the initial color of the sensor changes, associated with the degradation of the CCA. It should be noted that benzene, toluene and *p*-xylene, unlike, for example, *n*-pentane or *n*-heptane, can lead to the irreversible destruction of the stimuli-responsive matrix due to dissolution or adhesion of PS particles. Therefore, an experiment was carried out with cyclic exposure to toluene vapor. The sensor matrix was exposed to saturated toluene vapors for 8 min. Then, the sensor was allowed to stand for a day to recover the photonic bandgap to its initial position, although 90% of recovery was reached already after 2 min, and the experiment was repeated.

From the results presented in Figure 7a, we can conclude that there is a wide spread in both the initial position of the PBG and

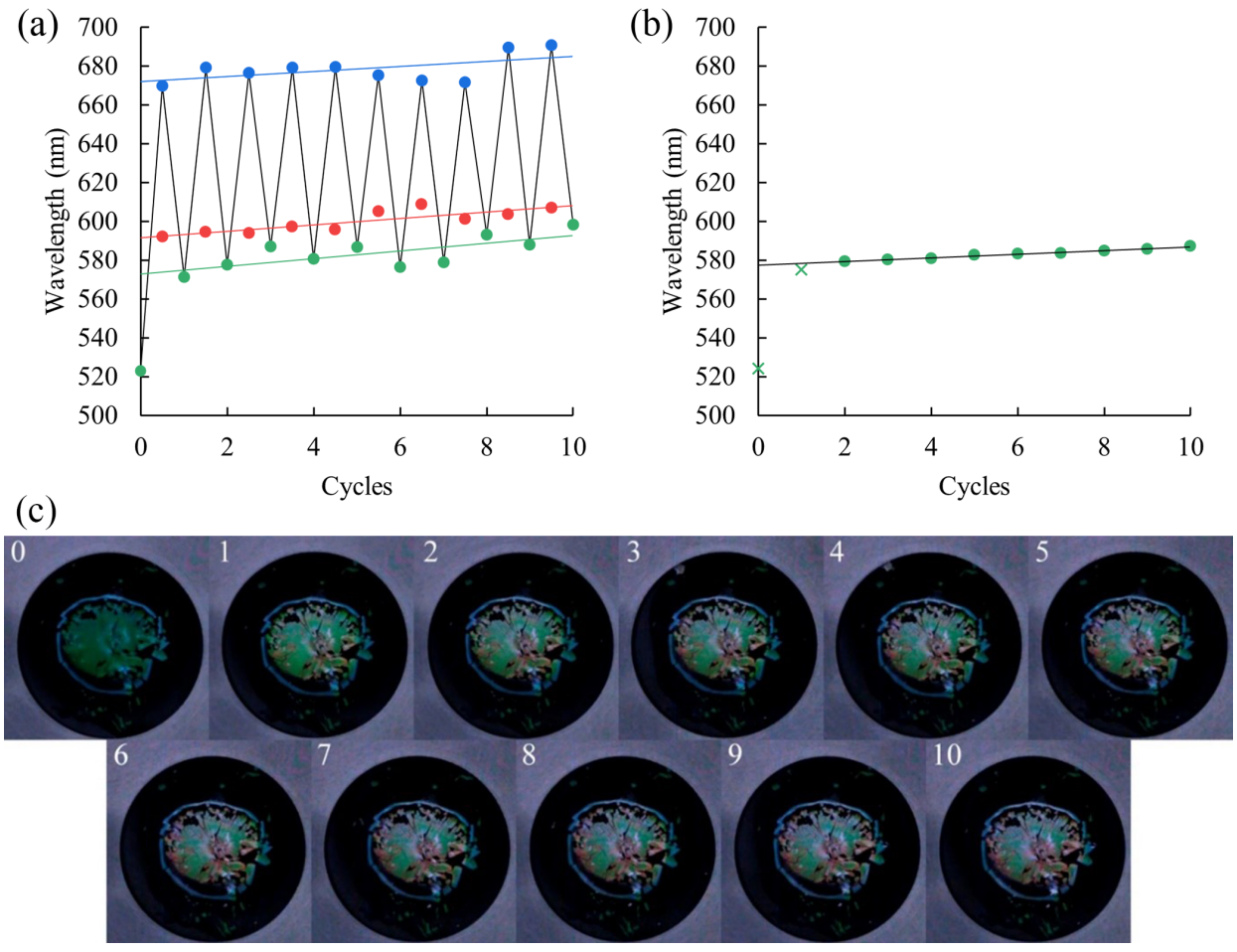


Figure 7: Reversibility of the response to toluene vapor: (a) position of the reflection maximum: green – before exposure to toluene vapor, red – at the response point, blue – 8 min after the exposure (data obtained with an "eye-one Pro" mini-spectrophotometer). (b, c) The starting position of the maximum reflection and initial photo images of the sensor before the next cycle of exposure to toluene vapor (data obtained with a "Ci7800" spectrophotometer).

the final one, but this is explained by the heterogeneity of the sensor degradation over the surface area and the small aperture of the mini-spectrophotometer (4.5 mm), which is smaller than the treated sensor area. Before each experiment, the diffuse reflectance spectra were recorded using a device with a larger aperture (10 mm) than the sample size (Figure 7b,c). Even though a partial degradation of the sensor occurs after each detection, it is already linear after the second detection (R^2 = 0.988) and can be taken into account accordingly.

Conclusion

An approach is proposed for the qualitative determination of aromatic and aliphatic hydrocarbons using stimuli-responsive materials based on 3D photononic crystals. The kinetic regular interactions of organic nonpolar solvents with a photonic crystal-based sensor, having a PDMS sensor matrix, were studied by diffuse reflectance spectroscopy. Vapors of a *p*-xylene/toluene mixture containing the components in different proportions were detected. The possibility of determining the concentration of compounds in a two-component mixture is confirmed.

It was found that after stopping the exposure, the position of the photonic bandgap is almost completely recovered. This fact allows one to perform chemical cycles or online environmental monitoring. However, when exposed to aromatic solvents, sensor degradation is observed, but its linear direction should be noted.

Experimental

Materials

Submicrometer particles from linear polystyrene have been synthesized in the Institute of Fine Chemical Technologies RTU MIREA [42]. The sensor matrix has been developed from PDMS "Sylgard 184 silicone elastomer" (Dow Corning, USA). The following organic solvents have been used as analytes: benzene "pur." and toluene "p.a." (Reakhim, Russia); *p*-xylene "pur.", *n*-pentane, "puriss.", *n*-heptane "puriss. spec." and *n*-decane "pur." (EKOS-1, Russia); *n*-octane "pur." (Acros Organics, Belgium/US).

Instruments

The average hydrodynamic radius of the PS particles has been determined by using the DLS method on a "Zetasizer Nano ZS" (Malvern Panalytical Ltd, UK) device. Microstructures of sensor matrices have been tested by using the SEM method on an "NVision 40" (Carl Zeiss, Inc., Germany) device and a specular reflectance spectrophotometer "Lambda 950" (PerkinElmer, Inc., USA) in the visible range of the electromagnetic spectrum. The diffuse reflectance spectra have been recorded on a spectrophotometer "Ci7800" (X-Rite, Inc., USA) in the visible range of the electromagnetic spectrum in SCI and SCE modes. The studies of kinetics have been carried out using a mini-spectrophotometer "eye-one Pro" (X-Rite, Inc., USA). The thickness of the stimuli-responsive layer (PDMS and CCA) has been measured by using a "Constant K5" thickness gauge (KONSTANTA LLC, Russia) with an ID2 induction converter. The SEM images have been obtained at the Centre of Shared Equipment of IGIC RAS.

Sensors

A composite sensor based on 3D PhC, which has a sandwich design, has been used for the experiments. The opal structure is formed on a glass or polymer (polycarbonate or polyethylene terephthalate) substrate. The structure has a close-packed crystal lattice, the nodal points of which contain spherical submicrometer particles of polystyrene with a hydrodynamic diameter of 239.5 nm (polydispersity index 0.101), determined by the DLS method. The CCA has been obtained by self-organization from a water–ethanol suspension [43]. The formed structure was covered with a hydrophobic polymer material layer, that is, polydimethylsiloxane of a specified thickness, which serves as a sensitive layer and mechanically protects the CCA. Sensors with a glass carrier have better optical characteristics but are inferior to polymer regarding material strength.

Method

Figure 8a shows the scheme of the experimental equipment. It consists of the spectrophotometer "eye-one Pro" and a peripheral device, which is made of black composite material based on epoxy resins for visible-light absorption and to elude backward reflection. The diffuse reflectance spectra have been recorded automatically by using the standard software "i1Share v1.4" (X-Rite, Incorporated, USA) and a scripting language program that allowed for receiving data on a preset periodic base. Temperature, pressure and humidity were monitored by a BMP280 sensor (Robert Bosch GmbH, Germany).

A sample of the PhC sensor (Figure 8b) was installed on a cuvette with an analyte solution and fixed with a clamp to avoid vapor leakage during the exposure. The sensitive side of the sample was faced into the cuvette with an analyte and the diffuse reflectance spectra were recorded through the optically transparent carrier. A negligible reflection of the polycarbonate substrate is in the blue spectrum region (below 420 nm) and does not overlap with the reflection of the photonic crystal. As a result of the experiment, we obtained spectra measured at a predetermined time interval (Figure 8c). The color of the sensor changed from green to red (Figure 8d).

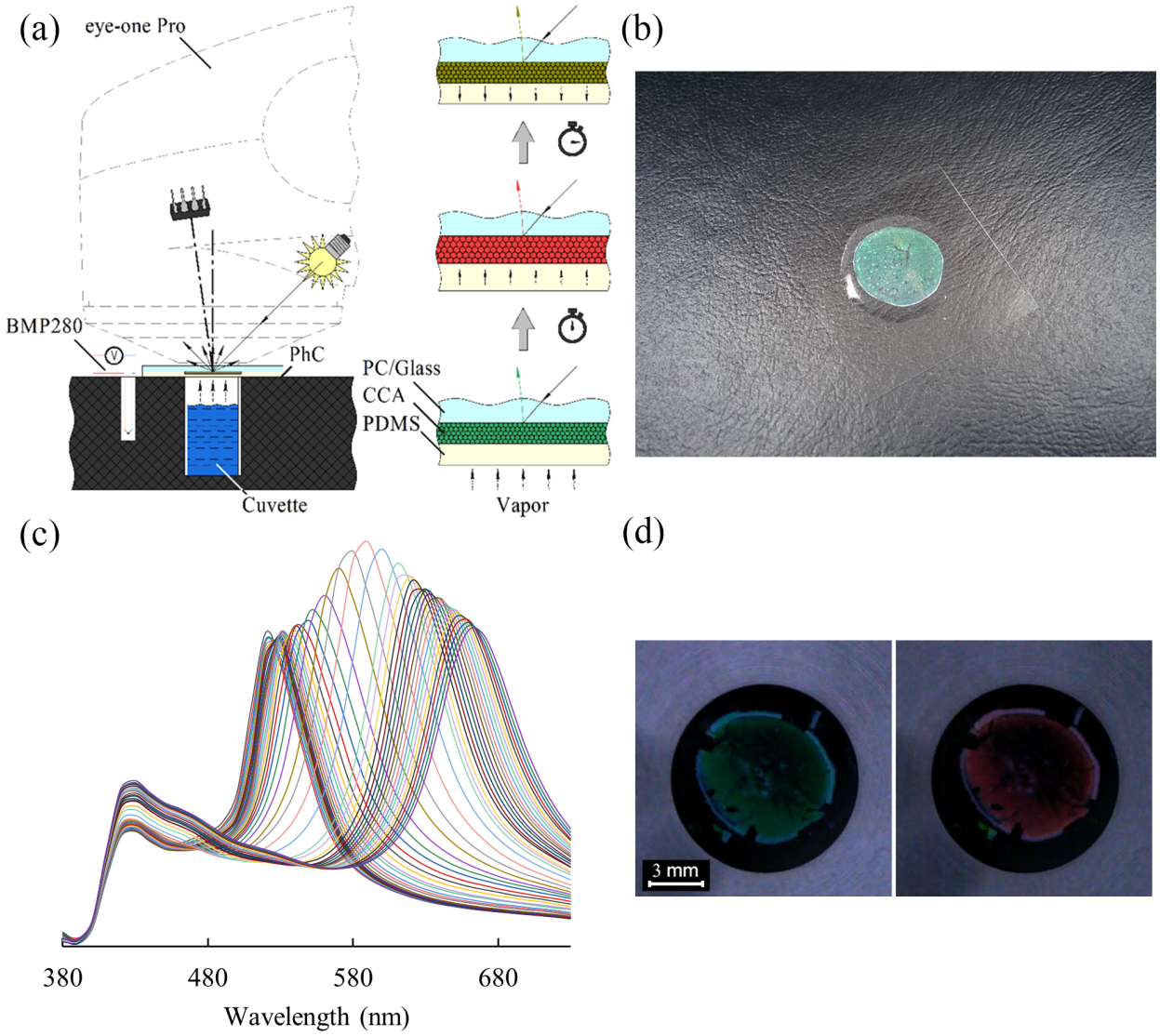


Figure 8: Key points of the experiments: (a) scheme of the experimental equipment; (b) a photo image of the sensor; (c) redshift upon exposure of saturated hydrocarbon vapors on the sensor; (d) photo image of the sensor before and during the exposure.

Funding

A part of this work was performed under a state assignment on basic scientific research for the Kurnakov Institute of General and Inorganic Chemistry, Russian Academy of Sciences (Moscow, Russia) using the equipment of the Joint research centre for physical methods of research of IGIC RAS (JRC PMR IGIC RAS).

ORCID® iDs

Evgenii S. Bolshakov - https://orcid.org/0000-0003-3557-826X
Aleksander V. Ivanov - https://orcid.org/0000-0002-3356-0405
Elena V. Isanbaeva - https://orcid.org/0000-0002-7277-4895
Aleksander E. Baranchikov - https://orcid.org/0000-0002-2378-7446

References

1. Wang, Z.; Zhang, J.; Li, J.; Xie, J.; Li, Y.; Liang, S.; Tian, Z.; Li, C.; Wang, Z.; Wang, T.; Zhang, H.; Yang, B. *J. Mater. Chem.* **2011,** *21,* 1264–1270. doi:10.1039/c0jm02655g
2. Smith, N. L.; Hong, Z.; Asher, S. A. *Analyst* **2014,** *139,* 6379–6386. doi:10.1039/c4an01485e
3. Elsherif, M.; Hassan, M. U.; Yetisen, A. K.; Butt, H. *ACS Nano* **2018,** *12,* 5452–5462. doi:10.1021/acsnano.8b00829
4. Lova, P.; Comoretto, D. *AIP Conf. Proc.* **2018,** *1981,* 020097. doi:10.1063/1.5045959
5. Chen, C.; Dong, Z.-Q.; Shen, J.-H.; Chen, H.-W.; Zhu, Y.-H.; Zhu, Z.-G. *ACS Omega* **2018,** *3,* 3211–3217. doi:10.1021/acsomega.7b02046
6. Qi, F.; Yan, C.; Meng, Z.; Li, S.; Xu, J.; Hu, X.; Xue, M. *Anal. Bioanal. Chem.* **2019,** *411,* 2577–2585. doi:10.1007/s00216-019-01700-w

7. Burratti, L.; Casalboni, M.; De Matteis, F.; Pizzoferrato, R.; Prosposito, P. *Materials* **2018,** *11,* 1547. doi:10.3390/ma11091547
8. Sato, A.; Ikeda, Y.; Yamaguchi, K.; Vohra, V. *Nanomaterials* **2018,** *8,* 169. doi:10.3390/nano8030169
9. Burratti, L.; De Matteis, F.; Casalboni, M.; Francini, R.; Pizzoferrato, R.; Prosposito, P. *Mater. Chem. Phys.* **2018,** *212,* 274–281. doi:10.1016/j.matchemphys.2018.03.039
10. Li, G.; Xiao, F.; Liao, S.; Chen, Q.; Zhou, J.; Wu, Z.; Yu, R. *Sens. Actuators, B* **2018,** *277,* 591–597. doi:10.1016/j.snb.2018.09.059
11. Hong, W.; Li, H.; Hu, X.; Zhao, B.; Zhang, F.; Zhang, D. *Chem. Commun.* **2012,** *48,* 4609–4611. doi:10.1039/c2cc30927k
12. Yuan, Y.; Li, Z.; Liu, Y.; Gao, J.; Pan, Z.; Liu, Y. *Chem. – Eur. J.* **2012,** *18,* 303–309. doi:10.1002/chem.201102001
13. Zhang, Y.-H.; Ren, H.-H.; Yu, L.-P. *Anal. Methods* **2018,** *10,* 101–108. doi:10.1039/c7ay02283b
14. Busch, K.; John, S. *Phys. Rev. E* **1998,** *58,* 3896–3908. doi:10.1103/physreve.58.3896
15. Wang, F.; Zhu, Z.; Xue, M.; Xue, F.; Wang, Q.; Meng, Z.; Lu, W.; Chen, W.; Qi, F.; Yan, Z. *Sens. Actuators, B* **2015,** *220,* 222–226. doi:10.1016/j.snb.2015.05.057
16. Kuo, W.-K.; Weng, H.-P.; Hsu, J.-J.; Yu, H. H. *Mater. Chem. Phys.* **2016,** *173,* 285–290. doi:10.1016/j.matchemphys.2016.02.014
17. Baca, J. T.; Finegold, D. N.; Asher, S. A. *Analyst* **2008,** *133,* 385–390. doi:10.1039/b712482a
18. Arunbabu, D.; Sannigrahi, A.; Jana, T. *Soft Matter* **2011,** *7,* 2592–2599. doi:10.1039/c0sm01136c
19. Lin, F. Y.; Yu, L. P. *Anal. Methods* **2012,** *4,* 2838–2845. doi:10.1039/c2ay25408e
20. Ruan, J.-L.; Chen, C.; Shen, J.-H.; Zhao, X.-L.; Qian, S.-H.; Zhu, Z.-G. *Polymers (Basel, Switz.)* **2017,** *9,* 125. doi:10.3390/polym9040125
21. Zeng, F.; Wu, S.; Sun, Z.; Xi, H.; Li, R.; Hou, Z. *Sens. Actuators, B* **2002,** *81,* 273–276. doi:10.1016/s0925-4005(01)00965-0
22. Sharma, A. C.; Jana, T.; Kesavamoorthy, R.; Shi, L.; Virji, M. A.; Finegold, D. N.; Asher, S. A. *J. Am. Chem. Soc.* **2004,** *126,* 2971–2977. doi:10.1021/ja038187s
23. Walker, J. P.; Asher, S. A. *Anal. Chem. (Washington, DC, U. S.)* **2005,** *77,* 1596–1600. doi:10.1021/ac048562e
24. Xiao, F.; Li, G.; Wu, Y.; Chen, Q.; Wu, Z.; Yu, R. *Anal. Chem. (Washington, DC, U. S.)* **2016,** *88,* 9207–9212. doi:10.1021/acs.analchem.6b02457
25. Song, Y.; Bai, J.; Zhang, R.; He, H.; Li, C.; Wang, J.; Li, S.; Peng, Y.; Ning, B.; Wang, M.; Gao, Z. *Anal. Chem. (Washington, DC, U. S.)* **2018,** *90,* 1388–1394. doi:10.1021/acs.analchem.7b04655
26. Yan, C.; Qi, F.; Li, S.; Xu, J.; Liu, C.; Meng, Z.; Qiu, L.; Xue, M.; Lu, W.; Yan, Z. *Talanta* **2016,** *159,* 412–417. doi:10.1016/j.talanta.2016.06.045
27. Xu, J.; Yan, C.; Liu, C.; Zhou, C.; Hu, X.; Qi, F. *IOP Conf. Ser.: Mater. Sci. Eng.* **2017,** *167,* 012024. doi:10.1088/1757-899x/167/1/012024
28. Guo, C.; Zhou, C.; Sai, N.; Ning, B.; Liu, M.; Chen, H.; Gao, Z. *Sens. Actuators, B* **2012,** *166-167,* 17–23. doi:10.1016/j.snb.2011.10.082
29. Sai, N.; Ning, B.; Huang, G.; Wu, Y.; Zhou, Z.; Peng, Y.; Bai, J.; Yu, G.; Gao, Z. *Analyst* **2013,** *138,* 2720–2728. doi:10.1039/c3an36829g
30. Matsuguchi, M.; Uno, T. *Sens. Actuators, B* **2006,** *113,* 94–99. doi:10.1016/j.snb.2005.02.028
31. Alizadeh, T.; Rezaloo, F. *Int. J. Environ. Anal. Chem.* **2013,** *93,* 919–934. doi:10.1080/03067319.2012.708744
32. Shim, D.-Y.; Chang, S.-M.; Kim, J. M. *Sens. Actuators, B* **2021,** *329,* 129143. doi:10.1016/j.snb.2020.129143
33. Bol'shakov, E. S.; Ivanov, A. V.; Kozlov, A. A.; Abdullaev, S. D. *Russ. J. Phys. Chem. A* **2018,** *92,* 1530–1534. doi:10.1134/s0036024418080083
34. Woodcock, L. V. *Nature* **1997,** *385,* 141–143. doi:10.1038/385141a0
35. Abrarov, S. M.; Kim, T. W.; Kang, T. W. *Opt. Commun.* **2006,** *264,* 240–246. doi:10.1016/j.optcom.2006.05.039
36. Fudouzi, H. *J. Colloid Interface Sci.* **2004,** *275,* 277–283. doi:10.1016/j.jcis.2004.01.054
37. Gajiev, G. M.; Golubev, V. G.; Kurdyukov, D. A.; Medvedev, A. V.; Pevtsov, A. B.; Sel'kin, A. V.; Travnikov, V. V. *Phys. Rev. B* **2005,** *72,* 205115. doi:10.1103/physrevb.72.205115
38. Sinitskii, A. S.; Khokhlov, P. E.; Abramova, V. V.; Laptinskaya, T. V.; Tretyakov, Y. D. *Mendeleev Commun.* **2007,** *17,* 4–6. doi:10.1016/j.mencom.2007.01.002
39. Schneider, F.; Draheim, J.; Kamberger, R.; Wallrabe, U. *Sens. Actuators, A* **2009,** *151,* 95–99. doi:10.1016/j.sna.2009.01.026
40. Sultanova, N.; Kasarova, S.; Nikolov, I. *Acta Phys. Pol., A* **2009,** *116,* 585–587. doi:10.12693/aphyspola.116.585
41. Rumens, C. V.; Ziai, M. A.; Belsey, K. E.; Batchelor, J. C.; Holder, S. J. *J. Mater. Chem. C* **2015,** *3,* 10091–10098. doi:10.1039/c5tc01927c
42. Shragin, D. I.; Gritskova, I. A.; Kopylov, V. V.; Milushkova, E. V.; Zlydneva, L. A.; Levachev, S. M. *Silicon* **2015,** *7,* 217–227. doi:10.1007/s12633-014-9265-4
43. Ivanov, A. V.; Kozlov, A. A.; Koreshkova, A. N.; Abdullaev, S. D.; Fedorova, I. A. *Moscow Univ. Chem. Bull. (Engl. Transl.)* **2017,** *72,* 19–23. doi:10.3103/s0027131417010060

License and Terms

This is an open access article licensed under the terms of the Beilstein-Institut Open Access License Agreement (https://www.beilstein-journals.org/bjnano/terms), which is identical to the Creative Commons Attribution 4.0 International License (https://creativecommons.org/licenses/by/4.0). The reuse of material under this license requires that the author(s), source and license are credited. Third-party material in this article could be subject to other licenses (typically indicated in the credit line), and in this case, users are required to obtain permission from the license holder to reuse the material.

The definitive version of this article is the electronic one which can be found at:
https://doi.org/10.3762/bjnano.13.9

BEILSTEIN JOURNAL OF NANOTECHNOLOGY

Piezoelectric nanogenerator for bio-mechanical strain measurement

Zafar Javed[1], Lybah Rafiq[2], Muhammad Anwaar Nazeer[2], Saqib Siddiqui[3], Muhammad Babar Ramzan[2], Muhammad Qamar Khan[4] and Muhammad Salman Naeem[*1]

Full Research Paper

Open Access

Address:
[1]School of Arts and Design, National Textile University, 37610, Faisalabad, Pakistan, [2]School of Engineering and Technology, National Textile University, 37610, Faisalabad, Pakistan, [3]Sapphire Finishing Mills Limited, Lahore, Pakistan and [4]Department of Clothing, Faculty of Textile Engineering, National Textile University, Karachi Campus, Pakistan

Email:
Muhammad Salman Naeem[*] - salman@ntu.edu.pk

* Corresponding author

Keywords:
electrospinning; human body angle measurement; nanofibers; piezoelectric; PVDF

Beilstein J. Nanotechnol. **2022,** *13,* 192–200.
https://doi.org/10.3762/bjnano.13.14

Received: 08 October 2021
Accepted: 25 January 2022
Published: 07 February 2022

This article is part of the thematic issue "Nanomaterial-based sensors for water remediation, healthcare and food monitoring applications".

Guest Editor: A. A. Oladipo

© 2022 Javed et al.; licensee Beilstein-Institut.
License and terms: see end of document.

Abstract

Piezoelectric materials have attracted more attention than other materials in the field of textiles. Piezoelectric materials offer advantages as transducers, sensors, and energy-harvesting devices. Commonly, ceramics and quartz are used in such applications. However, polymeric piezoelectric materials have the advantage that they can be converted into any shape and size. In smart textiles, polyvinylidene fluoride (PVDF) and other piezoelectric polymers are used in the form of fibers, filaments, and composites. In this research, PVDF nanofibers were developed and integrated onto a knitted fabric to fabricate a piezoelectric device for human body angle monitoring. Scanning electron microscopy and X-ray diffraction analyses were used to study the morphology and to confirm the beta phase in fibers. The results reveal that the nanofibers made from solutions with high concentration were smooth and defect-free, compared to the fibers obtained from solutions with low concentration, and possess high crystallinity as well. Under high dynamic strain more output voltage is generated than under low dynamic strain. The maximum current density shown by the device is 172.5 nA/cm^2. The developed piezoelectric nanofiber sensor was then integrated into a knitted fabric through stitching to be used for angle measurement. With increasing bending angle, the output voltage increased. The promising results show that the textile-based piezoelectric sensor developed in this study has a great potential to be used as an angle measuring wearable device for the human body due to its high current density output and flexibility.

Introduction

Smart textiles are normally elevated to value-added textile products with improved properties and characteristics [1]. They exhibit properties of a textile with some added characteristics. Smart textiles are obtaining by combining conventional textile techniques, such as knitting or weaving, with different technologies of electronics [2]. The world is moving towards intelligent or smart textiles. In 2012, the size of the smart textile market was almost $289.5 million and surged to $1,500 million in 2020. The integration of electronically active fibers or yarns in textile substrates is the basis of smart textiles [3]. Textile-based sensors and electrodes are composed of conductive fibers, threads, or fabrics [4]. Their use for physiological and medical examination has been rising rapidly in the last couple of years. Textile-based sensors, being flexible, are easy to fit in a garment and create no barrier to the wearer. Nowadays, wearable sensors based on conductive threads and conductive polymers are capable of measuring vital signs of the human body [4,5]. Tognetti et al. [6] designed and developed a resistive strain sensors for movement analysis. They integrated an electrically conductive elastomer into a fabric, which was then able to detect the posture and the movement of the human body. Retrieved data from these strain sensors were compared with conventional motion tracking systems. The results show promising performance for body posture classification and reconstruction. Similarly, for measuring human body angles, piezoresistive sensors were developed and characterized under bending and stretching regarding the application as strain sensors [7]. Knitted piezoresistive fabrics were used to develop sensors that were a wearable type of a goniometer. These sensors were then tested under static and dynamic conditions. For another application, researchers designed and developed a purely textile-based capacitive pressure sensor to be integrated and embedded into the garments to monitor and measure human body pressure. These sensors were beneficial for pressure sore prevention, rehabilitation, and the detection of movement during activities. Further, these sensors were comfortable and bendable and were applied onto the upper portion of an arm to detect the deflection of the forearm during muscle bending [8]. Park et al. [9] developed a self-powered piezoelectric sensor for monitoring the pulse rate in real time. A pressure sensor was attached to the epidermis for monitoring pulse and assessing personal health status. Traditional sensors for pulse monitoring can detect biosignals of the human body but they have the limitation of power supply, which will restrict the operation of the wearable devices for medical purposes. Hence, piezoelectric sensors were used for monitoring bio-signals of the human body without limitation of power supply. Moreover, Lorussi and co-workers developed a smart textile garment by embedding a strain sensor into an ordinary garment. For the piezoelectric effect, the conductive blend was applied onto the fabric, which resulted in a change in resistance under strain. This phenomenon was used in gloves, car seats, and leotards for determining body posture, shape, and gesture. They primarily focused on studying a leg pad that was able to perceive the knee movement and posture [10]. Piezoelectric sensors have a wide range of applications including sidewalks or crosswalks that collect energy from vibrations, which can be store in batteries [11]. Moreover, piezoelectric sensors can be used at workplaces and gyms to collect energy from machine vibrations [12]. These sensors are embedded under the shoes so that the pressure exerted during walking or running can be converted into energy and can be used for different applications. Piezoelectric sensors can also be used under mats and floors so the pressure due to footsteps can be utilized as a source to generate energy [13]. Besides these, piezoelectric sensors can also be used for sensing human body motion and monitoring physical health parameters, such as electrocardiograms [14-19]. Polyvinylidene fluoride (PVDF), having a semicrystalline structure, is generally synthesized through polymerization of vinylidene difluoride [20]. It generally has four crystalline phases, namely α, β, ε, and γ. Among them, the beta phase possesses the highest dipole movements, while the other phases are usually non-polar as their structural packing is antiparallel [21]. Usually, PVDF is non-reactive towards acids and bases. It was discovered in 1969 that PVDF can produce electrical signals. Thus, it can be used in various applications of energy harvesting, in various forms such as fibers, films, monofilaments, and powder. This material is trending in textile-based research where different researchers are working to manufacture smart textiles to generate energy [22,23]. Nanofibers have many technical applications such as in air and liquid filtration [24,25], tissue engineering [26,27], drug delivery [28], wound dressings [29], sound adsorption [30], cosmetics [31], and sensor devices [32-34]. In filtration processes, electrospun nanofibers can be employed for removing volatile organic compounds (VOCs) from the atmosphere. To protect people from bacteria, viruses, smog, and dust, nanofibers are utilized in medical face masks. These masks will not allow the particles to be inhaled because of the small pore size of the nanofibrous scaffold, while oxygen molecules are small enough to pass through these pores. Nanofibers are also used in other medical applications, for instance, for developing artificial organs and blood vessels, and in gene and drug delivery [35]. Monitoring joint angles through wearable systems enables human posture and gesture to be reconstructed as a support for physical rehabilitation both in clinics and at the patients' home [36]. To date, wearable sensors used for monitoring body movements in the market are battery-based. The battery needs to be worn all the time. Also, it needs to be charged or replaced, which makes its application impractical. In this work, we present a proof of concept for using a nanofi-

brous-based piezoelectric sensor composed of PVDF, which is capable of monitoring body angles. This sensor will be able to replace the battery being used in commonly available products and is more breathable, lightweight, and flexible. The developed sensor has been characterized through advanced techniques. The current density has been calculated and compared with the current state of the art. To the best of our knowledge, the PVDF-based nanofibrous device developed in this study is superior to previously reported ones.

Experimental

Materials

Polyvinylidene fluoride (PVDF) obtained from Alfa Aesar was used as a piezoelectric material. Dimethylformamide (DMF) and acetone from Sigma-Aldrich were used as solvents without any further purification. A conductive tape was used to make electrodes. Knitted fabric was used for the integration of the nanofibrous mesh for human body angle measurement.

Fabrication of the nanofibrous mesh and its characterization

PVDF solutions with varying concentrations (12, 14, and 16 wt %) were prepared in an acetone/DMF mixture (1:2.3 by volume). PVDF was dissolved in the acetone/DMF mixture at 120 °C in a sealed container under stirring for 4 h followed by incubating the solutions at room temperature for 24 h before electrospinning. A conventional electrospinning process was used to create the piezoelectric electrospun nanofibers. The polymeric solution was pumped from a metallic syringe needle of 0.4 mm inner diameter at a flow rate of 3.5 mL/h. The fibers were collected on a stationary collector placed at a working distance of 15 cm. A constant voltage of 15 kV was used for all the experiments. The nanofibrous meshs were first dried at room temperature in the fume hood for 24 h followed by drying in a vacuum oven until constant weight to ensure the complete evaporation of the solvents. PVDF nanofibers were characterized through scanning electron microscopy (SEM) and X-ray diffraction (XRD) to determine morphology and crystalline structure, respectively.

Sensor development, its embedding, and testing

The prepared PVDF nanofibrous mesh was folded into a square shape (4 cm^2) with 2 mm thickness for sensor development. Subsequently, conductive tape was attached to both sides of the film in a way that it covered the maximum area of the sheet (Figure 1).

The developed piezoelectric sensor was tested in knee angle measurements using a digital oscilloscope. The sensor was exposed to low and high dynamic strains with varying frequencies to examine their effect on the output voltage. Then the developed sensor was integrated and stitched on a knitted fabric to check the effect of the bending angle on the output voltage.

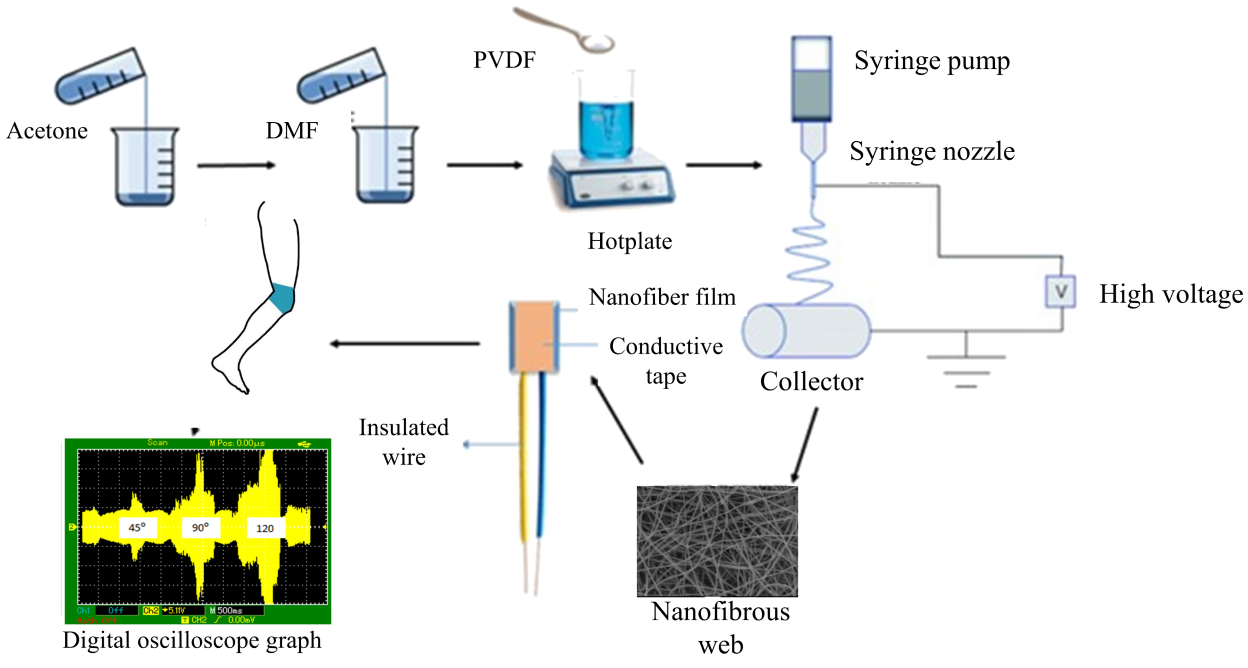


Figure 1: Illustration representing the scheme for sensor development.

Staple spun polyester thread was used to stitch the sensor onto the knitted fabric by using a lockstitch machine. The sensor was worn on the knee and the bending angle of the knee was changed from 0° to 45°, 90°, and 120° to check the piezoelectric output with a digital oscilloscope.

Results and Discussion

SEM analysis

SEM was used to study the diameter and morphology of PVDF nanofibers developed through three different PVDF solutions (12, 14, and 16 wt %). The secondary electron images, taken at 10,000× and 40,000×, magnifications of prepared PVDF electrospun films from a 12 wt % polymer solution are shown in Figure 2A. The images show that the nanofibers have a more bead-on-string-like structure than the nanofibers obtained from 14 wt % solution (Figure 2B) due to incomplete solvent evaporation. The optimum polymer solution concentration is essential to obtain defect-free smooth fibers [14,37]. The nanofibers obtained from 16 wt % solution were smooth and presented a bead-free morphology (Figure 2C). Therefore, these fibers were selected for developing the piezoelectric sensor. The average diameter of the fibers obtained from different solutions is provided in Figure 2D.

XRD analysis

PVDF exhibits four crystalline structures: α, β, γ, and δ [38]. Normally, all phases of PVDF show almost similar peaks with the exception of unique peaks that are used to identify the crystalline structure. X-ray diffractograms were used to analyze the crystalline structure [39] of prepared PVDF nanofibrous meshs obtained from different solutions to identify the beta phase in the fibers, which is primarily accountable for piezoelectric characteristics. PVDF showed its strongest peak near θ = 20°. The alpha phase has a peak around 18° [40], the γ phase has its intense peak at 19.2° [41], while the beta phase exhibits peaks between 20.04 and 22.03° (Figure 3).

It can be seen that the beta phase is dominant in the fibers obtained from the 16 wt % solution compared to the solutions of 12 and 14 wt %. The crystallinity was calculated from the XRD diffractograms and came out to be 52.3%, 54.6%, and 57.7% for the fibers made from 12, 14, and 16 wt % solutions, respectively. This phenomenon can be correlated with the high concentration of polymer solution. During evaporation of the solvent, polymer chains are more likely to form crystalline structures because they are closer together than in the solutions with lower concentration Also, when the polymer

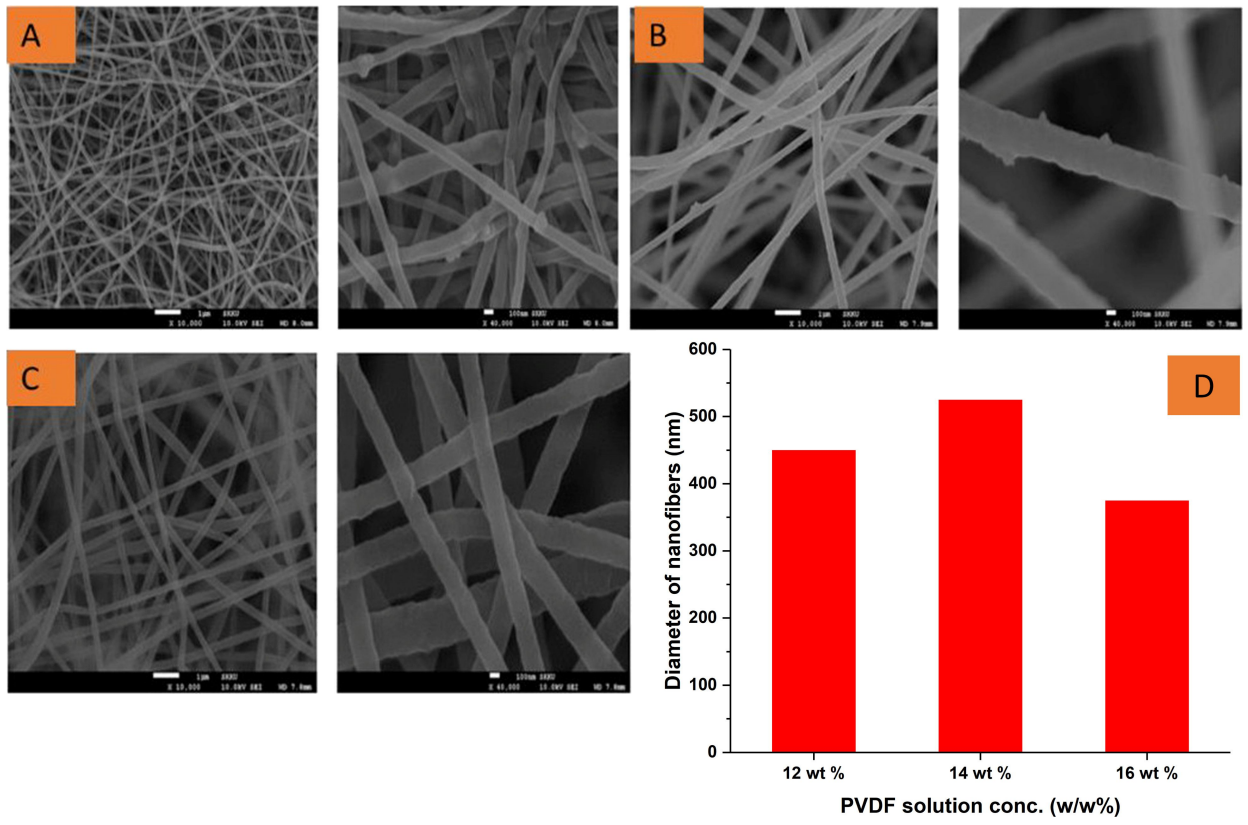


Figure 2: SEM images of nanofibers developed from 12 wt % (A), 14 wt % (B), and 16 wt % (C). PVDF solution and average diameter variation of nanofibers against different solution concentrations (D).

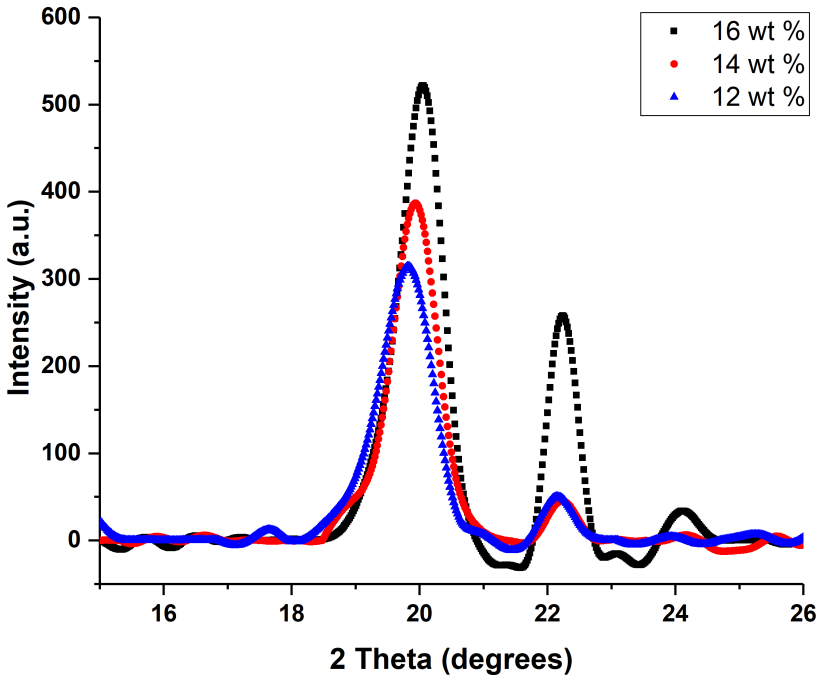


Figure 3: X-ray diffraction pattern of nanofibers at various concentrations.

amount increases in the solution it increases generation capacity [37].

Digital oscilloscope analysis

The nanofibrous mesh made from the 16 wt % solution was selected for developing the sensor (Figure 4F). These nanofibers have a smooth and defect-free morphology with highly crystalline regions, which indicate the complete evaporation of the solvent and the presence of a large amount of polymer. To check the piezoelectric output of the developed sensor, a digital oscilloscope was used and the sensor was tapped with the fingers. Silicon gloves were used to avoid any possible static charges influence [42].

The sensor was placed on a smooth surface and the wires of the sensor were connected to the probes of a digital oscilloscope. Low dynamic strain was applied onto the sensor by pressing the sensor with a finger and then lifting the finger. The process was repeated continuously to obtain the effect of low strain on the piezoelectric output. Figure 4A illustrates the result of the digital oscilloscope showing output voltage when the sensor was under to low strain. The graph showing the piezoelectric output of the PVDF nanofibrous sensor under low dynamic strain is presented in Figure 4B. It shows that under low dynamic strain the energy generation is small. To check the impact of high strain, the previous process was repeated by pressing the sensor with a high dynamic strain. Figure 4C demonstrates the result of the digital oscilloscope showing output voltage when the sensor was under high dynamic strain. The result of the piezoelectric output of PVDF nanofibrous sensor under high dynamic strain is shown in Figure 4D. Under high dynamic strain, the generated energy is higher than under low dynamic strain, which shows the direct relation between pressure and piezoelectric output. To check the impact of the frequency on the piezoelectric output, the sensor wires were attached to the probes of the digital oscilloscope and a high-frequency dynamic strain was applied onto the sensor by pressing the sensor with a finger and lifting the finger at high speed. Figure 4E shows the result of the digital oscilloscope showing the output voltage of the sensor under dynamic strain at high frequency.

To show the potential application of the developed sensor, the relation of the bending angle with the output voltage was established. For this, the sensor was integrated into a knitted fabric through stitching and a prototype representing a knee medical pad was developed (Figure 5A). The medical pad was worn onto a knee, and the knee was moved at different angles to check the output. The knee was moved from 0° degrees to 120° (Figure 5B). The effect of the bending angle on the output voltage was measured. When the bending angle was 45°, the output voltage was less than the output voltages at 90° and 120° because, with increasing angle, the sensor was more strained. Therefore, the bending angle and the output voltage are directly related. Figure 5C illustrates the voltage change with the change of the bending angle of the knee. The current density of the

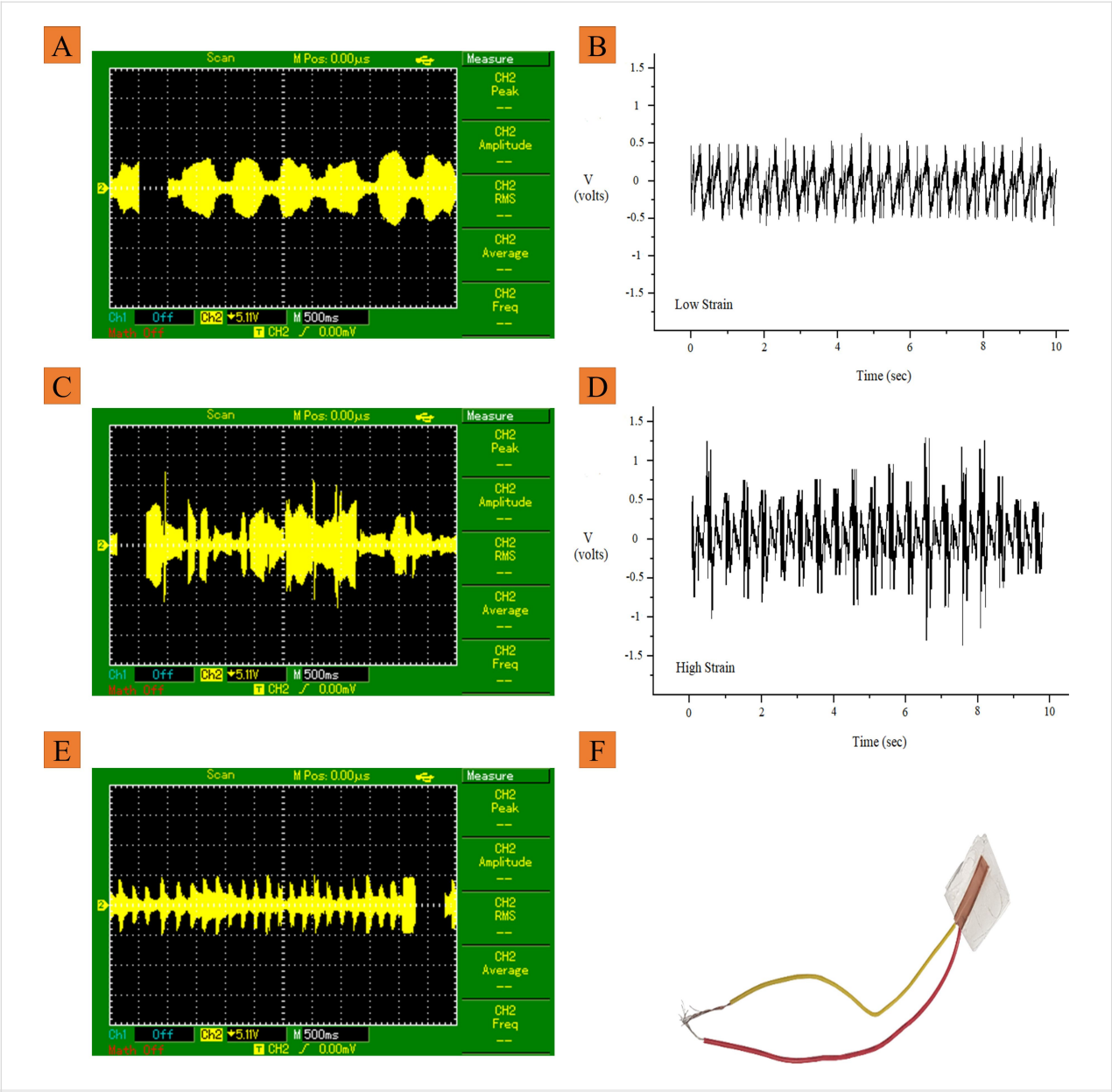


Figure 4: Digital oscilloscope graph of the sensor under low dynamic strain (A), the output voltage under low dynamic stress (B), digital oscilloscope graph of the sensor under high dynamic strain (C), the output voltage under high dynamic stress (D), digital oscilloscope graph of the sensor under low dynamic strain but with high frequency (E), and a piezoelectric sensor developed from 16 wt % solution (F).

device has been calculated and compared with the current state of the art (Table 1). Clearly, the highest efficiency is shown by the device developed in the current study.

Conclusion

An experimental study on a textile-based piezoelectric sensor for human body angle monitoring has been performed. In this research, the polymeric material PVDF was used for the development of a piezoelectric nanofibrous sensor. SEM and XRD analyses were performed to determine morphology and crystalline phases of the developed nanofibers, respectively. The SEM analysis of nanofibers confirmed smooth, defect-free, and uniform fibers produced from a solution of high concentration (16 wt %). Additionally, the highest content of the beta phase was present in the nanofibrous mesh developed from the highly concentrated solution. Therefore, these fibers were selected for developing a piezoelectric sensor for subsequent studies. For this, the sensor was integrated into a knitted fabric through stitching to make a wearable textile-based piezoelectric sensor for human body angle monitoring. The piezoelectric output was measured by using a digital oscilloscope. The output voltage was high for high dynamic strain, which was also confirmed by

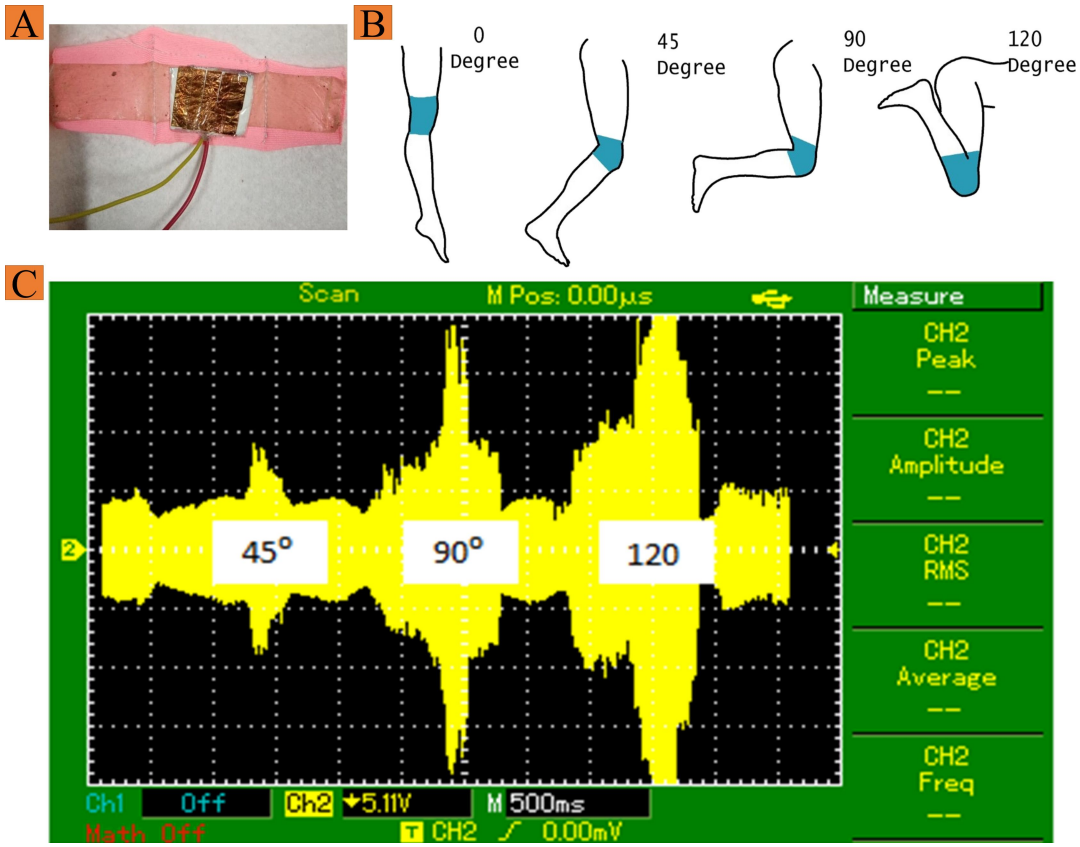


Figure 5: Integration of nanofibrous mesh into a knitted fabric for human body angle measurement (A), schematics showing the dressed knee at different bending angles (B), and digital oscilloscope graph at the corresponding angles (C).

Table 1: Comparative study of the current density.

Sr. No.	Functional material	Form	Volts (V)	Current (nA)	Current density (nA/cm^2)	Reference
1	PZT	nanotubes	1.00	40.00	—	[43]
2	PZT	single crystal	200.00	8000.00	150.00	[44]
3	PZT	composite	10.00	1300.00	0.20	[45]
4	PVDF-TrFE	thin film	7.00	58.00	0.56	[46]
5	PVDF	nanofiber	2.1	690	172.50	current study

changing the angle of the knee. The higher angle exerts more strain onto the sensor, which generates a high voltage in return. The piezoelectric output also increased when the frequency of the dynamic strain was increased. The textile-based piezoelectric sensor developed in this study has a great potential to be used as an angle measuring wearable device for the human body due to its high current density output and flexibility.

Funding

The authors sincerely acknowledge the financial support from the Higher Education Commission, Pakistan under the project of Technology Development Fund, grant number: TDF03-338.

ORCID® iDs

Muhammad Anwaar Nazeer - https://orcid.org/0000-0002-7906-8010
Muhammad Babar Ramzan - https://orcid.org/0000-0002-0401-4253

References

1. Orzan, C. M.; Florescu, M. S.; Zara, I. A.; Orzan, O. A. *Ind. Text. (Bucharest, Rom.)* **2020,** *71,* 572–575. doi:10.35530/it.071.06.202018
2. Song, Y.; Lee, S.; Choi, Y.; Han, S.; Won, H.; Sung, T.-H.; Choi, Y.; Bae, J. *Fash. Text.* **2021,** *8,* 6. doi:10.1186/s40691-020-00237-2
3. Dalsgaard, C.; Sterrett, R. *Market Opportunities for Smart Textiles;* Ohmatex: Denmark, 2014.
4. Baima, M.; Andrew, T. L. *Fibers* **2018,** *6,* 41. doi:10.3390/fib6020041

5. *2011 International Conference on Control, Automation and Systems Engineering (CASE),* IEEE, 2011.
6. Tognetti, A.; Bartalesi, R.; Lorussi, F.; De Rossi, D. *Trans. Inst. Meas. Control (London)* **2007,** *29,* 215–253. doi:10.1177/0142331207069487
7. Tognetti, A.; Lorussi, F.; Dalle Mura, G.; Carbonaro, N.; Pacelli, M.; Paradiso, R.; De Rossi, D. *J. NeuroEng. Rehabil.* **2014,** *11,* 56. doi:10.1186/1743-0003-11-56
8. *2006 10th IEEE International Symposium on Wearable Computers,* IEEE, 2006.
9. Park, D. Y.; Joe, D. J.; Kim, D. H.; Park, H.; Han, J. H.; Jeong, C. K.; Park, H.; Park, J. G.; Joung, B.; Lee, K. J. *Adv. Mater. (Weinheim, Ger.)* **2017,** *29,* 1702308. doi:10.1002/adma.201702308
10. Lorussi, F.; Tognetti, A.; Tesconi, M.; Pastacaldi, P.; De Rossi, D. *Stud. Health Technol. Inf.* **2004,** *108,* 266–270.
11. Yoshida, M.; Akiyama, S.; Moriyama, Y.; Takeshima, Y.; Kondo, Y.; Suwa, H.; Yasumoto, K. *Sens. Mater.* **2021,** *33,* 1–16. doi:10.18494/sam.2021.2999
12. Laumann, F.; Sørensen, M. M.; Jul Lindemann, R. F.; Hansen, T. M.; Tambo, T. *Energy Procedia* **2017,** *142,* 3062–3068. doi:10.1016/j.egypro.2017.12.445
13. Madokoro, H. Piezoelectric Sensors Used for Daily Life Monitoring. *Piezoelectricity - Organic and Inorganic Materials and Applications;* InTech: Rijeka, Croatia, 2018. doi:10.5772/intechopen.77724
14. Park, J.-S. *Adv. Nat. Sci.: Nanosci. Nanotechnol.* **2011,** *1,* 043002. doi:10.1088/2043-6262/1/4/043002
15. Alhasssan, Z. A.; Burezq, Y. S.; Nair, R.; Shehata, N. *J. Nanomater.* **2018,** 8164185. doi:10.1155/2018/8164185
16. Ding, Y.; Ji, C.; Yang, J.; Xu, M.; Yang, X. *Sens. Mater.* **2021,** *33,* 541–554. doi:10.18494/sam.2021.3094
17. Wu, M.; Wang, Y.; Gao, S.; Wang, R.; Ma, C.; Tang, Z.; Bao, N.; Wu, W.; Fan, F.; Wu, W. *Nano Energy* **2019,** *56,* 693–699. doi:10.1016/j.nanoen.2018.12.003
18. Sang, M.; Wang, S.; Liu, S.; Liu, M.; Bai, L.; Jiang, W.; Xuan, S.; Gong, X. *ACS Appl. Mater. Interfaces* **2019,** *11,* 47340–47349. doi:10.1021/acsami.9b16120
19. Yang, Y.; Pan, H.; Xie, G.; Jiang, Y.; Chen, C.; Su, Y.; Wang, Y.; Tai, H. *Sens. Actuators, A* **2020,** *301,* 111789. doi:10.1016/j.sna.2019.111789
20. Rana, D. S.; Chaturvedi, D.; Quamara, J. *J. Optoelectron. Adv. Mater.* **2009,** *11,* 705–712.
21. Sahu, M.; Hajra, S.; Lee, K.; Deepti, P.; Mistewicz, K.; Kim, H. J. *Crystals* **2021,** *11,* 85. doi:10.3390/cryst11020085
22. Zhang, Q. M.; Bharti, V.; Kavarnos, G. Poly(Vinylidene Fluoride) (PVDF) and its Copolymers. In *Encyclopedia of Smart Materials;* Schwartz, M., Ed.; John Wiley & Sons, Inc.: Hoboken, NJ, U.S.A., 2002. doi:10.1002/0471216275.esm063
23. Liu, Z. H.; Pan, C. T.; Lin, L. W.; Huang, J. C.; Ou, Z. Y. *Smart Mater. Struct.* **2014,** *23,* 025003. doi:10.1088/0964-1726/23/2/025003
24. Yalcinkaya, F.; Hruza, J. *Nanomaterials* **2018,** *8,* 272. doi:10.3390/nano8050272
25. Kaur, S.; Sundarrajan, S.; Rana, D.; Sridhar, R.; Gopal, R.; Matsuura, T.; Ramakrishna, S. *J. Mater. Sci.* **2014,** *49,* 6143–6159. doi:10.1007/s10853-014-8308-y
26. Nazeer, M. A.; Yilgor, E.; Yilgor, I. *Polymer* **2019,** *168,* 86–94. doi:10.1016/j.polymer.2019.02.023
27. Nazeer, M.; Yilgör, E.; Yilgör, I. Hydroxyapatite synthesis through sol-gel process and preparation of poly(lactic acid)/hydroxyapatite composites through electrospinning process. In *Conference: 15th AUTEX World Textile Conference 2015,* Bucharest, Romania, June 10–12, 2015; 2015.
28. Zhang, X.; Chi, C.; Chen, J.; Zhang, X.; Gong, M.; Wang, X.; Yan, J.; Shi, R.; Zhang, L.; Xue, J. *Mater. Des.* **2021,** *206,* 109732. doi:10.1016/j.matdes.2021.109732
29. Zhao, R.; Li, X.; Sun, B.; Zhang, Y.; Zhang, D.; Tang, Z.; Chen, X.; Wang, C. *Int. J. Biol. Macromol.* **2014,** *68,* 92–97. doi:10.1016/j.ijbiomac.2014.04.029
30. Kucukali Ozturk, M.; Nergis, F. B.; Candan, C. *Polym. Adv. Technol.* **2018,** *29,* 1255–1260. doi:10.1002/pat.4236
31. Miletić, A.; Pavlić, B.; Ristić, I.; Zeković, Z.; Pilić, B. *Appl. Sci.* **2019,** *9,* 2955. doi:10.3390/app9152955
32. Schoolaert, E.; Hoogenboom, R.; De Clerck, K. *Adv. Funct. Mater.* **2017,** *27,* 1702646. doi:10.1002/adfm.201702646
33. Pascariu, P.; Airinei, A.; Olaru, N.; Petrila, I.; Nica, V.; Sacarescu, L.; Tudorache, F. *Sens. Actuators, B* **2016,** *222,* 1024–1031. doi:10.1016/j.snb.2015.09.051
34. Singh, R. K.; Lye, S. W.; Miao, J. *Sens. Actuators, A* **2020,** *303,* 111841. doi:10.1016/j.sna.2020.111841
35. Zhao, Y.; Qiu, Y.; Wang, H.; Chen, Y.; Jin, S.; Chen, S. *Int. J. Polym. Sci.* **2016,** 4672839. doi:10.1155/2016/4672839
36. Gibbs, P. T.; Asada, H. H. *J. NeuroEng. Rehabil.* **2005,** *2,* 7. doi:10.1186/1743-0003-2-7
37. Cozza, E. S.; Monticelli, O.; Marsano, E.; Cebe, P. *Polym. Int.* **2013,** *62,* 41–48. doi:10.1002/pi.4314
38. Imamura, R.; Silva, A. B.; Gregorio, R., Jr. *J. Appl. Polym. Sci.* **2008,** *110,* 3242–3246. doi:10.1002/app.28851
39. Hajra, S.; Oh, Y.; Sahu, M.; Lee, K.; Kim, H.-G.; Panigrahi, B. K.; Mistewicz, K.; Kim, H. J. *Sustainable Energy Fuels* **2021,** *5,* 6049–6058. doi:10.1039/d1se01587g
40. Esterly, D. M.; Love, B. J. *J. Polym. Sci., Part B: Polym. Phys.* **2004,** *42,* 91–97. doi:10.1002/polb.10613
41. Martins, P.; Lopes, A. C.; Lanceros-Mendez, S. *Prog. Polym. Sci.* **2014,** *39,* 683–706. doi:10.1016/j.progpolymsci.2013.07.006
42. Mistewicz, K.; Jesionek, M.; Kim, H. J.; Hajra, S.; Kozioł, M.; Chrobok, Ł.; Wang, X. *Ultrason. Sonochem.* **2021,** *78,* 105718. doi:10.1016/j.ultsonch.2021.105718
43. Jung, W.-S.; Do, Y.-H.; Kang, M.-G.; Kang, C.-Y. *Curr. Appl. Phys.* **2013,** *13,* S131–S134. doi:10.1016/j.cap.2013.01.009
44. Park, K.-I.; Son, J. H.; Hwang, G.-T.; Jeong, C. K.; Ryu, J.; Koo, M.; Choi, I.; Lee, S. H.; Byun, M.; Wang, Z. L.; Lee, K. J. *Adv. Mater. (Weinheim, Ger.)* **2014,** *26,* 2514–2520. doi:10.1002/adma.201305659
45. Park, K.-I.; Jeong, C. K.; Ryu, J.; Hwang, G.-T.; Lee, K. J. *Adv. Energy Mater.* **2013,** *3,* 1539–1544. doi:10.1002/aenm.201300458
46. Pi, Z.; Zhang, J.; Wen, C.; Zhang, Z.-b.; Wu, D. *Nano Energy* **2014,** *7,* 33–41. doi:10.1016/j.nanoen.2014.04.016

License and Terms

This is an open access article licensed under the terms of the Beilstein-Institut Open Access License Agreement (https://www.beilstein-journals.org/bjnano/terms), which is identical to the Creative Commons Attribution 4.0 International License (https://creativecommons.org/licenses/by/4.0). The reuse of material under this license requires that the author(s), source and license are credited. Third-party material in this article could be subject to other licenses (typically indicated in the credit line), and in this case, users are required to obtain permission from the license holder to reuse the material.

The definitive version of this article is the electronic one which can be found at:
https://doi.org/10.3762/bjnano.13.14

BEILSTEIN JOURNAL OF NANOTECHNOLOGY

A non-enzymatic electrochemical hydrogen peroxide sensor based on copper oxide nanostructures

Irena Mihailova*[1], Vjaceslavs Gerbreders[1], Marina Krasovska[1], Eriks Sledevskis[1], Valdis Mizers[1], Andrejs Bulanovs[1] and Andrejs Ogurcovs[1,2]

Full Research Paper

Open Access

Address:
[1]G. Liberts' Innovative Microscopy Centre, Department of Technology, Institute of Life Sciences and Technology, Daugavpils University, Parades Street 1, Daugavpils, LV-5401, Latvia and [2]Institute of Solid State Physics, University of Latvia, Kengaraga street 8, Riga, LV-1063, Latvia

Email:
Irena Mihailova* - irena.mihailova@du.lv

* Corresponding author

Keywords:
copper oxide; electrochemical sensor; hydrogen peroxide; nanostructures

Beilstein J. Nanotechnol. **2022,** *13,* 424–436.
https://doi.org/10.3762/bjnano.13.35

Received: 25 February 2022
Accepted: 26 April 2022
Published: 03 May 2022

This article is part of the thematic issue "Nanomaterial-based sensors for water remediation, healthcare and food monitoring applications".

Guest Editor: A. A. Oladipo

© 2022 Mihailova et al.; licensee Beilstein-Institut.
License and terms: see end of document.

Abstract

This article describes the synthesis of nanostructured copper oxide on copper wires and its application for the detection of hydrogen peroxide. Copper oxide petal nanostructures were obtained by a one-step hydrothermal oxidation method. The resulting coating is uniform and dense and shows good adhesion to the wire surface. Structure, surface, and composition of the obtained samples were studied using field-emission scanning electron microscopy along with energy-dispersive spectroscopy and X-ray diffractometry. The resulting nanostructured samples were used for electrochemical determination of the H_2O_2 content in a 0.1 M NaOH buffer solution using cyclic voltammetry, differential pulse voltammetry, and *i–t* measurements. A good linear relationship between the peak current and the concentration of H_2O_2 in the range from 10 to 1800 µM was obtained. The sensitivity of the obtained CuO electrode is 439.19 µA·mM^{-1}. The calculated limit of detection is 1.34 µM, assuming a signal-to-noise ratio of 3. The investigation of the system for sensitivity to interference showed that the most common interfering substances, that is, ascorbic acid, uric acid, dopamine, NaCl, glucose, and acetaminophen, do not affect the electrochemical response. The real milk sample test showed a high recovery rate (more than 95%). According to the obtained results, this sensor is suitable for practical use for the qualitative detection of H_2O_2 in real samples, as well as for the quantitative determination of its concentration.

Introduction

Hydrogen peroxide, a strong oxidant and an essential intermediate product in many biomedical reactions, has recently attracted widespread research interest. In high concentrations it can cause serious harm to human health and the environment, despite the fact that, in living organisms, H_2O_2 is a by-product of metabolism for a wide range of biological and chemical processes, occurring under the influence of external stimuli and intracellular processes [1,2]. Disruption of the natural regulation

process and increasing concentration of H_2O_2 in the blood can cause severe diseases such as Alzheimer's and Parkinson's [3], premature aging of cells [4], death of nerve cells [3,5,6], loss of brain mass [7], and cancer [8-11]. For this reason, targeted monitoring of the concentration of H_2O_2 in body fluids can be used in the diagnosis of these diseases [12-15]. Rapid and accurate determination and control of H_2O_2 concentration is an important task in many other areas, including pharmaceuticals [16-18], environmental protection [19], and industrial areas (especially food production) [20-25].

Measurement techniques including fluorescence [26,27], luminescence [28], spectrometry [29,30], and electrochemistry [31-33] are widely used for H_2O_2 determination. Currently, the electrochemical method is most widely used due to its simplicity, selectivity, and low detection limit. Modified (with enzymes) and unmodified electrodes are used as working electrodes. In the case of modified electrodes, the surface is functionalized by redox-active enzymes (the most popular being horseradish peroxidase) [34-36], and detection is carried out through physicochemical processes of interaction between H_2O_2 and the enzyme. This type of sensor has high catalytic activity, sensitivity, and selectivity. However, enzyme sensors have a significant disadvantage, namely enzyme instability. Due to the nature of enzymes, they can be easily damaged thermally and chemically during production, transportation, and use of electrodes. In addition, enzymes are quite expensive, which significantly increases the production cost and total price of this type of sensor. Recently, research has focused on the development of non-enzymatic electrochemical sensors for the detection of H_2O_2 [37-39]. In this type of sensor, H_2O_2 interacts with the electrode material directly. Certain catalytic processes occurring between H_2O_2 and the electrode material provide an unambiguous electrochemical response and, as a consequence, the selectivity of the sensor. This type of sensor is characterized by good reproducibility of measurement, low production cost, fast response, high sensitivity and selectivity, and chemical and mechanical stability in aggressive environments [40-46]. Nanostructured materials are widely used as the working surface of the electrode [47-49]. The most common are transition metal nanoparticles [33,37,50-54], carbon nanotubes [8], metal oxides [55-64], graphene [32,33], and ordered mesoporous carbon [38,65,66]. Compared to bulk materials, nanostructures have higher catalytic activity and a significantly increased surface area-to-volume ratio, which makes it possible to significantly increase both sensitivity of the sensor and rate of detection of H_2O_2. Among the nanostructured materials used, the most promising candidate is copper oxide (CuO) [56,67-71]. It has selectivity for the determination of H_2O_2, high catalytic activity, and a variety of morphologies (e.g., nanoneedles, nanoplates, and nanorods). Various techniques have been used in the preparation of nanostructured epitaxial CuO coatings, such as thermal oxidation of copper electrodes in an oxygen atmosphere [72,73], hydrothermal chemical oxidation of copper surfaces [56], and hydrothermal synthesis using various precursors containing copper ions [74,75]. Copper oxide nanostructures can also be obtained as a powder and then applied to electrodes by dip- or drop-coating techniques, using a porous substrate or binder polymers [69,76,77]. However, despite the widespread use and simplicity of this method of electrode preparation, it has a number of significant disadvantages. First, there is the problem of homogenization of the nanostructured suspension in solution. Second, nanostructures are distributed randomly during the process of deposition, which can affect the electrochemical activity of the electrode and reduce the repeatability of the experiment. Third, the obtained coatings are characterized by their low adhesion and poor mechanical stability, and can, thus, be easily damaged during production, storage, and measurement. These disadvantages can be avoided by using an in situ growth process of CuO nanostructures directly on a copper substrate, in the presence of certain surfactants or additives. This method makes it possible to obtain nanostructures with a large active surface area, which ensures efficient electron charge transfer between CuO nanostructures and the copper substrate due to the formation of high-density, single-crystal nanopetals. Nanostructures are produced in one step, and can be directly used as sensor electrodes without additional treatments such as surface modification or enzyme immobilization. This article describes the process of obtaining wire electrodes with nanostructured CuO coatings by a one-step chemical hydrothermal oxidation method and their application in electrochemical measurements for the detection of H_2O_2. The article proves the higher efficiency of nanostructured electrodes compared to electrodes with less developed surface. The article shows the influence of the time of hydrothermal synthesis on the morphology of nanostructures and, as a result, the change in the sensitivity of the sensor. The most important electrochemical measurements were carried out to determine H_2O_2 concentration in aqueous solutions using the obtained sensor. It is shown that the obtained non-enzymatic sensor has high sensitivity and selectivity toward H_2O_2. Experiments were also carried out to detect H_2O_2 in real milk and mouthwash samples.

Materials and Methods

Materials

Ammonium persulfate ($(NH_4)_2S_2O_8$, CAS number: 7727-54-0), sodium hydroxide (NaOH, CAS number: 1310-73-2), and hydrogen peroxide solution (H_2O_2, 30%, CAS number: 7722-84-1) were purchased from Merck. Ascorbic acid ($C_6H_8O_6$, CAS number: 50-81-7), uric acid ($C_5H_4N_4O_3$, CAS number: 69-93-2), dopamine hydrochloride

($(HO)_2C_6H_3CH_2CH_2NH_2HCl$, CAS number: 62-31-7), glucose ($C_6H_{12}O_6$, CAS number: 50-99-7), acetaminophen ($CH_3CONHC_6H_4OH$, CAS number: 103-90-2), and sodium chloride (NaCl, CAS number: 7647-14-5) were purchased from Sigma-Aldrich. All reagents were ≥99.8% pure. Copper wire of 2 mm thickness (99.9% purity) was purchased from Sigma-Aldrich. Ag/AgCl wire was purchased from A-M Systems, USA. Printed circuit boards (PCBs) with ENIG (Electroless Nickel Immersion Gold) surface finish were purchased from Multi-CB (Germany). Distilled water was obtained in the laboratory.

CuO layer synthesis on copper wires

A smooth film coating of copper oxide was obtained by annealing the copper wire in an oxygen atmosphere. Before annealing, the copper wire was washed several times with water and ethanol to clean the surface of possible contamination. The wire was then fixed in a metal holder and placed in a Linn High Therm (Germany) furnace, where it was gradually heated to 500 °C and held at this temperature for 30 min. Then, the oven was turned off and left to cool naturally. The result was a wire with a uniform black coating.

Nanostructured samples were obtained by a one-step chemical hydrothermal oxidation. For this, copper wire was rinsed with water and ethanol in order to clean the surface of possible contamination. To prepare the working solution, 10 mL of a 10 M NaOH solution, 5 mL of a 1 M $(NH_4)_2S_2O_8$ solution and 26 mL of H_2O were combined. The wire samples were immersed in the resulting solution and then poured into a heat-resistant glass beaker with a lid. The beaker was placed in an oven preheated to 90 °C for 3 h, and then left to cool naturally. The obtained samples, covered with a nanostructured oxide layer, were repeatedly washed with distilled water in order to get rid of residual reagents, and then dried in an oven at 90 °C for 3 h in order to remove moisture.

To compare the dependence of the sensitivity of nanostructured samples on their morphology, samples were obtained after 1 and 6 h of synthesis time.

The morphology of the surface of the nanostructured CuO samples was studied via field-emission scanning electron microscopy (FESEM, Tescan MAIA 3). The chemical composition analysis was performed via energy-dispersive spectroscopy (EDS, Inca Synergy) integrated into the FESEM system.

The crystalline structure of the samples was defined using an X-ray diffractometer (RIGAKU Smart Lab, Cu Kα [λ = 1.543 Å]) using parallel beam scanning geometry and an additional Ge(220) × 2 bounce monochromator.

Electrochemical measurements

The obtained wire samples were cut into 2 cm long pieces, and at one end were stripped to pure copper over 5 mm length to provide electrical contact with the equipment. The measurements were carried out using an electrochemical station (Zanher, Germany), supplemented by a custom-made electrochemical cell (for more details about its structure, see our publication [71]). During the measurement, a three-electrode cell was used, using oxide-coated copper wire as a working electrode, 0.4 mm diameter Ag/AgCl wire as a reference electrode, and a 6 × 6 mm PCB electrode with ENIG surface finish as a counter electrode.

Cyclic voltammetry (CV) was carried out in the range from −0.8 to 0.1 V vs Ag/AgCl, with U_{start} = 0 V vs Ag/AgCl and a scan rate of 100 mV/s. As buffer solution, 0.1 M NaOH (pH 12.7) was used. For the determination of H_2O_2, 0.1, 0.25, 0.5, 0.65, 0.85, 1, and 5 mM concentrations were used. Measurements were carried out five times for each of the indicated concentrations, and the curves in the following sections show the averaged data from all measurements. To determine the optimal scanning parameters that provide the maximum sensitivity of the sensor, the dependence of the electrochemical response on the pH of the buffer solution and on the scanning speed was studied.

Impedance spectroscopy was carried out in the frequency range from 1 Hz to 100 kHz at an applied signal voltage of about 0.3V.

Differential pulse voltammetry

Before the measurement, the samples were maintained for 30 s at U = −0.8 V vs Ag/AgCl. The measurements were carried out using the following parameters: voltage range from −0.8 V to 0.1 V vs Ag/AgCl, pulse amplitude = 50 mV, pulse step = 3 mV, pulse width = 200 ms, and pulse frequency = 2 Hz. As buffer solution, 0.1 M NaOH was used. For the determination of H_2O_2, 0.033, 0.066, 0.1, 0.17, 0.25, 0.37, and 0.5 mM concentrations were used. The measurements were carried out five times for each of the indicated concentrations, and the curves in the following sections show the averaged data from all measurements.

To determine the scanning parameters that provide the maximum sensitivity of the sensor, the dependence of the differential pulse voltammetry (DPV) response on the pH of the buffer solution and on the pulse frequency was studied.

Current response study

For the current response study (i–t measurement), a constant voltage U = −0.7 V vs Ag/AgCl was applied to the cell

and the current was measured. 0.1 M NaOH was used as buffer solution. The measurement was started at 0 μM concentration, and after 600 s (time required for stabilization) the first 10 μM portion of H_2O_2 was added. Subsequent portions were added every 30 s with the following steps: 10 μM for the concentration range of 0–100 μM, 20 μM for the concentration range of 120–300 μM, 50 μM for the concentration range of 350–800 μM, and 100 μM for the concentration range of 900–1800 μM. The measurement was carried out with constant stirring using a magnetic stirrer.

Interference study

A constant voltage U = −0.7 V vs Ag/AgCl was applied to the cell and the current was measured. As buffer solution 0.1 M NaOH was used. The experiment was started at 0 μM concentration of H_2O_2, then every 60 s either H_2O_2 or an interfering substance at a concentration of 100 μM was added to the solution, in the following order: H_2O_2, ascorbic acid, uric acid, dopamine, NaCl, glucose, and acetaminophen. Then, the whole cycle was repeated two times. The measurement was carried out with constant stirring using a magnetic stirrer.

Real sample study

To demonstrate the possibility of practical application of the obtained nanostructured electrodes for the analysis of real samples, samples of ultrahigh-temperature processed (UHT) milk were investigated. H_2O_2 is present in milk samples either as a result of enzymatic activity or as an antibacterial agent [20-22]. For the experiment, we used 3.2% fat milk and Listerine antiseptic mouthwash from a local supermarket. To reduce the sample matrix effect, the samples were diluted in a 1:2 ratio with 0.1 M NaOH buffer solution. The resulting solution was maintained at pH 12.7. The amperometric response method was used for the analysis with U = −0.7 V vs Ag/AgCl.

Results and Discussion

CuO structure

The morphology of CuO is shown in Figure 1. The SEM image (Figure 1a,b) shows the surface morphology of a thermally obtained copper oxide film. The resulting film is a homogeneous, polycrystalline oxide layer consisting of grains of arbitrary shape. In practice, this layer exhibits poor adhesion to the surface and can be easily damaged mechanically during post-processing.

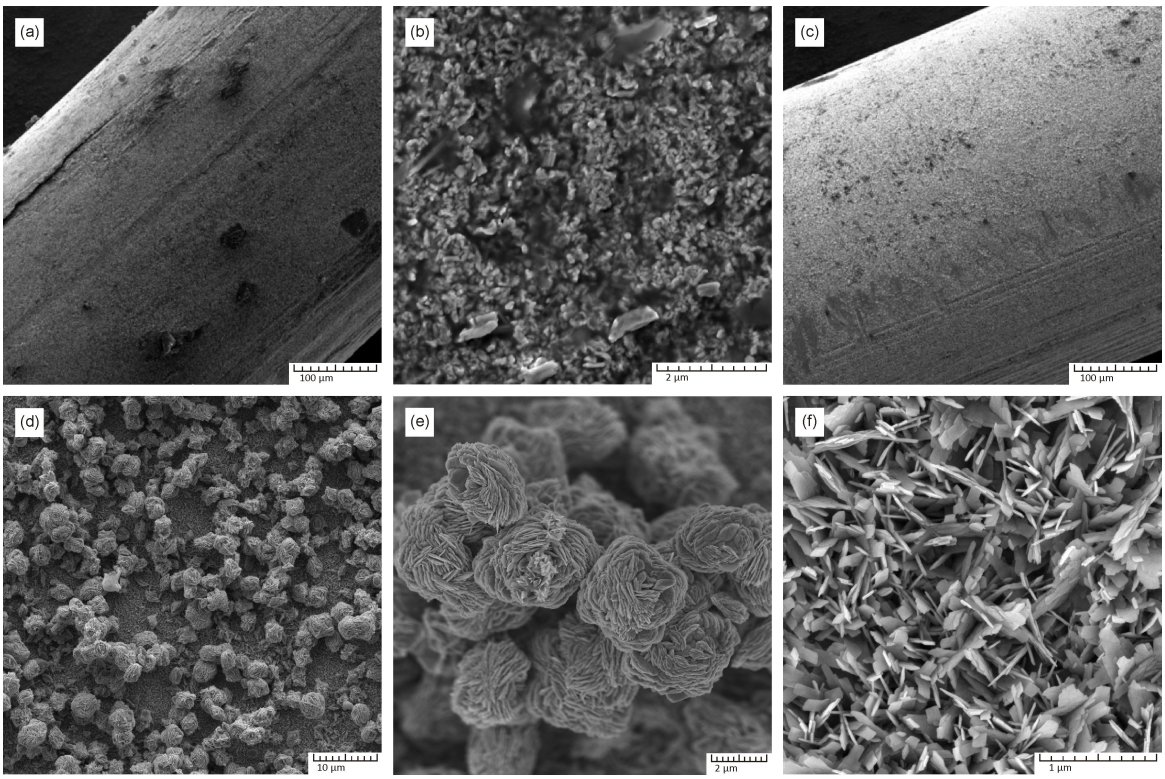


Figure 1: SEM images of copper oxide samples. (a, b) General view and morphology of a CuO film obtained by thermal oxidation on a copper wire; (c, d) general view of a copper wire with CuO layer obtained by chemical hydrothermal oxidation; (e) 3D flower-like nanostructured formations on the surface of the main CuO layer (f).

Figure 1c–f shows the morphology of the copper oxide layer obtained by chemical hydrothermal oxidation. The resulting coating is characterized by a high degree of uniformity, good adhesion to the copper surface and stability during post-processing. The resulting coating consists of a dense uniform layer of CuO petals several nanometres thick (Figure 1f). The surface of the main layer is covered with chaotically distributed, micrometre-sized 3D flower-like formations assembled from individual petals (Figure 1d,e).

EDS microanalysis showed that the samples consist of Cu (58.96 atom %) and O (41.04 atom %), which confirms the high chemical purity of the samples obtained and the absence of foreign impurities.

Figure 2 shows the XRD analysis results. The diffractogram shows only peaks corresponding to CuO and pure Cu (substrate peaks). Extraneous phases and inclusions were not detected. A low amorphous background indicates a high degree of crystallinity of the obtained samples. The X-ray diffraction pattern shows a large number of crystallographic planes corresponding to the CuO (tenorite) lattice; however, the dominant orientation corresponds to the direction perpendicular to the (002) and (111) planes.

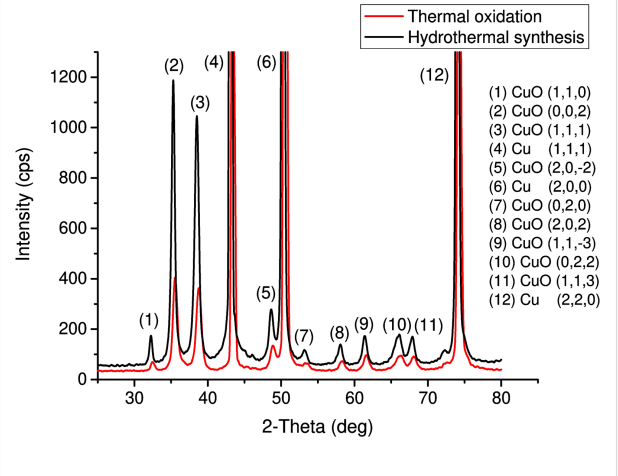


Figure 2: XRD pattern of CuO films. The red diffractogram corresponds to the sample obtained by thermal oxidation and the black diffractogram corresponds to the sample obtained by chemical hydrothermal oxidation.

The growth process of nanostructures can be explained as per the following reactions:

$$\mathrm{Cu} + 2\mathrm{NaOH} + \left(\mathrm{NH_4}\right)_2\mathrm{S_2O_8} \rightarrow \mathrm{Cu(OH)_2} + \mathrm{Na_2SO_4} + \left(\mathrm{NH_4}\right)_2\mathrm{SO_4} \quad (1)$$

$$\mathrm{Cu(OH)_2} + 2\mathrm{OH^-} \rightarrow \left[\mathrm{Cu(OH)_4}\right]^{2-} \quad (2)$$

$$\left[\mathrm{Cu(OH)_4}\right]^{2-} \rightarrow \mathrm{CuO} + 2\mathrm{OH^-} + \mathrm{H_2O} \quad (3)$$

When NaOH is added to the precursor solution containing $(NH_4)_2S_2O_8$, Cu^{2+} ions are released from Cu into solution, where they interact with the reagents according to Equation 1. Reference [56] mentions that at NaOH concentrations below 5 M a thin $Cu(OH)_2$ film is instantly formed on the copper surface. This film serves as a protective layer and blocks all further reactions, including crystal growth. The same processes are observed in the case when the reaction proceeds at relatively low temperatures, which explains why it is impossible to obtain the developed nanostructured CuO surface at room temperature. However, after increasing the concentration of NaOH to 10–15 M, the dissolution–secondary precipitation mechanism takes effect: $Cu(OH)_2$ reacts with OH^- ions to form the complex ion $[Cu(OH)_4]^{2-}$ (Equation 2). These complex ions decompose to CuO with a loss of two hydroxy ions and one water molecule (Equation 3). As a result of this process, a large number of nuclei are generated and captured by the surface. The growth of organized, evenly distributed petal-shaped nanostructures over the entire surface of the copper wire is observed.

This process is similar to the conventional hydrothermal growth of most metal oxides described in previous studies [74,78,79]; however, this work has a fundamental difference: Cu-containing salts are not used in the synthesis process. The copper wire itself acts as the precursor of Cu ions as well as a substrate for the nanostructure growth. In this case there is no need to use an additional seed layer of CuO [74], which greatly simplifies the electrode manufacturing process and improves the adhesion of the nanostructured layer to Cu.

The spherical shape of the obtained flower-like nanostructures indicates that their nucleation centre is not located in the plane of the substrate. The formation of spherical structures can be explained as follows: the presence of a large number of OH^- ions makes it possible to generate a large number of nucleation centres in solution in a short time. The particles begin to agglomerate in order to minimize the total surface energy, forming spherical seeds, which, according to the mechanism of dissolution–secondary precipitation [78,80], overgrow with CuO petals, thereby forming 3D structures in solution. Then, under the influence of gravity, these structures gradually descend to the substrate, where they are captured by the surface and immobilized.

Electrochemical measurements

Figure 3 shows the CV results for CuO in the solution containing 0.1 M NaOH and H_2O_2 at various concentrations. The curve shows a pair of oxidation peaks corresponding to Cu^0/Cu^+ and Cu^+/Cu^{2+} transitions, as well as a pair of reduction peaks corresponding to Cu^{2+}/Cu^+ and Cu^+/CuO transitions [68,81]. Figure 3a shows that the addition of H_2O_2 to the buffer solution affects the peak current values. The value of the maximum

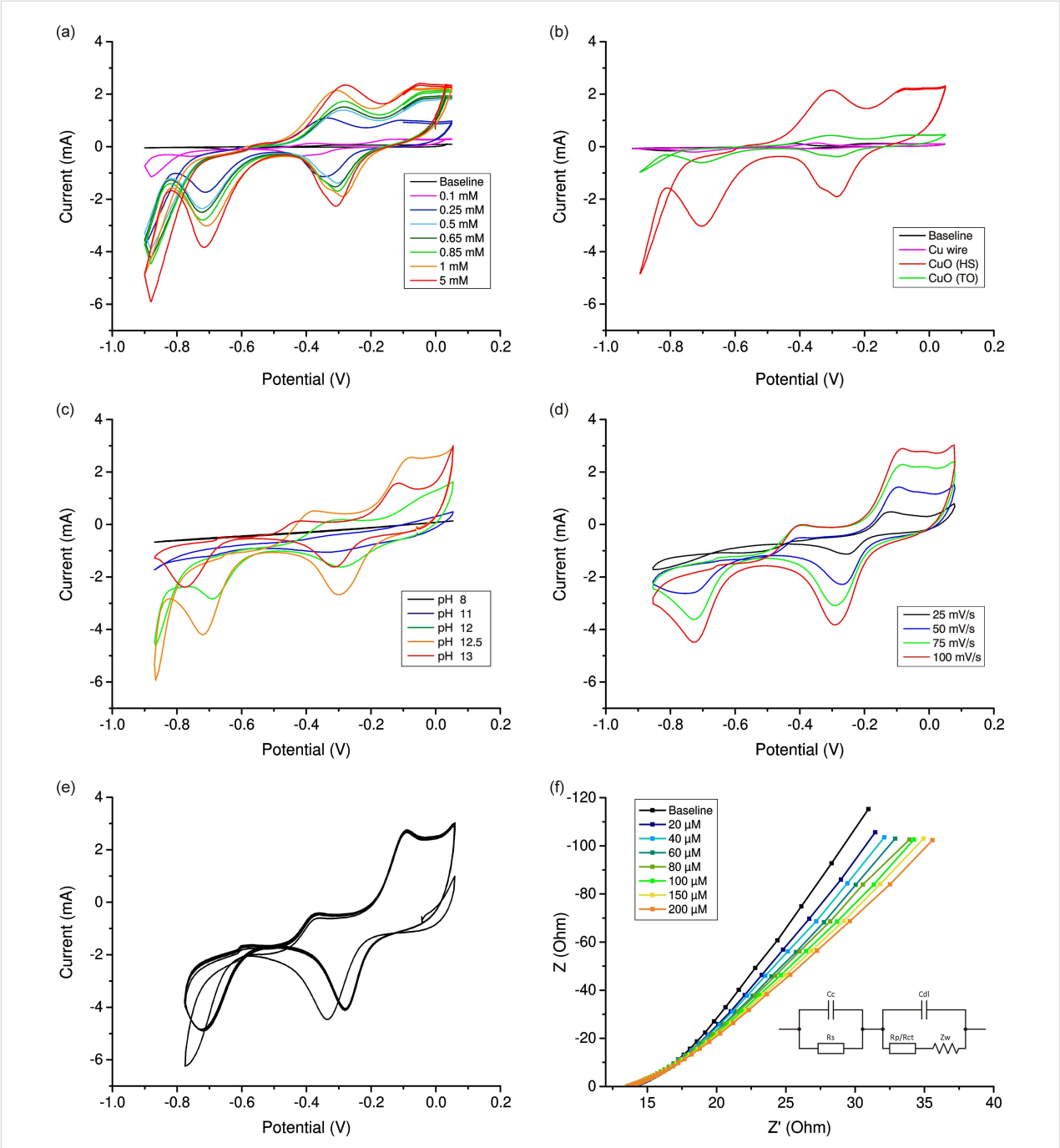


Figure 3: (a) CV results for a nanostructured CuO film in 0.1 M NaOH buffer solution (pH 12.7) and in solutions containing 0.1–5 mM H_2O_2. (b) Comparison of CV results for a pure Cu wire, a CuO film obtained via thermal oxidation (TO), and a nanostructured CuO film obtained by hydrothermal synthesis (HS). Measurements were carried out in 0.1 M NaOH solution containing 5 mM H_2O_2. (c) Comparison of CV curves obtained at different pH values of buffer solution containing 5 mM H_2O_2. (d) Comparison of CV curves obtained at different scan speeds. Measurements were carried out in 0.1 M NaOH solution containing 5 mM H_2O_2. (e) Electrode stability study over multiple CV cycles (n = 10). Measurements were carried out in 0.1 M NaOH solution containing 5 mM H_2O_2. (d) EIS analysis (frequency range from 1 Hz to 100 kHz at an applied signal voltage of about 0.3 V). Measurements were carried out in 0.1 M NaOH solution containing 0–200 µM H_2O_2.

current for all peaks increases with increasing concentration of added peroxide (from 0 to 5 mM).

The mechanism of electron transfer in the modified electrode can be explained as follows: In this catalytic process, during the reduction of H_2O_2 on the CuO surface, Cu^{2+} is electrochemically reduced to Cu^{+} and H_2O_2 to O_2. Then, Cu^{+} on the electrode surface is electrooxidized back to Cu^{2+}, and the catalytic cycle is repeated [55,81,82].

Figure 3b shows CV curves for a pure Cu wire and CuO film obtained by copper annealing compared to a nanostructured CuO film obtained by chemical hydrothermal oxidation. All measurements were carried out in 0.1 M NaOH with the addition of 5 mM H_2O_2. The baseline shows the CV results for a buffer solution with no peroxide added. It can be seen that under identical measurement conditions the electrochemical response of the hydrothermally obtained film is significantly higher than the response from the thermally oxidised film, which indicates a significant contribution of the electrode nanostructuring process to an increase in the sensitivity of the sensor. This can be explained by the fact that petal-like CuO nanostructures provide a much larger surface area, with an increased number of active bonds and high-speed paths for analyte molecule transfer due to the high porosity of the surface, as well as more efficient mass diffusion and electron transfer processes compared to the less developed film. The sensitivity of pure CuO wire is significantly inferior to samples containing CuO.

Figure 3c,d displays the CV curves obtained at various pH values of buffer solution and various scanning speeds. It can be seen that the parameters pH 12.7 and v = 100 mV/s provide the result with maximum sensitivity. Figure 3e displays the electrode stability over multiple CV cycles. It can be seen that starting from the second scanning cycle the curve takes its characteristic shape. The value of the current peak changes slightly with time, which indicates that the electrode stabilizes after a short time. Small differences in the initial scan cycles may be due to the wetting of nanostructures.

In Figure 3f, the EIS curve and the corresponding equivalent circuit are presented. The absence of characteristic semicircles formed by RCs by the circuit elements indicates a low charge transfer resistance and the predominance of Warburg diffusion over other processes in the electrochemical system. Figure 3f shows an unambiguous change in the EIS curves as a reaction to the addition of small concentrations of H_2O_2 to the solution.

The active surface area of an electrode can be calculated using the Randles–Sevcik equation [83-85], which at 25 °C is:

$$I_p = \left(2.69\times10^5\right) n^{3/2} A \cdot C^* \cdot D^{1/2} \cdot v^{1/2}, \quad (4)$$

where I_p represents the redox peak current (A), n is the number of electrons transferred in the redox reaction, D is the diffusion coefficient in solution ($D = 6.8 \times 10^{-5}$ cm^2·s^{-1}), C^* is the concentration (mol·cm^{-3}); v is the scan rate (100 mV·s^{-1}), and A denotes the effective surface area of the electrode (cm^2). The electrochemically active surface area was calculated to be 6.5 cm^2, that is, five times larger than the geometrical surface area of a bare electrode, which indicates the presence of a well-developed nanostructured surface.

Figure 4 displays the dependence of the sensor sensitivity on the morphology of CuO nanostructures obtained after different periods of synthesis time. It is shown that as a result of 1 h of growth, nanopetals are formed with a greater thickness and a significantly lower height than in the case of 3 h of growth. This change in aspect ratio leads to a decrease in the active surface area and, as a result, to a decrease in sensitivity (reduction of the current peak in the CV curves). An increase in the duration of hydrothermal synthesis to 6 h also leads to a change in the morphology of the nanostructures. The SEM picture shows that the nanoleaves grow together, forming dense spherical formations that are difficult for the solution to penetrate, which also leads to a decrease in the surface area and a deterioration in sensitivity (decrease of current peak value). Hence, it can be concluded that the chosen synthesis time of 3 h is optimal and provides maximum sensitivity.

Figure 5 shows the DPV results for the nanostructured CuO electrode. The measurements were carried out in 0.1 M NaOH buffer solution containing H_2O_2 at a concentration of 0–500 μM. The lowest considered concentration (33 μM) provides a noticeable electrochemical response, which indicates that the nanostructured CuO electrode has sufficiently high sensitivity. Figure 5b shows the dependence of the peak current values on the concentration of H_2O_2. The resulting dependence is linear over the entire concentration range.

Figure 5c,d displays the DPV curves at different pH values of buffer solution and different pulse frequency. It can be seen that the parameters pH 13 and 2 Hz provide the result with maximum sensitivity.

Figure 6a and Figure 7a show typical curves of the amperometric response for nanostructured CuO electrodes. After H_2O_2 injection, a fast, stable, and sensitive amperometric response was observed. The sharp jump in the current when H_2O_2 is added can be explained by a local increase in the H_2O_2 concen-

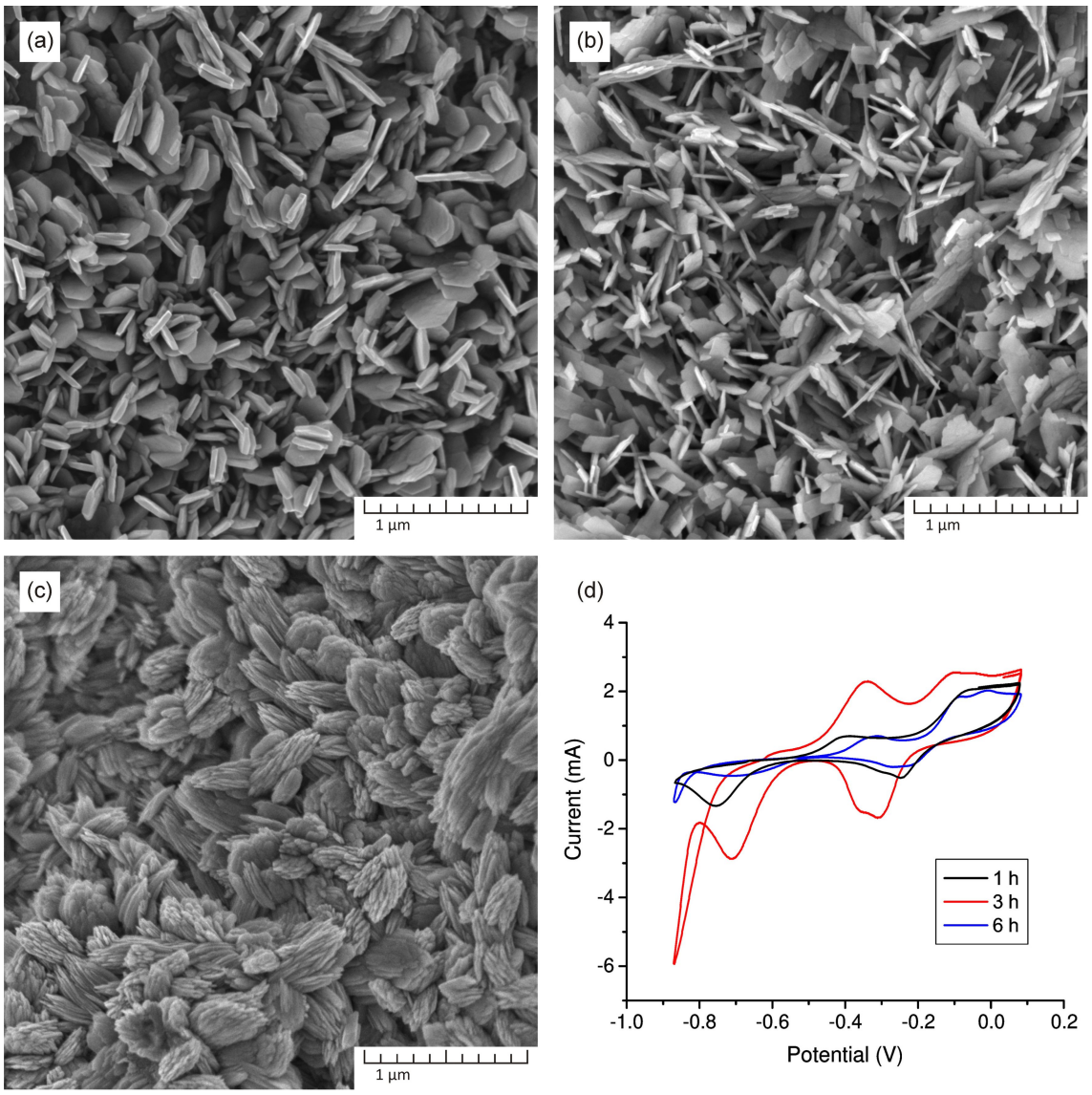


Figure 4: SEM images of CuO nanostructures obtained via hydrothermal oxidation method after (a) 1 h, (b) 3 h, and (c) 6 h. (d) CV curves of the CuO samples after 1, 3, and 6 h of synthesis time. Measurements were carried out in 0.1 M NaOH solution containing 1 mM H_2O_2.

tration near the electrode. However, it can be seen that the current reaches a steady-state value after less than 5 s, and then does not change significantly before the next portion of H_2O_2 is added, forming a plateau (Figure 7). Figure 7b shows the calibration curve for the dependence of the catalytic current values on the concentration of H_2O_2.

A linear relationship was obtained in the range from 10 to 1800 µM (R = 0.99874). The sensitivity of the obtained CuO electrode is 439.19 µA·mM^{-1}. The calculated limit of detection (LOD) is 1.34 µM, assuming signal-to-noise ratio of 3. The results indicate that the nanostructured CuO electrode can be used for accurate and precise detection of H_2O_2. The obtained results are comparable to several published studies where CuO nanostructures were used for electrode modification for H_2O_2 detection (Table 1).

For the successful practical application as a sensor material, a high selectivity of the obtained coating is of importance. Therefore, the selectivity of the petal-like CuO electrode was evaluated using four different interfering substances, namely ascorbic acid, uric acid, dopamine, and NaCl. These substances are most commonly encountered in clinical and pharmaceutical applications together with H_2O_2. They are also oxidizing agents that can react with CuO during electrochemical tests, leading to a false increase in the current signal. The amperometric response

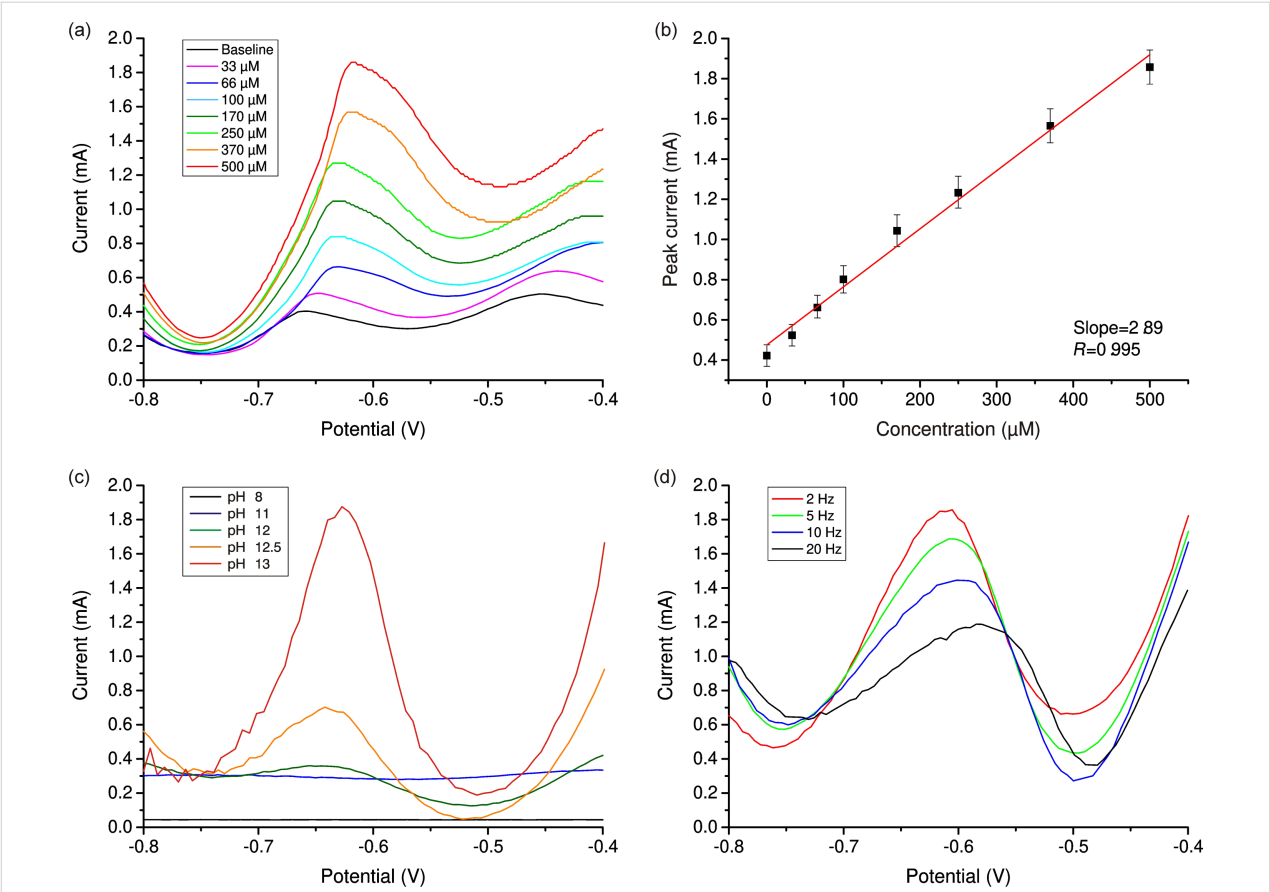


Figure 5: (a) DPV results for the nanostructured CuO electrode in 0.1 M NaOH buffer solution containing 33–500 µmol H_2O_2. (b) Dependence of the amperometric response on the concentration of added peroxide (SD = 3.5%, n = 5). (c) Comparison of DPV curves obtained at different pH values of buffer solution containing 500 µM H_2O_2. (d) Comparison of DPV curves obtained at different pulse frequences. Measurements were carried out in 0.1 M NaOH solution containing 500 µM H_2O_2.

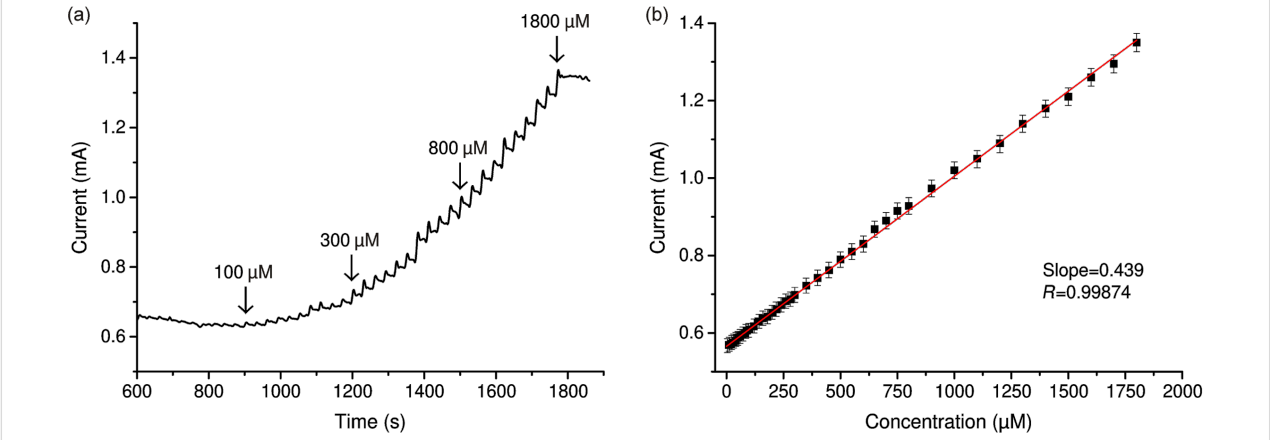


Figure 6: (a) Amperometric response of the nanostructured CuO electrode in 0.1 M NaOH with stepwise addition of H_2O_2 at concentrations from 10 to 1800 µM and (b) the corresponding calibration curve (SD = 3.5%, n = 5).

after sequential injection of 0.1 mM H_2O_2 and 0.1 mM interfering substance is shown in Figure 7a. There is an insignificant reaction of the sensor to the above substances, the current intensity of which is commensurate with the noise level. Thus, it can be concluded that the CuO petal-like electrode shows good selectivity for the detection of H_2O_2.

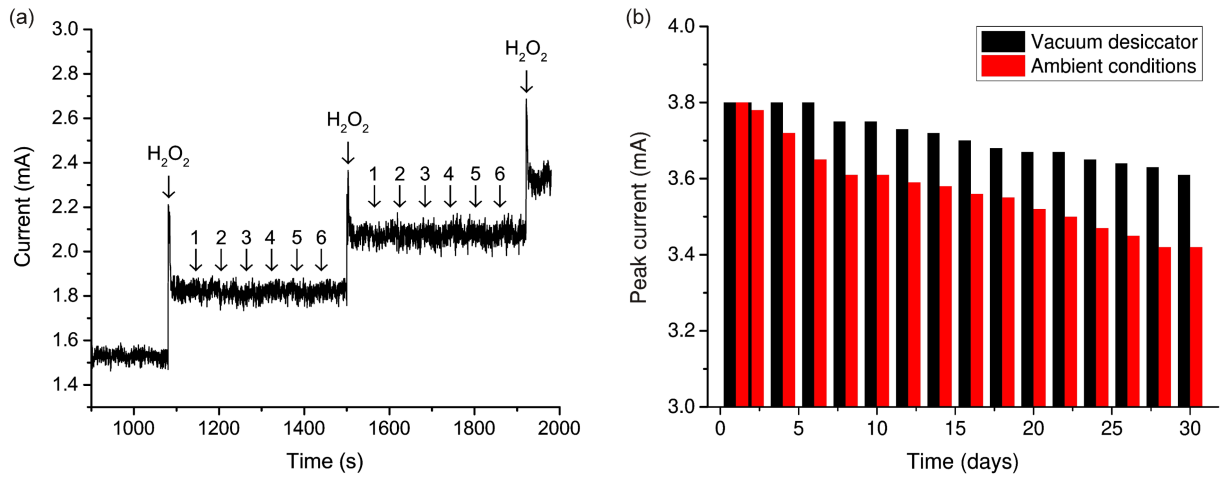


Figure 7: (a) Amperometric response of the nanostructured CuO electrode in 0.1 M NaOH with stepwise addition of H_2O_2 at concentrations from 100 to 300 μM and the most common interfering substances: (1) ascorbic acid, (2) uric acid, (3) dopamine, (4) NaCl, (5) glucose, and (6) acetaminophen. (b) Stability study and the dependence of the change in the electrochemical signal on the storage time of the samples.

Table 1: Analytical performance of the CuO sensor in this study compared with other reported H_2O_2 sensors.

Electrode	Morphology of nanostructured CuO	Linear range (μM)	Sensitivity (μA/mM)	LOD (μM)	Reference
Cu_2O/GCE	nanocubes	0.3–7.80	—	64.4	[70]
CuO/APGE	nanoparticles	5–1600	4.75	0.21	[68]
CuO/Cu foil	nanopetals	10–960	5030	2.1	[56]
CuO/GCE	nanograss	10–900	80.4	5.5	[82]
CuO/rGO	nanoparticles	0.05–532	57.6	0.0043	[69]
CuO/PAN	3D nanoflowers	0.5–125	—	0.12	[77]
CuO/CoO	3D nanoleaf	2–4000	6349	1.4	[52]
CuO/SiNWs	nanoparticles	10–13180	22.27	1.6	[67]
CuO/Cu wire	nanopetals	10–1800	439.19	1.34	this work

Table 2 shows the result of an amperometric study of real milk and mouthwash samples. As the possible amount of H_2O_2 can be below the detection limit, the samples were spiked with different amounts of H_2O_2 above the detection threshold and a standard sample recovery test was performed. It can be seen that the electrode has a high recovery rate (over 95% for all cases) and a low relative standard deviation for three samples of each spiked concentration not exceeding 5.5%. The results indi-

Table 2: Results of determination of hydrogen peroxide in real samples.

Milk				Mouthwash			
Added (μM)	Found (μM)	Recovery (%)	RSD (%) (n = 3)	Added (μM)	Found (μM)	Recovery (%)	RSD (%) (n = 3)
0	—	—	—	0	—	—	—
10	9.59	95.9	5.5	10	9.51	95.1	5.5
25	23.88	95.52	5.3	25	23.91	95.6	5.1
50	47.53	95.06	4.8	50	48.01	96.01	5.2
100	97.73	97.73	5.1	100	98.25	98.25	5.4

cate that this sensor can be successfully used to detect hydrogen peroxide in real samples.

To assess the long-term stability of the sensor, the obtained samples were stored under ambient conditions for one and four weeks. Measurements were taken every second day. The stabilities of each sample were assessed by the degree of reduction of the current peak value in the CV curve. For samples stored under environmental conditions (20 °C, 40% relative humidity) for one week, the signal level remained at 95% of the initial value. For samples stored under environmental conditions for a month, the signal level remained at 90% of the initial value. The influence of the environment and degree of sample degradation can be significantly reduced by ensuring that samples are stored in a vacuum desiccator. After a week of desiccator storage, the samples had not lost their original electrochemical properties at all, and after a month of storage they retained 95% of their initial values (Figure 7b). After a month of storage, no significant morphological changes were observed, which proves the stability of the samples. These results show that the nanostructured CuO coating has long-term stability and resistance to environmental influences, which is another advantage compared to enzyme sensors.

Conclusion

This article describes the preparation of a nanostructured coating of CuO and its application as a working electrode for the electrochemical determination of H_2O_2. The resulting coating is distinguished by high homogeneity and adhesion to the copper wire, which ensures high mechanical and chemical resistance of the sample. The nanostructured CuO coating develops a petal-shaped surface, which possesses significant peroxidase-like electrocatalytic activity, and makes it possible to detect H_2O_2 with a high degree of sensitivity compared to samples with less developed surface. It has been shown that the optimal time for hydrothermal synthesis is 3 h, since this period of time allows one to obtain a morphology with maximum electrochemical response towards H_2O_2.

The resulting electrode displays a linear current response in a concentration range from 10 to 1800 μM. The sensitivity of the resulting electrode was 439.19 $\mu A \cdot mM^{-1}$ and the calculated limit of detection (LOD) was 1.34 μM. The electrochemically active surface area was calculated to be 6.5 cm^2. Sensitivity testing showed a lack of electrochemical response to the most common interfering substances, showing the high selectivity of this electrode. This study also showed high long-term stability of the resulting coating stored under ambient conditions (the signal level remained at 95% of the initial value after one week and at 90% after a month). Storage in a vacuum desiccator helps to improve the stability of samples (the signal level remained at 100% of the initial value after one week and at 95% after a month). Real milk sample and mouthwash analysis demonstrated a high recovery rate (over 95%), which makes this sensor suitable for qualitative and quantitative detection of H_2O_2.

Further research will be aimed at studying this sensor in healthcare to analyse changes in the concentration of H_2O_2 in biological fluids. Also, a promising option to study more complex analytes and to significantly increase the sensitivity is the use of this nanostructured CuO sensor as part of a multisensor system based on several types of metal oxides (e.g., Co_2O_3, TiO_2, NiO, and Fe_2O_3).

Funding

This work was supported by ERDF project No. 1.1.1.2/16/I/001, research application number 1.1.1.2/VIAA/4/20/743 "Development of nanomaterial-based electrochemical sensor for detection of hydrogen peroxide".

ORCID® iDs

Irena Mihailova - https://orcid.org/0000-0002-1563-2209
Vjaceslavs Gerbreders - https://orcid.org/0000-0003-3385-4507
Marina Krasovska - https://orcid.org/0000-0002-5959-0442
Eriks Sledevskis - https://orcid.org/0000-0002-2921-6361
Valdis Mizers - https://orcid.org/0000-0001-9666-5549
Andrejs Bulanovs - https://orcid.org/0000-0002-5702-501X
Andrejs Ogurcovs - https://orcid.org/0000-0001-7211-8479

References

1. Grisham, M. B. *Comp. Biochem. Physiol., Part A: Mol. Integr. Physiol.* **2013,** *165,* 429–438. doi:10.1016/j.cbpa.2013.02.003
2. Halliwell, B.; Clement, M. V.; Long, L. H. *FEBS Lett.* **2000,** *486,* 10–13. doi:10.1016/s0014-5793(00)02197-9
3. Dev, S.; Kumari, S.; Singh, N.; Kumar Bal, S.; Seth, P.; Mukhopadhyay, C. K. *Free Radical Biol. Med.* **2015,** *86,* 78–89. doi:10.1016/j.freeradbiomed.2015.05.025
4. Totsuka, K.; Ueta, T.; Uchida, T.; Roggia, M. F.; Nakagawa, S.; Vavvas, D. G.; Honjo, M.; Aihara, M. *Exp. Eye Res.* **2019,** *181,* 316–324. doi:10.1016/j.exer.2018.08.019
5. Xiang, J.; Wan, C.; Guo, R.; Guo, D. *BioMed Res. Int.* **2016,** *2016,* 734396. doi:10.1155/2016/7343965
6. Whittemore, E. R.; Loo, D. T.; Watt, J. A.; Cotmans, C. W. *Neuroscience* **1995,** *67,* 921–932. doi:10.1016/0306-4522(95)00108-u
7. Guesmi, F.; Bellamine, H.; Landoulsi, A. *Appl. Physiol., Nutr., Metab.* **2018,** *43,* 1275–1281. doi:10.1139/apnm-2018-0107
8. Tavakkoli, H.; Akhond, M.; Ghorbankhani, G. A.; Absalan, G. *Microchim. Acta* **2020,** *187,* 105. doi:10.1007/s00604-019-4064-7
9. Lisanti, M. P.; Martinez-Outschoorn, U. E.; Lin, Z.; Pavlides, S.; Whitaker-Menezes, D.; Pestell, R. G.; Howell, A.; Sotgia, F. *Cell Cycle* **2011,** *10,* 2440–2449. doi:10.4161/cc.10.15.16870
10. Kolbasina, N. A.; Gureev, A. P.; Serzhantova, O. V.; Mikhailov, A. A.; Moshurov, I. P.; Starkov, A. A.; Popov, V. N. *Heliyon* **2020,** *6,* e04303. doi:10.1016/j.heliyon.2020.e04303

11. Lopez-Lazaro, M. *Cancer Lett.* **2007,** *252,* 1–8. doi:10.1016/j.canlet.2006.10.029
12. Abdalla, A.; Jones, W.; Flint, M. S.; Patel, B. A. *Electrochim. Acta* **2021,** *398,* 139314. doi:10.1016/j.electacta.2021.139314
13. Luo, Y.; Liu, H.; Rui, Q.; Tian, Y. *Anal. Chem. (Washington, DC, U. S.)* **2009,** *81,* 3035–3041. doi:10.1021/ac802721x
14. Lee, S.; Lee, Y. J.; Kim, J. H.; Lee, G.-J. *Chemosensors* **2020,** *8,* 63. doi:10.3390/chemosensors8030063
15. Liu, H.; Weng, L.; Yang, C. *Microchim. Acta* **2017,** *184,* 1267–1283. doi:10.1007/s00604-017-2179-2
16. Su, J.; Zhang, S.; Wang, C.; Li, M.; Wang, J.; Su, F.; Wang, Z. *ACS Omega* **2021,** *6,* 14819–14823. doi:10.1021/acsomega.1c00384
17. Yue, H.; Bu, X.; Huang, M.-H.; Young, J.; Raglione, T. *Int. J. Pharm.* **2009,** *375,* 33–40. doi:10.1016/j.ijpharm.2009.03.027
18. Perini, J. A. d. L.; Silva, B. C. e.; Tonetti, A. L.; Nogueira, R. F. P. *Environ. Sci. Pollut. Res.* **2017,** *24,* 6233–6240. doi:10.1007/s11356-016-7416-4
19. Huang, Y.; Wang, L.; Chen, B.; Zhang, Q.; Zhu, R. *Environ. Sci.: Water Res. Technol.* **2020,** *6,* 2396–2404. doi:10.1039/d0ew00234h
20. Vasconcelos, H.; Matias, A.; Jorge, P.; Saraiva, C.; Mendes, J.; Araújo, J.; Dias, B.; Santos, P.; Almeida, J. M. M. M.; Coelho, L. C. C. *Chem. Proc.* **2021,** *5,* 55. doi:10.3390/csac2021-10466
21. Navale, D. J.; Gupta, S. *Int. J. Latest Technol. Eng., Manage. Appl. Sci.* **2019,** *8,* 19–21.
22. Arefin, S.; Sarker, M. A. H.; Islam, M. A.; Harun-ur-Rashid, M.; Islam, M. N. *J. Adv. Vet. Anim. Res.* **2017,** *4,* 371–377. doi:10.5455/javar.2017.d236
23. Chen, Q.; Lin, T.; Huang, J.; Chen, Y.; Guo, L.; Fu, F. *Anal. Methods* **2018,** *10,* 504–507. doi:10.1039/c7ay02819a
24. Xing, L.; Zhang, W.; Fu, L.; Lorenzo, J. M.; Hao, Y. *Food Chem.* **2022,** *385,* 132555. doi:10.1016/j.foodchem.2022.132555
25. Rana, J.; Hossain, M. A.; Sarkar, D. K.; Alom, M. A.; Sarkar, S.; Rahman, M. H.; Islam, M. A.; Islam, M. N. *Asian-Australas. J. Biosci. Biotechnol.* **2021,** *6,* 19–25. doi:10.3329/aajbb.v6i1.54877
26. Ito, E.; Watabe, S.; Morikawa, M.; Kodama, H.; Okada, R.; Miura, T. *Methods Enzymol.* **2013,** *526,* 135–143. doi:10.1016/b978-0-12-405883-5.00008-9
27. Rezende, F.; Brandes, R. P.; Schröder, K. *Antioxid. Redox Signaling* **2018,** *29,* 585–602. doi:10.1089/ars.2017.7401
28. Moßhammer, M.; Kühl, M.; Koren, K. *Chemosensors* **2017,** *5,* 28. doi:10.3390/chemosensors5040028
29. Teodoro, K. B. R.; Migliorini, F. L.; Christinelli, W. A.; Correa, D. S. *Carbohydr. Polym.* **2019,** *212,* 235–241. doi:10.1016/j.carbpol.2019.02.053
30. Zhu, P.; Xu, Z.; Cai, L.; Chen, J. *Nanoscale Res. Lett.* **2021,** *16,* 41. doi:10.1186/s11671-021-03501-6
31. Gričar, E.; Kalcher, K.; Genorio, B.; Kolar, M. *Sensors* **2021,** *21,* 8301. doi:10.3390/s21248301
32. Gorduk, O.; Gorduk, S.; Sahin, Y. *ECS J. Solid State Sci. Technol.* **2020,** *9,* 061003. doi:10.1149/2162-8777/ab9c7a
33. Alencar, L. M.; Silva, A. W. B. N.; Trindade, M. A. G.; Salvatierra, R. V.; Martins, C. A.; Souza, V. H. R. *Sens. Actuators, B* **2022,** *360,* 131649. doi:10.1016/j.snb.2022.131649
34. Wang, Q.; Zhang, X.; Chai, X.; Wang, T.; Cao, T.; Li, Y.; Zhang, L.; Fan, F.; Fu, Y.; Qi, W. *ACS Appl. Nano Mater.* **2021,** *4,* 6103–6110. doi:10.1021/acsanm.1c00915
35. Bao-Kai, M.; Mian, L.; Ling-Zhi, C.; Xin-Chu, W.; Cai, S.; Qing, H. *J. Inorg. Mater.* **2020,** *35,* 131–138. doi:10.15541/jim20190139
36. Nestor, U.; Frodouard, H.; Theoneste, M. *Adv. Nanopart.* **2021,** *10,* 1–25. doi:10.4236/anp.2021.101001
37. Sardaremelli, S.; Hasanzadeh, M.; Seidi, F. *J. Mol. Recognit.* **2021,** *34,* e2928. doi:10.1002/jmr.2928
38. Heydaryan, K.; Almasi Kashi, M.; Sharifi, N.; Ranjbar-Azad, M. *New J. Chem.* **2020,** *44,* 9037–9045. doi:10.1039/d0nj00526f
39. Rashed, M. A.; Faisal, M.; Harraz, F. A.; Jalalah, M.; Alsaiari, M.; Alsareii, S. A. *J. Electrochem. Soc.* **2021,** *168,* 027512. doi:10.1149/1945-7111/abe44b
40. Nishan, U.; Niaz, A.; Muhammad, N.; Asad, M.; Shah, A.-u.-H. A.; Khan, N.; Khan, M.; Shujah, S.; Rahim, A. *Arabian J. Chem.* **2021,** *14,* 103164. doi:10.1016/j.arabjc.2021.103164
41. Karimi-Maleh, H.; Khataee, A.; Karimi, F.; Baghayeri, M.; Fu, L.; Rouhi, J.; Karaman, C.; Karaman, O.; Boukherroub, R. *Chemosphere* **2022,** *291,* 132928. doi:10.1016/j.chemosphere.2021.132928
42. Orooji, Y.; Asrami, P. N.; Beitollahi, H.; Tajik, S.; Alizadeh, M.; Salmanpour, S.; Baghayeri, M.; Rouhi, J.; Sanati, A. L.; Karimi, F. *J. Food Meas. Charact.* **2021,** *15,* 4098–4104. doi:10.1007/s11694-021-00982-y
43. Karimi-Maleh, H.; Karimi, F.; Fu, L.; Sanati, A. L.; Alizadeh, M.; Karaman, C.; Orooji, Y. *J. Hazard. Mater.* **2022,** *423,* 127058. doi:10.1016/j.jhazmat.2021.127058
44. Karimi-Maleh, H.; Darabi, R.; Shabani-Nooshabadi, M.; Baghayeri, M.; Karimi, F.; Rouhi, J.; Alizadeh, M.; Karaman, O.; Vasseghian, Y.; Karaman, C. *Food Chem. Toxicol.* **2022,** *162,* 112907. doi:10.1016/j.fct.2022.112907
45. Karimi-Maleh, H.; Alizadeh, M.; Orooji, Y.; Karimi, F.; Baghayeri, M.; Rouhi, J.; Tajik, S.; Beitollahi, H.; Agarwal, S.; Gupta, V. K.; Rajendran, S.; Rostamnia, S.; Fu, L.; Saberi-Movahed, F.; Malekmohammadi, S. *Ind. Eng. Chem. Res.* **2021,** *60,* 816–823. doi:10.1021/acs.iecr.0c04698
46. Karimi-Maleh, H.; Yola, M. L.; Atar, N.; Orooji, Y.; Karimi, F.; Senthil Kumar, P.; Rouhi, J.; Baghayeri, M. *J. Colloid Interface Sci.* **2021,** *592,* 174–185. doi:10.1016/j.jcis.2021.02.066
47. Karimi-Maleh, H.; Orooji, Y.; Karimi, F.; Alizadeh, M.; Baghayeri, M.; Rouhi, J.; Tajik, S.; Beitollahi, H.; Agarwal, S.; Gupta, V. K.; Rajendran, S.; Ayati, A.; Fu, L.; Sanati, A. L.; Tanhaei, B.; Sen, F.; Shabani-Nooshabadi, M.; Asrami, P. N.; Al-Othman, A. *Biosens. Bioelectron.* **2021,** *184,* 113252. doi:10.1016/j.bios.2021.113252
48. Trujillo, R. M.; Barraza, D. E.; Zamora, M. L.; Cattani-Scholz, A.; Madrid, R. E. *Sensors* **2021,** *21,* 2204. doi:10.3390/s21062204
49. Tang, X.; Wu, J.; Wu, W.; Zhang, Z.; Zhang, W.; Zhang, Q.; Zhang, W.; Chen, X.; Li, P. *Anal. Chem. (Washington, DC, U. S.)* **2020,** *92,* 3563–3571. doi:10.1021/acs.analchem.9b03933
50. Sheng, X.; Li, T.; Sun, M.; Liu, G.; Zhang, Q.; Ling, Z.; Gao, S.; Diao, F.; Zhang, J.; Rosei, F.; Wang, Y. *Electrochim. Acta* **2022,** *407,* 139892. doi:10.1016/j.electacta.2022.139892
51. Chen, S.; Yuan, R.; Chai, Y.; Hu, F. *Microchim. Acta* **2013,** *180,* 15–32. doi:10.1007/s00604-012-0904-4
52. Zhang, W.; Fan, G.; Yi, H.; Jia, G.; Li, Z.; Yuan, C.; Bai, Y.; Fu, D. *Small* **2018,** *14,* 1703713. doi:10.1002/smll.201703713
53. Guan, H.; Huang, S.; Ding, J.; Tian, F.; Xu, Q.; Zhao, J. *Acta Mater.* **2020,** *187,* 122–134. doi:10.1016/j.actamat.2020.01.044
54. Liu, H.; Li, X.; Ma, Z.; Sun, M.; Li, M.; Zhang, Z.; Zhang, L.; Tang, Z.; Yao, Y.; Huang, B.; Guo, S. *Nano Lett.* **2021,** *21,* 10284–10291. doi:10.1021/acs.nanolett.1c03381
55. Wang, Z.; Lei, Q.; Wang, Z.; Yuan, H.; Cao, L.; Qin, N.; Lu, Z.; Xiao, J.; Liu, J. *Chem. Eng. J.* **2020,** *395,* 125180. doi:10.1016/j.cej.2020.125180

56. Gao, P.; Liu, D. *Microchim. Acta* **2015,** *182,* 1231–1239. doi:10.1007/s00604-015-1476-x
57. Molodtsova, T.; Gorshenkov, M.; Saliev, A.; Vanyushin, V.; Goncharov, I.; Smirnova, N. *Electrochim. Acta* **2021,** *370,* 137723. doi:10.1016/j.electacta.2021.137723
58. Sekar, N. K.; Gumpu, M. B.; Ramachandra, B. L.; Nesakumar, N.; Sankar, P.; Babu, K. J.; Krishnan, U. M.; Rayappan, J. B. B. *J. Nanosci. Nanotechnol.* **2018,** *18,* 4371–4379. doi:10.1166/jnn.2018.15259
59. Balu, S.; Palanisamy, S.; Velusamy, V.; Yang, T. C. K. *Ultrason. Sonochem.* **2019,** *56,* 254–263. doi:10.1016/j.ultsonch.2019.04.023
60. Liu, W.; Zheng, Y.; Wang, Z.; Wang, Z.; Yang, J.; Qi, M.; Chen, M.; Rehman, S. U.; Shum, P. P.; Zhu, L.; Wei, L. *Adv. Mater. (Weinheim, Ger.)* **2021,** *8,* 202001978. doi:10.1002/admi.202001978
61. Li, T.; Yin, W.; Gao, S.; Sun, Y.; Xu, P.; Wu, S.; Kong, H.; Yang, G.; Wei, G. *Nanomaterials* **2022,** *12,* 982. doi:10.3390/nano12060982
62. Li, H.; Jiang, L.; Shao, D.; Wu, C.; Gao, Y.; Yang, Z.; Yang, Z. *Chin. J. Anal. Chem.* **2022,** *50,* 100060. doi:10.1016/j.cjac.2022.100060
63. Yang, M.; Wu, Z.; Wang, X.; Yin, Z.; Tan, X.; Zhao, J. *Talanta* **2022,** *244,* 123407. doi:10.1016/j.talanta.2022.123407
64. Ullah, R.; Rasheed, M. A.; Abbas, S.; Rehman, K.-u.; Shah, A.; Ullah, K.; Khan, Y.; Bibi, M.; Ahmad, M.; Ali, G. *Curr. Appl. Phys.* **2022,** *38,* 40–48. doi:10.1016/j.cap.2022.02.008
65. Zhang, X.; Tang, Y.; Zhang, F.; Lee, C.-S. *Adv. Energy Mater.* **2016,** *6,* 1502588. doi:10.1002/aenm.201502588
66. Li, G.; Yuan, H.; Mou, J.; Dai, E.; Zhang, H.; Li, Z.; Zhao, Y.; Dai, Y.; Zhang, X. *Compos. Commun.* **2022,** *29,* 101043. doi:10.1016/j.coco.2021.101043
67. Huang, J.; Zhu, Y.; Zhong, H.; Yang, X.; Li, C. *ACS Appl. Mater. Interfaces* **2014,** *6,* 7055–7062. doi:10.1021/am501799w
68. Kamyabi, M. A.; Hajari, N. *J. Braz. Chem. Soc.* **2017,** *28,* 808–818. doi:10.21577/0103-5053.20160232
69. Kumar, J. S.; Ghosh, S.; Murmu, N. C.; Mandal, N.; Kuila, T. *J. Nanosci. Nanotechnol.* **2019,** *19,* 5295–5302. doi:10.1166/jnn.2019.16834
70. Liu, M.; Liu, R.; Chen, W. *Biosens. Bioelectron.* **2013,** *45,* 206–212. doi:10.1016/j.bios.2013.02.010
71. Atacan, K.; Özacar, M. *Mater. Chem. Phys.* **2021,** *266,* 124527. doi:10.1016/j.matchemphys.2021.124527
72. Moise, C. C.; Enache, L.-B.; Anăstăsoaie, V.; Lazăr, O. A.; Mihai, G. V.; Bercu, M.; Enăchescu, M. *J. Alloys Compd.* **2021,** *886,* 161130. doi:10.1016/j.jallcom.2021.161130
73. Xiang, L.; Guo, J.; Wu, C.; Cai, M.; Zhou, X.; Zhang, N. *J. Mater. Res.* **2018,** *33,* 2264–2280. doi:10.1557/jmr.2018.215
74. Gerbreders, V.; Krasovska, M.; Mihailova, I.; Ogurcovs, A.; Sledevskis, E.; Gerbreders, A.; Tamanis, E.; Kokina, I.; Plaksenkova, I. *Surf. Interfaces* **2021,** *26,* 101332. doi:10.1016/j.surfin.2021.101332
75. Sonia, S.; Poongodi, S.; Suresh Kumar, P.; Mangalaraj, D.; Ponpandian, N.; Viswanathan, C. *Mater. Sci. Semicond. Process.* **2015,** *30,* 585–591. doi:10.1016/j.mssp.2014.10.012
76. Yang, G.; Chen, F.; Yang, Z. *Int. J. Electrochem.* **2012,** *2012,* 194183. doi:10.1155/2012/194183
77. Zheng, X.; Lian, Q.; Zhou, L.; Jiang, Y.; Gao, J. *ACS Sustainable Chem. Eng.* **2021,** *9,* 7030–7043. doi:10.1021/acssuschemeng.1c00723
78. Gerbreders, V.; Krasovska, M.; Sledevskis, E.; Gerbreders, A.; Mihailova, I.; Tamanis, E.; Ogurcovs, A. *CrystEngComm* **2020,** *22,* 1346–1358. doi:10.1039/c9ce01556f
79. Gerbreders, V.; Krasovska, M.; Mihailova, I.; Ogurcovs, A.; Sledevskis, E.; Gerbreders, A.; Tamanis, E.; Kokina, I.; Plaksenkova, I. *Sens. Bio-Sens. Res.* **2019,** *23,* 100276. doi:10.1016/j.sbsr.2019.100276
80. Krasovska, M.; Gerbreders, V.; Mihailova, I.; Ogurcovs, A.; Sledevskis, E.; Gerbreders, A.; Sarajevs, P. *Beilstein J. Nanotechnol.* **2018,** *9,* 2421–2431. doi:10.3762/bjnano.9.227
81. Song, M.-J.; Hwang, S. W.; Whang, D. *Talanta* **2010,** *80,* 1648–1652. doi:10.1016/j.talanta.2009.09.061
82. Gao, P.; Liu, D. *Sens. Actuators, B* **2015,** *208,* 346–354. doi:10.1016/j.snb.2014.11.051
83. Atacan, K. *J. Alloys Compd.* **2019,** *791,* 391–401. doi:10.1016/j.jallcom.2019.03.303
84. Demir, N.; Atacan, K.; Ozmen, M.; Bas, S. Z. *New J. Chem.* **2020,** *44,* 11759–11767. doi:10.1039/d0nj02298e
85. Jirjees Dhulkefl, A.; Atacan, K.; Bas, S. Z.; Ozmen, M. *Anal. Methods* **2020,** *12,* 499–506. doi:10.1039/c9ay02175b

License and Terms

This is an open access article licensed under the terms of the Beilstein-Institut Open Access License Agreement (https://www.beilstein-journals.org/bjnano/terms), which is identical to the Creative Commons Attribution 4.0 International License (https://creativecommons.org/licenses/by/4.0). The reuse of material under this license requires that the author(s), source and license are credited. Third-party material in this article could be subject to other licenses (typically indicated in the credit line), and in this case, users are required to obtain permission from the license holder to reuse the material.

The definitive version of this article is the electronic one which can be found at:
https://doi.org/10.3762/bjnano.13.35

BEILSTEIN JOURNAL OF NANOTECHNOLOGY

A nonenzymatic reduced graphene oxide-based nanosensor for parathion

Sarani Sen*[1,2], Anurag Roy[3], Ambarish Sanyal[1] and Parukuttyamma Sujatha Devi[4]

Full Research Paper

Open Access

Address:
[1]Functional Materials and Devices Division, CSIR-Central Glass & Ceramic Research Institute, 196 Raja S.C. Mullick Road, Jadavpur, Kolkata 700032, India, [2]National Institute of Technology Durgapur, Mahatma Gandhi Road, A-Zone, Durgapur, West Bengal 713209, India, [3]Environment and Sustainability Institute, University of Exeter, Penryn Campus, Cornwall TR10 9FE, United Kingdom and [4]Chemical Sciences and Technology Division, CSIR-National Institute of Interdisciplinary Science and Technology, Thiruvananthapuram, Kerala 695019, India

Email:
Sarani Sen* - sspst_rs@caluniv.ac.in

* Corresponding author

Keywords:
electrochemical nanosensor; graphene oxide; nonenzymatic approach; parathion; pesticides; square-wave voltammetry

Beilstein J. Nanotechnol. **2022,** *13,* 730–744.
https://doi.org/10.3762/bjnano.13.65

Received: 28 April 2022
Accepted: 15 July 2022
Published: 28 July 2022

This article is part of the thematic issue "Nanomaterial-based sensors for water remediation, healthcare and food monitoring applications".

Guest Editor: A. A. Oladipo

© 2022 Sen et al.; licensee Beilstein-Institut.
License and terms: see end of document.

Abstract

Organophosphate-based pesticides (e.g., parathion (PT)) have toxic effects on human health through their residues. Therefore, cost-effective and rapid detection strategies need to be developed to ensure the consuming food is free of any organophosphate-residue. This work proposed the fabrication of a robust, nonenzymatic electrochemical-sensing electrode modified with electrochemically reduced graphene oxide (ERGO) to detect PT residues in environmental samples (e.g., soil, water) as well as in vegetables and cereals. The ERGO sensor shows a significantly affected electrocatalytic reduction peak at −0.58 V (vs Ag/AgCl) for rapid quantification of PT due to the amplified electroactive surface area of the modified electrode. At optimized experimental conditions, square-wave voltammetric analysis exhibits higher sensitivity (50.5 $\mu A \cdot \mu M^{-1} \cdot cm^{-2}$), excellent selectivity, excellent stability (≈180 days), good reproducibility, and repeatability for interference-free detection of PT residues in actual samples. This electrochemical nanosensor is suitable for point-of-care detection of PT in a wide dynamic range of 3×10^{-11}–11×10^{-6} M with a lower detection limit of 10.9 pM. The performance of the nanosensor was validated by adding PT to natural samples and comparing the data via absorption spectroscopy. PT detection results encourage the design of easy-to-use nanosensor-based analytical tools for rapidly monitoring other environmental samples.

Introduction

Crop production is constantly increasing to fulfil the demands of the growing population. The protection of crops against insects is a big challenge for our society. Pesticides have indiscriminately been used in all sectors of agriculture. Among the various pesticides available for the aforementioned purpose, organophosphates (OPs) are commonly employed in agricul-

ture, households, gardens, and veterinary practices. This practice also jeopardizes food safety in all stages of the food supply chain, even after pesticide use. Due to its high nondegradability, pesticides can stay more often on the surface of fruits and vegetables; sometimes, it can also penetrate into the peel of vegetables and fruits [1]. Organophosphorus insecticides react with biomolecules either via deoxyribonucleic acid (DNA) alkylation or acetylcholinesterase (AChE) phosphorylation, involved in the initiation of the carcinogenic process and acute cholinergic toxicity, respectively [2]. Parathion (PT) is a highly toxic OP-based insecticide, potentially harmful to human health, and it may even cause death upon ingestion, inhalation, or dermal penetration [3,4]. Due to its extreme toxicity, it is necessary that easy-to-use, cost-effective diagnostic kits for routine screening of pesticides in fruits and vegetables are developed.

The high-throughput analytical methods such as chromatographic (gas, liquid) and spectroscopic (mass, absorption, fluorescence) techniques are time-consuming, laborious, costy, require specific and sophisticated instruments and trained personnel, and most often are not portable to enable on-site detection [5,6]. Electrochemical nanosensors are one of the preferred methodologies due of their fast and straightforward responsive nature, high sensitivity, and selectivity leading to real-time detection [7]. A combination of a receptor, an analyte, and a transducer is made up to obtain an electrochemical sensor, in which the surface of the electrode induces redox characteristics via selective binding with the analyte under a voltage for a different analyte which results in a quick qualitative signal. This approach promotes real-time label-free methods, providing more consistent and reproducible results.

Most of the electrochemical nanobiosensors for the detection of OPs (e.g., methyl parathion, ethyl parathion, fenitrothion, chlorpyrifos, paraoxon, ethion, and acephate) are based on the inhibition of acetylcholinesterase (AChE) activity (an indirect method) [8-10]. Some organic molecules and metal cations also act as an inhibitor of AChE. Thus, interference-free detection of OP in agricultural samples using enzyme-based nanosensors is challenging. The stability of bionanosensors also extensively depends on the viability of the corresponding biomolecule during the matrix immobilization course [9]. The main drawbacks of using bionanosensors for the selective detection of OP in actual samples are i) the high cost of the enzyme, ii) low stability of biomolecules at room temperature, and iii) difficulties in using interference-free selective detection of a specific OP. However, nonenzymatic electrochemical nanosensors could easily be employed as rapid, cost-effective, easy-to-handle, selective, sensitive, and point-of-care (POC) analytical tools for monitoring environmental pollutants [2,11]. They can also detect residual OPs based on their electrocatalytic activity and affinity toward nanomaterials, such as nanoparticles, carbon nanomaterials, and metal oxides [11]. In a few reports, hybrid carbon nanomaterials such as ferrocene-thiophene modified by carbon nanotubes, zinc(II) phthalocyanine-boron dipyrromethene attached single-walled carbon nanotubes were used for the direct detection of pesticides [12-15]. So far, only limited electrochemical nanosensors modified by nanomaterials have been reported to detect PT [16,17]. However, their sensitivity and detection limit for quantifying trace amounts of PT in environmental samples are improved. The inherent electrochemical behavior of nitroaromatic OPs (e.g., paraoxon, parathion, and fenitrothion) exhibit well-defined redox activities at the electrode surface, potentially leading to the fabrication of nonenzymatic electrochemical nanosensors for detecting specific OPs on the electroactive surface [2,11,17-19]. For example, electrochemical sensing platforms modified with zirconia-embedded PEDOT membrane, graphene nanoribbons doped with silver nanoparticles, rGO doped with ZrO_2, and $CuO–TiO_2$ hybrid nanocomposites were proposed to detect methyl parathion [19-22]. Rajaji et al. (2019) modified glassy carbon electrodes with graphene oxide encapsulated 3D porous chalcopyrite ($CuFeS_2$) nanocomposites to detect methyl paraoxon in vegetables [23]. Recently, Jangid et al. (2021) also described the electrocatalytic activity of fenitrothion on glassy carbon electrodes modified with nitrogen and sulfur co-doped activated carbon-coated multiwalled carbon nanotubes [24]. Nevertheless, the fabrication process of the sensing platform was not cost-effective, stable, and sensitive in order to develop a robust electrochemical nanosensor for on-site monitoring of organophosphates in agricultural samples. To date, no reliable sensing system is available for the rapid quantification of parathion residues in environmental samples. Thus, the primary goal of this report was to showcase the fabrication of a more effective, economical, electroactive surface in a simplified way to selectively detect PT residues in real samples. Thus, a robust sensing matrix can be used for designing a nonenzymatic POC device with a low detection limit and long-term stability at room temperature.

Graphene oxide (GO), consisting of a monolayer of sp^2-hybridized carbon atom network, has already been used in electrocatalysis, nanoelectronics, bionanosensors, and sustainable energy storage systems due to its larger active surface area, enhanced electron transport facility, excellent mechanical, thermal, and electrical stability [11,25-27]. The electronic structure and surface physicochemistry of graphene are beneficial for electron transfer. Several graphene-based nanocomposites based on complex synthesis processes are reported as excellent sensing matrices for detecting various analytes [11,21-23,28]. The "green synthesis" of graphene via electrochemical reduction is the most economical strategy for the mass production of

graphene compared to chemical or thermal reduction of GO [27,29]. Since no hazardous chemicals (e.g., hydrazine) as reductants or rapid heat treatment at high temperatures are required for the synthesis of electrochemically reduced GO (ERGO), controlled synthesis of ERGO films could be possible via optimization of electrochemical parameters. These parameters are the range of the applied voltage, numbers of cycles, the scan rate of cyclic voltammetry, or reduction time at a fixed potential in chronoamperometry [30-32].

However, the desired size and thickness of the film can be increased by controlling the amount of precursor GO deposited onto the electrode surface [31,32]. Optimizing the process parameters is a robust scientific approach to achieving the highest sensing performance of an electroactive analyte.

In this work, we proposed a simple, robust, and reliable ERGO-modified nonenzymatic electrochemical nanosensor as a good alternative for a POC-based easy diagnostic platform to monitor the level of PT residues in environmental samples, such as water, soil, crops, and vegetables. A straightforward and economic fabrication process with high sensitivity, selectivity, and stability with the lowest detection limit is the foremost advantage emerging from this study for the rapid on-site monitoring of PT. For this purpose, the electrochemical reduction of GO was tuned using various electrolytic buffers with different pH values, supporting the variation of the physicochemical characteristics of ERGO discussed in this work. Besides, this study highlights the scope of an interference-free nonenzymatic approach through electrochemical nanosensing which can also be used in other biosensing applications.

Experimental

Chemicals

The chemicals used in this work are summarized in Supporting Information File 1, Table S1. Sodium dihydrogen phosphate was used to prepare phosphate buffer saline (pH 4.6, 7.4, 9). Acetate buffer (20 mM, pH 4.5), and Britton–Robinson (BR) buffer (40 mM, pH 4) consisting of phosphoric acid, boric acid, and acetic acid were also prepared.

Synthesis of graphene oxide

Graphene oxide was synthesized from graphite powder using a modified Hummer's method [30,31]. In detail, 100 mg of sodium nitrate (Merck) was added to 250 mg of graphite powder (Alfa Aesar) and further acidified with ≈5 mL of concentrated sulfuric acid (Merck) at a temperature range of 0–5 °C followed by vigorous stirring. In the next step, 600 mg of $KMnO_4$ (Merck) was sequentially added to the aforementioned solution, during which the solution temperature was increased to 35 °C. After 30 min of the addition of $KMnO_4$, a brownish-grey paste was obtained. Deionized water (100 mL) was added to the paste under constant stirring at 90 °C for 30 min, followed by dropwise addition of 30% H_2O_2 (Merck, India). Finally, a dark brown solution was filtered and thoroughly washed with 100 mL of distilled water until a neutral pH value was achieved. The black product obtained after filtration was dispersed in water and sonicated for 1 h to get a well-dispersed suspension. Finally, the suspension was centrifuged twice at 3000 rpm for 15 min. The product (GO) was collected and dried at room temperature for further studies.

Fabrication of electrochemically reduced graphene oxide modified electrodes

Before surface modification of GO, a bare glassy carbon electrode (GCE, φ = 3 mm) was polished in 1.0, 0.3, and 0.05 micron alumina slurry (CHI Instruments) on micro cloth pads sequentially to a mirror-like finish with fine wet emery paper (grain size 4000), and rinsed with ultrapure water. Then the electrode was separately dipped into concentrated NaOH, nitric acid, and methanol for 120 s, followed by sonication in alcohol for 2 min, and finally dried in air. The as-prepared GO colloidal suspension (2 $mg{\cdot}mL^{-1}$) was deposited onto the surface of the pretreated GCE and dried at room temperature. The GO/GCE was submerged in 50 mM PBS, pH 4.6, for the electrochemical reduction of GO by a potentiostat technique at a potential of −0.9 V for 900 s using an Ag/AgCl reference electrode. The buffer and pH values of the electrolytes were optimized to fabricate electrochemically reduced GO (ERGO) modified GCE designated as ERGO/GCE.

Cyclic voltammogram (CV) measurements to assess the electrochemical behavior of parathion were performed from +0.5 to −1.0 V versus Ag/AgCl, with a scan rate of 100 $mV{\cdot}s^{-1}$. Square-wave voltammetry (SWV) analysis was performed from −0.3 to +0.9 V versus Ag/AgCl, with pulse amplitude of 100 mV, frequency of 25 Hz, and modulation time of 10 s in 50 mM PBS. The nanosensor was cycled 25 times for signal stabilization before PT detection.

Preparation of environmental and food samples for residual parathion analysis

The practical application of the proposed electrochemical nanosensor was studied by sensing PT in the groundwater, soil, tomato, and rice samples with different concentrations of PT. The groundwater and soil were collected from local agricultural land in Kolkata, India. As parathion is highly soluble in alcoholic compounds, we have used ethanol to extract residual PT from the collected food and environmental samples. The soil sample (1 g) was stirred for 1 h in 50% ethanol to disperse all organic and inorganic soil molecules in the liquid phase. Tomato as a sample vegetable was purchased from the local

market in Kolkata, India, and washed with running water before preparing the sample. The tomato samples (30 g) were smashed with 30 mL of 50% ethanol, and the juice was collected for further filtration. Boiled rice (20 g) was also smashed with 20 mL of 50% ethanol. All the samples were stored at 4 °C after filtration (pore size = 0.45 micron) to remove all the solid impurities. Actual samples were spiked with different concentrations of PT during electrochemical analysis. Each concentration of PT was tested five times, and the average value was represented with standard deviation. The results also validate the standard spectrophotometric analysis.

Quantification of parathion using spectrophotometry

The ultraviolet–visible (UV–vis) absorption spectroscopic study was performed to validate the results of the proposed nanosensor. A stock solution (1 mM) of PT was prepared in 99.9% ethanol (Empura, Merck). A 5 mL volume of working solutions of 1 to 35 μM was prepared in ethanol for monitoring the UV spectra in the range of 200–400 nm with a scan rate of 2 nm/s. The absorbance change of PT due to π–π* transition was noted at 273 nm using ethanol as blank, and a calibration curve was plotted to compare the results obtained from the proposed nanosensor.

Material characterization

Voltammetric studies were carried out using an IVIUMStat electrochemical analyzer (Model: A09050, Iviumstat Technologies, USA), which was connected by a three-electrode system, including a modified and/or unmodified GCE as the working electrode, a saturated Ag/AgCl as the reference electrode (RE), and a platinum wire as the counter electrode (CE). The electrochemical impedance spectroscopy (EIS) study of the modified electrodes was carried out in 5 mM of $[Fe(CN)_6]^{3-}$ and $[Fe(CN)_6]^{4-}$ with 0.1 M KCl within the frequency range from 1 MHz to 0.01 Hz, amplitude of 10 mV, at a fixed potential of 0.28 V.

The UV–visible absorbance spectra were obtained on a UV–vis–NIR spectrophotometer (SHIMADZU UV-3600). The Raman spectra of the samples were recorded in the 1000–3500 cm^{-1} region with a resolution of 1 cm^{-1} using a Renishaw via a Reflex micro-Raman spectrometer with an argon ion (514.6 nm) laser. The X-ray photoemission spectroscopy (XPS) data were obtained from a PHI 5000 Versa probe II scanning XPS microprobe (ULVAC-PHI, U.S.) with monochromatic Al Kα (hν = 1486.6 eV) radiation, and a beam size of 100 μm. The Fourier transform infrared (FTIR) absorption spectra of GO and ERGO were collected in the 4000–400 cm^{-1} region on a Perkin Elmer spectrometer as KBr (Sigma-Aldrich, Germany) pellets. The crystalline phase of GO and RGO was characterized by X-ray diffraction (XRD) using a X'pertpro MPD XRD (PAN analytical B.V., the Netherlands) with Cu Kα radiation (λ = 1.5406 Å).

Scanning electron microscopy (SEM) of the modified electrode was conducted on a JEOLEVO® 18 special edition (model: ZEISS EVO-MA 10) at an acceleration voltage of 15 kV. The morphological characteristics of the electrodeposited ERGO were obtained by field-emission scanning electron microscopy (FESEM, model: LEO 430i, Carl Zeiss) and high-resolution transmission electron microscopy (model: Tecnai G2 30ST, FEI) operating at 300 kV.

Results and Discussion

Optimization and characterization of electrochemically reduced graphene oxide formation

Figure 1A shows the UV spectra of GO and its change following the electrochemical reduction of GO. It is observed that the absorption peak of GO at 223 nm due to the π–π^* transition of the C=C bond disappeared in ERGO. The amount of residual oxygenated functional groups in ERGO films is likely to vary depending on the experimental conditions, such as applied potential, reduction times, and the electrolyte used [25]. The process parameters for electrochemical reduction were optimized to develop better functioning electrodes. Raman spectroscopy has been frequently used as a reliable technique to optimize the electrochemical parameters for the synthesis of ERGO in terms of the intensity ratio of D- (disordered band) to G-band (graphitic band) (I_D/I_G). It measures the change in size of the sp^2 ring clusters in a network of sp^3- and sp^2-bonded carbon [33]. Previous reports have indicated the possibility of converting GO to ERGO at different electrochemical parameters, but its effect on the I_D/I_G value have not been reported [25,29,33]. In this report, the pH value and buffer composition of the electrolyte were optimized to increase the deoxygenation of the GO sheet during ERGO formation. Figure 1B depicts three significant Raman peaks of GO at 1350 cm^{-1} for the D band (associated with defects in the sp^2 lattice), 1596 cm^{-1} for the G band (due to vibrations of the hexagonal lattice), and 2700 cm^{-1} for the 2D band (related to numbers of layers in the graphene sheet). Table 1 shows the values of I_D/I_G at different electrolytic buffers during one-step electroreduction of GO at a constant potential of −0.9 V. The intensity of I_D/I_G predominantly increased for ERGO compared to the that of the as-prepared GO, which suggests a decrease in size of the sp^2 domain due to extensive deoxygenation of the graphene sheets after electrochemical reduction. The comparative values of I_D/I_G (Table 1) also indicate that a higher defect in the sp^2 domain was observed at acidic pH values of the electrolytic buffer during electrochemical reduction of GO. The highest value of

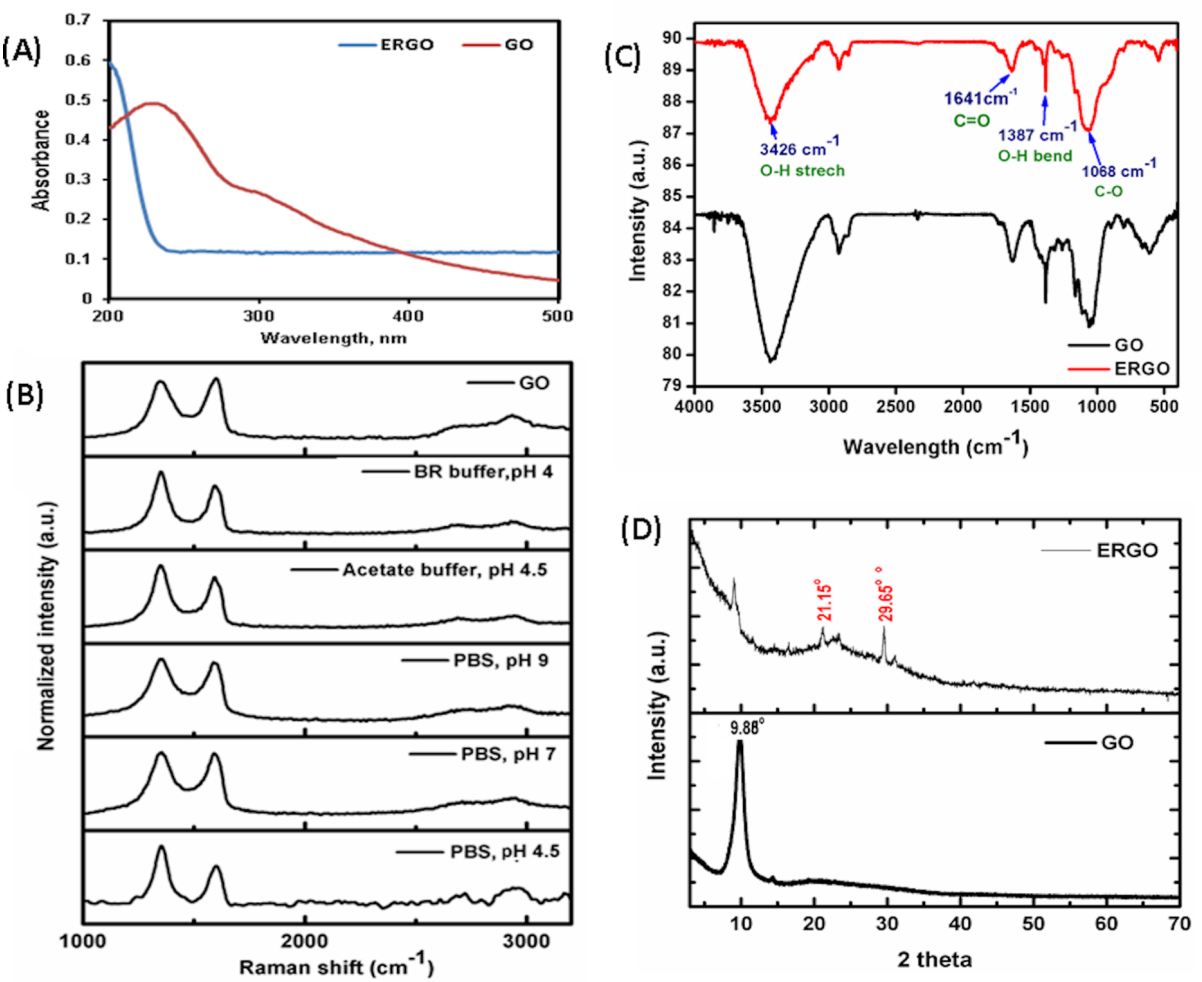


Figure 1: (A) UV–vis spectra of GO and ERGO. (B) Raman spectra for GO to ERGO conversion using different buffers as electrolytes. (C) FTIR spectra and (D) XRD patterns of GO and ERGO (PBS pH 4.5).

Table 1: Experimental sample table showing variation of Raman peak intensity ratio of ERGO using different electrolytes.

Sample in different pH	I_D	I_G	I_D/I_G	I_{2D}	I_{2D}/I_G
GO	0.975524	1.01748	0.958765	0.43182	0.442654
acetate buffer, pH 4.5	1.00602	0.819277	1.227936	0.21328	0.212004
BR buffer, pH 4	1.01807	0.792169	1.285168	0.225525	0.221522
PBS buffer pH 4.5	1.00301	0.68976	1.454143	0.33042	0.329428
PBS buffer, pH 7	1.03313	0.978915	1.055383	0.29371	0.284291
PBS buffer, pH 9	1.03012	0.942771	1.092651	0.25699	0.249476

I_D/I_G was found to be 1.454 for the conversion of ERGO using PBS (pH 4.5), which suggests the formation of higher defects between the graphene layers during electrochemical reduction [26,34]. Thus, 50 mM PBS, pH 4.5, has been chosen for an efficient conversion of GO to ERGO.

Figure 1C shows the characteristic FTIR spectra of GO and ERGO (in PBS, pH 4.5) to identify the change of functional groups due to electrolytic reduction of GO. The predominant characteristic absorption peaks of GO include a broad peak at 3426 cm^{-1} corresponding to the O–H stretching vibration origi-

nating from carboxyl groups. Besides, an intense peak at 1641 cm^{-1} was assigned to the C=O stretching of carboxyl and/or carbonyl groups, a sharp peak at 1387 cm^{-1} corresponding to a –OH bend, and a strong peak at 1068 cm^{-1} ascribed to an alkoxy and/or epoxy C–O stretching vibration. The significant reduction of the FTIR signal intensity of ERGO for –OH, –C=O, and –C–O suggests the successful formation of ERGO due to the electrochemical deoxygenation of GO, which corroborates the Raman analysis.

Figure 1D depicts a characteristic XRD peak of GO at 2θ = 9.98 (interplanar spacing = 0.843 nm) corresponding to 001 reflections. Two characteristic peaks of ERGO at 2θ = 21.15 (interplanar spacing = 0.413 nm) and 2θ = 29.65 (*d*-spacing = 0.343 nm) for the reflection of (020) and (200), respectively, confirm the successful formation of ERGO from GO.

Figure 2 represents the deconvoluted C 1s and O 1s XPS spectra of GO (Figure 2A and Figure 2B) and modified ERGO (Figure 2C and Figure 2D) electrodes. An asymmetric peak centered on ≈284.8 eV appeared due to the graphitic nature of GO and ERGO (Figure 2A and Figure 2B). Four different carbon types are observed from the deconvolution of the peaks shown in Figure 2A. They show an increase in binding energies evidencing the presence of C–OH, C–C, C–O–C, and C=O bonds in GO. The O 1s spectra of synthesized GO can be deconvoluted into three peaks, corresponding to contributions from carbonyl and carboxyl-type oxygen (531.4 eV), C–OH type (532.5 eV), and hydroxyl (533.6 eV). The intensity of the peaks is significantly reduced in RGO samples (Figure 2C and Figure 2D) compared to pristine GO, indicating considerable deoxygenation. The C 1s spectra of RGO (Figure 2C) can also be deconvoluted into four peaks at 284.7, 285.96, 292.8, and 295.7 eV. However, the relatively intense doublet appeared at 292.8 ± 0.1 eV and beyond 295 eV every time we performed the scan. Peaks in the range of 290 eV in these types of materials are mainly due to aromatic π–π* transitions. However, considering the intensity of the peak and our repeated measurements, we believe that the presence of a well-defined deconvoluted doublet peak beyond 290 eV corresponds

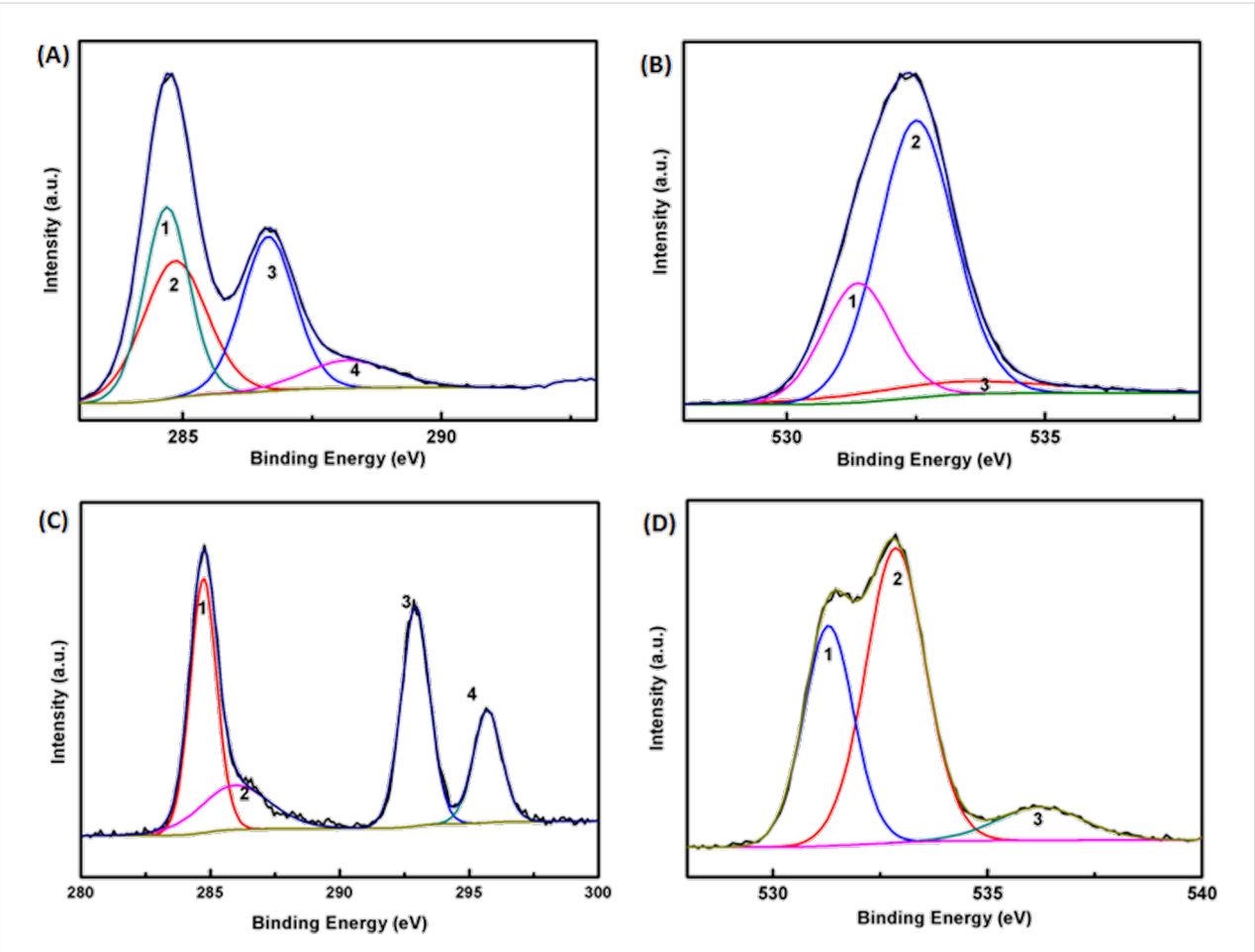


Figure 2: Deconvoluted XPS core-level spectrum of (A) C 1s, (B) O 1s for GO, (C) C 1s, and (D) O 1s for ERGO samples, respectively.

to K $2p_{3/2}$ and K $2p_{1/2}$, which may have resulted from the contribution coming from the potassium salt present in the buffer during electrochemical conversion. The deconvoluted analysis of the peaks and the relative atomic percentages of GO and RGO are summarized in Supporting Information File 1, Table S2.

Figure 3A–D depicts TEM micrographs of as-prepared GO and synthesized ERGO at different pH values, indicating that the intensity of the electrons is attenuated by the platelets of graphene sheets with varying transparencies due to thickness variation [26,31]. Dark areas of the micrograph suggest thick stacking layers of GO and/or RGO with intercalated oxygen-containing functional groups. A few layers of graphene sheet in ERGO (in PBS, pH 4.5) have areas with higher transparency due to the exfoliation of stacking layers of GO. This suggests an increased surface area due to delamination of graphene layers (thickness of about one to a few layers) by electrochemical reduction. The high-resolution TEM of ERGO shows a *d*-spacing of 0.413 nm (Figure 3E), indicating a reduced graphite nature of GO. This confirms that the oxygen functional groups were removed from the graphene layers by electrochemical reduction of GO, decreasing the interspacing distance between graphene layers which facilitates electron transport. Thus, the conductivity of ERGO was enhanced compared to that of GO. The SEM micrograph of ERGO (Figure 3G) also shows graphene sheet exfoliated layers compared to GO (Figure 3F). The FESEM image also depicts the flaked nanostructure of RGO (Figure 3H).

Electrochemical characterization of the modified electrode

The electronic properties of graphene materials depend on the number of layers and the distance between the layers, which can be changed by a variation of the synthesis protocol to achieve a higher electroactive surface area and electrical conductivity. Figure 4A displays a higher oxidation/reduction peak current of $Fe^{2+/3+}$ redox couple for the synthesized ERGO in PBS pH 4.5. It forms the highest electroactive surface area compared to other electrolytic buffers and pH values to prepare ERGO/GCE. To confirm the increase in the electroactive surface area of ERGO/GCE in comparison to bare GCE, CV was performed at different scan rates (10–300 mV/s) in 1.0 mM $K_3Fe(CN)_6$ as a redox probe (Supporting Information File 1, Figure S1). The electroactive surface areas were calculated according to Randles–Sevcik equation (Equation 1) [28,32]:

$$I_p = \left(2.69\times10^5\right) n^{3/2} A_c D_r^{\frac{1}{2}} v^{\frac{1}{2}} C_0, \quad (1)$$

where I_p is the peak current (A), ν is the scan rate (V s^{-1}), n is the number of electrons transferred (n = 1), A_c is the electrode active area (cm^2), D_r is the diffusion coefficient (7.6×10^{-6} $cm^2 \cdot s^{-1}$), and C_0 is the concentration of $K_3Fe(CN)_6$ ($mol \cdot cm^{-3}$). From the slope of the plot of I_p vs $v^{1/2}$, the effective surface area for bare GCE and ERGO/GCE was calculated to be 0.0707 and 0.121 cm^2, respectively, which indicates that the effective electroactive surface area of ERGO has been improved by ≈71.14% due to exfoliation of graphene sheets.

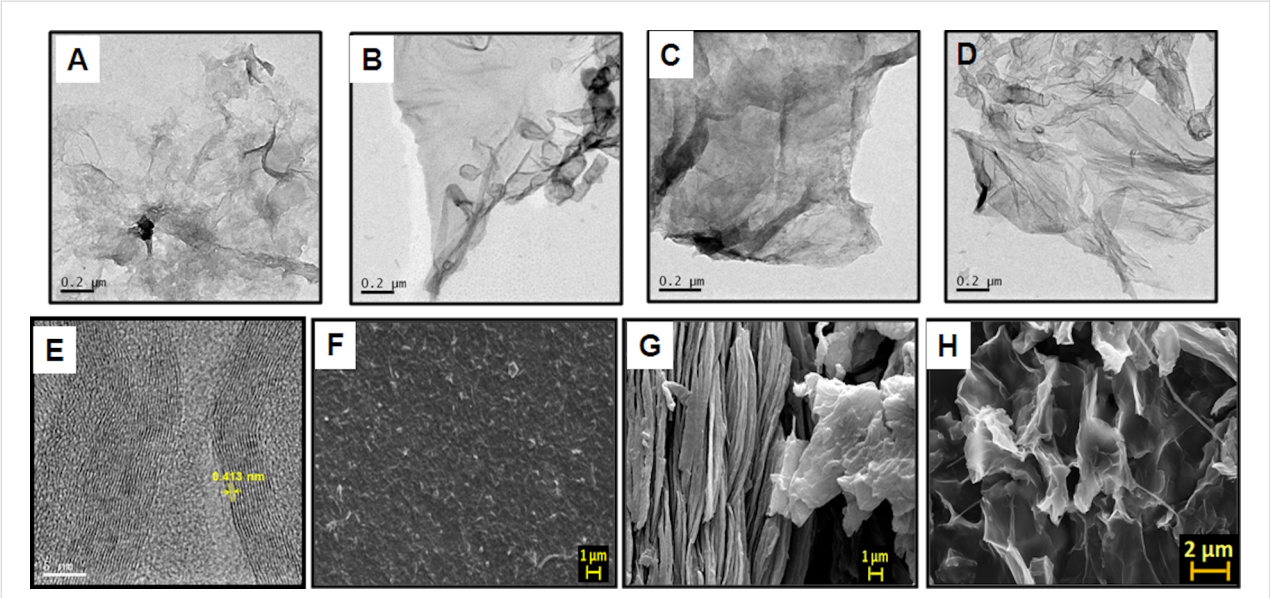


Figure 3: (A) TEM images of as-synthesized GO, ERGO synthesized in different electrolytes: (B) PBS pH 4.5, (C) pH 7, and (D) pH 9.6. (E) HRTEM image of ERGO in PBS pH 4.5. (F) SEM micrographs of as-synthesized GO, (G) ERGO in PBS pH 4.5 and (H) FESEM of ERGO in PBS pH 4.5 at different magnifications.

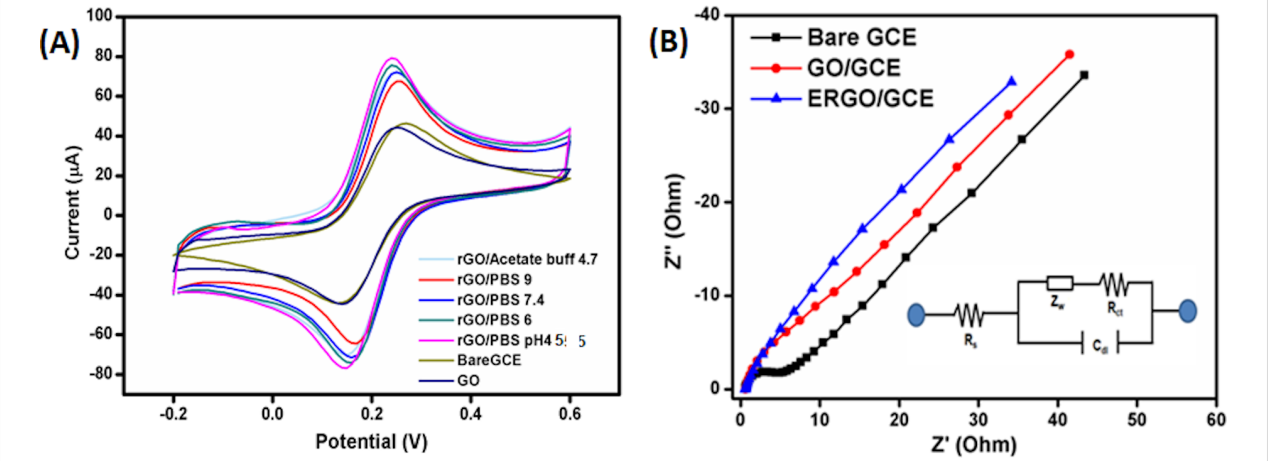


Figure 4: (A) Cyclic voltammograms of GO and ERGO using different electrolytic buffers: Acetate buffer pH 4.7, PBS pH 4.6, PBS pH 6, PBS pH 7.4, PBS pH 9. (B) Nyquist plot of bare GCE, GO/GCE, and ERGO/GCE in the presence of 1 mM $[Fe(CN)_6]^{4-/3-}$ containing 0.1 M KCl.

Electrochemical impedance spectroscopy was performed to investigate the electron transfer capability of ERGO (Figure 4B). Supporting Information File 1, Table S3 depicts the values of charge-transfer resistance (R_{ct}), capacitance (C_{dl}), and Warburg impedance (W) of bare GCE, GO/GCE, and ERGO/GCE. The Nyquist plot of the bare GCE electrode depicts a semicircle with R_{ct} of 4.692 Ω. A nearly straight line for ERGO with a negligible R_{ct} (1.618 Ω) value suggests opened porous microstructures of ERGO, which makes the graphene sheets more accessible to the electrolyte. It also facilitates electron transfer and diffusion of ions during the electrochemical process [28,34].

Electrochemical behavior of parathion at modified nanosensors

Figure 5A depicts the CVs (first cycle) of bare GCE, GO/GCE, and ERGO/GCE in PBS (0.05 M, pH 7) in 10 μM PT. The CV of PT on bare GCE (inset of Figure 5A), shows a reduction

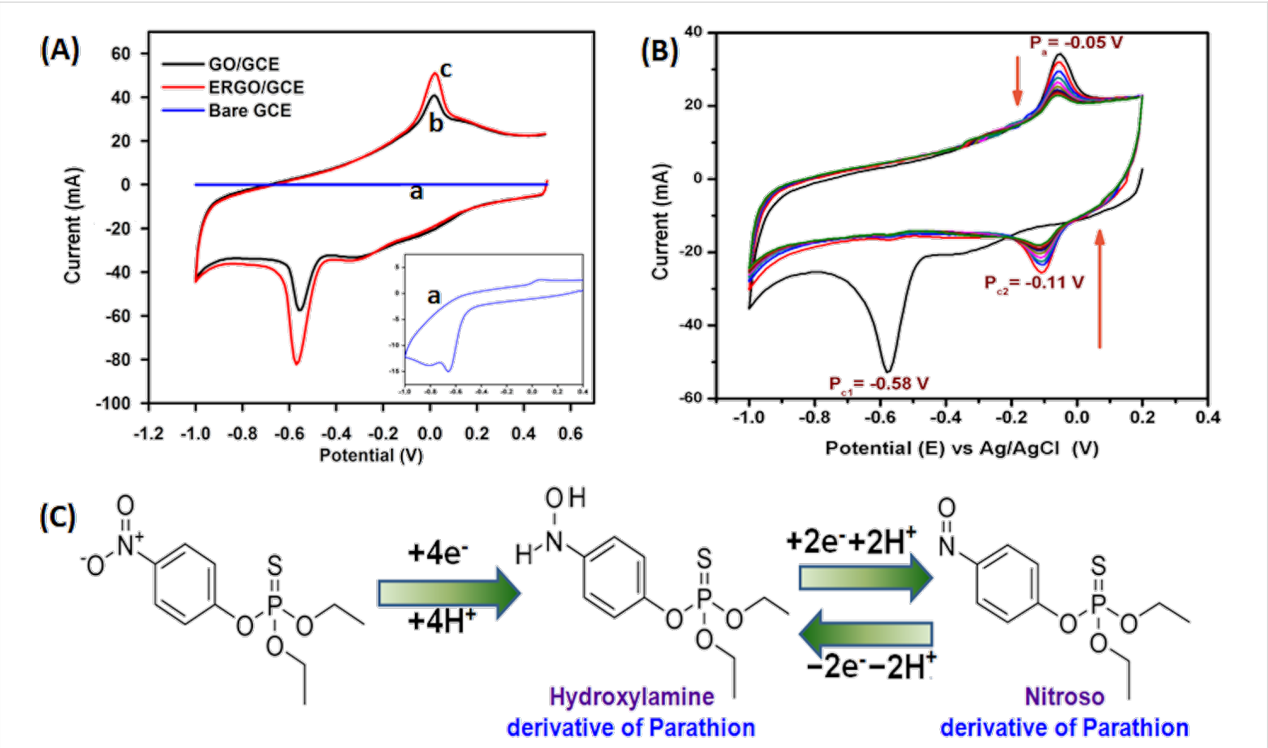


Figure 5: (A) Cyclic voltammograms of PT (10 mM) with bare GCE (a), GO/GCE (b), and ERGO/GCE (c). (B) Electrochemical behavior of PT at ERGO/GCE. (C) Schematic diagram of the proposed electrochemical reaction of parathion at ERGO/GCE.

peak at −0.65V and a little anodic peak due to autocatalysis of PT. A robust cathodic peak at −0.56 V and an anodic peak at +0.015 V were mainly observed on GO/GCE due to the absorption of PT through π stacking interaction between aromatic moieties of GO and the benzene ring of PT. In comparison, the highest cathodic/anodic peak was obtained at −0.58 and −0.05 V, respectively, for the electro-reduction/oxidation of PT on ERGO/GCE. The oxidation/reduction potentials of PT on ERGO/GCE were shifted to less positive values, effectively inhibiting the surface fouling caused by the reaction products, making ERGO-modified GCE more suitable for determining PT. The electrocatalytic ability of PT (10 µM) on the modified ERGO/GCE was investigated in PBS (pH 7) (Figure 5B) in the potential range from +0.2 to −1.0 V with a scan rate of 100 $mV{\cdot}s^{-1}$ and compared with the control group (bare GCE and GO/GCE). It is in good agreement with the literature reports that a sharp cathodic peak (E_{pc1}) at −0.58 V was observed in the first cycle due to the reduction of the nitro group of PT (NO_2–PT) to form its hydroxylamine derivatives (NHOH–PT) involving a four electron-transfer process as shown in Figure 5C [16-18,35]. An anodic peak appeared at −0.05 V in the backward segment of the first cycle, which is related to the oxidation of NHOH–PT to a nitroso group (NO–PT). This reversible two-electron-transfer process further generated a reduction peak (E_{pc1}) at −0.11 V during the second potential scan of CV (Figure 5C). Nitroaromatic OPs such as parathion, methyl parathion, ethyl parathion, and fenitrothion, paraoxon exhibit this kind of electrocatalytic behavior, which is consistent with previous reports [21,23,24]. In this study, we chose the irreversible reduction peak of PT (NO_2–PT to NHOH–PT) of the first cycle due to its suitability for important measurements in nanosensor applications.

The amount of exfoliated GO dispersed on bare GCE is vital in optimizing the sensing matrix. Figure 6A depicts the CVs using a variation of deposited GO on bare GCE to prepare ERGO/GCE to measure the reduction and oxidation peak current for 10 µM PT in PBS, pH 7. Figure 6B shows that the highest reduction peak for 10 µM PT was obtained using 8 µL of GO to prepare modified ERGO/GCE. As the autocatalytic response for the electrochemical oxidation/reduction process is an absorption process, the accumulation time is another vital parameter to

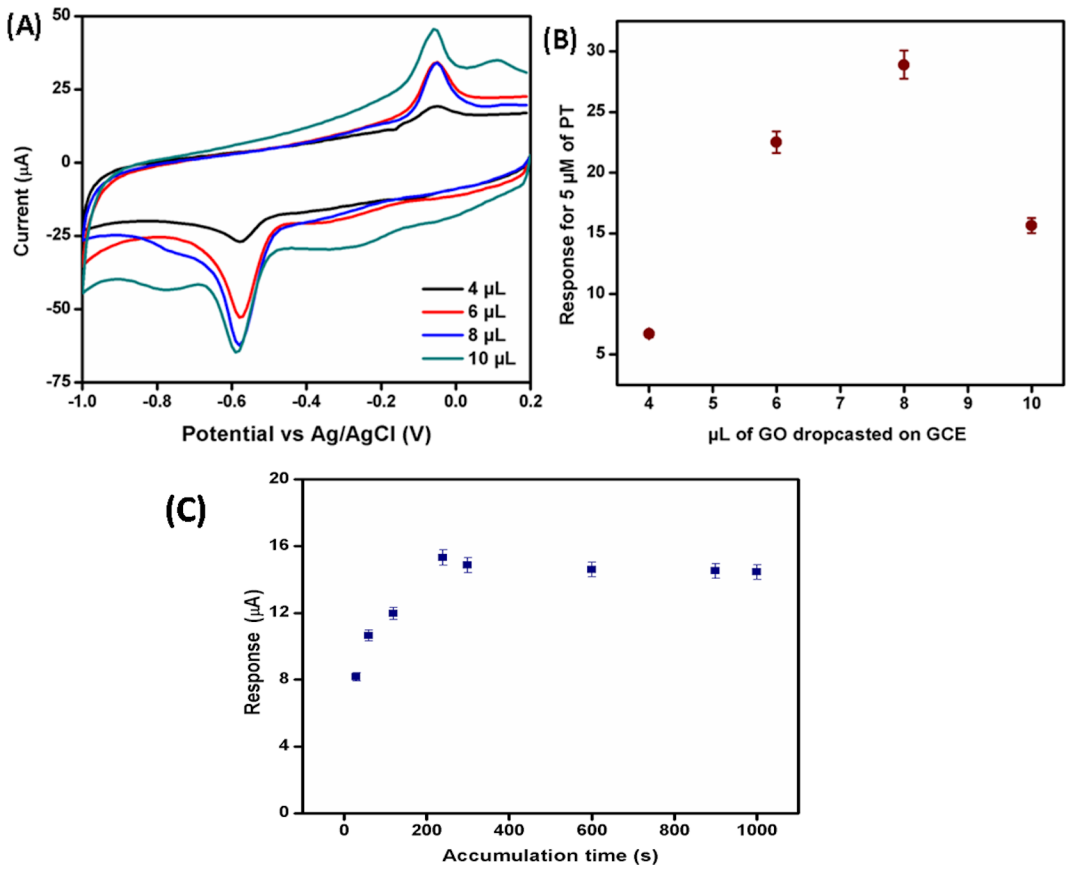


Figure 6: (A) Cyclic voltammograms of 10 µM PT in PBS, pH 7, with different amounts of GO deposited on bare GCE for the preparation of modified ERGO/GCE. (B) Peak current of cyclic voltammetry using 10 µM PT with different amounts of GO deposited on bare GCE for preparation of modified ERGO/GCE. (C) Peak response of 10 µM PT with variation of the accumulation time before voltammetric measurements.

achieve the highest response for monitoring the amount of parathion residue in samples [35,36]. It has been shown in Figure 6 that as the immersion time of the modified electrode in a PT solution increased, the accumulation of PT on the electrode surface also enhanced. It was found that the highest peak current for 10 µM PT was obtained after immersion for 240 s in the PT solution. A further increase in the accumulation time was unaffected as the active area of the electrode surface was saturated (Figure 6C).

Effect of scan rate and pH values on the electrolyte

The effect of scan rate on the reduction of PT at ERGO/GCE was investigated by applying different scan rates from 10 to 250 mV·s^{-1} (Figure 7A). The linear peak current increase with the scan rate suggests a surface-confined diffusion-controlled electrocatalytic process [21]. The slope of log I_{pc} as a function of log ν is 0.611 (>0.5), which confirms an adsorption-based reduction of PT on the modified electrode surface (Figure 7B). The reduction peak potential was shifted towards a more negative potential by increasing the scan rate. A linear equation of E_p as a function of log ν was represented as $E_p = -0.088\log \nu - 0.694$, with a correlation coefficient of (R^2) 0.992. From the Laviron's equation (Equation 2) for an irreversible reaction, E_p could be represented as

$$E_p = E^{\circ\prime} \pm \left(\frac{2.303RT}{\propto nF}\right)\log\left(\frac{RTk^\circ}{\propto nF}\right) \pm \left(\frac{2.303RT}{\propto nF}\right)\log \nu, \quad (2)$$

where ∝ is the transfer coefficient; n is the number of electron transfers; and R, T, F represent constants (R = 8.314 J·K^{-1}, T = 298 K, F = 96480 C·mol^{-1}). The standard redox potential ($E^{\circ\prime}$) was found to be −0.523 V from the linear plot of E_p as a function of ν ($E_p = -0.908\nu - 0.523$), at a scan rate 0 Vs^{-1}. The standard heterogeneous rate constant (k°) for electrocatalysis of PT was 38.81 s^{-1}. The value of $\propto n$ was calculated to be 0.672, and the n value was found to be 0.954 (i.e., one-electron transfer process [37]).

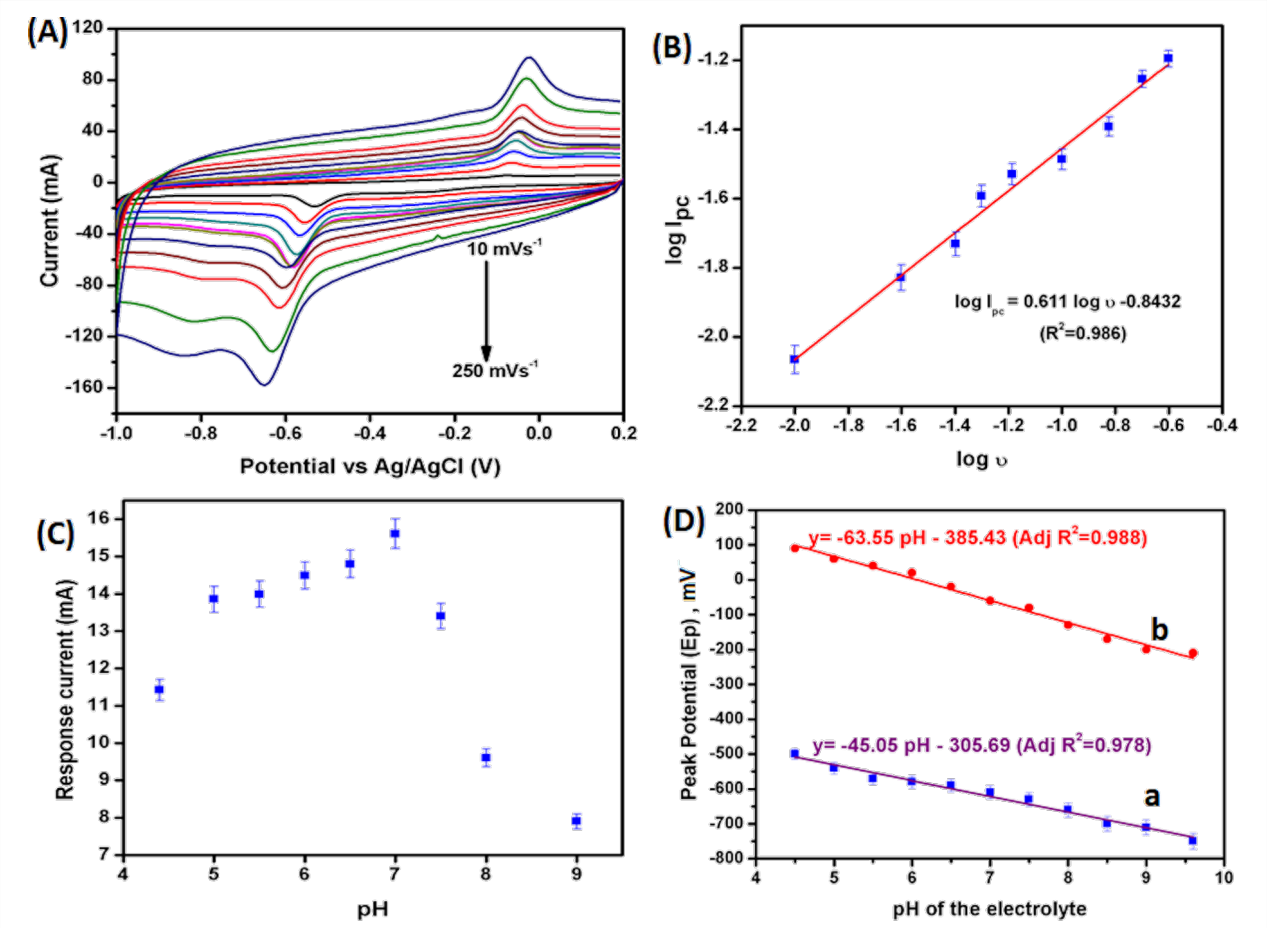


Figure 7: (A) Cyclic voltammograms of ERGO/GCE under different scanning rates (10, 25, 40, 50, 65, 80, 100, 125, 150, 200, 250 mV·s^{-1}) in PBS, pH 7, containing 10 µM PT. (B) Plot of the logarithm value of the reduction peak current as a function of the scanning rate (log I_{pc} as a function of log ν). (C) Plot of the reduction peak current of PT as a function of electrolyte pH. (D) Plot for the reduction (a) and oxidation (b) peak potential of PT (40 µM PT) as a function of the electrochemical cell pH, scan rate: 100 mV·s^{-1}.

The protonation reaction influences the electrochemical reaction. Figure 7C shows the effect of pH on the electroreduction of PT (40 µM) by varying the pH values of PBS from 4.6 to 9. The irreversible reduction potential of PT was shifted towards a more negative potential as the pH values of the electrolyte varied from 4.5 to 9 (Figure 7D). The slope of the reduction peak (E_{pc}) and oxidation peak (E_{pa}) potential of PT as a function of pH is near −59 mV, which suggests that the same number of e^- and H^+ is involved in the reaction [38,39].

Optimization of square-wave voltammetry parameters

Square-wave voltammetry analysis is more accurate compared to an electrochemical method such as cyclic voltammetry and differential pulse voltammetry. It can minimize background current to obtain an intense, sharp, and well-defined peak of the targeted analyte at a particular potential. To obtain the maximum peak current, the parameters of SWV were optimized using 10 µM PT in PBS (pH 7). The variation of reduction peak current with accumulation potential (A), starting potential of scan (B), frequency (C), and pulse amplitude (D) are shown Figure 8A–D.

Analytical performance and selectivity of the proposed nanosensor

Figure 9A represents SWV curves obtained from the ERGO modified electrode for sequential additions of PT into phosphate buffer (pH 7). A sharp increase in the reduction peak current was observed for each addition after dipping the electrode into a particular solution for 240 s at an applied potential of −0.1 V (i.e., deposition potential). The peak was shifted to a negative potential as the concentration of PT enhanced, indicating a diffusion-controlled process [40]. The concentration-dependent linear plot depicts good linearity (Figure 9B, Figure 9C) with a calibration equation of I_p (µA) = 3.5735 [PT] + 12.018 (R^2 = 0.9871) for the range of 0.1–11 µM, I_p (µA) = 0.2916 [PT] + 3.7526 (R^2 = 0.9936) for 3–15 nM, I_p (µA) = 19.176 [PT] + 4.2723 (R^2 = 0.9367) for 0.03–0.15 nM. The corresponding sensitivity was found to be 50.5 µA·µM^{-1}·cm^{-2} with a wide linear range for quantification

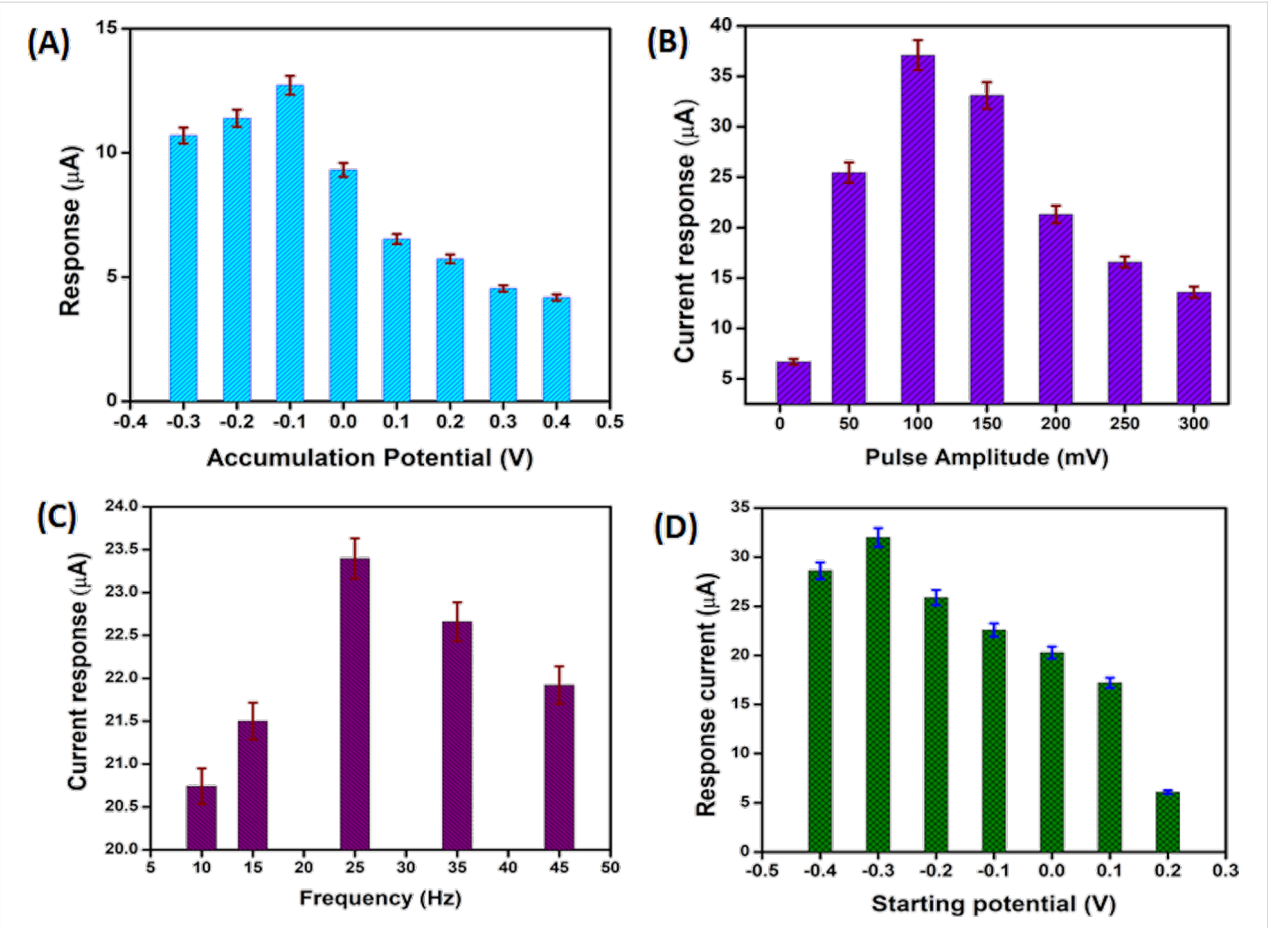


Figure 8: Relationship of stripping peak current in SWV measurements of 10 µM PT as a function of accumulation potential (A), starting potential of scan (B), frequency (C), and pulse amplitude (D). The optimized parameters for PT detection in SWV are: pulse amplitude: 100 mV, starting potential: 0.3 V, frequency: 25 Hz, accumulation potential: –0.1 V, and accumulation time: 240 s.

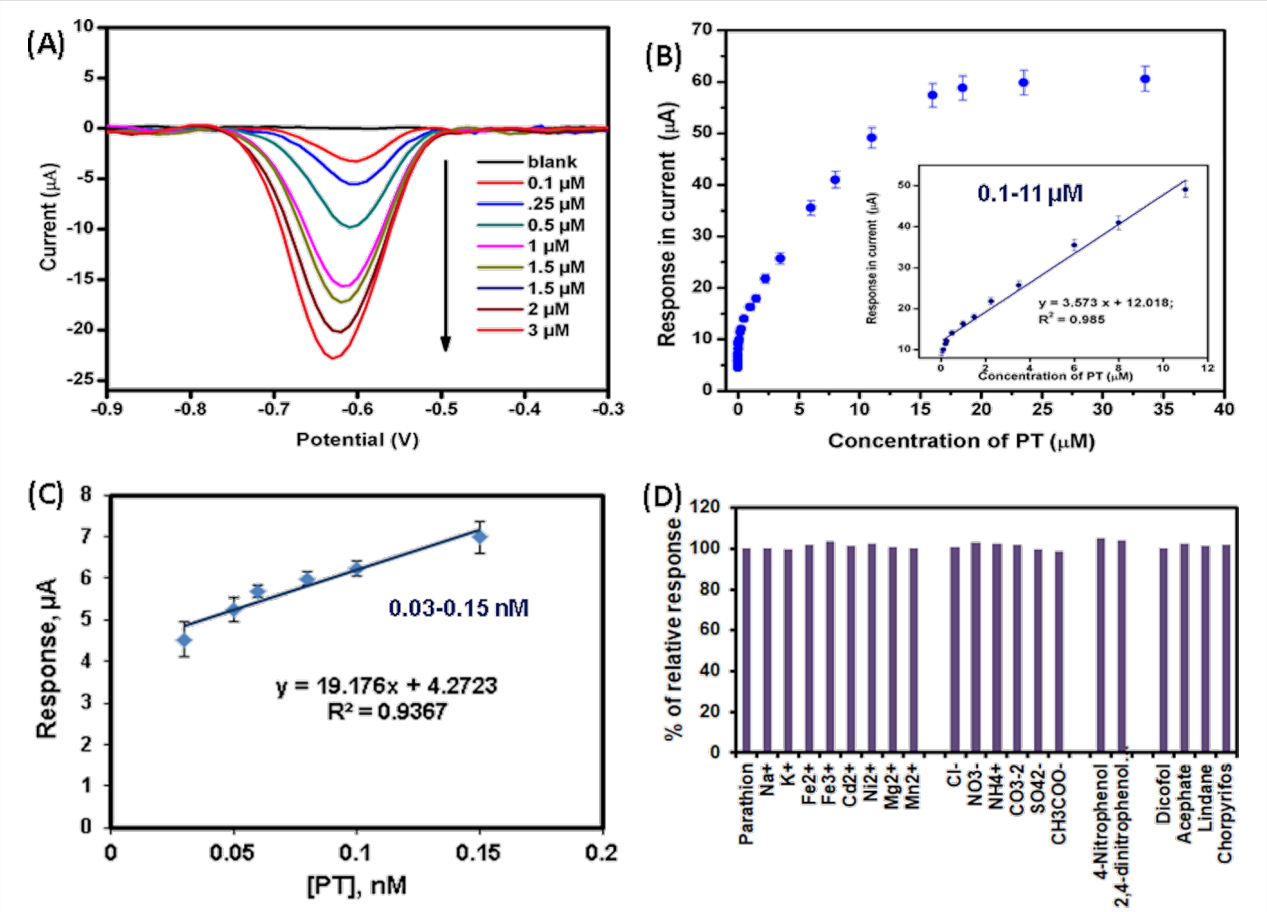


Figure 9: (A) SWV response of ERGO/GCE electrode in electrolytes (PBS, 0.05 M, pH 7) with different concentrations of PT ranging from 0.1 to 3 μM. (B) Calibration plot of peak current as a function of PT concentration for a wide range (i.e., 3×10^{-5} to 11 μM, inset: linear regression curve for 0.1 to 11 μM) and (C) 0.03–0.15 nM. (D) Selectivity studies of PT (10 μM) detection with probable interfering substances such as Na^+, K^+, Fe^{2+}, Fe^{3+}, Cd^{2+}, Ni^{2+}, Mg^{2+}, Mn^{2+}, NH_4^+, Cl^-, NO_3^-, CO_3^{2-}, SO_4^-, CH_3COO^-, 4-nitrophenol, 2,4-dinitrophenol, acephate, chlorpyrifos, dicofol, and lindane, respectively using SWV and keeping all other parameters constant. Experimental conditions: pulse amplitude: 100 mV, SWV frequency: 25 Hz, starting potential: 0.3 V, accumulation potential: –0.1 V, and accumulation time: 240 s.

of PT. The limit of detection (LOD = [(3 * standard deviation of blank)/slope of the lowest range of linear curve (i.e., 0.03–0.15 nM)] and limit of quantification (LOQ = [(10 * SD of blank)/slope]) were calculated as 10.9 pM and 36.5 pM, respectively, from the lower calibration equation [39,41].

The selectivity of the proposed ERGO/GCE modified nanosensor (Figure 9D) was investigated in the presence of other possible substances in water and soil samples. Square-wave voltammetry measurements were performed in PBS (50 mM, pH 7.0) containing 10 μM PT along with some inorganic ions (e.g., Na^+, K^+, Fe^{2+}, Fe^{3+}, Cd^{2+}, Ni^{2+}, Mg^{2+}, Mn^{2+}, NH_4^+, Cl^-, NO_3^-, CO_3^{2-}, SO_4^-, CH_3COO^-), nitroaromatic compounds (e.g., 4-nitrophenol, 2,4-dinitrophenol), and other pesticides, such as acephate, chlorpyrifos, dicofol, lindane. As shown in Figure 9D, the modified electrode showed almost the same peak current when PT coexists with other substances. This indicates that the added substances have no significant effect on PT sensing in environmental samples. Other interfering OP (acephate, chlorpyrifos) and organochloride (dicofol, lindane) pesticides also did not significantly affect the response current of PT reduction as they have different redox potential and adsorption potential on the modified electrode surface.

Reproducibility, repeatability, and stability are essential parameters for practical applications of electrochemical nanosensors. Inter-assay measurements of 10 μM PT using five independent ERGO/GCE were performed, and a 3.4% relative standard deviation (RSD) was obtained for five replicate scans, indicating good reproducibility of the proposed nanosensor. Similarly, a single modified electrode exhibits good repeatability with an RSD of 1.81% for five repeated measurements performed in PBS (50 mM, pH 7.0) containing 10 μM PT.

The analytical performance of the ERGO/GCE, such as detection limit and linear range, are compared with previously re-

ported modified electrodes for the detection of PT (Table 2) [16-18,36,42-44]. The proposed electrode showed better stability, sensitivity, and the lowest detection limit in comparison to previous reports [16-18,36,42-44]. As ERGO showed thermal and mechanical stability, ERGO/GCE could be a suitable electrode material for rapid screening of PT in actual samples.

To determine the storage stability, the electrocatalytic response of 10 μM PT was monitored in seven-day intervals for the first two months, and it retained about 96.17 ± 0.2% of its initial response. It was shown a consistent response to PT sensing during two months of storage. After that, the response was measured in intervals of 10 days, and 90.53 ± 0.3% of the initial response was retained after six months. This indicates good stability of the modified electrode at room temperature (Supporting Information File 1, Figure S2A). The feasibility of the proposed robust sensing platform was demonstrated by quantifying environmental samples such as groundwater and a soil sample from an agricultural land. Food (e.g., boiled rice) and vegetable (e.g., tomato collected from local market) samples were also analysed. As the concentration of PT in the collected samples was negligible, a specific amount of PT was spiked from the standard PT solution (1 mM). Supporting Information File 1, Figure S2B depicts the SWV response of groundwater spiked with 1.5, 2.5, and 5 μM PT, and detailed experimental results are shown in Table 3. The amount of spiked [PT] was monitored by the SWV response, and the results were validated using standard UV results. The UV spectra with increasing PT concentration (1–35 μM) are shown in Supporting Information File 1, Figure S3A. The concentration of PT in real samples was further calculated from the standard calibration curve obtained from UV spectra at 273 nm (Supporting Information File 1, Figure S3B). The quantitative spiked recoveries of PT ranged from 97.0–102.4%, with an RSD of 0.998–1.62%. In addition, the proposed method also depicts satisfactory relative error (1.53–3.96%) with standard absorption results for the quantification of PT in environmental samples.

Conclusion

A newly developed inexpensive and environmentally friendly techique, using an interference-free nonenzymatic approach was developed to fabricate a nonenzymatic electrochemical nanosensor based on ERGO for rapid detection of PT. The electrochemical parameters were optimized to achieve the highest performance of the ERGO-modified electrode, and the structure was characterized by Raman, XRD, XPS, TEM, FESEM, and EIS techniques. Square-wave voltammetry was performed to achieve excellent nanosensor performance, such as higher sensitivity, low detection limit (10.9 pM), linear response range (3×10^{-11}–11×10^{-6} M), and fast response time. The proposed ERGO/GCE nanosensor exhibits excellent electrocatalytic activity, long-term storage stability, reproducibility, repeatability, low-cost fabrication, and strong anti-interference ability to quantify PT residues in real samples. The low RSD value (0.998–1.62%) and relative error (1.9–3.9%) obtained from UV data confirmed the accuracy of this method, showing that the electrochemical nanosensor has good reliability for PT detection in real samples. It can be concluded that the feasible nonenzymatic electrochemi-

Table 2: Experimental sample table for a comparative analytical performance of the proposed nanosensor with the reported nonenzymatic nanosensor.

Modified electrode	Method	Molecule	Linear range (μM)	LOD (nM)	pH	Samples	Ref
NanoTiO$_2$-SAM/GCE	DPV	PT	0.05–10	10	PBS 5	cucumber, cabbage	[17]
NanoAg/Naf ion/GCE	DPV	PT	0.103–0.62	80	BR buffer, pH 2.56	water	[16]
		MP	0.300–1.444	0.0874			
ZrO$_2$/MAS/Au	SWV	PT	0.017–3.4	2.8	pH 6, 0.1 M KCl	vegetables, water	[43]
SPAN(sulfonated Pani)/GCE	DPV	PT	0.01–10	1.5	BR buffer 2.5	urine sample	[42]
ordered mesoporous carbon/GCE	DPV	PT	0.015–0.5	3.4	PBS 6	–	[44]
NiO-SPE	DPV	PT	0.1–30	24	0.05 M BR buffer, pH 6.0	urine, tomato	[18]
Al-doped mesoporous cellular foam (Al-MCF)	SWV	PT	0.01–1 mg/L	17.16	0.1 M KCl, pH 6.0	cabbage	[36]
ERGO/GCE	SWV	PT	3×10^{-5}–11	10.9×10^{-3}	PBS, pH 7	groundwater, soil, tomato, rice	present work

Table 3: Experimental sample table for recovery studies of spiked PT in actual samples.

Real samples	Added (μM)	Detected (μM)	Detected by UV–vis	Recovery (%)	Relative error (%)	RSD (%)
ground water	1.5	1.46	1.52	97.33	3.947	0.998
	2.5	2.48	2.52	99.20	1.587	1.518
	5	5.12	5.2	102.4	1.538	1.369
soil	1	0.97	1.01	97.00	3.961	1.620
	3	2.95	3.07	98.33	3.909	1.114
	5	4.96	5.04	99.20	1.587	1.240
tomato	1	0.96	0.99	96.00	3.030	1.120
	3	2.9	3.04	96.67	4.605	0.992
	7	7.07	7.18	101.00	1.532	1.060
rice	0.5	0.51	0.58	102.00	12.06	1.119
	5	5.12	5.16	102.40	0.775	0.991
	10	10.11	10.25	101.10	1.366	1.230

cal nanosensor could be a good alternative for on-site monitoring of PT usage in agricultural fields. The robust and straightforward electrochemical-sensing platform could also be a promising path for selective and sensitive analysis of other pesticides and environmental pollutants based on electrocatalytic activity.

Supporting Information

Table S1: Chemical sample table indicating corresponding CAS, supplier and other details. Table S2: Experimental sample table for composition analysis using binding energies of GO and RGO by XPS. Table S3: Experimental sample table for the modified glassy carbon electrode electrochemical characteristics. Figure S1: CV of ERGO/GCE at different scan rates (10–300 mV/s) in 1.0 mM $K_3Fe(CN)_6$ solution with 1 M KCl. Figure S2: (A) Storage stability of the proposed sensing matrix (ERGO/GCE), (B) SWV of PT (1.5, 2.5, 5 μM) added in groundwater. Figure S3: (A) Absorption spectra of parathion and (B) corresponding calibration plot.

Supporting Information File 1

Additional figures and tables.
[https://www.beilstein-journals.org/bjnano/content/supplementary/2190-4286-13-65-S1.pdf]

Funding

S.S. supports this work via the Council of Scientific & Industrial Research (India) grant (ACK. No. 381149/2K17/1). S.S. is also thankful to NIT Durgapur for the institutional postdoctoral fellowship. A.R. acknowledges UK-Saudi Challenge Fund 2022, funded by the British Council.

Acknowledgements

The authors acknowledge the help rendered by CSIR-Central Glass and the Ceramic Research Institute, Kolkata 700032, India, which provided materials synthesis and characterization facilities.

ORCID® iDs

Anurag Roy - https://orcid.org/0000-0002-2097-9442

References

1. Aktar, W.; Sengupta, D.; Chowdhury, A. *Interdiscip. Toxicol.* **2009,** *2,* 1–12. doi:10.2478/v10102-009-0001-7
2. Bhattu, M.; Verma, M.; Kathuria, D. *Anal. Methods* **2021,** *13,* 4390–4428. doi:10.1039/d1ay01186c
3. Upadhayay, J.; Rana, M.; Juyal, V.; Bisht, S. S.; Joshi, R. Impact of Pesticide Exposure and Associated Health Effects. In *Pesticides in Crop Production: Physiological and Biochemical Action;* Srivastava, P. K.; Singh, V. P.; Singh, A.; Tripathi, D. K.; Singh, S.; Prasad, S. M.; Chauhan, D. K., Eds.; John Wiley & Sons: Hoboken, NJ, USA, 2020; pp 69–88. doi:10.1002/9781119432241.ch5
4. Kim, K.-H.; Kabir, E.; Jahan, S. A. *Sci. Total Environ.* **2017,** *575,* 525–535. doi:10.1016/j.scitotenv.2016.09.009
5. Yang, T.-J.; Lee, M.-R. *Talanta* **2010,** *82,* 766–770. doi:10.1016/j.talanta.2010.05.053
6. Cheng, Z.; Dong, F.; Xu, J.; Liu, X.; Wu, X.; Chen, Z.; Pan, X.; Gan, J.; Zheng, Y. *Food Chem.* **2017,** *231,* 365–373. doi:10.1016/j.foodchem.2017.03.157
7. Bülbül, G.; Hayat, A.; Andreescu, S. *Sensors* **2015,** *15,* 30736–30758. doi:10.3390/s151229826
8. Arduini, F.; Guidone, S.; Amine, A.; Palleschi, G.; Moscone, D. *Sens. Actuators, B* **2013,** *179,* 201–208. doi:10.1016/j.snb.2012.10.016
9. Pundir, C. S.; Chauhan, N. *Anal. Biochem.* **2012,** *429,* 19–31. doi:10.1016/j.ab.2012.06.025
10. Swainson, N. M.; Aiemderm, P.; Saikaew, C.; Theeraraksakul, K.; Rimdusit, P.; Kraiya, C.; Unajak, S.; Choowongkomon, K. *Biotechnol. Lett.* **2021,** *43,* 1869–1881. doi:10.1007/s10529-021-03158-2

11. Tanwar, S.; Mathur, D. *J. Solid State Electrochem.* **2021,** *25,* 2145–2159. doi:10.1007/s10008-021-04990-2
12. Köksoy, B.; Akyüz, D.; Şenocak, A.; Durmuş, M.; Demirbas, E. *Food Chem. Toxicol.* **2021,** *147,* 111886. doi:10.1016/j.fct.2020.111886
13. Köksoy, B.; Akyüz, D.; Şenocak, A.; Durmuş, M.; Demirbaş, E. *Sens. Actuators, B* **2021,** *329,* 129198. doi:10.1016/j.snb.2020.129198
14. Şenocak, A.; Tümay, S. O.; Makhseed, S.; Demirbas, E.; Durmuş, M. *Biosens. Bioelectron.* **2021,** *174,* 112819. doi:10.1016/j.bios.2020.112819
15. Tümay, S. O.; Şenocak, A.; Sarı, E.; Şanko, V.; Durmuş, M.; Demirbas, E. *Sens. Actuators, B* **2021,** *345,* 130344. doi:10.1016/j.snb.2021.130344
16. Kumaravel, A.; Chandrasekaran, M. *J. Electroanal. Chem.* **2010,** *638,* 231–235. doi:10.1016/j.jelechem.2009.11.002
17. Li, C.; Wang, C.; Wang, C.; Hu, S. *Sens. Actuators, B* **2006,** *117,* 166–171. doi:10.1016/j.snb.2005.11.019
18. Khairy, M.; Ayoub, H. A.; Banks, C. E. *Food Chem.* **2018,** *255,* 104–111. doi:10.1016/j.foodchem.2018.02.004
19. Tian, X.; Liu, L.; Li, Y.; Yang, C.; Zhou, Z.; Nie, Y.; Wang, Y. *Sens. Actuators, B* **2018,** *256,* 135–142. doi:10.1016/j.snb.2017.10.066
20. Bui, M.-P. N.; Seo, S. S. *J. Appl. Electrochem.* **2015,** *45,* 365–373. doi:10.1007/s10800-015-0789-0
21. Govindasamy, M.; Mani, V.; Chen, S.-M.; Chen, T.-W.; Sundramoorthy, A. K. *Sci. Rep.* **2017,** *7,* 46471. doi:10.1038/srep46471
22. Tao, T.; Zhou, Y.; Ma, M.; He, H.; Gao, N.; Cai, Z.; Chang, G.; He, Y. *Sens. Actuators, B* **2021,** *328,* 128936. doi:10.1016/j.snb.2020.128936
23. Rajaji, U.; Murugan, K.; Chen, S.-M.; Govindasamy, M.; Chen, T.-W.; Lin, P. H.; Lakshmi prabha, P. *Composites, Part B* **2019,** *160,* 268–276. doi:10.1016/j.compositesb.2018.10.042
24. Jangid, K.; Sahu, R. P.; Pandey, R.; Chen, R.; Zhitomirsky, I.; Puri, I. K. *ACS Appl. Nano Mater.* **2021,** *4,* 4781–4789. doi:10.1021/acsanm.1c00376
25. de Camargo, M. N. L.; Santhiago, M.; Maroneze, C. M.; Silva, C. C. C.; Timm, R. A.; Kubota, L. T. *Electrochim. Acta* **2016,** *197,* 194–199. doi:10.1016/j.electacta.2015.09.022
26. Stobinski, L.; Lesiak, B.; Malolepszy, A.; Mazurkiewicz, M.; Mierzwa, B.; Zemek, J.; Jiricek, P.; Bieloshapka, I. *J. Electron Spectrosc. Relat. Phenom.* **2014,** *195,* 145–154. doi:10.1016/j.elspec.2014.07.003
27. Toh, S. Y.; Loh, K. S.; Kamarudin, S. K.; Daud, W. R. W. *Chem. Eng. J.* **2014,** *251,* 422–434. doi:10.1016/j.cej.2014.04.004
28. Mekassa, B.; Tessema, M.; Chandravanshi, B. S.; Baker, P. G. L.; Muya, F. N. *J. Electroanal. Chem.* **2017,** *807,* 145–153. doi:10.1016/j.jelechem.2017.11.045
29. Shao, Y.; Wang, J.; Engelhard, M.; Wang, C.; Lin, Y. *J. Mater. Chem.* **2010,** *20,* 743–748. doi:10.1039/b917975e
30. Saha, A.; Basiruddin, S.; Ray, S. C.; Roy, S. S.; Jana, N. R. *Nanoscale* **2010,** *2,* 2777–2782. doi:10.1039/c0nr00376j
31. Mandal, D.; Routh, P.; Nandi, A. K. *ChemistrySelect* **2017,** *2,* 3163–3171. doi:10.1002/slct.201700206
32. Sen, S.; Sarkar, P. *RSC Adv.* **2015,** *5,* 95911–95925. doi:10.1039/c5ra18889j
33. Peng, X.-Y.; Liu, X.-X.; Diamond, D.; Lau, K. T. *Carbon* **2011,** *49,* 3488–3496. doi:10.1016/j.carbon.2011.04.047
34. Yu, X.; Sheng, K.; Shi, G. *Analyst* **2014,** *139,* 4525–4531. doi:10.1039/c4an00604f
35. Tan, X.; Liu, Y.; Zhang, T.; Luo, S.; Liu, X.; Tian, H.; Yang, Y.; Chen, C. *RSC Adv.* **2019,** *9,* 345–353. doi:10.1039/c8ra08555b
36. Wei, L.; Huang, X.; Yan, F.; Zheng, L.; Wang, J.; Xie, L.; Ya, Y. *Int. J. Electrochem. Sci.* **2019,** *14,* 1986–1996. doi:10.20964/2019.02.77
37. Brahma, B.; Sen, S.; Sarkar, P.; Sarkar, U. *Anal. Chim. Acta* **2021,** *1168,* 338595. doi:10.1016/j.aca.2021.338595
38. Sen, S.; Sarkar, P. *Int. J. Biol. Macromol.* **2022,** *199,* 275–286. doi:10.1016/j.ijbiomac.2021.12.094
39. Sen, S.; Sarkar, P. *Sens. Lett.* **2013,** *11,* 428–435. doi:10.1166/sl.2013.2744
40. Sen, S.; Sarkar, P. *Anal. Chim. Acta* **2020,** *1114,* 15–28. doi:10.1016/j.aca.2020.03.060
41. Sen, S.; Chattopadhyay, S.; Sarkar, P. *J. Electrochem. Soc.* **2016,** *163,* B49–B55. doi:10.1149/2.0491603jes
42. Sreedhar, N. Y.; Kumar, M. S. *Anal. Bioanal. Electrochem.* **2013,** *5,* 635–646.
43. Zhou, J.-H.; Deng, C.-Y.; Si, S.-H.; Wang, S.-E. *Microchim. Acta* **2011,** *172,* 207–215. doi:10.1007/s00604-010-0483-1
44. Zhang, T.; Zeng, L.; Han, L.; Li, T.; Zheng, C.; Wei, M.; Liu, A. *Anal. Chim. Acta* **2014,** *822,* 23–29. doi:10.1016/j.aca.2014.03.023

License and Terms

This is an open access article licensed under the terms of the Beilstein-Institut Open Access License Agreement (https://www.beilstein-journals.org/bjnano/terms), which is identical to the Creative Commons Attribution 4.0 International License (https://creativecommons.org/licenses/by/4.0). The reuse of material under this license requires that the author(s), source and license are credited. Third-party material in this article could be subject to other licenses (typically indicated in the credit line), and in this case, users are required to obtain permission from the license holder to reuse the material.

The definitive version of this article is the electronic one which can be found at:
https://doi.org/10.3762/bjnano.13.65

BEILSTEIN JOURNAL OF NANOTECHNOLOGY

Recent advances in green carbon dots (2015–2022): synthesis, metal ion sensing, and biological applications

Aisha Kanwal[1], Naheed Bibi[2], Sajjad Hyder[3], Arif Muhammad[1], Hao Ren[*1], Jiangtao Liu[*4] and Zhongli Lei[*1]

Review

Open Access

Address:
[1]Key Laboratory of Applied Surface and Colloid Chemistry, School of Chemistry & Chemical Engineering, Shaanxi Normal University, Xi'an, 710119, China, [2]Department of Chemistry, Shaheed Benazir Bhutto Women University, Charsadda Road, Larama, Peshawar, Pakistan, [3]Department of Botany, Government College Women University, Sialkot, Pakistan and [4]College of Pharmacy, Shaanxi University of Chinese Medicine, Xianyang, 712046, China

Email:
Hao Ren[*] - renhao@snnu.edu.cn; Jiangtao Liu[*] - jtliu@sntcm.edu.cn; Zhongli Lei[*] - lzhl2016@snnu.edu.cn

* Corresponding author

Keywords:
bioimaging; carbon dots; carbon quantum dots; green synthesis; plant growth promotion; sensing

Beilstein J. Nanotechnol. **2022,** *13,* 1068–1107.
https://doi.org/10.3762/bjnano.13.93

Received: 30 April 2022
Accepted: 14 September 2022
Published: 05 October 2022

This article is part of the thematic issue "Nanomaterial-based sensors for water remediation, healthcare and food monitoring applications".

Guest Editor: A. A. Oladipo

© 2022 Kanwal et al.; licensee Beilstein-Institut.
License and terms: see end of document.

Abstract

Carbon dots (CDs) show extensive potential in various fields such as sensing, bioimaging, catalysis, medicine, optoelectronics, and drug delivery due to their unique properties, that is, low cytotoxicity, cytocompatibility, water-solubility, multicolor wavelength tuned emission, photo-stability, easy modification, strong chemical inertness, etc. This review article especially focuses on the recent advancement (2015–2022) in the green synthesis of CDs, their application in metal ions sensing and microbial bioimaging, detection, and viability studies as well as their applications in pathogenic control and plant growth promotion.

Introduction

Carbon dots (CDs) are a carbon-based nanomaterial with a few nanometers feature sizes. CDs consist of a carbon core, the surface of which is functionalized with various groups. Xu et al. accidentally discovered fluorescent carbon nanoparticles during electrophoretic purification of single-walled carbon nanotubes [1]. Sun et al. synthesized fluorescent carbon particles smaller than 10 nm, which were named "carbon dots" for the first time in 2006 [2]. Due to its significant fluorescent properties, this class of carbon nanomaterials has proved to be useful for applications in a variety of disciplines, including chemical or biological sensing, bioimaging, drug delivery, photodynamic therapy, electrocatalysis, and photocatalysis, with advantages over commonly used semiconductor dots or conventional fluorescent probes such as organic dyes. Moreover, CDs have unparalleled extraordinary properties, including cell compatibility, chemical inertness, emission at tunable wavelengths, low cost, high quan-

tum yield (QY), water dispersibility, small size, tunability, high biocompatibility, strong photostability (resistance to photobleaching), and efficient photoluminescence. CDs have a broad spectrum of applications in the analytical, medical, biotechnology, biology, and theranostics domains [3,4]. The typical photoluminescence yield of CDs is less than 10%. Surface-passivating chemicals are used to improve the photoluminescence. Surface passivation with different functional groups generates surface defects, which produces fluorescence and also generates new active sites for modification for specific applications. CDs can be chemically modified by many heteroatoms, including N, P, and S, and many other chemicals that increase their functional properties [5,6]. These exceptional optical and physicochemical properties make them ideal for transdisciplinary research. Fluorescent CDs can be manufactured using inexpensive, naturally rich carbon sources in an environmentally friendly manner. By adjusting the surface chemistry of CDs, the solubility and QY can be improved. The size of CDs and chemical functionality present on their surface can be discreetly tuned to change the electronic structure for their luminous features.

Various molecular precursors have been used earlier for the production of CDs, including ethylene glycol [6], phytic acid [7], phenylenediamine [8], ammonium citrate [9], citric acid [10], ethylene diamine tetra acetic acid [11], carbon nanotubes [12], and graphite [13]. Additionally, graphite, nanodiamonds, and activated carbon can be applied as precursor for the fabrication of CDs [14]. Meanwhile, a variety of green carbon precursors have been utilized for generating CDs, including fruits, their juices and peels [15-17], animal and animal-derived materials, such as milk and hair [18-20], and vegetables [21], flowers [22], and leaves [23]. The use of green, sustainable or waste materials for the production of CDs is congruous with the objectives of a sustainable development strategy. Owing to the recycling and re-use of organic waste products, environmental friendliness, and low-cost, green synthesis of CDs is preferred over other conventional methods.

There are, in general, two synthetic pathways for the formation of CDs, that is, “top-down” and “bottom-up” methods. In the top-down method, large carbon structures (such as carbon nanotubes or graphite) are decomposed into CDs. The top-down methods include arc discharge, laser abrasion [24], chemical and electrochemical oxidation, and ultrasonic synthesis. In the bottom-up methods, CDs are formed from molecular precursors by various techniques such as hydrothermal treatment [25-29], microwave synthesis [30], and pyrolysis [31].

A tremendous amount of work has been done regarding the synthesis and different techniques for improving synthesis, characterization, yield, and applications of CDs There are several outstanding review articles on different applications, such as photochemical and electrochemical applications [32], photocatalysis [33], optoelectronics [34], wastewater treatment [35], food safety applications [36], tumor marker detection [37], bioanalytical studies [38], biomedical [39,40] and biotechnological applications [3], biosensing and bioimaging [31,32], and fluorescence [41] and photoluminescence processes [42]. Many reviews about CDs obtained from natural resources have been published. Sharma et al. reported an excellent review article on the green synthesis of CDs in 2017 [43]. Recently, Tejwan et al. [44] and Lin et al. [45] also reported review articles about synthesis and applications of CDs obtained from green precursors. Meng et al. reviewed CDs made from biomass and their applications [46]. A study on recent advancements in the synthesis of CDs from natural resources and their applications in biomedicine and multisensing platforms was also published by Bag and co-workers [47]. The review presented here is focused on the latest progress in the field since 2015. It describes the synthesis of CDs, the effects of surface states on optical properties, the characterization of CDs, metal ion sensing, and biological and agricultural applications of CDs, that is, microbial bioimaging, detection, and viability studies, pathogen control, and plant growth promotion (Figure 1).

Review

Green synthesis of carbon dots

Green synthesis of CDs mainly utilizes biomass. Biomass synthesis makes use of natural raw materials (organisms, waste material, protein products, or natural polymers), instead of reaction precursors usually used in the traditional methods, and also requires external energy supply. Using diverse raw materials, CDs with different structures and properties can be obtained. Usually, a temperature of 100–200 °C is required, which is much lower than that required in the traditional methods, and the synthesis is carried out in aqueous media. Generally, hydrothermal or solvothermal treatments, ultrasonication, microwave irradiations, and microwave-assisted hydrothermal/pyrolysis are used in the green synthesis of CDs [41]. Hydrothermal methods convert the raw material into carbonized matter. Although relatively simple, the procedure takes several hours. Microwave irradiation, in contrast, provides homogenous and effective heating and speed up the reaction to merely a few minutes. Hence, this approach is considered the fastest and simplest amongst the synthesis methodologies and has become widely used.

The fluorescence emissions of CDs are usually blue and green (i.e., in the low-wavelength region). Since biomass is abundant in carbon and oxygen, the resulting CDs have carbonyl groups on their surface. Excited electrons resulting from n–π* transi-

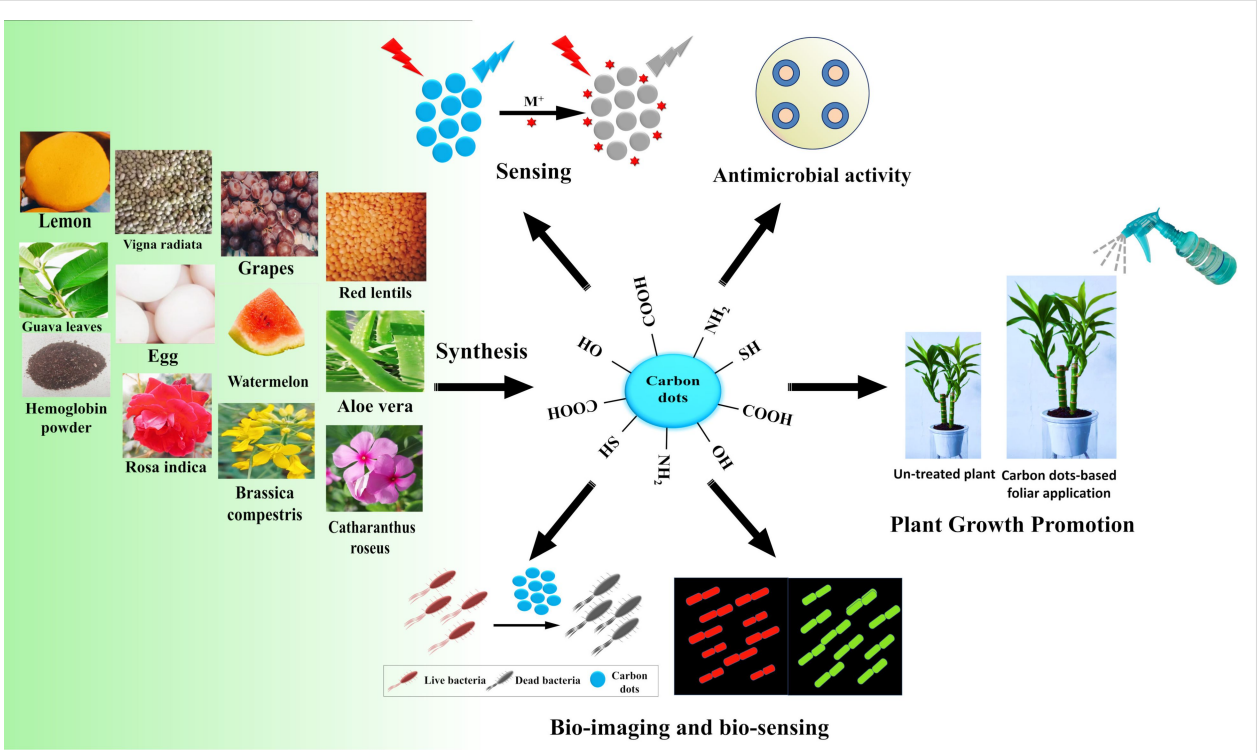


Figure 1: Illustration of the environmentally friendly sources employed for the synthesis of CDs and their applications from 2015–2022.

tions emit blue fluorescence on radiative recombination. In general, blue fluorescence arise as a result of π–π* transition of the carbon core, whereas, green fluorescence may correspond to n–π* transitions of the edge states [48,49].

The "top-down" approach involves breaking down bulky carbonaceous materials, such as carbon fibers, carbohydrates, proteins, and carbon soot, through chemical or physical methods. The carbon containing material is oxidized and broken down into CDs using oxidants such as sulfuric acid and nitric acid. As green methods are limited regarding the raw materials, the "top-down" method is not very common in green approaches [3,50].

The "bottom-up" method consist of carbonization of smaller organic molecules. This method basically involves four phases, that is, condensation of the molecules followed by polymerization, carbonization, and passivation. Small molecules are condensed into intermediate chains and then polymerized into clusters of carbonaceous material. Carbonization of this material at elevated temperatures leads to the formation of carbon cores. The residual groups on the surface act as surface-passivating agents and can be manipulated to ameliorate surface luminescence properties [38]. Biomass is rich in small organic compounds suitable for carbonization at elevated temperature and, hence, "bottom-up" approaches are extensively used for the green synthesis of CDs.

In this review, CDs have been classified into various categories based on their precursor materials, including plant sources, animal extracts, and food materials. We focus on the CDs obtained using various green precursors and their modification with or without different surface passivizing agents.

Plant sources

Synthesis of CDs from plant-based sources has the potential to be scaled up and comes with a number of benefits, including reduced chemical exposure, cost-effectiveness, renewability of sources, waste reduction, and ample source availability. It is thus environmentally friendly and advantageous [51,52]. Plant parts such as roots, stem, leaves, fruits, flowers, and seeds have been used for the production of CDs. Several low-value plant materials can also be converted into functional materials with excellent biocompatibility by manufacturing CDs from these plant components. Plant-based precursors that contain heteroatoms (nitrogen and sulfur) are preferred over carbon sources that demand supplementary heteroatoms for the synthesis of CDs [53].

Without surface-passivating agent: Plants are rich in biomolecules such as carbohydrates and proteins, which makes them a better option based on the fact that surface functionality of CDs can be achieved without adding extra substances for doping, modification and surface passivation [54]. A summary of CDs

synthesized from carbon-rich plant extract without surface-passivating agents and their quantum yield is provided in Table 1. Liu et al. used grass as a natural carbon source for the first time to prepare CDs [55]. Bhamore and co-workers reported fluorescent CDs without any surface-passivating agent by using a green precursor *Pyrus pyrifolia* fruit through a simple hydrothermal method at 180 °C for a period of 6 h [56]. *Gynostemma* has been used to prepare fluorescent CDs through a simple calcination method without any harmful substances or any surface modification [57].

A new method to recycle biomass was used by Wang et al. They synthesized CDs via simple hydrothermal methods by using ordinary biomass waste as carbon source, namely orange peel, ginkgo leaves, paulownia leaves, and magnolia flowers [58]. Water-soluble CDs using *Manilkara zapota* fruit as a natural source of carbon were reported where sulfuric acid and phosphoric acid were used to regulate the emission of CDs, producing CDs with blue, green, and yellow emission. For the blue, green, and yellow emitting CDs, the obtained QY values were 5.7%, 7.9%, and 5.2%, respectively. The reported average size

Table 1: Summary of CDs synthesized from carbon-rich plant extracts without surface-passivating agents with their quantum yield.

S. No	Precursor of CDs	Synthetic Method	Size (nm)	QY (%)	Ref
1	biomass waste	hydrothermal method at 200 °C for 8 h	2.60	8.13	[58]
2	*Manilkara zapota*	ultrasonication at 100 °C for 60 min	1.9 ± 0.3, 2.9 ± 0.7 and 4.5 ± 1.25	5.7, 7.9, 5.2	[48]
3	*Abelmoschus manihot*	hydrothermal at 220 °C for 4 h	9	30.8	[22]
4	*Prosopis juliflora*	hydrothermal method at 200 °C for 1 h	5.8	5	[23]
5	*Pyrus pyrifolia*	hydrothermal method at 180 °C for 6 h	2.0 ± 1.0	10.8	[56]
6	*Gynostemma*	calcination method at 400 °C for 4 h	2.5	—	[57]
7	*Borassus flabellifer*	thermal pyrolysis at 300 °C for 2 h	3 to 8 ±1	13.97	[59]
8	lemon juice/orange juice	hydrothermal method at 280 °C for 12 h	3–5	14.8 to 24.8	[60]
9	lychee waste	solvothermal at 180 °C for 5 h	3.13	23.5	[61]
10	spices	hydrothermal method at 200 °C for 12 h	3.5 ± 0.1	43.6	[62]
11	pseudo-stem of banana	hydrothermal treatment at 180 °C for 2 h	1–3	48	[63]
12	Cotton linter	microwave-assisted hydrothermal process in 5 min	10.14	—	[64]
13	*Brassica compestris*	hydrothermal reaction at 240 °C for 20 h	1.9	21	[65]
14	*Setcreasea purpurea* boom	pyrolysis at 300 °C for 2 h	3.9	18	[66]
15	*Aloe Vera*	pyrolysis method (160–250 °C) and time (10–30 min)	6–8	12.3	[67]
16	date palm fronds	one step carbonization method 300 °C	35	33.7	[68]
17	whey	pyrolysis at 220 °C	4	≈11.4	[69]
18	*Nigella sativa* seeds	hydrothermal method at 120 °C for 12 h	4	—	[18]
19	palmyra palm leaf	hydrothermal method at 180 °C for 12 h	5–10	—	[70]
20	guava leaf	hydrothermal method at 160 °C for 1 h	4–7	34	[71]
21	*Murraya koenigii* (curry leaves)	hydrothermal method at 180 °C for 4 h	2–8	5.4	[72]
22	roasted gram	pyrolysis at 200 °C (C-1) and 450 °C (C-2) for 8 h	5.5 and 2	—	[73]
23	rice fried *Codonopsis pilosula* (CP)	Ultrasonic-assisted solvent extraction at room temp for 4 h	9.60 and 11.54	12.8	[74]
24	rose pigments	hydrothermal method at 200 °C for 2 h	32	48	[75]
25	milk	hydrothermal treatment at 180 °C for 4 h	10	10	[76]
26	crop biomasses	hydrothermal process at 140 °C	2–5	—	[77]
27	corn stalk shell	hydrothermal process in NCW at 270 °C, pressure of 5 MPa for 10 min	1.2 to 3.2	16	[78]
28	banana peel	hydrothermal process at 200 °C for 24 h	5	20	[79]
29	*Calotropis gigantea*	microwave at 900 W	2.7 to 10.4	4.24	[80]
30	*Morus nigra*	hydrothermal process at 200 °C for 24 h	4.5	24	[81]
31	ginkgo kernels	hydrothermal process at 220 °C for 12 h	2.7	37.8	[82]

was 1.9 ± 0.3 nm for the blue emitting CDs, 2.9 ± 0.7 nm for the green emitting CDs, and 4.5 ± 1.25 nm for the yellow emitting CDs [48]. A new type of fluorescent CDs from the flowers of *Borassus flabellifer* (male tree) through a green thermal pyrolysis method without adding any chemicals was synthesized [59]. A high QY of up to 13.97% was obtained at an optimized temperature of 300 °C. Hoan et al. used lemon juice to produce highly luminous CDs via a simple, low-cost hydrothermal route. This novel study explained how hydrothermal time and source type affects the luminescence of CDs [60]. To study the effect of citric acid on the precursors, different precursors (such as ripe lemon juice, fresh lemon juice, and orange juice) were tested. It was found that the photoluminescence (PL) intensity of citric acid was higher than that of lemon juice, which, in turn, was higher than that of orange juice. This outcome is the result of lemon juice having a greater citric acid concentration than orange juice. Compared to ripe lemon juice, fresh lemon juice had a higher PL intensity (Figure 2). Because in the case of the ripe lemon juice, a significant reduction in the quality of the components occurred, which might have led to reduced PL emission. It was also found that longer hydrothermal times could lead to more carbonization. Apart from this, as the temperature increased from 150 to 280 °C, QY was found to increase from 14.86 to 24.89%. These outcomes might be explained by the efficient carbonization of naturally occurring acidic components as the hydrothermal temperature of the reaction rises [60]. The resulting CDs showed a direct relationship between PL intensity and heating temperature and time. These CDs had good green emission. The maximum emission wavelength clearly depends on the excitation wavelength at low temperatures. However, at high hydrothermal temperature, the luminous peak was almost completely independent of the excitation wavelength. The irregular size of the particles at low temperatures is the first reason. CDs of different sizes have different bandgaps. Particles of the same size will prioritize the emission when light of a particular wavelength is projected into CDs. Different sized particles will emit radiation when different wavelengths are projected. However, at high hydrothermal temperatures, uniformity of the particle size of the CD prevents the wavelength from being influenced by the excitation wavelength. The surface states are another factor. It is well known that surface functional groups, such as carbonyl and carboxylic groups, can produce their own energy levels. Hence, there will be a variety of routes for electrons to move from the excited state to the ground state of photon emission. Numerous functional groups can be found on the surface of CDs at low temperatures, but at high temperatures, the COOH, C–H, and C–O–C groups are eliminated and the C=O group takes their place. This explains why CDs generated at high hydrothermal temperatures exhibit excitation-independent luminescence.

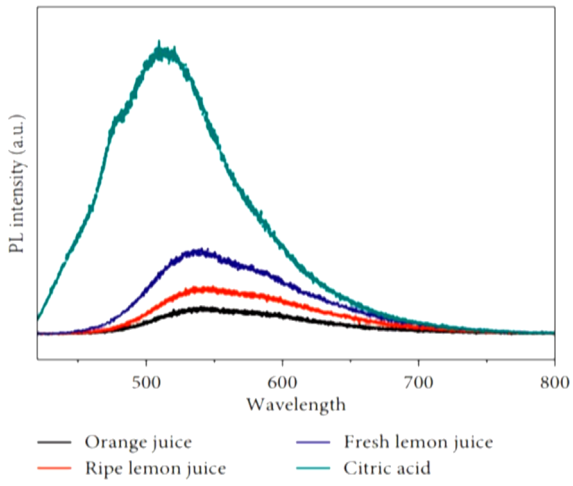


Figure 2: Luminescence of CDs synthesized from citric acid and various green sources. Figure 2 was reproduced from [60] (© 2020 B. T. Hoan et al., published by Hindawi, distributed under the terms of the Creative Commons Attribution 4.0 International License, https://creativecommons.org/licenses/by/4.0).

Sahoo et al. used the bark of lychee, without any other chemical, to synthesize CDs with a QY of 23.5% and the reported CDs were employed as a sensing probe for Fe^{3+} ions [61]. Devi et al. utilized *Carica papaya* waste as a natural source for a simple pyrolysis route and obtained a good QY of 23.7%. The reported CDs have a chromium sensitivity of 0.708 ppb in water [83]. Recently, a further increase in QY was obtained up to 30.8% by using *Abelmoschus manihot* flowers. It was found that 2,4,6-trinitrophenol (TNP) can quickly and sensitively quench the fluorescence intensity of these CDs. The linear response of TNP ranges from 25 nM to 40 μM and the LOD was 5 nM [22]. A good increase in QY was also obtained by Vasimalai et al. using various spices, such as cinnamon, red chili, turmeric, and black pepper, for a simple hydrothermal method. They found that black pepper yields CDs with the highest QY up to 43.6% [62].

Vandarkuzhali et al. also obtained a very high quantum yield of 48% using pseudo-stem of banana [63]. The source used here consists of cellulose, hemicellulose, and lignin, and hydrothermal treatment was carried out. Li et al. reported a very new approach to synthesize two types of CDs with different selectivities from Hongcaitai (*Brassica compestris* L. var. *Purpurea Bailey*) [65]. The two types were obtained based on the difference in solubility in ethanol. The ones that were soluble in ethanol were called “CDs-A” and the insoluble ones were called “CDs-B”. Different characterizations were carried out that revealed that the surfaces of these two CDs have different functional groups resulting in different selectivity. CDs-A and CDs-

B were utilized to detect ClO^- and Hg^{2+} in tap water and river water, respectively.

Using cotton linters as a green source, water-dispersed fluorescent CDs were reported, obtained through a microwave-assisted hydrothermal method. This method provides CDs for fast, low-cost, and convenient cancer imaging applications. The particle size of the CDs was 10.14 nm as calculated by TEM [64].

Zhai et al. compared different synthetic methods to find the most suitable route to obtain fluorescent CDs from the green precursor *Setcreasea purpurea* boom [66]. The different methods used were hydrothermal method, and pyrolysis in a vacuum tube furnace or a muffle furnace. Due to incomplete carbonization and oxidation in the hydrothermal method and pyrolysis in the muffle furnace, respectively, pyrolysis in a vacuum tube furnace was selected as a suitable synthesis method to prevent over-oxidation of CDs. It was found that blue fluorescent CDs with high QY were obtained at 300 °C with 2 h reaction time. Increased temperatures, however, may cause a complete carbonization process as well as small CDs, which can lead to higher QY.

A simple and easy preparatory method that does not require complex post-chemical and ultrafiltration treatments, dialysis, and centrifugation was reported using table sugar. The resulting CDs aggregate and scatter light and help to visually detect Pb^{2+} ions by the turbidimetry method. It was found that there is a direct linear relationship between the concentration of Pb^{2+} ions and the turbidity [84].

Aloe vera extract, without any other chemical reagent, was used to prepare CDs using a one-step pyrolysis method by Devi et al. Different characterization results demonstrated that the CDs displayed excitation-independent behavior and had surface groups such as carboxyl and hydroxy groups. *Aloe vera* has intrinsic antimicrobial properties, so the bactericidal activity of these CDs was investigated by the agar well diffusion method, and the sensing ability towards Fe^{3+} was also reported [67]. Kavitha et al. used date palm fronds with no other chemical reagent. The lignin content of the leaves and shafts of date palm leaves is 25 g/100 g, which helped to obtain mesoporous CDs of high quality having high storage and photostability [68]. Leaves of *Prosopis juliflora* as a natural and inexpensive precursor yielded CDs that acted as a dual fluorescence sensor for both Hg^{2+} ions and chemet drugs [23].

An acid oxidation approach was applied to synthesize nano-sized fluorescent CDs of various colors by using *Ananas comosus* without any passivating agent by Gupta et al. The synthesized CDs showed three emission peaks at 438, 516, and 543 nm when excited at 325, 417, and 425 nm, respectively. Their selectivity for various metal ions indicated that only Fe^{3+} ions significantly quenched the emission intensity at 438 nm and the CDs were used as fluorescence sensors to detect Fe^{3+} ions [85]. Devi et al. adopted an eco-friendly, simple, and green synthesis strategy to prepare CDs by using whey (a major dairy waste). NMR analysis showed that during pyrolysis, polymerization of lactose, which is the main component of the green source used, takes place [69].

Sharma et al. reported *Nigella sativa* seeds for the preparation of CDs that act as a dual sensor for tetracycline and L-lysine. The fluorescence of CDs is quenched by adding tetracycline and regained by introducing L-lysine [18].

Palmyra leaves were utilized by Athinarayanan et al. for the production of CDs. The cellular toxicity of the CDs was analyzed, and the CDs were found to have excellent biocompatibility with cells [70].

Ramanarayanan and Swaminathan utilized guava leaves to prepare CDs, which were then utilized for the synthesis of a CD-TiO_2 nanocomposite. The CD-TiO_2 nanocomposite possesses good photocatalytic ability to degrade methylene blue dye [71].

White pepper as a natural precursor was reported by Long et al. to prepare CDs via refluxing in anhydrous alcohol for 24 h. The prepared CDs exhibit dual emission at 520 and 668 nm by using the same excitation wavelength of 420 nm. The red emission around 668 nm was hardly affected by metal ions and amino acids and acts as a reference while the green emission around 520 nm was quenched by Cu^{2+} ions and enhanced by CoA (Figure 3). The reported CDs were used as an "off–on" ratiometric fluorescence nanosensor for the detection of CoA [86].

Another green precursor, *Murraya koenigii* (curry leaves), was used to synthesize CDs via hydrothermal route. The reported CDs showed good selectivity for Cd^{2+} ions with a wide linear range and limit of detection of 0.01–8 μM and 0.29 nM, respectively [72].

Chaudhary et al. reported CDs using roasted gram as a green precursor, which act as a humidity sensor. Two different carbonization temperatures (200 and 450 °C) were used to prepare CDs, namely C-1 and C-2, respectively, via pyrolysis. To examine the interaction of functional groups present on the CDs with water vapor, theoretical modeling was also carried out by using the DFT-based B3LYP hybrid functional at 6–31G diffused and polarized basis sets. An excellent agreement was found between theoretical data and experimental results [73].

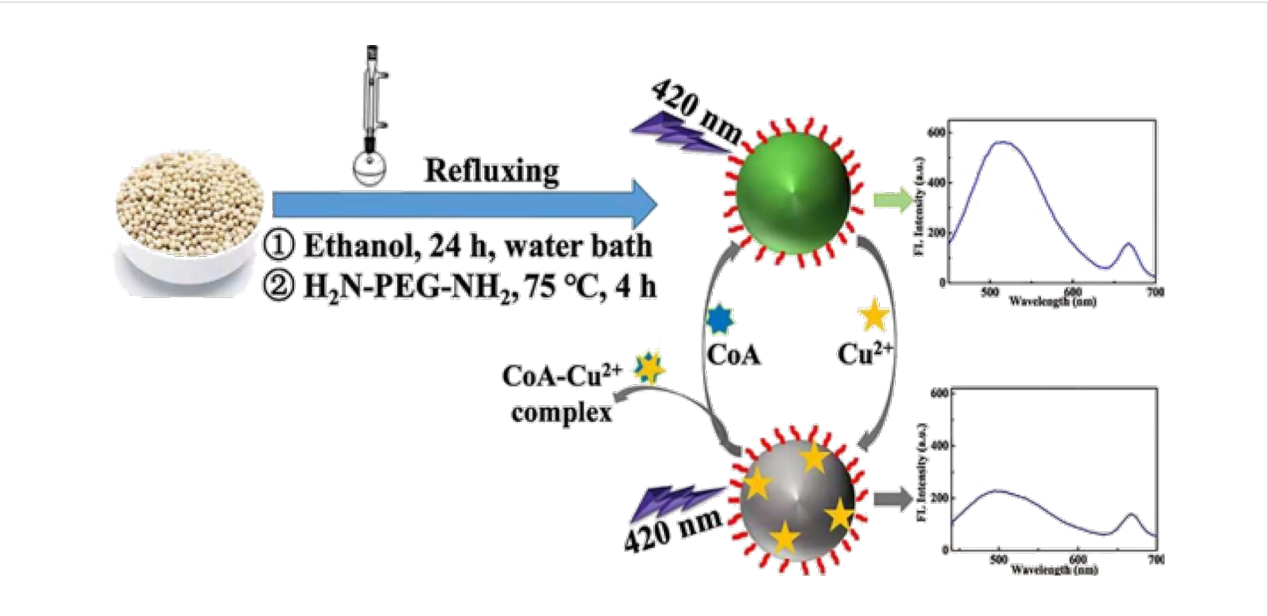


Figure 3: Strategy for the synthesis of ratiometric CDs obtained from white pepper. Figure 3 was reprinted from [86], Food Chemistry, vol. 315, by R. Long; Y. Guo; L. Xie; S. Shi; J. Xu; C. Tong; Q. Lin; T. Li, "White pepper-derived ratiometric carbon dots for highly selective detection and imaging of coenzyme A", article no. 126171, Copyright Elsevier (2020), with permission from Elsevier. This content is not subject to CC BY 4.0.

An ultrasonic-assisted solvent extraction approach was employed to synthesize CDs from rice fried *Codonopsis pilosula* (CP). The CP-CDs possess good sensitivity and selectivity towards the detection of Cr^{6+} ions. Linear range and limit of detection obtained were 0.03−50 μM and 15 nM, respectively [74].

Shekarbeygi et al. synthesized CDs from aqueous and alcoholic extracts of blue, yellow, and red rose flowers through a hydrothermal approach. They also studied the outcome of different synthesis methodologies on the optical properties of the prepared CDs. The CDs obtained from the alcoholic extract of yellow petals were more stable and had a high quantum yield. The reported CDs were efficiently employed for the detection of diazinon [75].

Flax straw was recently used for the synthesis of CDs via a hydrothermal method. The obtained CDs acted as fluorescence on-off-on sensors for the detection of Co^{2+} or Cr^{6+} ions and ascorbic acid, respectively [87]. Using a hydrothermal process, a new form of CD material was produced from common crop wastes, such as corn straw, wheat straw, and rice straw by Ding et al. These CDs were utilized to detect Fe^{3+}, which could be useful in areas of environmental remediation and medical diagnosis [77]. A hydrothermal technique employing near-critical water has been utilized recently to develop a simple, cost-effective, and environmentally friendly synthetic route for CDs from corn stalk shell [78]. This process transformed biomass, which was previously thought to be waste material, into carbon nanomaterials with tremendous potential. Another method for the synthesis of biocompatible fluorescent CDs from the extract of leaves of the medicinal plant *Calotropis gigantea*, also known as crown flower was developed. The resulting CDs were applied as a fluorescent probe for bioimaging [80].

With surface-passivating agents: To obtain CDs with increased electron density, fluorescent properties, and QY, researchers are focusing on synthesizing CDs containing surfactants that contain nitrogen, phosphorus, or sulfur [16,88]. Usually, CDs synthesized from a single precursor without any doping agent have low QYs and are inadequate for bioimaging and other applications. Numerous researches claim that co-doping, or the simultaneous doping of two or more distinct atoms, can mitigate the drawbacks of CDs. The optical characteristics and applications of CDs may be enhanced by doping them with nitrogen, sulfur, and other elements. Due to the synergistic interaction between the doped heteroatoms in CDs, the co-doping with heteroatoms has started to attract greater attention since it can produce novel electronic structures. The electronic structure of CDs can be modified to produce n-type or p-type carriers by adding atomic impurities, such as nitrogen, boron, sulfur, or phosphorus. The QY of CDs could also be considerably enhanced by heteroatom doping, according to current research.

Xie et al. used ethylenediamine (EDA) as a surface-passivating agent to obtain hydrophilic N-CDs via a facile hydrothermal method from highland barley. The reaction was maintained at

200 °C for 24 h. A high QY of 14.4% was obtained by using an optimal amount of 1.33 mL of EDA. Because nitrogen-containing groups could passivate the surface-active sites of the CDs, a greater QY was obtained. Thus, the PL characteristics of the N-CDs were improved, and as a result, the QY of N-CDs was greater than that of the majority of N-CDs derived from biomass [89].

Bandi et al. reported N-CDs synthesized via a hydrothermal method by using *Lantana camara* berries and EDA as carbon and nitrogen source, respectively. The synthesis consisted of many steps, including hydrolysis, dehydration, and decomposition, through which carbohydrates and glycosides are converted into small molecules. The obtained molecules were then converted into N-CDs by passing through polymerization, aromatization, and carbonization processes. Optimized conditions of 180 °C, 3 h time, and 80 µL EDA yielded N-CDs with a QY up to 33.15% [90].

A very good QY up to 53% was obtained by using glutathione, as a dopant for both S and N, and a green source of celery leaves to synthesize CDs. Low-cost celery leaves containing folic acid with many –COOH and $–NH_2$ groups contribute to high QYs. The reported CDs were novel fluorescent paper sensors and showed remarkable sensitivity and selectivity in the detection of nitrophenol [4].

Varisco et al. reported CDs from wine lees via combustion and used two extraction procedures, namely ultrasonication and microwave-assisted extraction, from the black mass. The wine lees consist of different compounds that can act as reactants for the preparation of CDs, that is, easily degradable organic compounds to make the CD core and long-chain carboxylic acids to act as passivating agents. To increase the number of carboxylic acids and amine-containing molecules on the CD surface, oxidation in HNO_3 and reaction with $SOCl_2$ were performed (Figure 4). The carboxylic groups react with EDA to increase

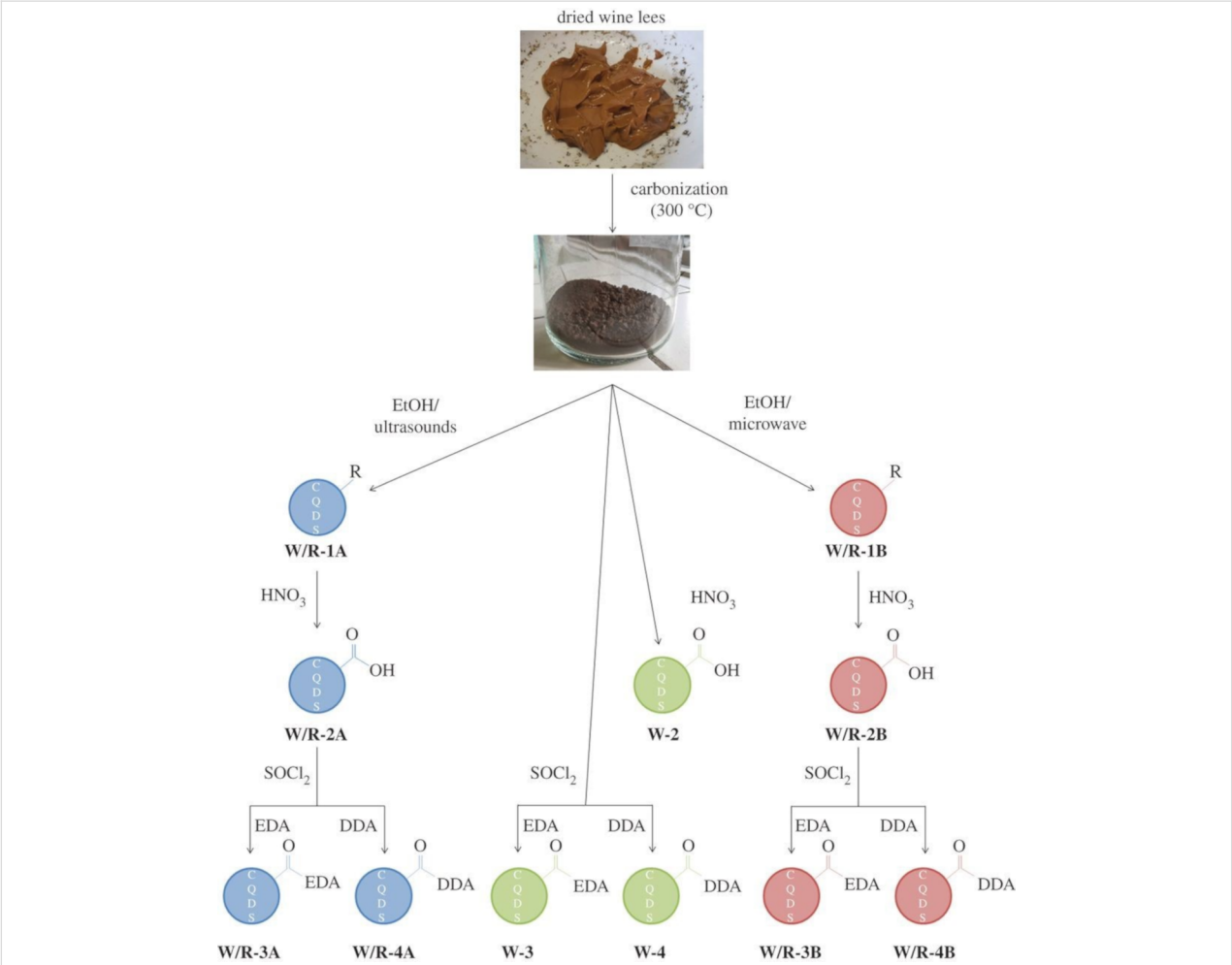


Figure 4: Graphical illustration of the procedure followed with wine lees. Figure 4 was reproduced from [91] (© 2017 M. Varisco et al., published by the Royal Society, distributed under the terms of the Creative Commons Attribution 4.0 International License, https://creativecommons.org/licenses/by/4.0).

the QY and with dodecyl amine (DDA) to obtain CDs dispersible in polar solvents [91].

CDs doped with nitrogen and sulfur (N,S-CDs) were synthesized using rose petals as a natural precursor, and L-cysteine and EDA as N and S dopants, respectively, by Sharma et al. Cysteine and EDA help in hydrolysis and dehydration, respectively, which are part of the bottom-up approach. After completion of aromatization, the N,S-doped CDs are made from nuclear bursts [5]. Pal et al. used branched-chain PEI (bPEI) as a surface passivator and curcumin as a green precursor to synthesize hydrophilic CDs [92]. Aqueous ammonia was used as a nitrogen dopant for many natural source materials such as *Hylocereus undatus* (*H. undatus*), *Chionanthus retusus* (*C. retusus*), *Phyllanthus emblica* (*P. emblica*), and *Phyllanthus acidus* (*P. acidus*) to obtain N-CDs [93,96]. A good QY up to 31.7% was obtained by using EDA as N-dopant with orange juice as carbon source to give N-CDs via hydrothermal decomposition [17].

Das et al. have adopted a new strategy using κ-carrageenan as the carbon source and lemon juice as the sulfur source. Surface quaternization was performed with benzalkonium chloride to synthesize luminescent CDs. The surface functionalities were determined using small-angle neutron scattering, in which incident neutrons interact elastically with the specimen and give information about the surface and mass of the specimen [14].

Empty fruit bunch carboxymethylcellulose as carbon source and EDA as nitrogen dopant to synthesize N-CDs via one-pot hydrothermal carbonization approach have been used. Three different operating parameters, that is, synthesis temperature (230–270 °C), synthesis time (2–6 h), and EDA mass (10%–23.3%) were studied using response surface methodology. The highest values of temperature, time, and EDA mass were found satisfactory to get high QY values up to 22.9%. The factor that has the greatest influence on the QY was found to be the optimized temperature, followed by time and EDA mass [97]. Linear polyethyleneimines (LPEI) were used by the same group instead of EDA to synthesize fluorescent N-CDs and got an increase in QY up to 47% [98].

Blue luminous CDs, based on carrots and aqueous trisodium phosphate (TSP) as precursors, were prepared by a convenient reflux method. The obtained CDs were globular and about 3–8 nm in size as revealed by transmission electron microscopy [21].

Cassava peels as a natural carbon precursor and poly(ethylene glycol) (PEG) as a surface passivizing agent was used by Putro et al. to prepare CDs via the hydrothermal method [99]. Tu et al. used non-toxic fungal biomass *Ganoderma lucidum* along with EDA and diammonium hydrogen phosphate to synthesize water-soluble CDs and N,P-CDs through a facile hydrothermal method. The reported CDs and N,P-CDs presented high sensitivity and selectivity toward 2,4-dinitrophenol and 4-nitrophenol. The obtained QY for CDs and N,P-CDs were 3.54% and 11.41%, respectively [100].

Surendran et al. used honey, garlic, and ammonia as green source, sulfur source, and nitrogen source, respectively to prepare N,S-CDs via a simple hydrothermal technique. The Z-scan methodology was used for non-linear optical characterization and the agar well diffusion methodology was used to explore the antimicrobial performance of CDs against foodborne pathogens [101].

Recently, a hydrothermal technique to build effective CDs using ginkgo kernels has been employed [82]. A unique technique was used to evaluate nitrites in corn sausage, ham sausage, preserved Szechuan pickle, and hot dog samples, yielding good results. In addition, the CDs had high water solubility, fluorescence stability, decreased cytotoxicity, and excellent biocompatibility with MCF7 cells, so they were also successful in bioimaging MCF7 cells. Xu et al. reported red emitting CDs using spinach as a natural source. PEI was used for the modification of the surface of CDs. They observed the change in PL characteristics of CDs during a period of one to four weeks and concluded that when amino-rich CDs come in contact with oxygen in the air, agglomeration of CDs is induced, and, hence, luminescence changes slowly from red to green color (Figure 5) [102]. A summary of CDs synthesized from carbon-rich plant extracts with different surface-passivating agents and their quantum yield is provided in Table 2.

The majority of CDs have a low QY, which are insufficient for bioimaging and other applications. Heteroatom doping has been suggested as a way to enhance the fluorescence characteristics of CDs. Mostly, surface-passivating agents are used to dope CDs with nitrogen and phosphorus to increase their QY. Various plant extracts rich in such ingredients have been used. A list of the reported heteroatom-doped CDs made from natural materials is shown in Table 3. It can be categorized into three groups based on the distinct doped atoms: nitrogen, nitrogen/sulfur, and nitrogen/phosphorus. Hydrothermal treatment as well as pyrolysis, microwave heating, and acid oxidation have been extensively used to synthesize the heteroatom-doped CDs. Nitrogen-doped CDs have been found to have high QY because nitrogen atom doping helps to stabilize the surface defects of CDs and enhances fluorescence emission. Moreover, owing to its five valence electrons and an atomic size that is similar to carbon, nitrogen is a common dopant and the most frequently

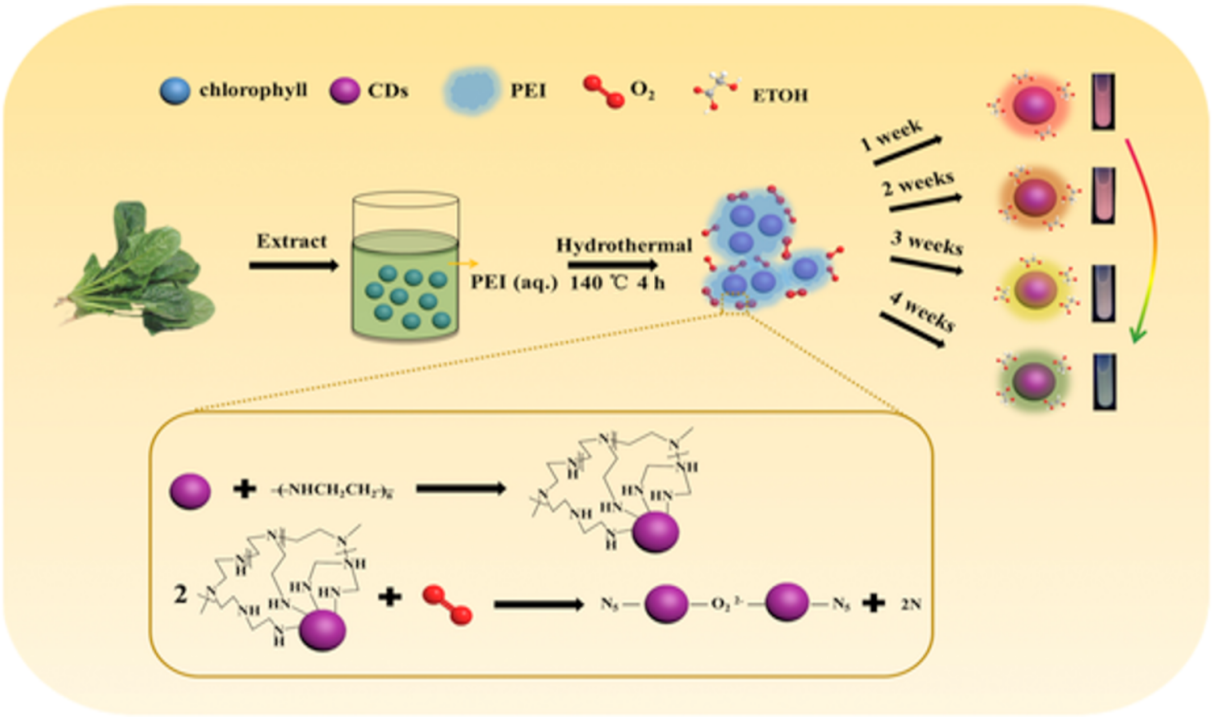


Figure 5: Schematic representation of the whole process. Figure 5 was reprinted from [102], Journal of Luminescence, vol. 227, by X. Xu; L. Cai; G. Hu; L. Mo; Y. Zheng; C. Hu; B. Lei; X. Zhang; Y. Liu; J. Zhuang, "Red-emissive carbon dots from spinach: Characterization and application in visual detection of time", article no. 117534, Copyright Elsevier (2020), with permission from Elsevier. This content is not subject to CC BY 4.0.

Table 2: Summary of CDs synthesized from carbon-rich plant extracts with different surface-passivating agents and their quantum yields.

S. No	Precursor of CDs	Synthetic method	Surface-passivating agent	Size (nm)	QY (%)	Ref
1	celery leaves	hydrothermal method at 200 °C for 4 h	glutathione	2.08	53	[4]
2	*Rosa indica*	hydrothermal treatment at 180 °C for 5 h	EDA and L-cysteine.	4.51–1.46	—	[5]
3	edible carrot	reflux	TSP	3–8	—	[21]
4	*Carica papaya*	pyrolysis	EDTA	7	23.7	[83]
5	table sugar	microwave assisted synthesis at 120 °C for 3 min	ammonia solution	3.5	2.5	[84]
6	white pepper	reflux method at 75 °C for 4 h	H_2N-PEG-NH_2	6.3	10.4	[86]
7	flax straw	hydrothermal method at 160 °C for 10 h	EDA	2.2	20.7	[87]
8	*Lantana camara* berries	hydrothermal 180 °C for 3 h	EDA	5 ± 3	33.15	[90]
9	curcumin	hydrothermal synthesis at 200 °C temp for 12 h	branched PEI (bPEI)	4–5	—	[92]
10	*Hylocereus undatus*	hydrothermal at 180 °C for 12 h	aqueous ammonia	2.5	—	[93]
11	*Phyllanthus emblica*	hydrothermal method at 180 °C for 12 h	aqueous NH_3	4.08	—	[95]
12	*Phyllanthus acidus*	hydrothermal method at 180 °C for 8 h	aqueous ammonia	4.5 ± 1	14	[96]
13	orange juice	hydrothermal decomposition method at 200 °C for 4 h	EDA	0.5–3.0	31.7	[17]
14	oil palms empty fruit bunch	hydrothermal treatment at 260 °C for 2 h	polyethyleneimines (LPEI)	3.4	47	[97]

Table 2: Summary of CDs synthesized from carbon-rich plant extracts with different surface-passivating agents and their quantum yields. (continued)

15	oil palms empty fruit bunch	hydrothermal treatment at 270 °C for 6 h	EDA	4.7	22.9	[98]
16	*Cassava* peels	hydrothermal at 160°C for 4 h	PEG	—	—	[99]
17	*Ganoderma lucidum*	hydrothermal treatment at 200 °C for 6 h	diammonium hydrogen phosphate and EDA	2.95 and 3.12	3.54 and 11.41	[100]
18	natural honey	hydrothermal method at 200 °C for 6 h	ammonia	8.29	≈4.192	[101]
19	spinach	hydrothermally method at 140 °C for 4 h	polyethylenimine (PEI)	3	—	[102]
20	*Lycii fructus*	hydrothermal treatment at 200 °C for 5 h	ammonia solution	3.3	17.2	[29]
21	*Chionanthus retusus*	hydrothermal-carbonization method at 180°C for 6 h	ammonia solution	5 ± 2	9	[94]

Table 3: Summary of doped CDs synthesized from plant extracts with their quantum yield.

S. No	Precursor	Synthesis method	Size (nm)	Doped atom	QY (%)	Ref
1	*Magnolia liliiflora*	hydrothermal treatment at 240 °C for 12 h	4 ± 1	nitrogen	11	[103]
2	*Bauhinia* flower	microwave, 1000 W for 10 min	3.4	nitrogen	27	[104]
3	*Prunus cerasifera*	hydrothermal method at 200 °C for 20 h	3–5	nitrogen	—	[49]
4	seaweed *(Sargassum fluitans)*	hydrothermal method at 180 °C for 5 h	2–8	nitrogen	18.2	[105]
5	watermelon juice	hydrothermal at 180 °C for 3 h	3–7	nitrogen	10.6	[16]
6	*Azadirachta indica*	hydrothermal treatment at 150 °C temp for 4 h	3.2	nitrogen	27.2	[106]
7	grass	hydrothermal at 180 °C for 3 h	3 to 5	nitrogen	4.2	[55]
8	banana peel waste	24 h at 200 °C	5	nitrogen	20	[79]
9	*Lonicera maackii*	hydrothermal process at 230 °C for 5 h	2–3	nitrogen	10.6	[107]
10	lily bulbs	microwave treatment for 6 min	3.15	nitrogen, phosphorus	17.6	[108]
11	*Dunaliella salina*	hydrothermal synthesis at 200 °C for 3 h	4.7	nitrogen, phosphorus	8	[109]
12	ginkgo leaves	hydrothermal treatment at 180 °C for 12 h	2.22	nitrogen, sulfur	—	[82]
13	*Allium fistulosum*	hydrothermal treatment at 220 °C for 3 h	4.22	nitrogen, sulfur	10.48	[110]
14	gardenia fruit	hydrothermal method at 180 °C for 5 h	2.1	nitrogen, sulfur	10.7	[53]

employed method of enhancing PL properties of CDs. By introducing electrons into CDs and altering the internal electronic states, nitrogen atoms significantly enhance the fluorescence characteristics of these molecules. The N-CDs produced perform exceptionally well in biomedical applications, including bioimaging and biosensing. A huge number of synthesis procedures have been investigated in order to produce CDs from environmentally friendly materials that contain nitrogen and carbon. *Magnolia liliiflora* was used to obtain N-CDs via an easy hydrothermal approach by Atchudan et al. The hydrothermal temperature and time used were 240 °C and 12 h, respectively. The obtained size was about 4 ± 1 nm and the quantum yield was up to 11% [103]. Huang et al. achieved an increase in QY up to 27% by using a bauhinia flower to synthesize N-CDs via a facile microwave method, without any further surface passivation or modification [104]. *Prunus cerasifera* fruit was used to synthesize highly luminescent CDs via a hydrothermal method. The reaction temperature and time used were 200 °C and 20 h, respectively. Characterization techniques such as TEM, FTIR, and XPS were used to study the CDs which were almost spherical and had high nitrogen content [49].

Godavarthi et al. used seaweed (*Sargassum fluitans*) to synthesize N-CDs. ^{1}H NMR and ^{13}C NMR were used to analyze *Sargassum fluitans* and showed that amino acids acted as a nitrogen source, for the preparation of N-CDs. The reported

N-CDs were used as a fluorescence probe to detect DNA, and gel electrophoresis was used to compare its efficiency with some traditional organic fluorophores [105]. *Lycii fructus* was used by Sun et al. to develop an efficient method to prepare CDs by using a hydrothermal approach. The reported CDs showed good water solubility and excellent bio-compatibility, and the obtained QY was 17.2% [29]. Grass was used as a natural source to prepare immensely photoluminescent N-CDs through a hydrothermal method. Six different dyes, that is, acid blue, acid red, eosin Y, eriochrome black T, methyl orange, and methylene blue underwent degradation in the presence of radiation, which confirmed the catalytic activity of the product. Adsorption of heavy ions from water samples was investigated to find the activity on the surface of the product, and it was found that the mentioned CDs can remove Cd^{2+} ions by 37% and Pb^{2+} ion by 75% from the water sample [111]. Watermelon juice-based N-CDs with a calculated fluorescence QY of 10.6% were also reported, which were found to selectively detect Fe^{3+} ions. These N-CDs/Fe^{3+} systems could be used to sense cysteine, based on fluorescence "turn on" effects (see below Figure 9). The reported N-CDs showed temperature-dependent fluorescence behavior and were investigated to be used as a nanoscale thermometer for determining the intracellular temperature [16]. Numerous research groups have been actively examining co-doped N,S-CDs. Because the sulfur atom can supply energy or emissive trap states for photostimulated electron capture, which alters the electronic structure of CDs, N,S-CDs have drawn more interest in recent years. Li et al. reported a simple and economical one-pot hydrothermal carbonization route to prepare N,S-CDs by using ginkgo leaves as a natural precursor. XPS results demonstrated that the reported CDs were having elemental contents of 1.2% S, 60.4% C, 34.6% O, and 3.8% N [112]. Wei et al. reported N,S-CDs using *Allium fistulosum* as a green precursor. The prepared CDs revealed a diameter of about 4.22 nm by TEM and the QY obtained was up to 10.48% [110]. *Azadirachta indica* leaves was used to prepare fluorescent N-CDs by Yadav et al. The QYs obtained were as high as 27.2% [106]. Sun et al. used gardenia fruit as a green source to prepare N,S-CDs. The fluorescence intensity of the N,S-CDs was quenched by adding Hg^{2+} ions and recovered when cysteine was introduced to the system. Hence, an "on–off–on" sensor was developed that could detect Hg^{2+} and cysteine in a linear range of 2–20 μM and 0.1–2.0 μM for Hg^{2+} and Cys, respectively [53]. When compared to un-doped CDs, CDs co-doped with nitrogen and phosphorus (N,P-CDs) display novel and surprising features. After doping with N, the CDs become n-type semiconductors. In contrast to nitrogen, phosphorus atoms are larger than carbon atoms. As a result, it has the potential to act as an n-type donor and create substitutional defects in the carbon cluster, changing the electronic and optical characteristics of CDs with great impact on polarizability, quantum yield, and electrochemical properties. Lily bulbs as a green source to synthesize N,P-CDs via a facile, fast, and eco-friendly one-pot microwave-assisted method was reported by Gu et al. Lily bulbs rich in carbohydrates, proteins, lipids, and amino acids, can be easily used to prepare such CDs [108]. The microalgae *Dunaliella salina* was used to prepared low-cost N,P-CDs without any external agent. The algal biomass consists of amino acids and proteins, and XPS revealed that the CDs contain pyrrolic nitrogen and phosphate groups showing that these molecules were doped into the lattice of N,P-CDs [109]. Using banana peel waste as carbon and nitrogen source, novel CDs have been prepared using a simple hydrothermal carbonization technique in an ecofriendly approach by Atchudan et al. [79]. Their excitation-dependent fluorescence characteristics have been used successfully as a fluorescent probe in multicolor imaging applications of nematodes. Bi et al. described the synthesis of green fluorescent N-CDs from *Lonicera maackii* fruits using a one-step hydrothermal technique. The CDs could not only detect Fe^{3+} but also overcome the limitations of short-wavelength fluorescence CDs from natural materials, providing a basis for future applications in other disciplines [107]. Atchudan et al. reported a hydrothermal synthesis technique that yields CDs from *Morus nigra* (black mulberry) fruit juice [81]. This low-cost synthesis approach provides an effective, robust, and eco-friendly nanoscale sensor for the measurement of Fe^{3+}. The CDs were also found to be appropriate FL probes for imaging human colon cancer (HTC-116) cells. Recently, Lin et al. proposed a unique antimicrobial compound for the preservation of Atlantic mackerel by synthesizing antimicrobial CDs through a hydrothermal synthesis approach using food materials as the precursor, including onion, ginger, garlic, and mackerel [113]. The sulfur content of the CDs based on onion and garlic was higher than that of the CDs derived from ginger and fish. Surprisingly, the onion-based CDs had the best antibacterial efficacy against *Pseudomonas fragi*, as well as good pH stability.

Animal extract

Dehvari et al. converted seafood waste into valuable materials by using crab shell as a natural precursor to form highly fluorescent N-CDs by a sono-chemical approach. A N-CDs/folic acid nanoprobe was synthesized by conjugating N-CDs with folic acid, which could be used to target folate-receptor cancer cells [114]. Pork-based CDs without any surface-passivating agent were synthesized. Pork meat, itself, is composed of many organic molecules that can provide multiple heteroatoms in the CDs. The resulting CDs have excellent advantages such as a high QY of 17.3% and good stability to chemicals [115]. Zhang et al. obtained urine-based CDs through a simple sephadex filtration approach and a via a hydrothermal route (Figure 6). Different characterization techniques revealed that both types of

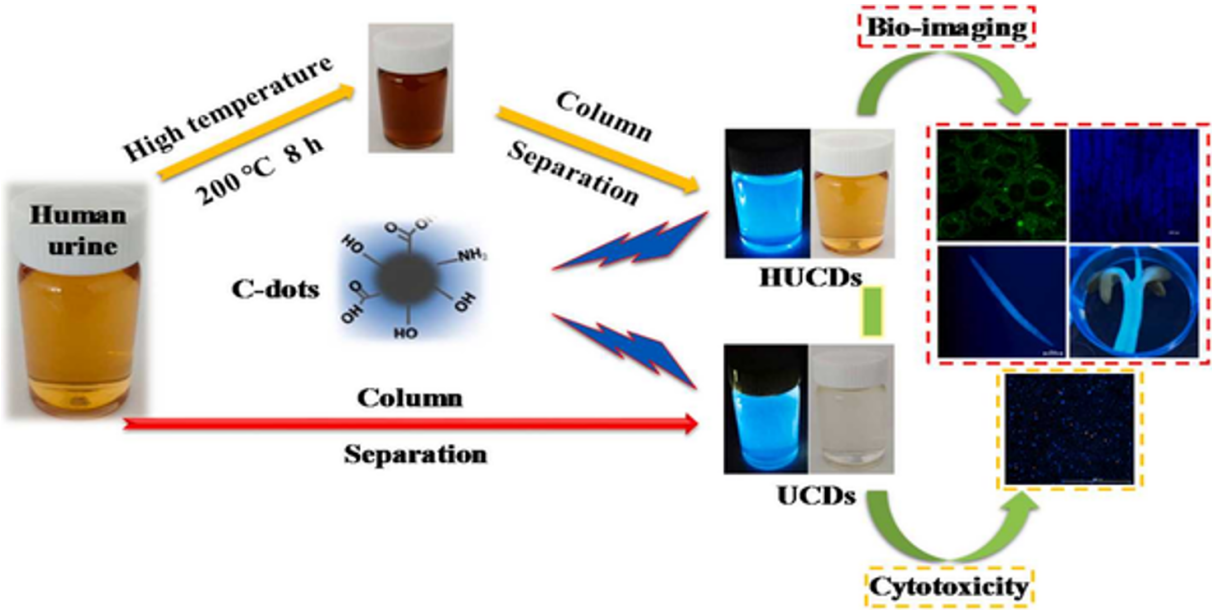


Figure 6: Graphical illustration for the synthesis of CDs from human urine and their application for bioimaging. Figure 6 was reprinted from [116], Methods, vol. 168, by X. Zhang; J. Li; J. Niu; X. Bao; H. Zhao; M. Tan, "Fluorescent carbon dots derived from urine and their application for bioimaging", pages 84-93, Copyright Elsevier (2019), with permission from Elsevier. This content is not subject to CC BY 4.0.

CDs consisted of carbon and oxygen and indicated the existence of different functional groups such as amino, carboxylate, carbonyl, and hydroxy groups. The cytotoxicity study showed good biocompatibility and applicability in both in vitro and in vivo imaging [116].

Recently, milk was used by Al-Hashimi et al. as a natural precursor to synthesize N-CDs via a solvothermal method. These nanodots served as fluorophore in the inner filter effect (IFE) sensing platform to detect tetracycline in pharmaceutical doses [76]. Highly water-soluble and blue emitting CDs were synthesized from hemoglobin by Chakraborty et al., which can be used to detect H_2O_2 [117].

Food materials

Different food materials such as beans are also a good source of carbohydrates, which can be easily used to synthesize CDs. Hydrochar was produced from food waste via hydrothermal carbonization and utilized to synthesize CDs by Zhou et al. Specific temperatures (195, 225, and 255 °C) were used for 12 h, followed by the use of vacuum filtration to separate the hydrothermal product. The hydrochar was refluxed in nitric and sulfuric acid, and dialysis membranes of different sizes were used to get CDs emitting four different colors, that is, blue, green, yellow, and red (Figure 7A,B) [118]. EDTA was used in a solution containing different ions for quenching iron ions specifically.

Researchers have employed different beans to synthesize high-quality CDs. Jia et al. used black soya beans as a natural resource to prepare N-CDs by a one-step pyrolysis method. The obtained N-CDs had good photoluminescence characteristics. The reported QY was as high as 38.7 ± 0.64% [119]. Kaur et al. obtained a very high QY up to 58% by using EDA as nitrogen source with *Vigna radiata* (mung bean) to produce N-CDs. The reaction conditions EDA concentration and time were optimized to increase the QY. The concentration of EDA used per 10 mL of *Vigna radiata* extract ranged from 200 to 2000 µL, and the time range was from 5 to 36 h. A direct relationship between the concentration of EDA and the fluorescence intensity was found [120]. Khan et al. used red lentils as a carbon source in a simple, one-step, inexpensive preparation of water-soluble N-CDs. The reported N-CDs showed bright blue fluorescence under an ultraviolet lamp with a wavelength of 365 nm, and the QY was up to 13.2% [121].

Sesame as a natural source was also used to synthesize highly efficient CDs naturally doped with N, P and Ca ions by Yu et al. The reported CDs have a good QY up to 48.5% and emit strong blue fluorescence [122]. Soni et al. synthesized CDs, co-doped with nitrogen and sulfur, from palm shell powder as a natural precursor with trifilic acid. The obtained CDs had a graphite-like structure, a narrow size distribution, and showed intense green fluorescence. These CDs had fluorescence characteristics independent of the excitation wavelength and were

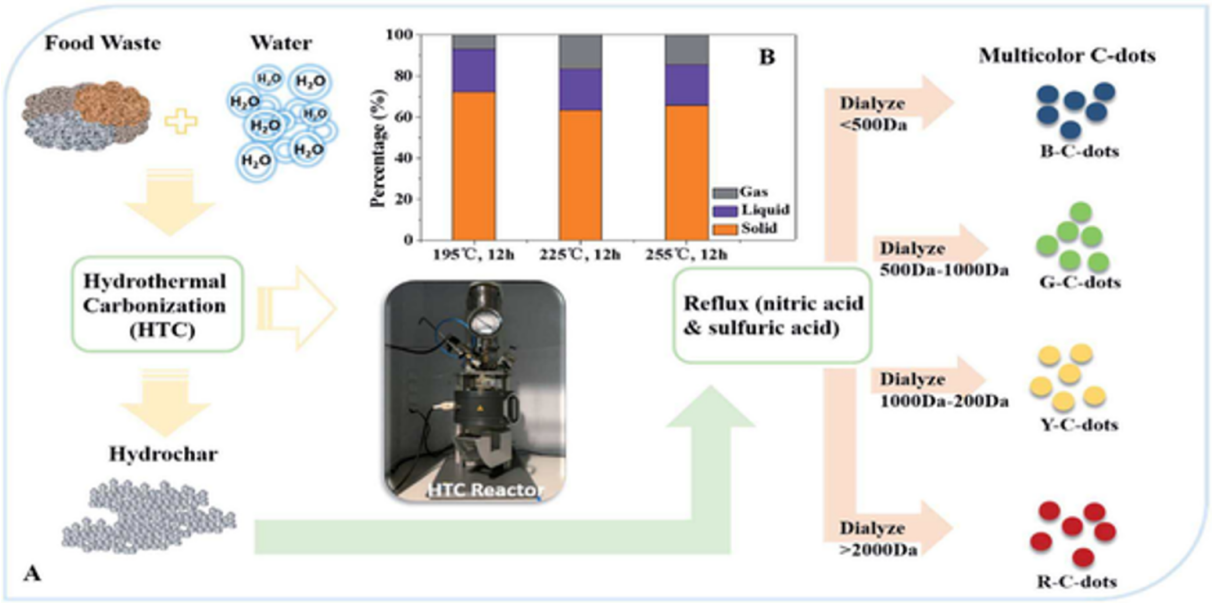


Figure 7: (A) Flow chart of multicolor CDs production. (B) Carbon distribution in gas, liquid, and solid phase from the new precursor production process. Figure 7 was reproduced from [118] ("Multicolor carbon nanodots from food waste and their heavy metal ion detection application", © 2018 Y. Zhou et al., published by The Royal Society of Chemistry, distributed under the terms of the Creative Commons Attribution Noncommercial 3.0 Unported License, https://creativecommons.org/licenses/by-nc/3.0/). This content is not subject to CC BY 4.0.

used as fluorescent probes with LOD values of 0.079, 0.165, and 0.082 μM for 4-nitrophenol, 2,4-dinitrophenol and 2,4,6-trinitrophenol, respectively [123]. CDs synthesized from animal extracts and food materials, are summarized in Table 4.

Natural polymer-based CDs

Numerous natural polymers, including proteins and polysaccharides, have been used to obtain CDs (Table 5). Chen and co-workers used starch as a source to synthesize graphene quantum dots (CDs) via a one-pot hydrothermal method. They also described the reaction mechanism, which involves hydrolyzation of starch to form glucose, and then glucose is condensed to form CDs by ring-closure condensation. These CDs have been effectively used in bioimaging of cervical cancer cells as a suitable PL probe [124]. Wen et al. have created an incredibly eco-friendly and cost-effective method for creating highly luminous CDs from cotton by pyrolysis and microwave treatments. The CDs exhibit high fluorescence QY, great biocompatibility, low toxicity, and adequate stability. The CDs have found applications in various fields, including multicolor imaging, patterning, and sensing, as a result of their advantageous characteristics [125]. Han and co-workers extracted cow milk-derived CDs (CM-CDs) from aqueous solution using ethyl acetate to create amphiphilic CM-CDs (ACMCDs). A unique ACMCD-Ag/poly-

Table 4: Summary of CDs synthesized from animals extracts and food materials, with their quantum yields.

S. No	Precursor	Synthetic method	Size (nm)	QY (%)	Ref
1	pork	hydrothermal method at 200 °C for 10 h	3.5	17.3	[115]
2	crab shells	ultra sonicationat 70 °C for 12 h	8	14.5	[114]
3	urine	urine based CDs (sephadex filtration method)	2.5	4.8%	[116]
		urine based CDs (hydrothermal method) 200 °C for 8 h	5.5	17.8%	
4	hemoglobin	muffle furnace 120 °C for 1 h	≈4.0	≈73	[117]
5	black soya beans	pyrolysis at 200 °C for 4 h	5.16 ± 0.30	38.7 ± 0.64	[119]
6	*Vigna radiate*	hydrothermal at 180 °C for 24 h	<10	58	[120]
7	red lentils	hydrothermal at 200 °C for 5 h	6	13.2	[121]
8	sesame	hydrothermal process at 150 to 200 °C for 1–5 h	25	48.5	[122]
9	palm shell	hydrothermal method at 150 °C for 10 h	4–10	—	[123]

Table 5: Summary of CDs synthesized from various polymers, with their quantum yields and applications.

S. No.	Precursor of CDs	Synthetic method	Size (nm)	QY (%)	Application	Ref
1	starch	hydrothermal, 190 °C, 120 min	2.50–2.75	—	bioimaging	[124]
2	cotton	pyrolysis, 300 °C for 2 h	4.9 ± 0.10	14.8	multicolor imaging, patterning, and Fe^{3+} detection	[125]
3	cow milk	hydrothermal, 180 °C, 12 h	1–5	—	antimicrobial	[28]
4	egg white	hydrothermal, 220 °C, 48 h	2.1	61	Fe^{3+} detection bioimaging, optical devices	[126]
5	lignin	hydrothermal, 180 °C, 40 min	2 to 10	—	bioimaging	[127]
6	peanut shells	pyrolysis, 400 °C, 4 h	3.3	10.6	Cu^{2+} detection	[128]
7	raw cashew gum	microwave (800 W), 30–40 min	9 ± 3	8.7	—	[129]
8	*Schisandra chinensis*	hydrothermal, 200 °C, 8 h	2.31	—	Fe^{3+} detection	[130]

methylmethacrylate antibacterial film was produced utilizing the solvent casting process after the ACMCDs were supported by silver nanoparticles, employing them as both a reducing agent and a template. The nanocomposite antibacterial film is anticipated to have a lot of potential applications such as food packaging, water purification, and disinfecting sanitary equipment because of its superior antibacterial, light-admitting, and flexible features [28]. In another report, CDs were prepared from egg white using a one-step hydrothermal method. Carbonization, N-doping, and surface functionalization all occurred simultaneously during the hydrothermal reaction. The CDs were employed as probes for detecting metal ions and in live-cell imaging, and they had a high quantum yield of 61% [126]. Chen et al. proposed a quick method for producing highly luminous CDs by hydrothermally treating lignin with H_2O_2. It is well recognized that under the photoassisted catalysis of Fe^{3+}/Fe^{2+} in water, H_2O_2 can be split into hydroxyl radicals, and the ensuing radical is an incredibly potent oxidizing species. The treatment time lasted from 10 to 60 min, with 40 min yielding the highest CD luminescence. The resulting CDs (2–10 nm) have excellent penetration into HeLa cells, minimal cytotoxicity, high water solubility and photostability [127]. Fiber-rich peanut shells were used to produce fluorescent CDs (1.8–4.2 nm) that had a QY of 10.6% and better photostability than rhodamine B. The CDs were produced using a straightforward one-pot pyrolysis procedure at 400 °C for 4 h, and they were effectively used for Cu^{2+} detection, which was attributed to the fluorescence quenching effect of the ions [128]. A unique and quick microwave-assisted method that requires two steps was reported by Pires for the synthesis of CDs with an average size of 9 nm from an aqueous solution of a polysaccharide, that is, raw cashew gum. Through the autohydrolysis of cashew gum, some monomer units are produced in the first phase (partial depolymerization in solution), and a trace amount of 5-hydroxymethyl furfural can be produced. The formation of a polyfuranic structure through polycondensation and polymerization is followed by aromatization, carbonization, and nuclear fusion in the second phase. As a result, a composite of partially depolymerized cashew gum and CDs was produced [129]. Wu and co-workers used *Schisandra chinensis* polysaccharide as carbon source that also has a naturally nitrogen-containing structure for endogenous nitrogen-doping in a green synthesis of CD-based room-temperature phosphorescent (RTP) materials. The materials had lifetimes of up to 271.2 ms with a lower energy gap and 350 nm of excitation (0.32 eV). Furthermore, when iron ions (Fe^{3+}) were introduced, they displayed appropriate quenching. Additionally, the generated CD-based RTP materials have extremely stable optical and physical characteristics, opening up a new avenue for using them as low-cost, environmentally friendly luminescent sensors for Fe^{3+} detection [130].

Surface state effects on the optical features of CDs

The surface state of CDs, which is closely linked to their fluorescence emission and serves as the most commonly acknowledged luminescence mechanism until now, includes the level of surface functional groups, surface oxidation, and molecular fluorescence.

Surface oxidation level: Numerous investigations have demonstrated that the level of surface oxidation in CDs is what causes their luminescence. The amount of oxygen on the surface of CDs directly influences its redshifted emission. The number of surface defects increases with the surface oxidation level. The surface defects trap excitons, and the radiation from the recombination of trapped excitons causes the redshifted emission. Liu et al. reported the synthesis of highly photoluminescent CDs,

which were then further separated into yellow emitting crystalline graphene quantum dots and green emitting amorphous carbon nanodots using a silica gel column. Even though they have the same chemical surface groups and particle size distribution, they both have varying levels of surface oxidation. The emission wavelength moved from 518 to 543 nm as the degree of surface oxidation increased, which gives an indication about the reduction of band gap between LUMO and HOMO [50].

Surface functional groups: A correlation between the surface states and the functional groups found on the surface of CDs has been established by many researchers. Functional groups such as C=O and C=N are strongly associated with the fluorescence of CDs. Diverse fluorophores or energy levels can be introduced into CDs by different surface functional groups. Wang et al. demonstrated that by adjusting the functional groups on the surface of CDs, the emission wavelength could be dramatically altered. In some unique edge states, which were made up of many carbon atoms and functional groups (such as carbonyl) on the edge of the carbon backbone, the emission centers of CDs were equally distributed. Therefore, by affecting the emission centers, the functional groups on the surface of CDs may ultimately alter the fluorescence [131].

Molecular fluorescence: According to recent research, most of the emission from CDs is caused by fluorescent impurities, which are produced during the bottom-up chemical synthesis, or molecular fluorescence. Yang et al. proved that 1,2,3,5-tetrahydro-5-oxo-imidazol[1,2-a]pyridine-7-carboxylic acid (IPCA), which is a fluorescent molecule, was responsible for the bright blue fluorescence of CDs synthesized using citric acid and EDA. It has been established that the CDs are a mixture of IPCA, polymers, and carbon cores [132]. Essner and co-workers carried out the synthesis of CDs using citric acid (paired with urea or ethylenediamine as a nitrogen source). They showed that luminous impurities formed as byproducts during the synthesis of CDs mostly contribute to fluorescence emission by eliminating the molecular fluorophores [133]. By using fluorescence correlation spectroscopy and time-resolved electron paramagnetic resonance spectroscopy, Righetto and co-workers proved that free molecules are the source of the fluorescence in CDs. In the excitation range from 320 to 450 nm, CDs were produced by the emission of small fluorescent molecules dispersed in solution. In contrast, poorly emitting carbon cores predominate in the emission at excitation levels above 480 nm. Since small organic molecules are free in solution, it follows that even when carbon cores do exist,

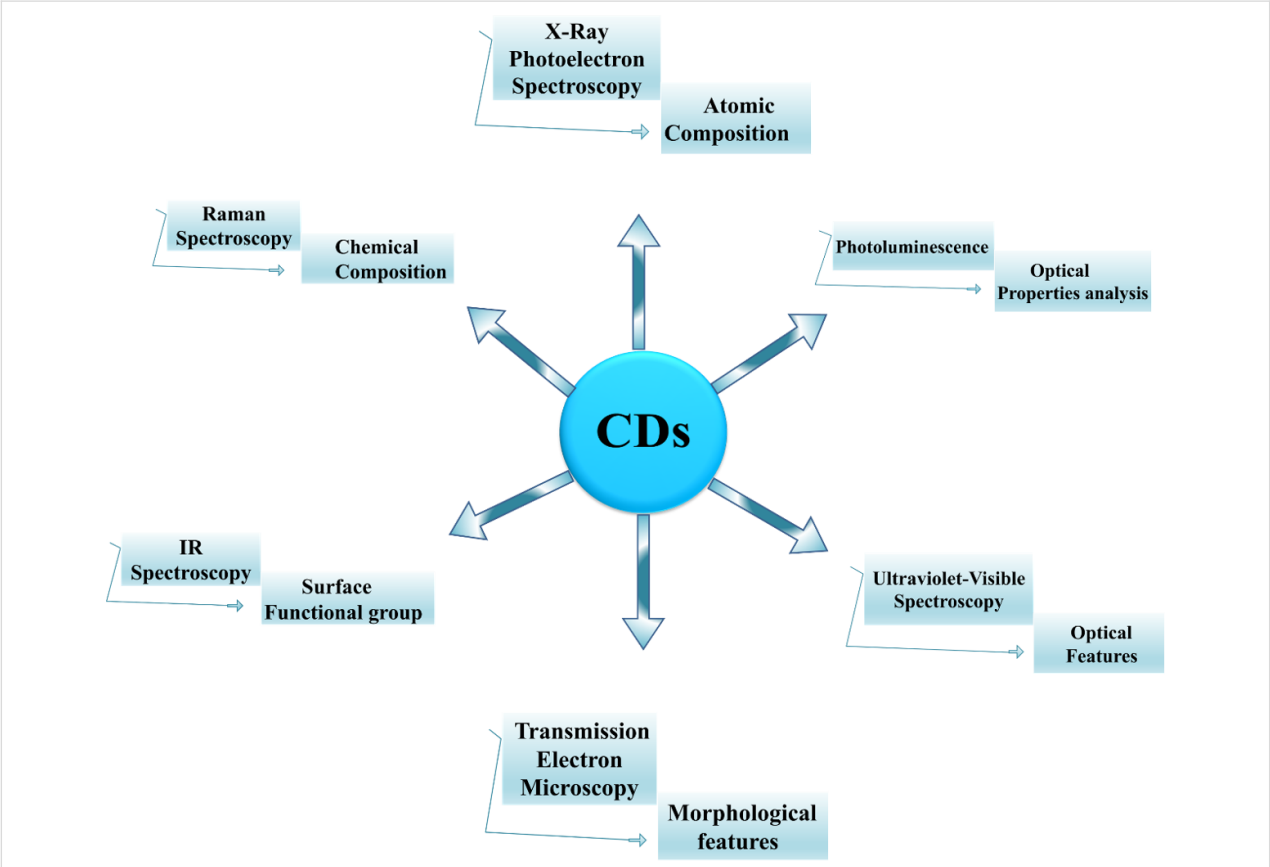


Figure 8: Structural characterization techniques used to study CDs.

the origin of the fluorescence is attributed to these molecules [134].

Characterization of CDs

There are several published analytical methods for characterization, illustrating physical characteristics, demonstrating the crystalline structure, and determining type and sufficiency of functionalization groups attached on the surface of the CDs (Figure 8). A brief description is provided in this review.

Transmission electron microscopy

Because of its great resolution of 0.1–0.2 nm, TEM can be used to determine the morphology of CDs. Since CDs have a particle size of less than 10 nm, high-resolution techniques such as TEM are frequently used to investigate the morphology and the particle size distribution. High-resolution TEM (HR-TEM) can also be utilized to examine the intricate structure of the CDs. HR-TEM can reveal the fine structure of CDs and whether they are crystalline or amorphous. Additional morphological data can be obtained using SAED patterns. The phrase "interlayer spacing" is used to describe lattice fringes produced through HRTEM analysis with a fringe width spacing around 0.34 nm, whereas the term "in-plane lattice spacing" is used for a fringe width of 0.24 nm.

Photoluminescence

Due to the vast range of applications, photoluminescence, which results from the quantum confinement effect, is now regarded as the most intriguing aspect of CDs. Because of their unique optical characteristics, CDs may be able to reflect impacts from particles of different sizes, shapes, internal structures, and compositions. CDs also has a variety of emissive sites spread across the surface. The emission spectrum of CDs typically ranges from the visible to the near-infrared region, with a characteristic red shift as the excitation wavelength increases, which is regarded as a remarkable characteristic of the PL of CDs. Despite a lot of research in this area, the precise mechanism of PL emission in CDs is still unknown.

Fourier-transform infrared spectroscopy

FTIR spectroscopy is a method for determining the presence of functional groups on the surface of CDs that is based on the detection of electromagnetic radiation absorption at wavelengths between 4000 and 400 cm^{-1}. The majority of the CD surfaces are rich in hydroxy, carbonyl, ether, and carboxylic acid groups because the synthesis process involves partial oxidation of the carbon source [135]. Therefore, exploration of functional groups is essential for characterization. Using elemental doping and composite fabrication, the structure of CDs has been modified to enhance analytical performance. The degree of surface passivation can be assessed using FTIR analysis.

Ultraviolet–visible spectroscopy

CDs made using a variety of procedures often exhibit strong UV absorption. However, the positions of the UV absorption peaks change significantly depending on the synthesis method. In general, CDs show strong optical absorbance in the UV range between 260 and 320 nm, with a tail that extends into the visible spectrum. Pure CDs often contain two absorption peaks, that is, one for the n–π^* transition of surface functional groups such as carbonyl, hydroxy, ester, and carboxyl groups, and one for the π–π^* transition of aromatic sp^2 domains [38]. However, surface groups and synthetic process have a significant impact on where the absorption peaks are located. Doping heteroatoms or incorporating them into a composite material has a significant impact on the absorption wavelength of CDs because of the change in the π–π^* energy level [136]. The commonly occurring broad absorption spectra of CDs are caused by the surface defects.

X-ray photoelectron spectroscopy

For surface chemical investigation and characterization of nanoscale materials, X-ray photoelectron spectroscopy is an effective analytical tool. The electrical structure, elemental composition, and oxidation states of the elements in a material can all be determined using this method, which depends on the photoelectric effect [137]. Surface chemical modification, core–shell topologies, and various components of CDs can all be investigated using XPS.

Raman spectroscopy

Raman analysis is frequently used to measure the vibrational modes and provide structural data about molecules. Raman analysis can be used to assess the optical and electrical characteristics, crystalline or amorphous nature, and other characteristics of CDs. Usually, CDs exhibit two distinctive Raman peaks called the D band and the G band. Owing to the oscillations of vastly disordered sp^2-hybridized graphitic dangling bonds on the termination plane, the D band is typically detected at a wavelength of about 1352 cm^{-1}. The E_2g mode of the 2D hexagonal lattice of graphite correlates to the vibrations of the sp^2-linked carbon atoms that cause the G band, which is visible at about 1585 cm^{-1} [27].

Applications as metal ion sensors

As CDs possess unique photoluminescence and excitation-based emissions, quenching and reversal of quenching processes can be used as an analytical tool for detection of certain analytes. CDs have been widely used as sensors for metal ions such as Fe^{3+} [49,59,85,138-141], Fe^{2+} [25], Hg^{2+}

[109,142,143], Cu^{2+} [86,108,144-146], Cd^{2+} [147], Cr^{6+} [52,148-152], Co^{2+} [153], Au^{3+} [154], As^{3+} [155,156], Pb^{2+} [157], and Ag^{+} [158]. This sensing application is based on the principle that fluorescence is either quenched or increases when the functional groups on the surface of the CDs interact with the metal ions creating new electron–hole pairs via energy transfer. Different sensing/quenching mechanisms include inner filter effect (IFE), fluorescence resonance energy transfer (FRET), electron transfer (ET), static quenching effect (SQE), dynamic quenching effect (DQE), aggregation-induced emission enhancement (AIEE) effect, and aggregation-induced emission quenching (AIEQ) effect.

Static quenching occurs when fluorophore/CDs interact with the quencher and form a ground non-fluorescent complex [54,94,119].

Dynamic quenching occurs when an excited state of CDs returns to ground state by energy/charge transfer between the quencher and the CDs. This quenching only affects excited states, and, hence, no difference is observed in the absorption spectra of CDs [89,97,104].

Fluorescence resonance energy transfer (FRET) is a process where photonic energy of a fluorophore/CDs is transferred to another fluorophore/CDs, which then transmits it. FRET occurs between CDs and quencher in their excited and ground state, respectively, when the emission spectrum of CDs overlap with the absorption spectrum of the quencher [19].

The inner filter effect (IFE) occurs when there is a good spectral overlap between the absorption spectrum of the quencher and the excitation/emission band of the fluorophore/CDs [113,120].

Electron transfer (ET) may cause quenching when metal ions combine with various functional groups on the surface of CDs and lead to electron transfer from CDs to the ions. CDs act as electron source and generate excited electrons on irradiation, which are then transferred to the electron-deficient metal ions, and, hence, quenching occurs [109].

Aggregation-induced emission enhancement effect (AIEE) may arise as a result of aggregation of CDs. The aggregation increases the π conjugation and hinders the rotational vibration of the functional groups, which enhances the radiative rate and lowers the non-radiative rate.

Aggregation-induced emission quenching effect (AIEQ) occurs when fluorescent CDs aggregate and the energy of the excited fluorophores is transferred to the ground-state fluorophores without radiative transition, leading to a decrease or even complete quenching of fluorescence [154].

Detection of metal ions and efficient monitoring of their concentrations in aqueous and various biological samples is important because of their biological role and the toxicity, above certain thresholds, to the environment, human health, plants, and animals. Detection through CDs is advantageous because of the ease of operation, and high selectivity and sensitivity.

Fe^{3+} ion sensing

Fe^{3+} ions are one of the most abundant metal ions and play a vital role in biological systems as well in environmental systems. Fe^{3+} ions participate in biological processes such as metabolism, electron transfer systems, and oxygen supply of hemoglobin. They accumulate in the form of ferritin in liver and spleen. Both, deficiency and excess of the ions lead to serious disorders, such as certain kind of cancers or anemia. Hence, it is essential to monitor the Fe^{3+} levels in the environment and in biological systems. Various CDs are sensitive and selective towards Fe^{3+} ions [97-99].

Highly stable and water-soluble CDs, prepared from *Boswellia ovalifoliolata* by hydrothermal carbonization, exhibited high selectivity towards Fe^{3+} ions through quenching, with a LOD of 0.41 μM, in addition to useful applications such as free radical scavenging and bioimaging. The quenching is believed to proceed through a dynamic quenching mechanism. Groups such as –OH and –COOH on the surface of CDs facilitate complexation with Fe^{3+} ions, electron transfer occurs from the excited state of the CDs to unoccupied orbitals of Fe^{3+} and, hence, quenching occurs [138].

Citrus limetta-based CDs synthesized through pyrolysis, were found to have a wide range of applications. The CDs performed well in sensing Fe^{3+} ions with a LOD of 19.8 ppb. Fluorescence quenching was observed, which was explained based on the presence of –COOH groups on the CDs having a high affinity for the metal ions, which leads to static quenching. Composites of these nanoscale lights or CDs with TiO_2 nanofibers were found to be efficient for water splitting application. They also exhibited fast catalytic degradation of methylene blue, bactericidal behavior, and their general non-toxicity makes them good candidates for bioimaging as well [139].

Fluorescent CDs synthesized from betel leaves exhibit selective detection of Fe^{3+} ions with a LOD of 50–150 nM leading to the quenching of their fluorescence activity. The quenching process was explained based on charge transfer of –COOH on the CDs to the ferric ion (Figure 9) [140].

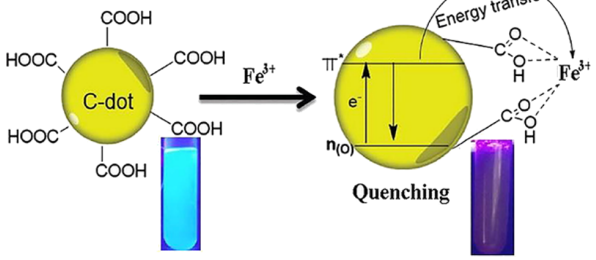


Figure 9: The proposed quenching mechanism of CDs prepared from betel leaves. Figure 9 was reprinted from [140], Materials Today: Proceedings, vol. 34, by D. Raja; D. Sundaramurthy, "Facile synthesis of fluorescent carbon quantum dots from Betel leafs (Piper betle) for Fe^{3+} sensing", pages 488-492, Copyright Elsevier (2021), with permission from Elsevier. This content is not subject to CC BY 4.0.

CDs and doped CDs (phosphorus and nitrogen) have been obtained from *Miscanthus grass*, where the N-doped CDs have the potential to selectively detect Fe^{3+} ions in the presence of other ions, with a LOD of 20 nM. Blue fluorescence was observed under UV, which was quenched when Fe^{3+} is added, and was explained based on a strong affinity of the metal ions to coordinate with amino and –COOH groups of the N-doped CDs. All CDs and doped CDs were found to exhibit excitation-dependent emission in addition to fluorescence [141].

Gupta et al. synthesized CDs from pine apple (*Ananas comosus*) through an acid oxidation approach. The reported CDs exhibited three colors under UV light, that is, blue (B-CDs), green (G-CDs), and yellow (Y-CDs). It was found that only B-CDs were sensitive to Fe^{3+} ions. The functional groups present on the B-CD surface coordinates with Fe^{3+} ions resulting in dramatic changes in the morphology and size of the B-CDs. From analyzing HR-TEM images and fluorescence spectra, it was concluded that fluorescence detection of Fe^{3+} occurs because of aggregation of B-CDs and the IFE [85].

Huang et al. used bauhinia flowers to synthesize N-CDs, which acted as a turn-off/on fluorescence sensor for the detection of Fe^{3+} and adenosine triphosphate (ATP), respectively. They described that the fluorescence quenching (turn-off) in case of Fe^{3+} ions occurs due to coordination of Fe^{3+} with surface functional groups of N-CDs, which resulted in non-radiative electron/hole recombination. Recovery of the fluorescence intensity (turn-on) by ATP is due its interaction with Fe^{3+} via Fe–O–P bonds [104]. The same mechanism for Fe^{3+} ion detection was also described by Ma et al. for CDs prepared via a hydrothermal route using *Prunus cerasifera* fruit as a carbon source [49].

Murugan and Sundramoorthy used *Borassus flabellifer* (male tree) as raw material to obtain CDs and used them to detect Fe^{3+} ions. Fe^{3+} have a $3d^5$ electron configuration. Thus, excited-state electrons of CDs can move to the half-filled 3d orbital of Fe^{3+} ions via coordination interaction resulting in non-radiative electron/hole recombination and fluorescence quenching [59].

The N-CDs prepared from water melon juice by Lu et al., acted as fluorescence turn-off/on sensor to detect Fe^{3+} and cysteine, respectively. The selectivity concerning Fe^{3+} was assigned to coordination of Fe^{3+} ions with hydroxy, amine, and carboxyl functional groups present on the N-CD surface resulting in interruption of radiative transition and fluorescence quenching. They used the N-CDs/Fe^{3+} system to sense cysteine because cysteine can compete with N-CDs regarding Fe^{3+} ions and lead to their removal and, hence, recovery of the fluorescence [16].

CDs derived from grapes and onions, which were found to have a reducing ability, were reported and employed for the determination of Fe^{3+}. The CDs reduce Fe^{3+} ions to Fe^{2+} and, hence, provide a colorimetric approach for Fe^{3+} detection. The reducing ability of grape-based CDs was better than that of the onion-derived CDs [159].

Starch fermentation wastewater was used for the synthesis of S,N-CDs that showed selectivity towards Fe^{3+}. It was investigated that the fluorescence of the S,N-CDs was quenched mainly because Fe^{3+} is a strong electron acceptor and, therefore, captures the excited electrons from the CDs with surface functional groups. The fluorescence quenching was reversed through the addition of phosphate at pH 7 [160].

Devi et al. prepared *Aloe vera*-derived CDs with Fe^{3+} sensing ability. Their selectivity towards Fe^{3+} is due to the presence of –COOH and –OH groups on the surface of the CDs. The fluorescence quenching was observed to decrease with increasing Fe^{3+} concentrations linearly [67].

Fluorescent N-CDs were synthesized by Atchudan et al. using *Magnolia liliiflora* as a carbon source, which exhibited excellent sensing towards Fe^{3+}. The N-CDs were investigated to have a high number of nitrogen- and oxygen-containing functional groups. The sensing of Fe^{3+} was attributed to a mechanism where N-CDs get complexed with Fe^{3+} through functional groups, quenching the fluorescence [103].

Arumugham et al. developed carbon quantum dots using leaves of white *Catharanthus roseus* through a one-pot hydrothermal method, without employing any oxidizing agents and surface passivation. These water-soluble carbon quantum dots were sensitive towards Al^{3+} and Fe^{3+} ions. Quenching occurs when electrons are transferred from the excited CD to the empty orbitals of Fe^{3+}, leading to non-radiative electron–hole recombi-

nation. With Al^{3+}, the fluorescence increases as the ions coordinate with the CDs forming aggregates leading to aggregation-based high photoluminescence emission [161]. Antioxidant potential against 2,2-diphenyl-1-picrylhydrazyl was also measured and was found to improve with increasing concentration of the CDs. MCF-7 cells were treated with CDs and in vitro bioimaging was carried out using fluorescence microscopy under UV excitation. However, no significant cell decline was observed. In addition, they demonstrated non-toxicity towards both breast cancer cell lines and normal breast epithelial cells.

Bi et al. synthesized green fluorescent CDs from *Lonicera maackii* fruit through a hydrothermal process, which were efficient in Fe^{3+} detection in actual water samples with a LOD of 0.1–10 μM. The short fluorescence time indicated rapid electron transfer from the excited state to the empty d orbitals of Fe^{3+} causing quenching. Besides, the CDs have phenolic hydroxy groups containing lone pairs of electrons, which, on reaction with Fe^{3+}, get transferred to its empty d orbitals resulting in non-radiative electrons/hole recombination. This process causes a further decrease in fluorescence [107]. Similarly, Ding et al. prepared CDs from typical crop waste such as wheat straw, corn straw, and rice straw using hydrothermal methods for the detection of Fe^{3+}, displaying similar properties [77].

Fe^{2+} ion sensing

Shi et al. used cornstalk as a green precursor to prepared CDs for the detection of both Fe^{2+} ions and H_2O_2. They observed no change in fluorescence intensity when Fe^{2+} and H_2O_2 were added to an aqueous solution of CDs indicating that there was no effect on either Fe^{2+} or H_2O_2 alone. A significant decrease in fluorescence intensity was only observed when both were added together. The surface of prepared CDs is composed of plenty of hydroxy and oxygen functional groups. Thus, the reduction in fluorescence of CD was mainly attributed to the formation of metal hydroxide complexes on the CD surface with quenching probably occurring via electron or energy transfer with surface of CDs. They designed a CD–H_2O_2 system for Fe^{2+} ion detection and a CD–Fe^{2+} system for H_2O_2 detection and obtained LOD values of 0.18 and 0.21 μM for Fe^{2+} and H_2O_2, respectively [25].

Hg^{2+} ion sensing

Mercury is a heavy metal and highly toxic to humans and the environment. High levels of Hg^{2+} severely damage the central nervous system and other vital organs, and even lead to death. Mercury appears in Hg^{2+} form in water. Besides, elemental and organic mercury compounds are also found in polluted waters. The allowed level in drinking water is 1 μg/L. Liu et al. reported highly fluorescent CDs from China grass carp scales using a one-step hydrothermal method, which showed high sensitivity towards Hg^{2+} ions owing to the presence of sulfhydryl groups. The Hg^{2+} strongly coordinates with the sulfur atoms of the cysteine in the CDs, forming a hairpin structure S–Hg^{2+}–S and, thus, quenching their fluorescence (Figure 10). A linear decrease in fluorescence intensity was observed with increased concentration of mercury ions with a LOD of 0.014 μmol/L. The low cytotoxicity and enhanced cell-permeability of the CDs make them sensible probes for Hg^{2+} detection in environmental and biological systems [142].

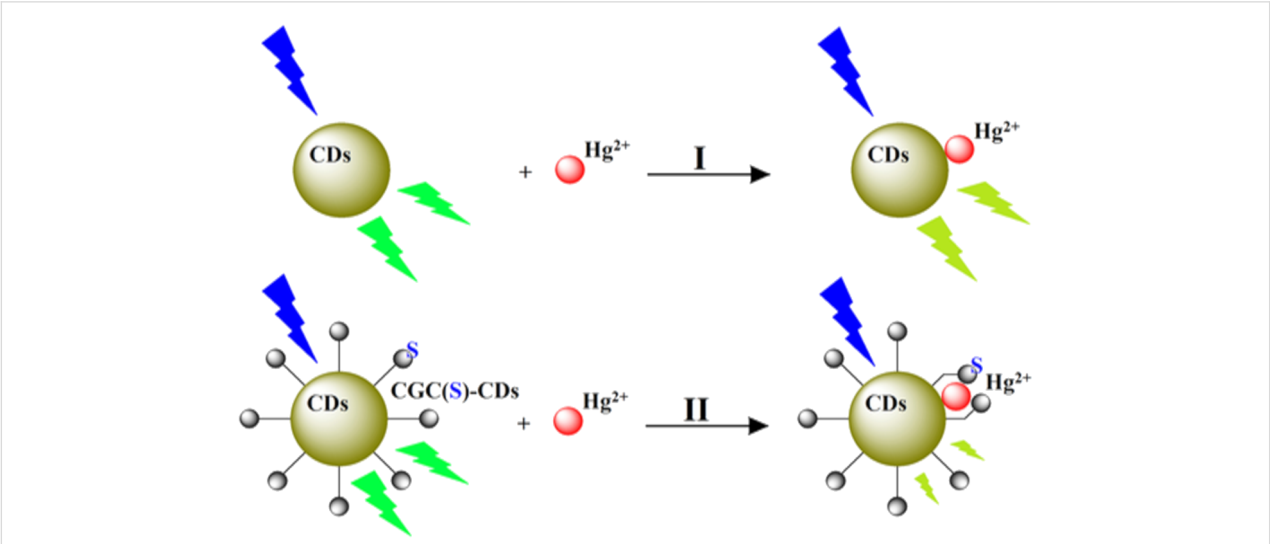


Figure 10: Detection mechanism of Hg^{2+} by using the CGCS-CDs as fluorescence probe. Figure 10 was reprinted from [142], Microchemical Journal, vol. 145, by G. Liu; H. Jia; N. Li; X. Li; Z. Yu; J. Wang; Y. Song, "High-fluorescent carbon dots (CDs) originated from China grass carp scales (CGCS) for effective detection of Hg(II) ions", pages 718-728, Copyright Elsevier (2019), with permission from Elsevier. This content is not subject to CC BY 4.0.

Highly stable, fluorescent, nitrogen-doped CDs obtained from citrus lemon juice were reported by Tadesse et al. The CDs were prepared via a hydrothermal method and showed high sensitivity and high selectivity towards Hg^{2+} ions with a LOD of 5.3 nM. The presence of oxygen- and nitrogen-containing groups on the surface of CDs facilitates coordination to Hg^{2+} by donating electron pairs to the metal ion, quenching the fluorescence of CDs. The quenching was ascribed to non-radiative electron–hole annihilation. Besides, human breast adenocarcinoma cells were tested for biocompatibility with these CDs. Very low cytotoxicity values were observed and, hence, the CDs could be used for bioimaging applications [143].

Pourreza et al. used *Prosopis juliflora* leaves to prepare CDs, which act as an off-on fluorescence sensor for Hg^{2+} ions and chemet detection, respectively. The addition of Hg^{2+} ions caused fluorescence quenching because of electrostatic interaction and non-radiative recombination of excitations via the transfer of electron between Hg^{2+} ions and oxygen-carrying groups present on the CD surface. When the Hg–CD system was treated with chemet, the fluorescence intensity of CDs was regained because of the strong interaction of Hg^{2+} ion with chemet (Figure 11) [23].

Li et al. reported the synthesis of N-CDs by using orange juice as a green source and EDA as a surface-passivating agent and used the CDs to detect Hg^{2+} ions. When the concentration of Hg^{2+} ions was increased, a decline in fluorescence intensity of N-CDs occurred and the full width at half maximum of the N-CDs emission peak slowly broadened because a complex formed between Hg^{2+} and carboxyl groups on the surface of the N-CDs [17].

Singh et al. used *Dunaliella salina* to synthesize N,P-CDs, which acted as a sensor for both Hg^{2+} and Cr^{6+} ions. The quenching through Hg^{2+} and Cr^{6+} occurred through dynamic quenching and IFE + dynamic quenching mechanisms, respectively [109].

Li et al. used Hongcaitai (*Brassica compestris L. var. purpurea Bailey*) to prepare CDs that were categorized into two parts because of solubility differences. The one that was soluble in

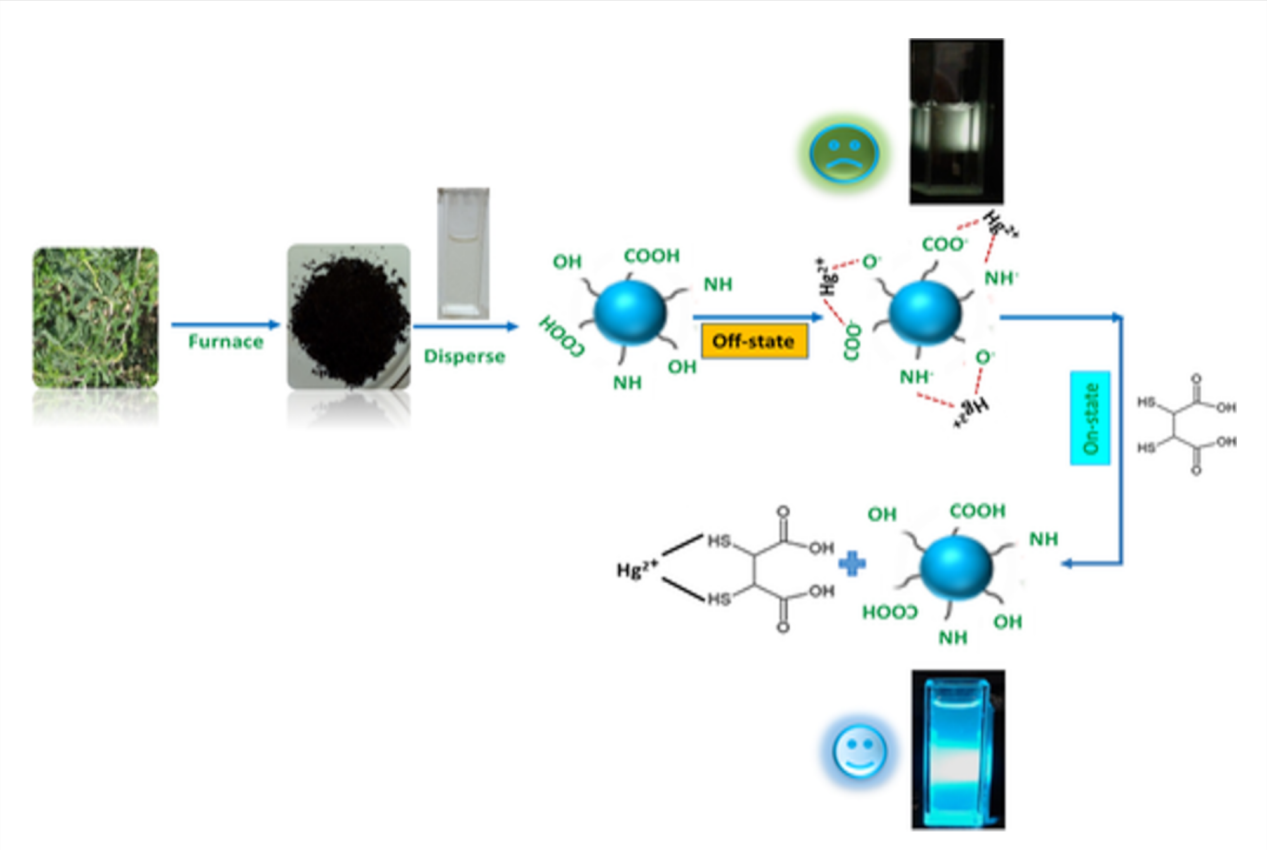


Figure 11: Schematic representation of off-on fluorescence of CDs prepared from *Prosopis juliflora.* Figure 11 was reprinted from [23], Materials Science and Engineering: C, vol. 98, by N. Pourreza; M. Ghomi, "Green synthesized carbon quantum dots from *Prosopis juliflora* leaves as a dual off-on fluorescence probe for sensing mercury (II) and chemet drug", pages 887-896, Copyright Elsevier (2019), with permission from Elsevier. This content is not subject to CC BY 4.0.

ethanol was named "CDs-A" and was used for ClO^- detection. The ethanol-insoluble CDs were named "CDs-B" and were used for Hg^{2+} detection. At pH 3, the strong oxidant HClO is mainly present, resulting in significant fluorescence quenching because of the oxidation of hydroxy groups present on the surface of the CDs. With the increase of pH, the concentration of ClO^-, with lower oxidation strength as HClO, increased, which led to a decrease in fluorescence quenching. The fluorescence quenching by Hg^{2+} was assigned to its interaction with sulfur-containing functional groups on the surface of CDs-B, which resulted in non-radiative electron transfer [65].

Highland barley-derived N-CDs were produced via a hydrothermal process, where EDA was used for N-doping. The fluorescence intensity of the N-CDs diminished with increased concentration of Hg^{2+}, which is likely due to a strong chelation of the metal ions by the –COOH groups on the surface of N-CDs causing static quenching [89].

Fluorescent N,S-CDs derived from gardenia fruit by Sun et al. via a hydrothermal method were highly stable in a wide pH range, high concentrations of sodium chloride, and under ultraviolet radiation. N,S-CDs exhibited on/off response towards cysteine and Hg^{2+}. The fluorescence quenching was credited to the formation of Hg^{2+}–S bonds, leading to a static quenching mechanism. Addition of cysteine resulted in a reversal of the quenching phenomenon because the interaction of the metal ions with sulfhydryl of the cysteine is stronger [53].

Cu^{2+} ion sensing

Copper is an essential trace element with different biological roles. However, high concentrations above a normal level of 100–150 μg/dL (15.7–23.6 μM) may cause toxicity causing Menkes and Wilsons diseases, gastrointestinal damage, and certain neurodegenerative diseases. Copper may enter the human body through drinking water polluted with Cu^{2+} ions above the permissible levels of 1.3 ppm. Many researchers have investigated CDs for efficient and easy-to-use Cu^{2+} sensing, suitable for use in aqueous and biological environments.

Polyolefin residues, resulting from pyrolytic degradation of waste plastic, are rich in carbon, and devoid of other heteroatoms, hence, a potential carbon source to be used for the preparation of CDs. Waste polyolefin residues, as a precursor, are advantageous in terms of reduced production cost. CDs as a probe for Cu^{2+} ions have been investigated. Kumari et al. obtained green fluorescent CDs from the pyrolytic residues of polyolefins via chemical oxidation without using any surface-passivating agents. The CDs exhibited green emission under UV light at 365 nm. These CDs exhibited high selectivity for Cu^{2+} ions in the presence of many other ions, under normal room temperature, with a detection limit of 1–8 μM/L. These CDs could also be used for a visual detection of Cu^{2+} ions, as a color change under UV light from a darker shade of green to a lighter one occurred upon addition of Cu^{2+} ions. Similarly, fluorescence quenching was detected with increased Cu^{2+} addition in tap water and mineral water samples, despite the presence of interfering minerals. The quenching was suggested to occur through a dynamic quenching mechanism, where Cu^{2+} ions coordinate to the carbonyl groups on the surface of the CDs [144]. These CDs also proved to be promising probes for breast cancer cell imaging (MDA-MB 468), owing to their significant cell permeability and reduced cytotoxicity.

Banana juice is rich in carbohydrates and, hence, a precursor for CDs. Chaudhary et al. reported on N,S-CDs prepared from banana juice via a hydrothermal method, exhibiting high fluorescence (blue emission) at pH 6. A decrease in fluorescence was observed below pH 6 and above 8. The N,S-CDs had high solubility in aqueous media with a wide range of detection for copper ions (1–800 μg/mL), observed in the form of fluorescence quenching. The N,S-CDs have a net negative charge and functional groups, such as hydroxy, carboxylic, and carbonyl groups, which assist in binding to Cu^{2+} ions, leading to formation of coordination bonds. This leads to a decrease in fluorescence activity, showing up as a redshift in the emission spectrum [162].

Biocompatible and highly stable blue CDs, derived from radish, were prepared through a hydrothermal method. The CDs were used for sensing of Cu^{2+} in water samples and vapors of acetic acid through an opto-electronic nose with CDs as sensing material. On addition of Cu^{2+} ions, fluorescence quenching was observed with a LOD of 0.16 μM. Owing to their high electron-donating ability, the –COOH groups on the CDs undergo complexation with Cu^{2+} ions, resulting in fluorescence quenching. A filter paper-based sensor incorporated with CDs was prepared with an improved detection limit of 6.8 μM. A measurement of the acetic acid concentration in a series of acetic acid/methanol mixtures was performed, with a limit of detection of around 15%. Vinegar samples were also tested accurately. A cytotoxicity assay of the CDs against MCF-7 breast cancer cells showed their biocompatibility with high cell viability, suggesting prospective applications in cell-imaging, biosensing, and drug delivery [145].

Eleusine coracana-derived green CDs were investigated as turn-off sensor for Cu^{2+}. The strong affinity and selectivity of the CDs towards the metal ions were attributed to the presence of oxygen-rich functional groups, mainly –COOH, –NH, and –OH, on the surface of CDs. The Cu^{2+} ions are good electron acceptors and coordinate to the functional groups. Moreover,

the paramagnetic Cu^{2+} ions adsorb in a relatively facile way on aromatic C=C bonds of the CDs, causing effective quenching [146].

Lily bulbs were used by Gu et al. to prepared N,P-CDs. The synthesized CDs were used to detect Cu^{2+} ions due to their dynamic affinity for different functional groups present on CDs surface, that is–COOH, –OH, and $–NH_2$. A LB–CD complex is formed, which promises to boost charge shift and inhibits radiative recombination of excitons, resulting in a unique fluorescence quenching effect [108].

White pepper has been used as a green precursor for dual-emission CDs, which exhibited high selectivity towards coenzyme A. Emission at 520 nm (green) turned on the Cu^{2+}-aided sensing, keeping the red emission at 668 nm as a reference. The fluorescence activity reduced slowly with an increase in the ion concentration from 0 to 65 μM. However, no significant decrease was observed when the concentration increased from 65 μM to 80 μM. When 65 μM Cu^{2+} were added to CDs, the absorption wavelength did not change, but intensity and fluorescence lifetime dropped. This indicated an interaction between the surface functional groups of the CDs and Cu^{2+}. With the addition of CoA, fluorescence was restored, which was attributed to a strong conjugation between the phosphate and amino groups of CoA and Cu^{2+}. The intensity of the fluorescence was observed to vary linearly with the concentration of coenzyme A [86].

Highly fluorescent CDs from coconut coir synthesized by a hydrothermal method demonstrated strong biocompatibility towards bacteria, various fungal strains, aquatic animals, and some plants when in low concentration. A sensor based on the synthesized CDs showed selectivity towards Cd^{2+} ions with a LOD of 0.18 nM (turn on) and Cu^{2+} ions (turn off) with a LOD of 0.28 nM in different media including sewage and groundwater systems. The fluorescence quenching in the presence of Cu^{2+} occurs due to a strong affinity of the metal ion for the hydroxy, carboxyl, and amino groups on the CDs, which leads to complex formation and non-radiative charge–hole annihilation. The emission intensity increased in the presence of Cd^{2+} ions, which was attributed to the induction of an intrinsic radiative recombination of the CDs (Figure 12). Furthermore, the chemical interaction between the surface of CDs and the Cd^{2+} ions also has an influence on the excitation of CDs [51].

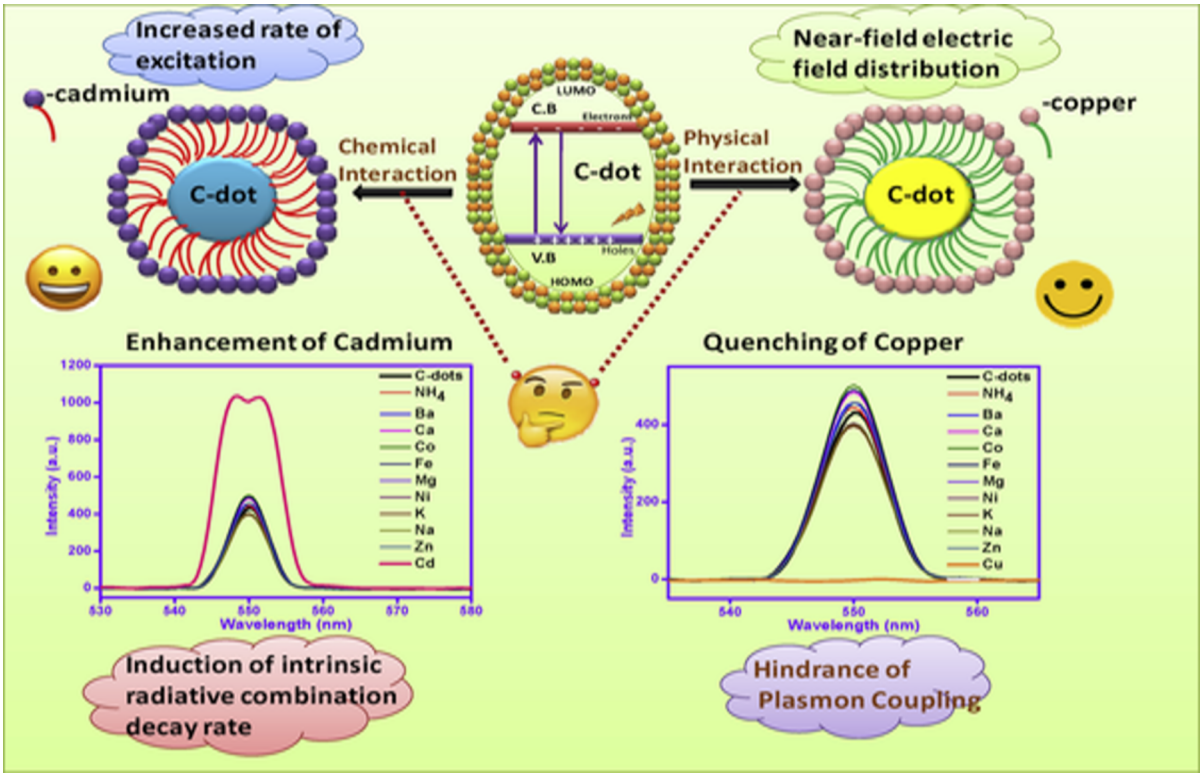


Figure 12: Schematic illustration of the sensing mechanism of CDs in the presence of Cd^{2+} and Cu^{2+} ions. Figure 12 was reprinted from [51], Materials Today Chemistry, vol. 16, by P. Chauhan; S. Dogra; S. Chaudhary; R. Kumar, "Usage of coconut coir for sustainable production of high-valued carbon dots with discriminatory sensing aptitude toward metal ions", article no. 100247, Copyright Elsevier (2020), with permission from Elsevier. This content is not subject to CC BY 4.0.

Cd^{2+} ion sensing

Cadmium ions are highly poisonous heavy metal ions used for dying, electroplating, and in the semiconductor industries. The Cd^{2+} ions are toxic to animals and human beings and mainly affect liver, kidneys, lungs, and central nervous system. Cadmium poisoning manifests itself in the form of breath shortage, general weakness, pneumonia, and death in extreme cases. According to WHO, the permissible level of Cd^{2+} ions in drinking water is 3 ppb.

Murraya koenigii, commonly known as curry leaves were used for the synthesis of CDs by Pandey et al., which exhibited quenching with Cd^{2+} ions (LOD = 0.29 nM). The Cd^{2+} ions have vacant d orbitals, which bond with the –COOH and amino groups on the CDs through LMCT, leading fluorescence quenching. High selectivity for Cd^{2+} ions was exhibited even in the presence of other interfering metal ions such as Zn^{2+} [72].

Rice husk-based CDs prepared by Zainal Abidin et al. were functionalized with amino and carboxyl groups using EDA and ascorbic acid and denoted as N-CD and C-CDs, respectively. The PL of the C-CDs is reduced/quenched when an increased amount of ascorbic acid is added, which causes protonation of the CDs. Lowering of PL with increasing ascorbic acid concentration indicates reduced recombination of holes and electrons on the surface of the CDs. An increase in emission wavelength is observed, which is due to increased protonation of the negative CDs, leading to extensive electrostatic interactions among the CDs and agglomeration. A reverse trend was observed with the N-CDs and EDA. Both N-CDs and C-CDs exhibit a linear response to Cd^{2+}, that is, a decrease in PL activity with increase in Cd^{2+} concentration. The quenching was thought to be due to electrostatic interactions between the metal cations and the negatively charged CDs, which are rich in oxygen-containing groups, leading to agglomeration. Moreover, electron transfer between the CDs and Cd^{2+} may result in reducing the latter to Cd. The quenching due to –COOH groups is stronger than that due to amino groups, because of high electronegativity of–COOH [147].

Pb^{2+} ion sensing

Lead is a heavy metal and is hazardous to human health. Lead poisoning causes serious damage to nervous system, kidneys, brains, and other vital organs. Pb^{2+} ions from water pipes containing lead enter into water when corrosion occurs due to acidic water. According to WHO, the upper limit of lead in drinking water is 0.05 $mg{\cdot}L^{-1}$. Boobalan et al. used oyster mushrooms (*Pleurotus* species) as a green precursor to prepare CDs for the detection of Pb^{2+} ions. They reported that quenching of CDs is because of the formation of a complex between Pb^{2+} ions and hydroxy and carboxyl groups present on the surface of the CDs (Figure 13) [157].

Ocimum sanctum (Tulsi leaves)-based fluorescent CDs were found to detect Pb^{2+} ions with excellent sensitivity and selectivity. The amine groups on the surface of CDs have great binding affinity with the vacant d orbital of the metal ion. Donation of an electron pair from the nitrogen of the functional groups to the empty d orbital of Pb^{2+} takes place and results in quenching of the fluorescence of CDs [163].

Table sugar-based CDs were reported, which acted as an efficient naked-eye sensor for lead ions. Small concentrations of Pb^{2+} ions, even at ppb levels turned the CD solutions turbid, which was explained by the formation of aggregates. Large aggregates scatter light and, hence, appear turbid. No other ions exhibited such behavior with these CDs [84].

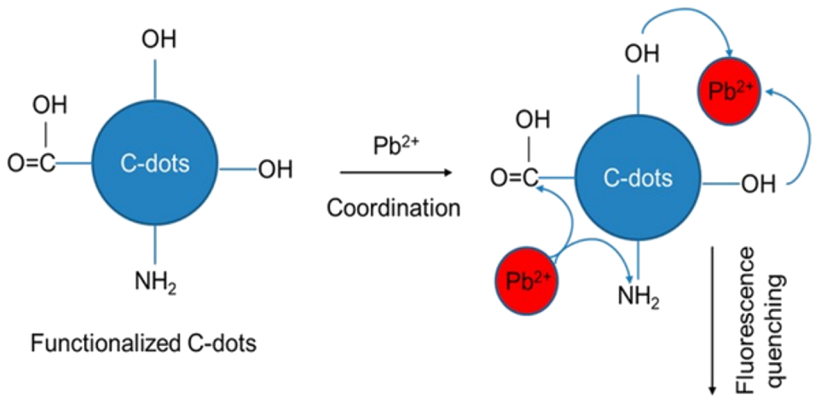


Figure 13: Schematic representation of Pb^{2+} ion sensing using oyster mushroom-derived CDs. Reprinted with permission from [157], Copyright 2020 American Chemical Society. This content is not subject to CC BY 4.0.

Cr^{6+} ion sensing

Chromium has great importance in metallurgy, textile, dyes and leather tanning. However, it is highly toxic and carcinogenic. Two oxidation states, Cr(VI) and Cr(III) are more common and possess entirely different properties. The Cr(VI) compounds, due to their high solubility cause adverse effects in living organisms, whereas, the Cr(III) species are less toxic and important micronutrients. The permissible limit of the chromate(VI) (CrO_4^{2-}), according to WHO, is 0.05 $mg{\cdot}L^{-1}$.

Athika et al. synthesized CDs from denatured milk by a hydrothermal method, which demonstrated sensitivity towards Cr^{6+} with a detection limit of 14 mM in various water samples. Fluorescence quenching of the CDs was observed on adding Cr^{6+} mainly due to the inner filter effect. The CD electrode was found to exhibit a capacitance of 95 $F{\cdot}g^{-1}$ and stability over 1000 cycles [148]. *Hibiscus sabadariffa*-derived CDs prepared through a hydrothermal method were found to be suitable for bioimaging of breast cancer cells in addition to sensing Cr^{6+} ions [52].

CDs and N-CDs originated from groundnuts synthesized through a hydrothermal method showed remarkable selectivity towards certain metal ions. The CDs showed selective detection of Hg^{2+}, Fe^{3+}, and Cr^{6+}, whereas the N-CDs sensed Cr^{6+} ions with a LOD of 0.1 mg/L. The fluorescence excitation/emission spectra showed that Cr^{6+} blocks the excitation wavelength of the N-CDs and also absorbs the emission intensity of CDs. Non-radiative electron–hole annihilation is also possible. The quenching mechanism in N-CDs was reversed with humic acid and glutathione. Humic acid and glutathione reduce Cr^{6+} to Cr^{3+}, which reverses quenching as the N-CDs are not reactive towards Cr^{3+}. The CDs were biocompatible with low cytotoxicity values, making them suitable for bioimaging of MCF-7 cells [149].

Das et al. proposed a sustainable way to use jute caddies to synthesize CDs by a sonochemical approach. The CDs modified with benzalkonium chloride were reported to detect Cr^{6+} by luminescence quenching and selectively restore its fluorescence to detect ascorbic acid (Figure 14). The IFE was proposed to be a possible quenching mechanism because a significant spectral overlap between the absorption band of Cr^{6+} and the excitation and emission spectra of the CDs occurs when AA was introduced into the CD/Cr^{6+} system. AA reduces Cr^{6+} to Cr^{3+} or some lower oxidation state, which helped to eliminate the IFE and to restore the fluorescence intensity. Thus, a fluorescence turn-off/on sensor was developed [150].

Luo et al. used luffa sponge to synthesize CDs by a chemical oxidation approach. The fluorescence quenching effect of Cr^{6+} on the CDs was studied. The results showed that the addition of Cr^{6+} changed the intensity of the characteristic absorption peaks of CDs and led to the static quenching of the fluorescence. The IFE was used to explain the fluorescence quenching. The Cr^{6+} ions show absorption at 260, 360, and 440 nm. The excitation spectra of CDs exhibit prominent excitation and emission bands at 360 and 473 nm, respectively. There is an obvious overlap in the 360 nm excitation spectra, which indicates that Cr^{6+} can shield the excitation light of CD. Therefore, an increase in Cr^{6+} concentration may result in a stronger fluorescence quenching of CD [151]. The same mechanism was also proposed by Shreya Bhatt et al. to detect Cr^{6+}. They used tulsi leaves to synthesize CDs and reported a LOD and linear range of 4.5 ppb and 1.6 to 50 μM, respectively [152].

Recently, Hu used flax straw as a green source to synthesize CDs by a hydrothermal method. The reported CDs possess "on-off" fluorescence behavior in the presence of Co^{2+} or Cr^{6+} ions, which is further protracted to "on-off-on" behavior for ascorbic acid detection (Figure 15). The "on-off" fluorescence behavior is based on static quenching and the IFE and "on-off-on" fluorescence behavior occurs because ascorbic acid can reduce Cr^{6+} to Cr^{3+} due to which the IFE weakens and fluorescence of CDs recovers [87].

CDs prepared from dried rice fried *Codonopsis pilosula* by Qiu et al. were found to be highly selective and sensitive towards Cr^{6+} in water bodies and industrial affluents. The absorption band of Cr^{6+} overlapped with the excitation band of the CDs pointing to an IFE process [74].

CDs synthesized from *Carica papaya* waste via pyrolysis were utilized for detecting the content of Cr^{6+} and Cr^{3+} in water. Functional groups, such as carbonyl and carboxylic groups, on the CDs help in their modification with EDTA, producing EDTA-functionalized CDs (fCDs). The fCDs, then coordinate with the chromium ions through oxygen and nitrogen of the functionalized ethylene diamine (Figure 16) [83].

Co^{2+} ion sensing

Cobalt is an essential trace metal, which controls the production of red blood cells and also regulates many other vital processes involving the catalytic activity of some important enzymes. Besides, it is an important component of vitamin B_{12}. Excessive levels of cobalt give rise to low blood pressure, asthma, dermatitis, and myocardial infarction. The permissible levels of cobalt in water for irrigation and livestock are 0.05 and 1 $mg{\cdot}L^{-1}$, respectively.

Kelp-based CDs with ethylenediamine as nitrogen dopant prepared via microwave irradiation were found to be highly pH

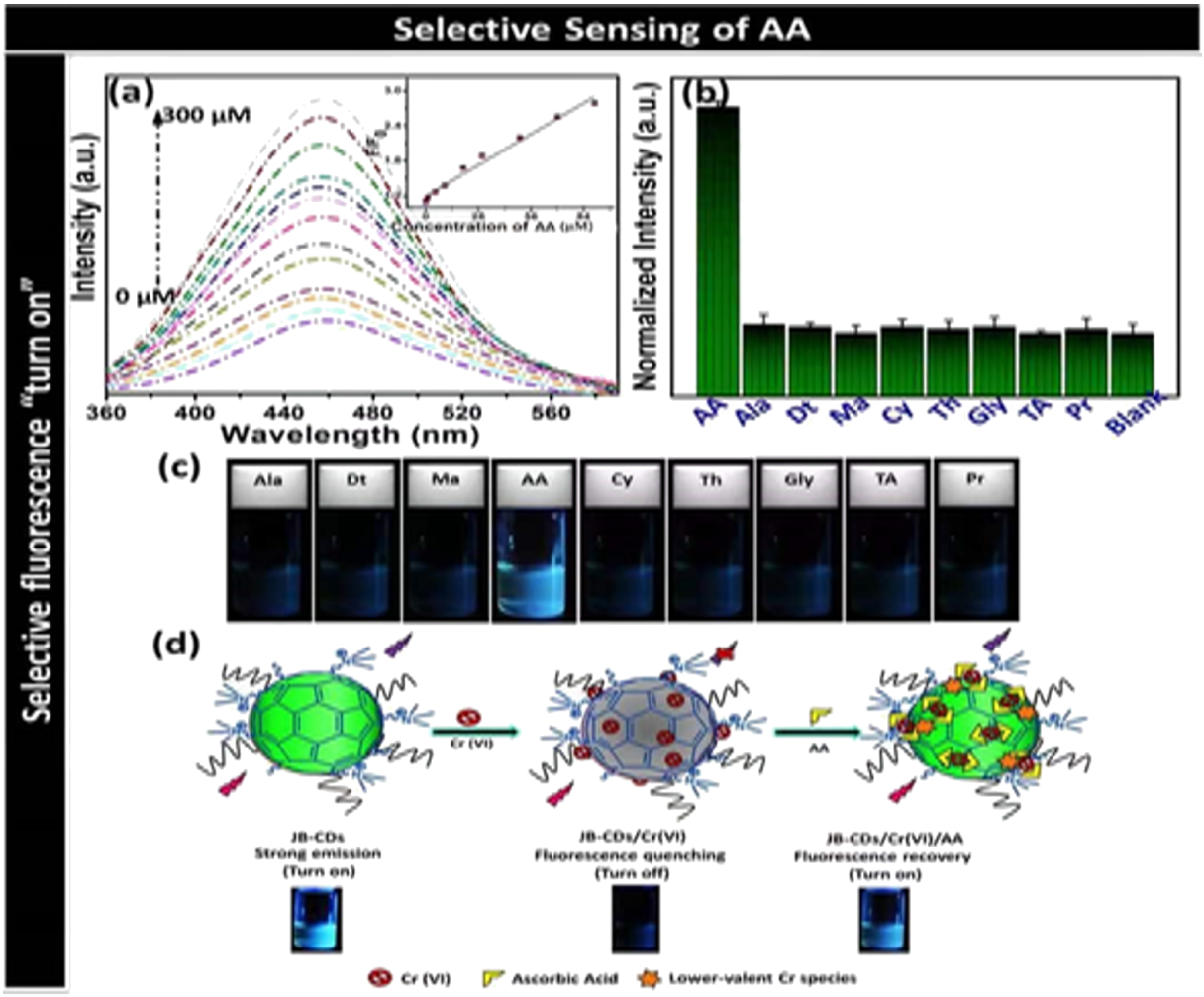


Figure 14: Fluorescence quenching and restoration of jute caddies based modified CDs, in the presence of Cr^{6+} and AA. Reprinted with permission from [150], Copyright 2020 American Chemical Society. This content is not subject to CC BY 4.0.

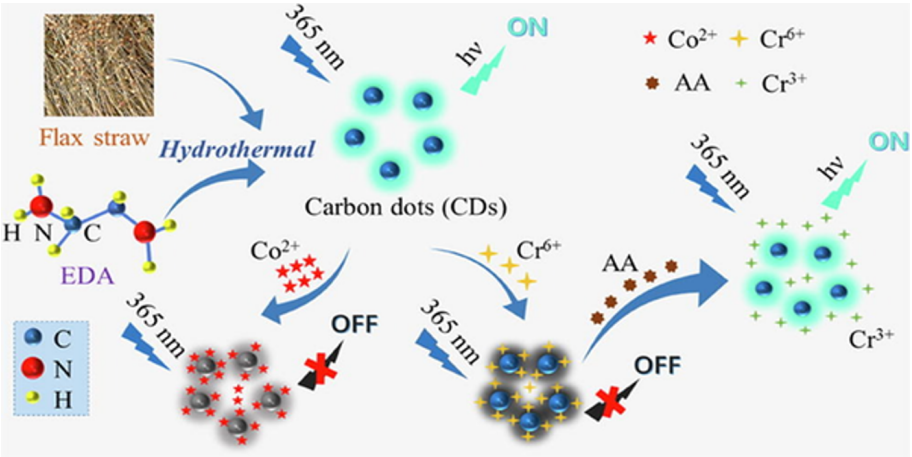


Figure 15: Schematic illustration of the CD synthesis from flax straw and the detection of Co^{2+}, Cr^{6+}, and AA. Figure 15 was reprinted from [87], Journal of Colloid and Interface Science, vol. 579, by G. Hu; L. Ge; Y. Li; M. Mukhtar; B. Shen; D. Yang; J. Li, "Carbon dots derived from flax straw for highly sensitive and selective detections of cobalt, chromium, and ascorbic acid", pages 96-108, Copyright Elsevier (2020), with permission from Elsevier. This content is not subject to CC BY 4.0.

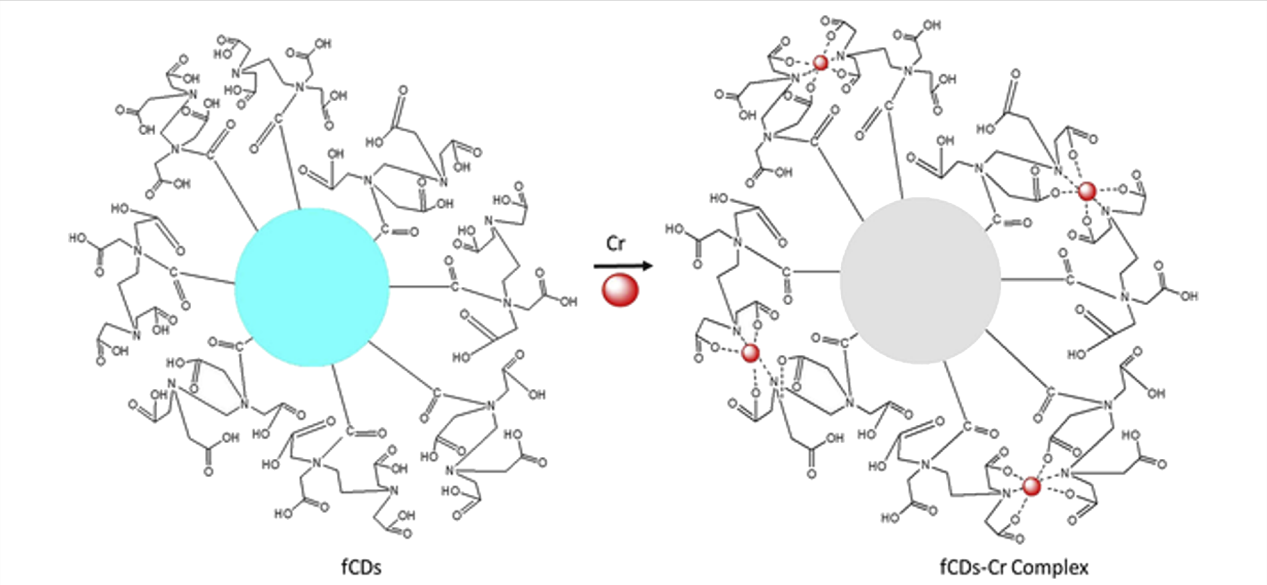


Figure 16: Proposed mechanism of chromium sensing with f-CDs. Figure 16 was reprinted from [83], Sensors and Actuators B: Chemical, vol. 283, by P. D.; L. Singh; A. Thakur; P. Kumar, "Green synthesis of glowing carbon dots from *Carica papaya* waste pulp and their application as a label-freechemo probe for chromium detection in water", pages 363-372, Copyright Elsevier (2019), with permission from Elsevier. This content is not subject to CC BY 4.0.

sensitive. High pH values resulted in decreased fluorescence, with a linear pattern in the range of 3–8. They also showed selectivity and sensitivity towards Co^{2+} ions (LOD = 0.39 μmol·L^{-1}) with an immediate color change from transparent to yellowish-brown. The fluorescence was found to be quenched linearly with increasing concentration of Co^{2+} ions. A good spectral overlap of the absorption spectra of the metal ions and emission spectra of the CDs suggested IFE or FRET to be in action. However, the fluorescence lifetime decay data was the same with and without metal ions, which suggested that the FRET mechanism was not possible. Thus, IFE was the predicted mechanism for the quenching process [153].

Au^{3+} ion sensing

Gold is a widely used noble metal in catalysis and medicine. However, it induces harmful effects in the human body and other biological systems owing to its strong affinity and reactivity towards DNA and some enzymes. The adverse effects include deterioration of the peripheral nervous system, nephrotoxicity, and liver damage [114,115].

Arumugam et al. reported CDs synthesized from denatured sour milk and used them to detect gold ions by simply mixing the aqueous dispersion of CDs with ascorbic acid (AA). The addition of Au^{3+} did not disturb the fluorescence intensity of CD, which ruled out the possibility of reduced electron transfer or metal ion-induced aggregation. In the current case, the CD/AA system fluorescence quenching can be attributed to the AA-mediated reduction of Au^{3+} to AuNPs and ensuing IFE or FRET. The LOD obtained by the said system was approximately 0.95 μM [19].

Ramanan et al. also designed a sensor for Au^{3+} from waste expanded polystyrene (EPS). A detailed exploration suggests that PL quenching is because of "coordination-induced aggregation" (Figure 17). The LOD and linear range obtained were 53 nM and 0 to 35 μM, respectively [154].

As^{3+} ion sensing

Arsenic toxicity manifests itself by disrupting cellular energy pathways, where arsenic deactivates enzymes. It also adversely affects DNA synthesis and repair. Arsenic poisoning is associated with nausea, vomiting, and diarrhea. The allowed limit of Ar^{3+} in drinking water is 10 μg·L^{-1}, as recommended by WHO.

Prickly pear cactus-based surface-passivated CDs were reported by Radhakrishnan et al. using a hydrothermal method. The synthesized CDs exhibited a turn-off response to As^{3+} and ClO^{-}. Glutathione was used a surface-passivating agent that contains various functional groups. The resulting CDs have a negative charge due to the presence of –COOH, –C=O, and –OH groups and, hence, efficiently chelate the As^{3+} ions, quenching fluorescence through IFE (Figure 18) [156].

Ramezani et al. synthesized CDs to detect As^{3+} by using quince fruit (*Cydonia oblonga*) as a green source. Determination of As^{3+} is based on its oxidation by MnO^{4-}. Oxidants, such as $KMnO_4$, are reported to generate holes in CD. This process

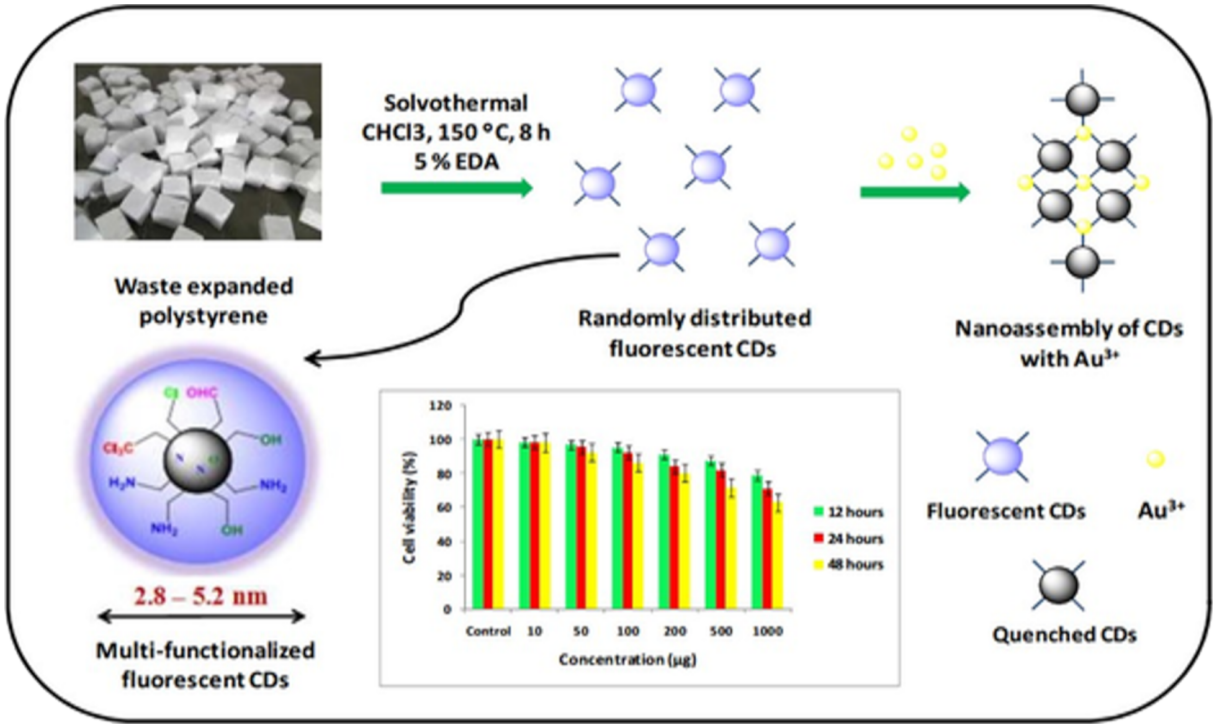


Figure 17: Highly luminescent, multi-functionalized, cell-viable CDs were prepared from waste expanded polystyrene and demonstrated as an efficient probe for Au^{3+} sensing. Reprinted with permission from [154], Copyright 2020 American Chemical Society. This content is not subject to CC BY 4.0.

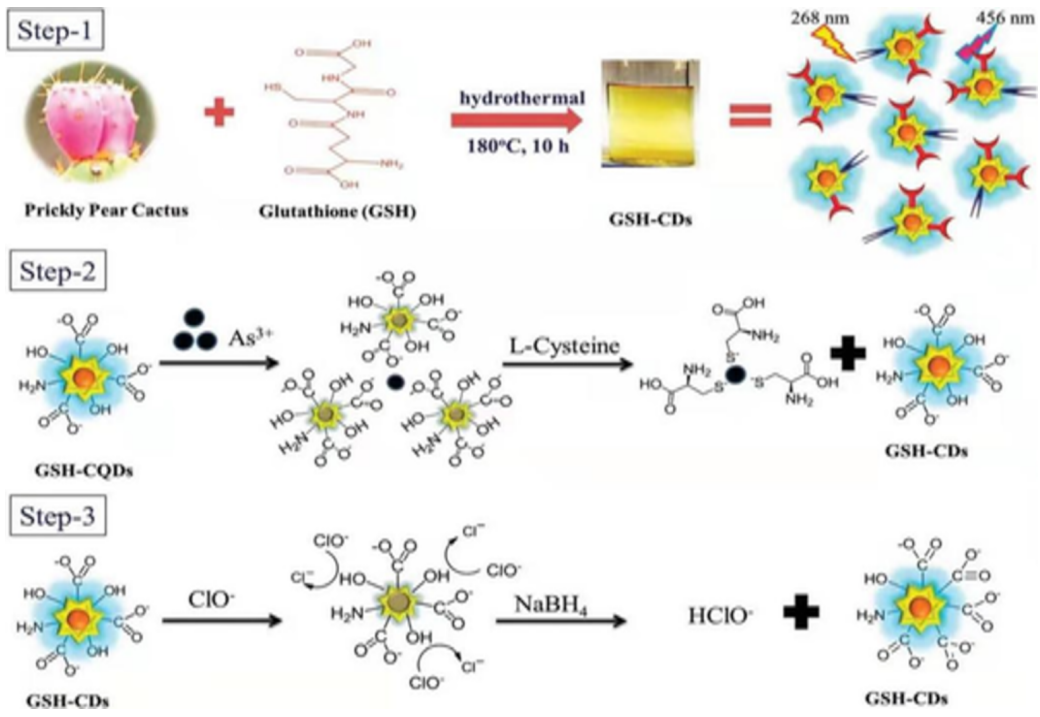


Figure 18: Schematic illustration of the design and working principle of prickly pear cactus-based CDs. Reproduced from [156] ("Green synthesis of surface-passivated carbon dots from the prickly pear cactus as a fluorescent probe for the dual detection of arsenic(iii) and hypochlorite ions from drinking water ", © 2018 K. Radhakrishnan et al., published by The Royal Society of Chemistry, distributed under the terms of the Creative Commons Attribution 3.0 Unported License, https://creativecommons.org/licenses/by/3.0/).

rises the number of holes in the CDs and increases electron–hole annihilation. As a result, the energy release in the form of chemiluminescence (CL) emission and fluorescence quenching at the maximum emission wavelength of CDs was obtained. Adding As^{3+} to MnO^{4-} before mixing with CD increases photoluminescence compared to solely permanganate. This increase was linear with As^{3+} concentration in the range of 0.1 to 2 $\mu g \cdot L^{-1}$ [155].

Ag+ ion sensing

Cryptococcus podzolicus-based blue fluorescent CDs exhibited remarkable selectivity and sensitivity towards Ag^+, 2,4-dinitrophenol, and 4-nitrophenol. It was established that a static quenching mechanism dominated when Ag^+ was added to the fluorescent CDs, whereas IFE dominated with 2,4-dinitrophenol and 4-nitrophenol. The absorption spectra of the CDs were different with and without Ag^+, indicating the formation of a new compound. Hence, static quenching could be predicted. No change was detected in the absorption spectra of CDs with or without 2,4-dinitrophenol and 4-nitrophenol, and, hence, no SQ could occur. The absorption bands of the nitrophenols overlapping with the excitation spectra condoned the inference that IFE might be the possible quenching mechanism [158]. Table 6 shows the color of various green source-derived CDs, their fluorescence under UV light, LOD, linear range, and sensing strategies for different metal ions.

Applications in bioimaging, detection, sensing, and viability studies

Agriculture is a backbone of various industries and aimed to feed people and animals. Plant pathogens result in huge economic losses by deteriorating the quality and quantity of the produce. To devise the best disease management strategies under greenhouse and open field conditions, accurate and rapid identification of plant pathogens is the first important step. Traditional disease diagnostic methods and a few latest technologies, such as quantitative polymerase chain reaction (Q-PCR), are expensive, time-consuming, and lack high sensitivity. In recent years, engineered nanoparticles are getting more attention due to their wide application spectra [164]. CDs, due to their smaller size, non-toxicity, biocompatibility, water-solubility [165], synthesized from organic waste matter are exten-

Table 6: Green CDs used for sensing metal ions, against their limit of detection, linear ranges, and sensing strategy.

No.	Source	Color under UV light	Sensing	Source of analyte	LOD	Linear range	Sensing strategy	Ref
1	*Boswellia ovalifoliolata*	blue	Fe^{3+}	simulated water sample	0.41 μM	up to 500 μM	fluorometry	[138]
2	*Citrus limetta*	blue	Fe^{3+}	simulated water sample	19.8 ppb	50–100 ppb	fluorometry	[139]
3	betel leaves	blue	Fe^{3+}	simulated water sample	50 nM	50–150 nM	fluorometry	[140]
4	*Miscanthus grass*	blue	Fe^{3+}	simulated water sample	20 nM	0.02 to 2000 mM	fluorometry	[141]
5	*Ananas comosus*	blue/green/ yellow	Fe^{3+}	urine, drugs, and plasma	0.03 μM	0.05–500 μM	fluorometry	[85]
6	*Bauhinia flower*	blue	Fe^{3+}/ATP	tap water and human serum	0.01 μM/ 0.005 μM	10–350 μM/ 0.01 to 450 μM	fluorometry	[104]
7	*Prunus cerasifera*	blue	Fe^{3+}	simulated water sample	—	0–0.5 mM	fluorometry	[49]
8	*Borassus flabellifer*	blue	Fe^{3+}	simulated water sample	10 nM	0 to 30 nM	fluorometry	[59]
9	watermelon juice	blue	Fe^{3+}/cys	simulated water sample	0.16 μM/ 0.27 μM	0–300 μM/ 0–250 μM	fluorometry	[16]
10	grape and onion	–	Fe^{3+}	tap water and river water	0.1 mM	4.6–160 mM	colorimetry	[159]
11	starch	green	Fe^{3+}	waste water treatment plant, lake water and tap water	3.2 nM	0.01 to 16 μM	fluorometry	[160]
12	*Aloe vera*	blue	Fe^{3+}	simulated water sample	33 ppb	70 ppb–10 ppm	fluorometry	[67]
13	*Magnolia liliiflora*	blue	Fe^{3+}	simulated water sample	1.2 μM	1–1000 μM	fluorometry	[103]

Table 6: Green CDs used for sensing metal ions, against their limit of detection, linear ranges, and sensing strategy. (continued)

14	*Catharanthus roseus*	green	Fe^{3+}	simulated water sample	—	0 to 0.4 μg·L^{-1}	fluorometry	[161]
15	*Lonicera maackii*	green	Fe^{3+}	tap water and urine samples	0.08 μM	0.1–10 μM	fluorometry	[107]
16	crop biomass	blue	Fe^{3+}	—	—	0–500 μM	fluorometry	[77]
17	cornstalk	blue	Fe^{2+} and H_2O_2	simulated water sample	0.18 μM and 0.21 μM	0 to 18.0 μM (Fe^{3+})	fluorometry	[25]
18	china grass carp scales	blue	Hg^{2+}	lake water	0.014 μM	0.014–30 μM	fluorometry	[142]
19	citrus lemon juice	blue	Hg^{2+}	tap water and packed water sample	5.3 nM	0.01 to 0.05 mM	fluorometry	[143]
20	*Prosopis juliflora*	blue	Hg^{2+}/chemet	river, waste water samples from saponification company and petrochemical company, and serum samples	1.26 ng·mL^{-1}/ 1.4 ng·mL^{-1}	5–500 ng·mL^{-1} and 2.5–22.5 ng·mL^{-1}	fluorometry	[23]
21	orange juice	blue	Hg^{2+}	tap water	—	0.0–32.0 μM	fluorometry	[17]
22	*Dunaliella salina*	blue	Hg^{2+}/Cr^{2+}	distilled water	0.018 μM	0.03–0.20 μM/ 0.03–0.18 μM)	fluorometry	[109]
23	*Hongcaitai*	blue	Hg^{2+}/ClO^-	tap water, river water	0.06 μM/ 0.015 μM	0.2–15 μM/ 0.05–15 μM	fluorometry	[65]
24	highland barley	blue	Hg^{2+}	simulated water sample	0.48 μM	10–160 μM	fluorometry	[89]
25	*Gardenia fruit*	blue	Hg^{2+}/Cys	simulated water sample	320 nM/ 271 nM	2–20 μM/ 0.1–2.0 μM	fluorometry	[53]
26	polyolefin residues	green	Cu^{2+}	bottled mineral water and tap water	6.33 nM	1–8.0 M	fluorometry	[144]
26	banana juice	blue	Cu^{2+}	simulated water sample	0.3 μg·mL^{-1}	1–800 μg·mL^{-1}	fluorometry	[162]
27	radish	blue	Cu^{2+}, acetic acid vapors	tap water and river water	0.16 μM/ 15.5%	—	fluorometry, optical electronic nose	[145]
28	*Eleusine coracana*	blue	Cu^{2+}	tap and river water	10 nM	0 to 100 μM	fluorometry	[146]
29	lily bulbs	blue	Cu^{2+}	tap water and lake water	12.8 nM	0.05–2.0 μM	fluorometry	[108]
30	white pepper	green	coenzyme A, Cu^{2+}	pig liver samples	8.75 nM	0–150 μM	fluorometry	[86]
31	coconut coir	blue	Cu^{2+}, Cd^{2+}	deionized water, tap water, sewage water, and ground water	0.28 nM/ 0.18 nM	0.28–0.93 nM/ 0.18–0.61 nM	fluorometry	[51]
32	*Murraya koenigii*	blue	Cd^{2+}	tap water and pond water	0.29 nM	0.01–8 μM	fluorometry	[72]
33	rice husks	green	Cd^{2+}	simulated water sample	—	—	fluorometry	[147]
34	oyster mushroom (*Pleurotus species*)	green	Pb^{2+}	simulated water sample	58.63 μM	10–200 μM	colorimetry	[157]
35	*Ocimum sanctum*	green	Pb^{2+}	pond water, tap water and mineral water	0.59 nM	0.01–1.0 M	fluorometry	[163]

Table 6: Green CDs used for sensing metal ions, against their limit of detection, linear ranges, and sensing strategy. (continued)

36	table sugar	blue	Pb^{2+}	tap water, well water and lake	67 nM	—	turbidimetry	[84]
37	denatured milk	blue	Cr^{6+}	drinking water	14 μM	—	fluorometry	[148]
38	*Hibiscus sabadariffa*	blue	Cr^{6+}	simulated water sample	—	—	fluorometry	[52]
39	*Groundnuts*	—	Cr^{6+}	simulated water sample	0.1 ppm (1.9 μM)	—	fluorometry	[149]
40	jute caddies	blue	Cr^{6+}/AA	tap water	0.03 μM	1–140 μM	fluorometry	[150]
41	luffa sponge	green	Cr^{6+}	tap water	—	—	fluorometry	[151]
42	tulsi leaves	blue	Cr^{6+}	tap water	4.5 ppb	1.6 to 50 μM	fluorometry	[152]
43	flax straw	blue	Co^{2+}/Cr^{6+}/ AA	tap water, river water	0.38/0.19/ 0.35 μM	0–500/0.5–80/ 0–200 μM	fluorometry	[87]
44	rice fried *Codonopsis pilosula* (CP)	blue	Cr^{6+}	river, tap and lake water	15 nM	0.03–50 μM	fluorometry	[74]
45	*Carica papaya*	blue	Cr^{3+}, Cr^{6+}	ground, tap and well water	0.708 ppb	10–1000 ppb	fluorometry	[83]
46	kelp	blue	Co^{2+}	river water	0.39 μM	1–200 μM	fluorometry	[153]
47	denatured sour milk	blue	Au^{3+}	drinking water	0.95 μM	10–150 μM	fluorometry	[19]
48	waste expanded polystyrene	blue	Au^{3+}	mineral water, tap water, pond, lake and sea water	53 nM	0 to 35 μM	fluorometry	[154]
49	prickly pear cactus	blue	As^{3+}/ClO^{-}	pond, river and industrial waste water	2.3 nM/ 0.016 μM	2–25 nM/ 10–200 μM	fluorometry	[156]
50	quince fruit (*Cydoniaoblon*)	blue	As^{3+}	tap water	0.04 μg·mL^{-1}	0.1 to 2 μg·L^{-1}	fluorometry	[155]
51	*Cryptococcus Podzolicus*	blue	Ag^{+}/ (2,4-DNP)/ (4-NP)	tap water, river water and waste water	113.57 nM/ 73.36 nM/ 86.47 nM	0–15 μM/ 0–30 μM/ 0–37.5 μM	fluorometry	[158]

sively applied in different sectors such as wastewater sensors, switches, agro-fertilizers [166], as bactericides, fungicides, and nanoscale fertilizers [167]. Anand et al. published a mini-review in which they highlighted the utilization and potential of CDs in biosensing, nanomedicine, photo-catalysis, bioimaging, and as antimicrobial agents [168].

Recent reports on the utilization of CDs in bioimaging [26,123], sensing [57,106], and catalysis [27,96] have gained the attention of the scientific community. The use of fluorescence techniques in imagining microorganisms has gained much popularity to study the structure and state of microorganisms. This study is helpful for microbial quantification, viability testing, and Gram-type identification of microorganisms [43]. Various recent reports are available on the successful utilization of green CDs in bioimaging of bacterial strains such as *Escherichia coli*, *Staphylococcus aureus* [169], *Pseudomonas aeruginosa* and fungal cells of *Fusarium avenaceum* [170], *Bacillus subtilis* and fungus *Aspergillus aculeatus* [171], and other fungal agents such as *Fomitopsis* spp. [48] and yeast cells [94].

Kasibabu et al. [170] prepared fluorescent CDs from pomegranate fruits and successfully used them in bioimaging of *P. aeruginosa* and *F. avenaceum*. In a similar study, Atchudan et al. [94] synthesized N-CDs from *Chionanthus retusus* fruit extract and used them as a biological probe to study *Candida albicans* and *Cryptococcus neoformans* under a fluorescence microscope. Wang et al. [15] synthesized CDs from papaya and used them as a probe for fluorescence sensing of *Escherichia coli* bacteria. Amphiphilic CDs are used for microbial monitoring. A research study [172] successfully manipulated these CDs for the detection of bacteria.

Microbial viability testing is carried out in microbial monitoring, detection, and antibiotic development. Usually, the plate count method is employed, which is laborious and time-consuming. Newly developed technologies such as surface-enhanced Raman scattering [173] and Fourier-transform infrared spectroscopy [174] are more accurate than conventional plate counting. However, they are costly, time-consuming, and require more expertise. In contrast, the use of CDs as probes for

microbial viability testing has opened new research dimensions. Bacteria-derived and yeast extract-based CDs probes have been successfully employed in microbial viability testing, which has broadened their applications in bio-medical sciences [141,142].

Gram staining is a very basic technique used to identify the bacterial types Gram-positive and Gram-negative. This is important to choose which type of antibiotics can be used to treat a bacterial infection. The traditional Gram staining procedure is laborious and can also produce false-positive results [175,176]. The use of fluorescent CDs in Gram-type identification is more accurate and rapid. In a study, vancomycin-conjugated CDs were employed to identify Gram-positive *S. aureus* and many other bacteria [177].

Atchudan et al. [94] utilized the hydrothermal carbonization technique to prepare N-CDs from the fruit extract of *Chionanthus retusus*. The N-CDs showed strong fluorescence properties and low cytotoxicity and were used in metal ion detection. The prepared N-CDs, due to their water solubility, cell permeability, high fluorescence, and low cytotoxicity, were employed in various biomedical applications. Furthermore, these N-CDs were used as biological probes to obtain fluorescent microscopy images of yeast infection in living samples. Bhamore et al. [48] obtained multicolor emitting CDs from *Manilkara zapota* fruits. Due to no cytotoxicity and strong biocompatibility, these CDs were effectively employed in the bioimaging of various bacterial and fungal cells.

In a similar study, Pal et al. [92] prepared surface-passivated CDs (CDPs) from the curcumin plant. Due to their smaller cytotoxicity, these CDP were successfully used in the biolabeling of cancer cells. The prepared CDPs were also applied in the bioimaging of Zebrafish embryos. Fluorescent N-CDs were prepared from the extracts of *Hylocereus undatus* and were characterized by using different methods [93]. The prepared N-CDs displayed less cytotoxicity and good biocompatibility on L-929 and MCF-7 cells and showed promising catalytic potential towards the reduction of methylene blue. Luminous CDs displaying less cytotoxicity and strong biocompatibility were prepared from apple juice and were successfully employed in the bioimaging of various bacterial and fungal cells [178]. In another study of Zhang et al. [116], urine-based CDs (UCDs) and hydrothermally treated urine CDs (HUCDs) were synthesized by utilizing a simple sephadex filtration procedure and a hydrothermal reaction approach. The prepared UCDs and HUCDs were used for in vivo and in vitro bioimaging of cells and displayed good biocompatibility and no toxicity to normal rat kidney cells.

CDs have become an attractive materials class for killing pathogenic microbes, including bacteria [179-181], and viruses [182]. Positively charged CDs interact with the negatively charged surface of bacteria, resulting in bacterial cell death by damaging the bacterial cell surface. In addition to these CDs, antimicrobial cationic CDs and negatively charged CDs also showed antibacterial potential [144]. Fungus-derived photosensitizer-conjugated CDs such as MCDs were successfully employed to kill bacterial agents [138].

Despite great potential, only a few reports are available on the extensive application of nanoscale carbon materials in plant disease control. In a research study by Han et al. [28], cow milk-derived CDs were synthesized, which showed promising antibacterial efficacy against *Staphylococcus aureus* and *E. coli* bacteria. Surendran et al. [101] prepared fluorescent CDs from natural honey by using a hydrothermal method. The spherical shape of the CDs was determined by XRD and HRTEM, while the presence of nitrogen and sulfur atoms was confirmed using FTIR and XPS analysis. For the first time, self-defocusing nonlinearity and strong nonlinear characteristics were identified by using the Z-scan. These CDs showed antimicrobial potential against foodborne pathogens in vitro. Similarly, CdS CDs were prepared from the leaf extract of *Camellia sinensis* and found to possess strong antibacterial potential against different bacterial strains [183]. These CdS-CDs also showed cytotoxicity against A549 cancer cells and the results were comparable to those of the standard drug cisplatin. These CDs inhibited the cancer cell growth by encountering with the cells during the S phase of the cell cycle and they also produced high-contrast fluorescence images of A549 cancer cells.

Recently, Das et al. [14] utilized jute industry waste to prepare fluorescent surface-quaternized CDs (JB-CDs) with high water solubility and photostability. These were successfully used in the biosensing of chromium ions in water. Furthermore, JB-CDs displayed significant growth inhibition of *E. coli* and *S. aureus*. These JB-CDs also exhibited a pH-responsive release of ciprofloxacin at pH 7.4. In another study of Boobalan et al. [157], fluorescent blue/green CDs were synthesized from *Pleurotus* species and were reported to display the potential of metal ion detection. These CDs showed promising applications as a fluorescent probe for DNA detection and showed effective antibacterial potential against *S. aureus*, *K. pneumoniae*, and *P. aeruginosa*. These CDs also displayed anticancer potential against breast cancer cells.

In a similar study, CDs were prepared from *Lawsonia inermis* plant by employing a low-cost hydrothermal method and these were found to be effective antibacterial agents against various Gram-positive and Gram-negative bacterial strains [184]. In

another study of Yallappa et al. [185], nanoscale carbons (NCs) with strong fluorescent potential and biocompatibility were prepared from the waste groundnut shells. The biocidal potential of these NCs was tested against *Escherichia coli*, *Chromobacterium violaceum,* and *Bacillus cereus.* The NCs were found to possess strong antibacterial potential. Another study highlighted the promising bioimaging and antibacterial potential of fluorescent CDs [186]. CDs were prepared from sugarcane bagasse and were characterized by employing various techniques. The findings showed excellent antibacterial efficacy of the CDs against numerous Gram-positive and Gram-negative bacterial strains.

Das et al. [14] prepared CDs (KLB-CDs) from seaweed-derived κ-carrageenan and lemon juice, which showed promising water solubility, upconversion photoluminescence, and photostability. These KLB-CDs were successfully used as a biosensor for the detection of chromium and showed antibacterial potential against *E. coli*. Devi et al. [67] employed a one-step pyrolysis approach for the preparation of CDs from *Aloe vera*. The CDs displayed excellent biosensing and antibacterial potential. CDs derived from *Artemisia argyi* leaves showed selective antibacterial efficacy [187]. These CDs showed remarkable biocidal activity against Gram-negative bacteria by disturbing the bacterial enzymatic secondary structures and activities of cell wall-related enzymes, whereas they were less effective against Gram-positive bacteria.

Applications in controlling phytopathogens and plant growth promotion

CDs with high hydrophilicity and high cell permeability are frequently applied in various biological applications. The antimicrobial application of CDs from green synthesis is less explored. Recently, CDs prepared from pomegranate and watermelon peel were evaluated against *Fusarium oxysporum*, *Staphylococcus aureus*, *Pseudomonas aeruginosa*, *Bacillus subtilis*, and *Escherichia coli*. The pomegranate-based CDs showed antibacterial and antifungal potential [188]. In another relevant study of Wang et al. [189], N-CDs synthesized from the roots of *Moringa oleifera* showed inhibitory effects against *Corynespora cassiicola* and *Phytophtora nicotianae*. In recent years, antimicrobial potential of CDs prepared from green synthesis were reported by many other researchers [190-192]. This could reduce the dependency on toxic synthetic compounds to control the pathogens [79].

CDs have been successfully employed in agriculture to enhance plant growth and produce of the crop. It was revealed that CDs being structurally similar to plant-hormones increased the activity of RuBisCO and liberated CO_2. The CDs served as a fuel for anabolic photosynthetic pathways in rice plants [193]. It was revealed that the application of carbon-based nanomaterials enhanced the cell culture growth in tobacco and increase seed germination and plant growth in tomato seedlings [194].

In a similar study, the effect of water-soluble CDs on wheat plants was tested both under dark and light conditions. The application of these CDs supports the uptake of nutrients and water and significantly enhances the root and shoot growth [195]. Growth promotion behavior of CDs was also studied well in Rome lettuce [196], *Morus alba* [197], soybeans (*Glycine max*), and tomatoes (*Solanum lycopersicum*). The CDs have a wide application window and low toxicity effects and, hence, can be employed to get better crop production. The role of nanomaterials in microbial bioimaging, detection, sensing, viability testing, microbial control, and plant growth promotion is presented in Table 7.

Critical appraisal, future perspectives, and challenges

(1) Inconsistencies were observed in different synthesis procedures for CDs regarding size distribution and PL properties. Furthermore, low yield and prolonged purification restraint the applications. Effective synthesis strategies need to be devised to elevate the quantum yields with small size distribution. A further investigation into the non-uniformity of physical properties of CDs is required to unveil their true nature and explore their potentiality.

(2) The synthesis and purification methods are time-consuming, and the CDs exhibit rather high detection limits and low sensitivity, which need to be addressed. Some of the functional groups on the surface of CDs interfere with their sensitivity towards various metal ions and, hence, may show response towards more than one metal ion, rendering them less sensitive towards a specific metal ion.

(3) A complete understanding of the PL phenomena (multiphoton emissions) calls for attention, which would pave way for multifaceted applications. The PL quenching mechanisms are not clear and have been assigned mostly based on assumptions and hypotheses due to incomplete information. An approach based on theoretical calculations coupled with experimental results could help in getting a clearer picture of the actual phenomena.

(4) Efforts are required to tune the PL emissions to higher wavelengths than green and blue. So far, mostly blue and green emissions in green source-derived CDs have been reported.

(5) To promote stability and in attempt to achieve emission at longer wavelengths, doping with various reagents is performed.

Table 7: Green sources, methods of preparation, and applications of CDs synthesized from different sources.

S. No	Source	Method of preparation	Application	Ref
1	*Escherichia coli*	hydrothermal synthesis process	imaging and detection of p-nitrophenol	[198]
2	tulsi leaves	one step hydrothermal process	Cr sensor, bioimaging and as a patterning agent	[152]
3	apple juice	one step hydrothermal process	bioimaging of mycobacterium and fungal cells	[178]
4	*Cannabis sativa*	one-step pyrolysis method	antibacterial activity	[199]
5	wheat straw	hydrothermal treatment	labeling, imaging, and sensing	[200]
6	*Lycii fructus*	one step hydrothermal process	detection of phoxim in environmental and fruit samples	[201]
7	cow milk	hydrothermal treatment	antibacterial activity	[28]
8	coriander leaves	one-step hydrothermal treatment	antioxidants, biosensors and bioimaging	[26]
9	tamarind and calf thymus DNA	–	antimicrobial potential, cytotoxicity, and DNA binding	[202]
10	rapeseed pollen	one-step hydrothermal treatment	bioimaging and plant growth promotion	[196]
11	natural honey	hydrothermal treatment	photonic and antibacterial activity	[101]
12	*Chionanthus retusus*	hydrothermal-carbonization method	metal ion sensing and biological activities	[94]
13	mushroom	hydrothermal-carbonization method	metal ion detection, antibacterial and anticancer activities	[157]
14	nitrogenase extracted from Azotobacter	–	improvements in nitrogen fixation ability of *Azotobacter chroococcum*	[203]
15	*Actinidia deliciosa*	one-step hydrothermal treatment	catalytic activity and cytotoxicity applications	[204]
16	chicken egg whites	one-step heating reaction	sensing of bacteria and curcumin	[169]

This increases cytotoxicity and compromises the biocompatibility, rendering the CDs less suitable for biological applications. Alternative ways to achieve the aforementioned objectives need to be investigated.

(6) Green synthesis of CDs has opened many ways to explore their application in a variety of fields. So far, these green source CDs, due to their cost-effectiveness, biocompatibility, and low toxicity, are extensively employed in the detection of metal ions, biosensing, bioimaging, and as antibacterial and antifungal agents in biomedical sciences. In other major sectors such as agriculture, the potential role of green CDs has not yet been explored and only a few studies are available. Crops are attacked by various notorious phytopathogens including viruses, bacteria, fungi, and nematodes. These phytopathogens could result in devastating crop yield and economic losses. The extensive application of synthetic pesticides is a major threat to humans, animals, and the environment. Extensive testing and utilization of green source CDs in phytopathogen detection, bioimaging, and as biocontrol agents could provide an environmentally friendly alternative to synthetic agrochemicals.

(7) Very limited information is available on the interaction mechanisms and impact of CDs on the soilborne microbes beneficial for plants. A few reports have highlighted the positive impact of CDs on the soil microbiome. However, exposure to CDs may also harm the beneficial microbes and their nutrient recycling activities. However, the mechanism of toxicity is not well elaborated. It is important to explore the fate and effects of CDs under the relevant environmental conditions to incorporate them into agricultural systems.

(8) Easy, efficient, inexpensive, and sustainable strategies need to be explored with main focus on biocompatibility and low cytotoxicity for biomedical diagnostics and therapeutic applications.

(9) Structural characteristics of the CDs need to be unfolded to fully understand and exploit their applications in bioimaging and other biological applications.

(10) CDs derived from green sources mostly have low cytotoxicity. Therefore, their potential applications in areas such as

drug delivery, radiation prevention, and early detection of illnesses need to be extensively investigated, as there is little to no work available. Similarly, no work is reported on the use of CDs in photodynamic and photothermal therapy.

Conclusion

Since the discovery of carbon dots in 2004, there has been extensive research on the synthesis, modifications, properties, and applications, because of their distinctive and tunable physicochemical, optical, and electronic properties. We have attempted to review the recent advances in the field focusing on the synthesis of CDs from various green sources, their applications as sensing probes, in addition to their biological applications. Carbon dots prepared through green synthesis processes display multifaceted characters and broad-spectrum applications. Due to inexpensiveness and the low toxicity, CDs are widely employed in sensing and various biological applications, such as microbial bioimaging, detection, and viability studies as well as in pathogen inhibition and plant growth promotion. Their features make CDs ideal to be used in biological and other disciplines such as bioimaging, cancer therapy, gene and drug delivery, sensors and biosensors, catalysts, and energy applications. Regarding the green synthesis of CDs, there is a dire need to improve and standardize the synthesis mechanisms to obtain a high yield of CDs. Also mechanisms of quenching need to be investigated more. So far, applications of CDs in phytopathology are very limited. Wide experimental testing and research is needed to explore their natural potential in controlling notorious plant pathogens and plant growth promotion. Moreover, in medical science, there is a broad window to improve their efficiency and utilization in the early detection of diseases and in maintaining public health.

Funding

The authors are grateful for the financial support from Key Research and Development Program of Guangxi, China (GuikeAB18050026), China Postdoctoral Science Foundation (2017M613047), Natural Science Foundation of Shaanxi Province (No. 2020JQ-406), and the Fundamental Research Funds for the Central Universities (GK202205013).

References

1. Xu, X.; Ray, R.; Gu, Y.; Ploehn, H. J.; Gearheart, L.; Raker, K.; Scrivens, W. A. *J. Am. Chem. Soc.* **2004,** *126,* 12736–12737. doi:10.1021/ja040082h
2. Sun, Y.-P.; Zhou, B.; Lin, Y.; Wang, W.; Fernando, K. A. S.; Pathak, P.; Meziani, M. J.; Harruff, B. A.; Wang, X.; Wang, H.; Luo, P. G.; Yang, H.; Kose, M. E.; Chen, B.; Veca, L. M.; Xie, S.-Y. *J. Am. Chem. Soc.* **2006,** *128,* 7756–7757. doi:10.1021/ja062677d
3. Iravani, S.; Varma, R. S. *Environ. Chem. Lett.* **2020,** *18,* 703–727. doi:10.1007/s10311-020-00984-0
4. Qu, Y.; Yu, L.; Zhu, B.; Chai, F.; Su, Z. *New J. Chem.* **2020,** *44,* 1500–1507. doi:10.1039/c9nj05285b
5. Sharma, V.; Singh, S. K.; Mobin, S. M. *Nanoscale Adv.* **2019,** *1,* 1290–1296. doi:10.1039/c8na00105g
6. Jaiswal, A.; Ghosh, S. S.; Chattopadhyay, A. *Chem. Commun.* **2012,** *48,* 407–409. doi:10.1039/c1cc15988g
7. Wang, W.; Li, Y.; Cheng, L.; Cao, Z.; Liu, W. *J. Mater. Chem. B* **2014,** *2,* 46–48. doi:10.1039/c3tb21370f
8. Vedamalai, M.; Periasamy, A. P.; Wang, C.-W.; Tseng, Y.-T.; Ho, L.-C.; Shih, C.-C.; Chang, H.-T. *Nanoscale* **2014,** *6,* 13119–13125. doi:10.1039/c4nr03213f
9. Fang, L.; Zhang, L.; Chen, Z.; Zhu, C.; Liu, J.; Zheng, J. *Mater. Lett.* **2017,** *191,* 1–4. doi:10.1016/j.matlet.2016.12.098
10. Schneider, J.; Reckmeier, C. J.; Xiong, Y.; von Seckendorff, M.; Susha, A. S.; Kasák, P.; Rogach, A. L. *J. Phys. Chem. C* **2017,** *121,* 2014–2022. doi:10.1021/acs.jpcc.6b12519
11. Liu, F.; Zhang, W.; Chen, W.; Wang, J.; Yang, Q.; Zhu, W.; Wang, J. *Chem. Eng. J.* **2017,** *310,* 187–196. doi:10.1016/j.cej.2016.10.116
12. Shinde, D. B.; Pillai, V. K. *Chem. – Eur. J.* **2012,** *18,* 12522–12528. doi:10.1002/chem.201201043
13. Joseph, J.; Anappara, A. A. *ChemPhysChem* **2017,** *18,* 292–298. doi:10.1002/cphc.201601020
14. Das, P.; Ganguly, S.; Bose, M.; Ray, D.; Ghosh, S.; Mondal, S.; Aswal, V. K.; Das, A. K.; Banerjee, S.; Das, N. C. *New J. Chem.* **2019,** *43,* 6205–6219. doi:10.1039/c8nj06308g
15. Wang, N.; Wang, Y.; Guo, T.; Yang, T.; Chen, M.; Wang, J. *Biosens. Bioelectron.* **2016,** *85,* 68–75. doi:10.1016/j.bios.2016.04.089
16. Lu, M.; Duan, Y.; Song, Y.; Tan, J.; Zhou, L. *J. Mol. Liq.* **2018,** *269,* 766–774. doi:10.1016/j.molliq.2018.08.101
17. Li, Z.; Zhang, Y.; Niu, Q.; Mou, M.; Wu, Y.; Liu, X.; Yan, Z.; Liao, S. *J. Lumin.* **2017,** *187,* 274–280. doi:10.1016/j.jlumin.2017.03.023
18. Sharma, N.; Yun, K. *Dyes Pigm.* **2020,** *182,* 108640. doi:10.1016/j.dyepig.2020.108640
19. Arumugam, S. S.; Xuing, J.; Viswadevarayalu, A.; Rong, Y.; Sabarinathan, D.; Ali, S.; Agyekum, A. A.; Li, H.; Chen, Q. *J. Photochem. Photobiol., A* **2020,** *401,* 112788. doi:10.1016/j.jphotochem.2020.112788
20. Singh, A.; Eftekhari, E.; Scott, J.; Kaur, J.; Yambem, S.; Leusch, F.; Wellings, R.; Gould, T.; Ostrikov, K.; Sonar, P.; Li, Q. *Sustainable Mater. Technol.* **2020,** *25,* e00159. doi:10.1016/j.susmat.2020.e00159
21. Jayanthi, M.; Megarajan, S.; Subramaniyan, S. B.; Kamlekar, R. K.; Veerappan, A. *J. Mol. Liq.* **2019,** *278,* 175–182. doi:10.1016/j.molliq.2019.01.070
22. Wan, Y.; Wang, M.; Zhang, K.; Fu, Q.; Gao, M.; Wang, L.; Xia, Z.; Gao, D. *Microchem. J.* **2019,** *148,* 385–396. doi:10.1016/j.microc.2019.05.026
23. Pourreza, N.; Ghomi, M. *Mater. Sci. Eng., C* **2019,** *98,* 887–896. doi:10.1016/j.msec.2018.12.141
24. Sun, Y.-P.; Wang, X.; Lu, F.; Cao, L.; Meziani, M. J.; Luo, P. G.; Gu, L.; Veca, L. M. *J. Phys. Chem. C* **2008,** *112,* 18295–18298. doi:10.1021/jp8076485
25. Shi, J.; Ni, G.; Tu, J.; Jin, X.; Peng, J. *J. Nanopart. Res.* **2017,** *19,* 209. doi:10.1007/s11051-017-3888-5
26. Sachdev, A.; Gopinath, P. *Analyst* **2015,** *140,* 4260–4269. doi:10.1039/c5an00454c
27. Gu, J.; Zhang, X.; Pang, A.; Yang, J. *Nanotechnology* **2016,** *27,* 165704. doi:10.1088/0957-4484/27/16/165704

28. Han, S.; Zhang, H.; Xie, Y.; Liu, L.; Shan, C.; Li, X.; Liu, W.; Tang, Y. *Appl. Surf. Sci.* **2015,** *328,* 368–373. doi:10.1016/j.apsusc.2014.12.074
29. Sun, X.; He, J.; Yang, S.; Zheng, M.; Wang, Y.; Ma, S.; Zheng, H. *J. Photochem. Photobiol., B* **2017,** *175,* 219–225. doi:10.1016/j.jphotobiol.2017.08.035
30. Başoğlu, A.; Ocak, Ü.; Gümrükçüoğlu, A. *J. Fluoresc.* **2020,** *30,* 515–526. doi:10.1007/s10895-019-02428-7
31. Aji, M. P.; Susanto; Wiguna, P. A.; Sulhadi. *J. Theor. Appl. Phys.* **2017,** *11,* 119–126. doi:10.1007/s40094-017-0250-3
32. De, B.; Karak, N. *J. Mater. Chem. A* **2017,** *5,* 1826–1859. doi:10.1039/c6ta10220d
33. Wang, R.; Lu, K.-Q.; Tang, Z.-R.; Xu, Y.-J. *J. Mater. Chem. A* **2017,** *5,* 3717–3734. doi:10.1039/c6ta08660h
34. Yuan, F.; Li, S.; Fan, Z.; Meng, X.; Fan, L.; Yang, S. *Nano Today* **2016,** *11,* 565–586. doi:10.1016/j.nantod.2016.08.006
35. Rani, U. A.; Ng, L. Y.; Ng, C. Y.; Mahmoudi, E. *Adv. Colloid Interface Sci.* **2020,** *278,* 102124. doi:10.1016/j.cis.2020.102124
36. Shi, X.; Wei, W.; Fu, Z.; Gao, W.; Zhang, C.; Zhao, Q.; Deng, F.; Lu, X. *Talanta* **2019,** *194,* 809–821. doi:10.1016/j.talanta.2018.11.005
37. Pirsaheb, M.; Mohammadi, S.; Salimi, A. *TrAC, Trends Anal. Chem.* **2019,** *115,* 83–99. doi:10.1016/j.trac.2019.04.003
38. Zuo, P.; Lu, X.; Sun, Z.; Guo, Y.; He, H. *Microchim. Acta* **2016,** *183,* 519–542. doi:10.1007/s00604-015-1705-3
39. Zheng, X. T.; Ananthanarayanan, A.; Luo, K. Q.; Chen, P. *Small* **2015,** *11,* 1620–1636. doi:10.1002/smll.201402648
40. Zhao, A.; Chen, Z.; Zhao, C.; Gao, N.; Ren, J.; Qu, X. *Carbon* **2015,** *85,* 309–327. doi:10.1016/j.carbon.2014.12.045
41. Liu, M. L.; Chen, B. B.; Li, C. M.; Huang, C. Z. *Green Chem.* **2019,** *21,* 449–471. doi:10.1039/c8gc02736f
42. Xu, Q.; Kuang, T.; Liu, Y.; Cai, L.; Peng, X.; Sreenivasan Sreeprasad, T.; Zhao, P.; Yu, Z.; Li, N. *J. Mater. Chem. B* **2016,** *4,* 7204–7219. doi:10.1039/c6tb02131j
43. Sharma, V.; Tiwari, P.; Mobin, S. M. *J. Mater. Chem. B* **2017,** *5,* 8904–8924. doi:10.1039/c7tb02484c
44. Tejwan, N.; Saha, S. K.; Das, J. *Adv. Colloid Interface Sci.* **2020,** *275,* 102046. doi:10.1016/j.cis.2019.102046
45. Lin, X.; Xiong, M.; Zhang, J.; He, C.; Ma, X.; Zhang, H.; Kuang, Y.; Yang, M.; Huang, Q. *Microchem. J.* **2021,** *160,* 105604. doi:10.1016/j.microc.2020.105604
46. Meng, W.; Bai, X.; Wang, B.; Liu, Z.; Lu, S.; Yang, B. *Energy Environ. Mater.* **2019,** *2,* 172–192. doi:10.1002/eem2.12038
47. Bag, P.; Maurya, R. K.; Dadwal, A.; Sarkar, M.; Chawla, P. A.; Narang, R. K.; Kumar, B. *ChemistrySelect* **2021,** *6,* 2774–2789. doi:10.1002/slct.202100468
48. Bhamore, J. R.; Jha, S.; Park, T. J.; Kailasa, S. K. *J. Photochem. Photobiol., B* **2019,** *191,* 150–155. doi:10.1016/j.jphotobiol.2018.12.023
49. Ma, H.; Sun, C.; Xue, G.; Wu, G.; Zhang, X.; Han, X.; Qi, X.; Lv, X.; Sun, H.; Zhang, J. *Spectrochim. Acta, Part A* **2019,** *213,* 281–287. doi:10.1016/j.saa.2019.01.079
50. Liu, M. L.; Yang, L.; Li, R. S.; Chen, B. B.; Liu, H.; Huang, C. Z. *Green Chem.* **2017,** *19,* 3611–3617. doi:10.1039/c7gc01236e
51. Chauhan, P.; Dogra, S.; Chaudhary, S.; Kumar, R. *Mater. Today Chem.* **2020,** *16,* 100247. doi:10.1016/j.mtchem.2020.100247
52. Komalavalli, L.; Amutha, P.; Monisha, S. *Mater. Today: Proc.* **2020,** *33,* 2279–2285. doi:10.1016/j.matpr.2020.04.195
53. Sun, D.; Liu, T.; Wang, C.; Yang, L.; Yang, S.; Zhuo, K. *Spectrochim. Acta, Part A* **2020,** *240,* 118598. doi:10.1016/j.saa.2020.118598
54. Zulfajri, M.; Abdelhamid, H. N.; Sudewi, S.; Dayalan, S.; Rasool, A.; Habib, A.; Huang, G. G. *Biosensors* **2020,** *10,* 68. doi:10.3390/bios10060068
55. Liu, S.; Tian, J.; Wang, L.; Zhang, Y.; Qin, X.; Luo, Y.; Asiri, A. M.; Al-Youbi, A. O.; Sun, X. *Adv. Mater. (Weinheim, Ger.)* **2012,** *24,* 2037–2041. doi:10.1002/adma.201200164
56. Bhamore, J. R.; Jha, S.; Singhal, R. K.; Park, T. J.; Kailasa, S. K. *J. Mol. Liq.* **2018,** *264,* 9–16. doi:10.1016/j.molliq.2018.05.041
57. Wei, X.; Li, L.; Liu, J.; Yu, L.; Li, H.; Cheng, F.; Yi, X.; He, J.; Li, B. *ACS Appl. Mater. Interfaces* **2019,** *11,* 9832–9840. doi:10.1021/acsami.9b00074
58. Wang, C.; Shi, H.; Yang, M.; Yan, Y.; Liu, E.; Ji, Z.; Fan, J. *Mater. Res. Bull.* **2020,** *124,* 110730. doi:10.1016/j.materresbull.2019.110730
59. Murugan, N.; Sundramoorthy, A. K. *New J. Chem.* **2018,** *42,* 13297–13307. doi:10.1039/c8nj01894d
60. Hoan, B. T.; Tam, P. D.; Pham, V.-H. *J. Nanotechnol.* **2019,** 2852816. doi:10.1155/2019/2852816
61. Sahoo, N. K.; Jana, G. C.; Aktara, M. N.; Das, S.; Nayim, S.; Patra, A.; Bhattacharjee, P.; Bhadra, K.; Hossain, M. *Mater. Sci. Eng., C* **2020,** *108,* 110429. doi:10.1016/j.msec.2019.110429
62. Vasimalai, N.; Vilas-Boas, V.; Gallo, J.; de Fátima Cerqueira, M.; Menéndez-Miranda, M.; Costa-Fernández, J. M.; Diéguez, L.; Espiña, B.; Fernández-Argüelles, M. T. *Beilstein J. Nanotechnol.* **2018,** *9,* 530–544. doi:10.3762/bjnano.9.51
63. Vandarkuzhali, S. A. A.; Jeyalakshmi, V.; Sivaraman, G.; Singaravadivel, S.; Krishnamurthy, K. R.; Viswanathan, B. *Sens. Actuators, B* **2017,** *252,* 894–900. doi:10.1016/j.snb.2017.06.088
64. Eskalen, H.; Uruş, S.; Cömertpay, S.; Kurt, A. H.; Özgan, Ş. *Ind. Crops Prod.* **2020,** *147,* 112209. doi:10.1016/j.indcrop.2020.112209
65. Li, L.-S.; Jiao, X.-Y.; Zhang, Y.; Cheng, C.; Huang, K.; Xu, L. *Sens. Actuators, B* **2018,** *263,* 426–435. doi:10.1016/j.snb.2018.02.141
66. Zhai, H.; Zheng, B.; Yang, F.; Wang, M.; Xiao, D. *Anal. Methods* **2018,** *10,* 151–157. doi:10.1039/c7ay02631e
67. Devi, P.; Thakur, A.; Bhardwaj, S. K.; Saini, S.; Rajput, P.; Kumar, P. *J. Mater. Sci.: Mater. Electron.* **2018,** *29,* 17254–17261. doi:10.1007/s10854-018-9819-0
68. Kavitha, T.; Kumar, S. *Sci. Rep.* **2018,** *8,* 16269. doi:10.1038/s41598-018-34349-z
69. Devi, P.; Kaur, G.; Thakur, A.; Kaur, N.; Grewal, A.; Kumar, P. *Talanta* **2017,** *170,* 49–55. doi:10.1016/j.talanta.2017.03.069
70. Athinarayanan, J.; Periasamy, V. S.; Alatiah, K. A.; Alshatwi, A. A. *Sustainable Chem. Pharm.* **2020,** *18,* 100334. doi:10.1016/j.scp.2020.100334
71. Ramanarayanan, R.; Swaminathan, S. *Mater. Today: Proc.* **2020,** *33,* 2223–2227. doi:10.1016/j.matpr.2020.03.805
72. Pandey, S. C.; Kumar, A.; Sahu, S. K. *J. Photochem. Photobiol., A* **2020,** *400,* 112620. doi:10.1016/j.jphotochem.2020.112620
73. Chaudhary, P.; Maurya, D. K.; Yadav, S.; Pandey, A.; Tripathi, R. K.; Yadav, B. C. *Sens. Actuators, B* **2021,** *329,* 129116. doi:10.1016/j.snb.2020.129116
74. Qiu, Y.; Gao, D.; Yin, H.; Zhang, K.; Zeng, J.; Wang, L.; Xia, L.; Zhou, K.; Xia, Z.; Fu, Q. *Sens. Actuators, B* **2020,** *324,* 128722. doi:10.1016/j.snb.2020.128722

75. Shekarbeygi, Z.; Farhadian, N.; Khani, S.; Moradi, S.; Shahlaei, M. *Microchem. J.* **2020,** *158,* 105232. doi:10.1016/j.microc.2020.105232
76. Al-Hashimi, B.; Omer, K. M.; Rahman, H. S. *Arabian J. Chem.* **2020,** *13,* 5151–5159. doi:10.1016/j.arabjc.2020.02.013
77. Ding, S.; Gao, Y.; Ni, B.; Yang, X. *Inorg. Chem. Commun.* **2021,** *130,* 108636. doi:10.1016/j.inoche.2021.108636
78. Li, Z.; Wang, Q.; Zhou, Z.; Zhao, S.; Zhong, S.; Xu, L.; Gao, Y.; Cui, X. *Microchem. J.* **2021,** *166,* 106250. doi:10.1016/j.microc.2021.106250
79. Atchudan, R.; Jebakumar Immanuel Edison, T. N.; Shanmugam, M.; Perumal, S.; Somanathan, T.; Lee, Y. R. *Phys. E (Amsterdam, Neth.)* **2021,** *126,* 114417. doi:10.1016/j.physe.2020.114417
80. Sharma, N.; Sharma, I.; Bera, M. K. *J. Fluoresc.* **2022,** *32,* 1039–1049. doi:10.1007/s10895-022-02923-4
81. Atchudan, R.; Edison, T. N. J. I.; Perumal, S.; Vinodh, R.; Sundramoorthy, A. K.; Babu, R. S.; Lee, Y. R. *Colloids Surf., A* **2022,** *635,* 128073. doi:10.1016/j.colsurfa.2021.128073
82. Zhang, Q.; Tian, F.; Zhou, Q.; Zhang, C.; Tang, S.; Jiang, L.; Du, S. *Inorg. Chem. Commun.* **2022,** *140,* 109442. doi:10.1016/j.inoche.2022.109442
83. D, P.; Singh, L.; Thakur, A.; Kumar, P. *Sens. Actuators, B* **2019,** *283,* 363–372. doi:10.1016/j.snb.2018.12.027
84. Ansi, V. A.; Renuka, N. K. *Sens. Actuators, B* **2018,** *264,* 67–75. doi:10.1016/j.snb.2018.02.167
85. Gupta, D. A.; Desai, M. L.; Malek, N. I.; Kailasa, S. K. *J. Mol. Struct.* **2020,** *1216,* 128343. doi:10.1016/j.molstruc.2020.128343
86. Long, R.; Guo, Y.; Xie, L.; Shi, S.; Xu, J.; Tong, C.; Lin, Q.; Li, T. *Food Chem.* **2020,** *315,* 126171. doi:10.1016/j.foodchem.2020.126171
87. Hu, G.; Ge, L.; Li, Y.; Mukhtar, M.; Shen, B.; Yang, D.; Li, J. *J. Colloid Interface Sci.* **2020,** *579,* 96–108. doi:10.1016/j.jcis.2020.06.034
88. Mary Alex, A.; Kiran, M. D.; Hari, G.; Krishnan, A.; Jayan, J. S.; Saritha, A. *Mater. Today: Proc.* **2020,** *26,* 716–719. doi:10.1016/j.matpr.2019.12.409
89. Xie, Y.; Cheng, D.; Liu, X.; Han, A. *Sensors* **2019,** *19,* 3169. doi:10.3390/s19143169
90. Bandi, R.; Dadigala, R.; Gangapuram, B. R.; Guttena, V. *J. Photochem. Photobiol., B* **2018,** *178,* 330–338. doi:10.1016/j.jphotobiol.2017.11.010
91. Varisco, M.; Zufferey, D.; Ruggi, A.; Zhang, Y.; Erni, R.; Mamula, O. *R. Soc. Open Sci.* **2017,** *4,* 170900. doi:10.1098/rsos.170900
92. Pal, T.; Mohiyuddin, S.; Packirisamy, G. *ACS Omega* **2018,** *3,* 831–843. doi:10.1021/acsomega.7b01323
93. Arul, V.; Edison, T. N. J. I.; Lee, Y. R.; Sethuraman, M. G. *J. Photochem. Photobiol., B* **2017,** *168,* 142–148. doi:10.1016/j.jphotobiol.2017.02.007
94. Atchudan, R.; Edison, T. N. J. I.; Chakradhar, D.; Perumal, S.; Shim, J.-J.; Lee, Y. R. *Sens. Actuators, B* **2017,** *246,* 497–509. doi:10.1016/j.snb.2017.02.119
95. Arul, V.; Sethuraman, M. G. *ACS Omega* **2019,** *4,* 3449–3457. doi:10.1021/acsomega.8b03674
96. Atchudan, R.; Edison, T. N. J. I.; Aseer, K. R.; Perumal, S.; Karthik, N.; Lee, Y. R. *Biosens. Bioelectron.* **2018,** *99,* 303–311. doi:10.1016/j.bios.2017.07.076
97. Abdullah Issa, M.; Abidin, Z. Z.; Sobri, S.; Abdul-Rashid, S.; Mahdi, M. A.; Ibrahim, N. A.; Pudza, M. Y. *Chin. J. Chem. Eng.* **2020,** *28,* 584–592. doi:10.1016/j.cjche.2019.04.003
98. Issa, M. A.; Abidin, Z. Z.; Sobri, S.; Rashid, S.; Mahdi, M. A.; Ibrahim, N. A.; Pudza, M. Y. *Nanomaterials* **2019,** *9,* 1500. doi:10.3390/nano9101500
99. Putro, P. A.; Roza, L.; Isnaeni, I. *Indonesien J. Sci. Educ.* **2019,** *3,* 76. doi:10.31002/ijose.v3i2.1209
100. Tu, Y.; Wang, S.; Yuan, X.; Wei, Y.; Qin, K.; Zhang, Q.; Chen, X.; Ji, X. *Dyes Pigm.* **2020,** *178,* 108316. doi:10.1016/j.dyepig.2020.108316
101. Surendran, P.; Lakshmanan, A.; Priya, S. S.; Balakrishnan, K.; Rameshkumar, P.; Kannan, K.; Geetha, P.; Hegde, T. A.; Vinitha, G. *Nano-Struct. Nano-Objects* **2020,** *24,* 100589. doi:10.1016/j.nanoso.2020.100589
102. Xu, X.; Cai, L.; Hu, G.; Mo, L.; Zheng, Y.; Hu, C.; Lei, B.; Zhang, X.; Liu, Y.; Zhuang, J. *J. Lumin.* **2020,** *227,* 117534. doi:10.1016/j.jlumin.2020.117534
103. Atchudan, R.; Edison, T. N. J. I.; Aseer, K. R.; Perumal, S.; Lee, Y. R. *Colloids Surf., B* **2018,** *169,* 321–328. doi:10.1016/j.colsurfb.2018.05.032
104. Huang, Q.; Li, Q.; Chen, Y.; Tong, L.; Lin, X.; Zhu, J.; Tong, Q. *Sens. Actuators, B* **2018,** *276,* 82–88. doi:10.1016/j.snb.2018.08.089
105. Godavarthi, S.; Mohan Kumar, K.; Vázquez Vélez, E.; Hernandez-Eligio, A.; Mahendhiran, M.; Hernandez-Como, N.; Aleman, M.; Martinez Gomez, L. *J. Photochem. Photobiol., B* **2017,** *172,* 36–41. doi:10.1016/j.jphotobiol.2017.05.014
106. Yadav, P. K.; Singh, V. K.; Chandra, S.; Bano, D.; Kumar, V.; Talat, M.; Hasan, S. H. *ACS Biomater. Sci. Eng.* **2019,** *5,* 623–632. doi:10.1021/acsbiomaterials.8b01528
107. Bi, X.; Hou, X.; Zhang, X.; Liu, W.; Ren, G.; Xu, S.; Wang, H.; Wei, W. *ChemistrySelect* **2021,** *6,* 3729–3736. doi:10.1002/slct.202100286
108. Gu, D.; Zhang, P.; Zhang, L.; Liu, H.; Pu, Z.; Shang, S. *Opt. Mater. (Amsterdam, Neth.)* **2018,** *83,* 272–278. doi:10.1016/j.optmat.2018.06.012
109. Singh, A. K.; Singh, V. K.; Singh, M.; Singh, P.; Khadim, S. R.; Singh, U.; Koch, B.; Hasan, S. H.; Asthana, R. K. *J. Photochem. Photobiol., A* **2019,** *376,* 63–72. doi:10.1016/j.jphotochem.2019.02.023
110. Wei, Z.; Wang, B.; Liu, Y.; Liu, Z.; Zhang, H.; Zhang, S.; Chang, J.; Lu, S. *New J. Chem.* **2019,** *43,* 718–723. doi:10.1039/c8nj05783d
111. Sabet, M.; Mahdavi, K. *Appl. Surf. Sci.* **2019,** *463,* 283–291. doi:10.1016/j.apsusc.2018.08.223
112. Li, L.; Wang, X.; Fu, Z.; Cui, F. *Mater. Lett.* **2017,** *196,* 300–303. doi:10.1016/j.matlet.2017.03.112
113. Lin, R.; Cheng, S.; Tan, M. *Food Funct.* **2022,** *13,* 2098–2108. doi:10.1039/d1fo03426j
114. Dehvari, K.; Liu, K. Y.; Tseng, P.-J.; Gedda, G.; Girma, W. M.; Chang, J.-Y. *J. Taiwan Inst. Chem. Eng.* **2019,** *95,* 495–503. doi:10.1016/j.jtice.2018.08.037
115. Zhao, C.; Jiao, Y.; Hu, F.; Yang, Y. *Spectrochim. Acta, Part A* **2018,** *190,* 360–367. doi:10.1016/j.saa.2017.09.037
116. Zhang, X.-D.; Li, J.; Niu, J.-N.; Bao, X.-P.; Zhao, H.-D.; Tan, M. *Methods* **2019,** *168,* 84–93. doi:10.1016/j.ymeth.2019.04.005
117. Chakraborty, D.; Sarkar, S.; Das, P. K. *ACS Sustainable Chem. Eng.* **2018,** *6,* 4661–4670. doi:10.1021/acssuschemeng.7b03691
118. Zhou, Y.; Liu, Y.; Li, Y.; He, Z.; Xu, Q.; Chen, Y.; Street, J.; Guo, H.; Nelles, M. *RSC Adv.* **2018,** *8,* 23657–23662. doi:10.1039/c8ra03272f
119. Jia, J.; Lin, B.; Gao, Y.; Jiao, Y.; Li, L.; Dong, C.; Shuang, S. *Spectrochim. Acta, Part A* **2019,** *211,* 363–372. doi:10.1016/j.saa.2018.12.034
120. Kaur, N.; Sharma, V.; Tiwari, P.; Saini, A. K.; Mobin, S. M. *Sens. Actuators, B* **2019,** *291,* 275–286. doi:10.1016/j.snb.2019.04.039

121. Khan, Z. M. S. H.; Rahman, R. S.; Shumaila; Islam, S.; Zulfequar, M. *Opt. Mater. (Amsterdam, Neth.)* **2019,** *91,* 386–395. doi:10.1016/j.optmat.2019.03.054
122. Yu, C.; Xuan, T.; Yan, D.; Lou, S.; Hou, X.; Chen, Y.; Wang, J.; Li, H. *Sens. Actuators, B* **2017,** *253,* 900–910. doi:10.1016/j.snb.2017.07.043
123. Soni, H.; Pamidimukkala, P. S. *Mater. Res. Bull.* **2018,** *108,* 250–254. doi:10.1016/j.materresbull.2018.08.033
124. Chen, W.; Li, D.; Tian, L.; Xiang, W.; Wang, T.; Hu, W.; Hu, Y.; Chen, S.; Chen, J.; Dai, Z. *Green Chem.* **2018,** *20,* 4438–4442. doi:10.1039/c8gc02106f
125. Wen, X.; Shi, L.; Wen, G.; Li, Y.; Dong, C.; Yang, J.; Shuang, S. *Sens. Actuators, B* **2015,** *221,* 769–776. doi:10.1016/j.snb.2015.07.019
126. Zhang, Z.; Sun, W.; Wu, P. *ACS Sustainable Chem. Eng.* **2015,** *3,* 1412–1418. doi:10.1021/acssuschemeng.5b00156
127. Chen, W.; Hu, C.; Yang, Y.; Cui, J.; Liu, Y. *Materials* **2016,** *9,* 184. doi:10.3390/ma9030184
128. Ma, X.; Dong, Y.; Sun, H.; Chen, N. *Mater. Today Chem.* **2017,** *5,* 1–10. doi:10.1016/j.mtchem.2017.04.004
129. Pires, N. R.; Santos, C. M. W.; Sousa, R. R.; De Paula, R. C. M.; Cunha, P. L. R.; Feitosa, J. P. A. *J. Braz. Chem. Soc.* **2015,** *26,* 1274–1282. doi:10.5935/0103-5053.20150094
130. Wu, X.; Ma, C.; Liu, J.; Liu, Y.; Luo, S.; Xu, M.; Wu, P.; Li, W.; Liu, S. *ACS Sustainable Chem. Eng.* **2019,** *7,* 18801–18809. doi:10.1021/acssuschemeng.9b03281
131. Wang, L.; Zhu, S.-J.; Wang, H.-Y.; Qu, S.-N.; Zhang, Y.-L.; Zhang, J.-H.; Chen, Q.-D.; Xu, H.-L.; Han, W.; Yang, B.; Sun, H.-B. *ACS Nano* **2014,** *8,* 2541–2547. doi:10.1021/nn500368m
132. Song, Y.; Zhu, S.; Zhang, S.; Fu, Y.; Wang, L.; Zhao, X.; Yang, B. *J. Mater. Chem. C* **2015,** *3,* 5976–5984. doi:10.1039/c5tc00813a
133. Essner, J. B.; Kist, J. A.; Polo-Parada, L.; Baker, G. A. *Chem. Mater.* **2018,** *30,* 1878–1887. doi:10.1021/acs.chemmater.7b04446
134. Righetto, M.; Privitera, A.; Fortunati, I.; Mosconi, D.; Zerbetto, M.; Curri, M. L.; Corricelli, M.; Moretto, A.; Agnoli, S.; Franco, L.; Bozio, R.; Ferrante, C. *J. Phys. Chem. Lett.* **2017,** *8,* 2236–2242. doi:10.1021/acs.jpclett.7b00794
135. Roy, P.; Chen, P.-C.; Periasamy, A. P.; Chen, Y.-N.; Chang, H.-T. *Mater. Today* **2015,** *18,* 447–458. doi:10.1016/j.mattod.2015.04.005
136. Li, X.; Lau, S. P.; Tang, L.; Ji, R.; Yang, P. *Nanoscale* **2014,** *6,* 5323–5328. doi:10.1039/c4nr00693c
137. Mahmood, A., Ed. *Handbook of Nanoparticles;* Springer International Publishing: Cham, Switzerland, 2015. doi:10.1007/978-3-319-15338-4
138. Venkatesan, G.; Rajagopalan, V.; Chakravarthula, S. N. *J. Environ. Chem. Eng.* **2019,** *7,* 103013. doi:10.1016/j.jece.2019.103013
139. Thakur, A.; Devi, P.; Saini, S.; Jain, R.; Sinha, R. K.; Kumar, P. *ACS Sustainable Chem. Eng.* **2019,** *7,* 502–512. doi:10.1021/acssuschemeng.8b04025
140. Raja, D.; Sundaramurthy, D. *Mater. Today: Proc.* **2021,** *34,* 488–492. doi:10.1016/j.matpr.2020.03.096
141. Picard, M.; Thakur, S.; Misra, M.; Mohanty, A. K. *RSC Adv.* **2019,** *9,* 8628–8637. doi:10.1039/c8ra10051a
142. Liu, G.; Jia, H.; Li, N.; Li, X.; Yu, Z.; Wang, J.; Song, Y. *Microchem. J.* **2019,** *145,* 718–728. doi:10.1016/j.microc.2018.11.044
143. Tadesse, A.; Hagos, M.; RamaDevi, D.; Basavaiah, K.; Belachew, N. *ACS Omega* **2020,** *5,* 3889–3898. doi:10.1021/acsomega.9b03175
144. Kumari, A.; Kumar, A.; Sahu, S. K.; Kumar, S. *Sens. Actuators, B* **2018,** *254,* 197–205. doi:10.1016/j.snb.2017.07.075
145. Praneerad, J.; Thongsai, N.; Supchocksoonthorn, P.; Kladsomboon, S.; Paoprasert, P. *Spectrochim. Acta, Part A* **2019,** *211,* 59–70. doi:10.1016/j.saa.2018.11.049
146. Murugan, N.; Prakash, M.; Jayakumar, M.; Sundaramurthy, A.; Sundramoorthy, A. K. *Appl. Surf. Sci.* **2019,** *476,* 468–480. doi:10.1016/j.apsusc.2019.01.090
147. Zainal Abidin, N. H.; Wongso, V.; Hui, K. C.; Cho, K.; Sambudi, N. S.; Ang, W. L.; Saad, B. *J. Water Process Eng.* **2020,** *38,* 101634. doi:10.1016/j.jwpe.2020.101634
148. Athika, M.; Prasath, A.; Duraisamy, E.; Sankar Devi, V.; Selva Sharma, A.; Elumalai, P. *Mater. Lett.* **2019,** *241,* 156–159. doi:10.1016/j.matlet.2019.01.064
149. V, R.; Misra, S.; Santra, M. K.; Ottoor, D. *J. Photochem. Photobiol., A* **2019,** *373,* 28–36. doi:10.1016/j.jphotochem.2018.12.028
150. Das, P.; Maruthapandi, M.; Saravanan, A.; Natan, M.; Jacobi, G.; Banin, E.; Gedanken, A. *ACS Appl. Nano Mater.* **2020,** *3,* 11777–11790. doi:10.1021/acsanm.0c02305
151. Luo, B.; Yang, H.; Zhou, B.; Ahmed, S. M.; Zhang, Y.; Liu, H.; Liu, X.; He, Y.; Xia, S. *ACS Omega* **2020,** *5,* 5540–5547. doi:10.1021/acsomega.0c00195
152. Bhatt, S.; Bhatt, M.; Kumar, A.; Vyas, G.; Gajaria, T.; Paul, P. *Colloids Surf., B* **2018,** *167,* 126–133. doi:10.1016/j.colsurfb.2018.04.008
153. Zhao, C.; Li, X.; Cheng, C.; Yang, Y. *Microchem. J.* **2019,** *147,* 183–190. doi:10.1016/j.microc.2019.03.029
154. Ramanan, V.; Siddaiah, B.; Raji, K.; Ramamurthy, P. *ACS Sustainable Chem. Eng.* **2018,** *6,* 1627–1638. doi:10.1021/acssuschemeng.7b02852
155. Ramezani, Z.; Qorbanpour, M.; Rahbar, N. *Colloids Surf., A* **2018,** *549,* 58–66. doi:10.1016/j.colsurfa.2018.04.006
156. Radhakrishnan, K.; Panneerselvam, P. *RSC Adv.* **2018,** *8,* 30455–30467. doi:10.1039/c8ra05861j
157. Boobalan, T.; Sethupathi, M.; Sengottuvelan, N.; Kumar, P.; Balaji, P.; Gulyás, B.; Padmanabhan, P.; Selvan, S. T.; Arun, A. *ACS Appl. Nano Mater.* **2020,** *3,* 5910–5919. doi:10.1021/acsanm.0c01058
158. Ji, X.; Yuan, X.; Nian, H.; Song, P.; Xiang, Y.; Wei, Y.; Wang, S.; Qin, K.; Zhang, Q.; Tu, Y. *Dyes Pigm.* **2020,** *182,* 108621. doi:10.1016/j.dyepig.2020.108621
159. Shariati-Rad, M.; Mohseninasab, T.; Parno, F. *RSC Adv.* **2018,** *8,* 2173–2180. doi:10.1039/c7ra12139c
160. Man, Y.; Li, Z.; Kong, W.-L.; Li, W.; Dong, W.; Wang, Y.; Xie, F.; Zhao, D.; Qu, Q.; Zou, W.-S. *Microchem. J.* **2020,** *159,* 105338. doi:10.1016/j.microc.2020.105338
161. Arumugham, T.; Alagumuthu, M.; Amimodu, R. G.; Munusamy, S.; Iyer, S. K. *Sustainable Mater. Technol.* **2020,** *23,* e00138. doi:10.1016/j.susmat.2019.e00138
162. Chaudhary, N.; Gupta, P. K.; Eremin, S.; Solanki, P. R. *J. Environ. Chem. Eng.* **2020,** *8,* 103720. doi:10.1016/j.jece.2020.103720
163. Kumar, A.; Chowdhuri, A. R.; Laha, D.; Mahto, T. K.; Karmakar, P.; Sahu, S. K. *Sens. Actuators, B* **2017,** *242,* 679–686. doi:10.1016/j.snb.2016.11.109
164. Lin, F.; Bao, Y.-W.; Wu, F.-G. *C–Open Access Carbon Res. J.* **2019,** *5,* 33. doi:10.3390/c5020033
165. Dinç, S.; Kara, M. *J. Apither. Nat.* **2018,** *1,* 33–37.
166. Peralta-Videa, J.; Sreenivasan, S. T.; Narayan, M. *Processes* **2020,** *8,* 445. doi:10.3390/pr8040445
167. Elmer, W.; White, J. C. *Annu. Rev. Phytopathol.* **2018,** *56,* 111–133. doi:10.1146/annurev-phyto-080417-050108

168. Anand, A.; Manavalan, G.; Mandal, R. P.; Chang, H.-T.; Chiou, Y.-R.; Huang, C.-C. *Curr. Pharm. Des.* **2020,** *25,* 4848–4860. doi:10.2174/1381612825666191216150948
169. Baig, M. M. F.; Chen, Y.-C. *J. Colloid Interface Sci.* **2017,** *501,* 341–349. doi:10.1016/j.jcis.2017.04.045
170. Kasibabu, B. S. B.; D'souza, S. L.; Jha, S.; Singhal, R. K.; Basu, H.; Kailasa, S. K. *Anal. Methods* **2015,** *7,* 2373–2378. doi:10.1039/c4ay02737j
171. Kasibabu, B. S. B.; D'souza, S. L.; Jha, S.; Kailasa, S. K. *J. Fluoresc.* **2015,** *25,* 803–810. doi:10.1007/s10895-015-1595-0
172. Nandi, S.; Ritenberg, M.; Jelinek, R. *Analyst* **2015,** *140,* 4232–4237. doi:10.1039/c5an00471c
173. Zhou, H.; Yang, D.; Ivleva, N. P.; Mircescu, N. E.; Schubert, S.; Niessner, R.; Wieser, A.; Haisch, C. *Anal. Chem. (Washington, DC, U. S.)* **2015,** *87,* 6553–6561. doi:10.1021/acs.analchem.5b01271
174. Gu, Y.; Hu, Y.; Zhao, X.; Chen, X.; Wang, P.; Zheng, Z. *Opt. Express* **2018,** *26,* 15842. doi:10.1364/oe.26.015842
175. Hua, X.-W.; Bao, Y.-W.; Wang, H.-Y.; Chen, Z.; Wu, F.-G. *Nanoscale* **2017,** *9,* 2150–2161. doi:10.1039/c6nr06558a
176. Song, Y.; Li, H.; Lu, F.; Wang, H.; Zhang, M.; Yang, J.; Huang, J.; Huang, H.; Liu, Y.; Kang, Z. *J. Mater. Chem. B* **2017,** *5,* 6008–6015. doi:10.1039/c7tb01092c
177. Zhong, D.; Zhuo, Y.; Feng, Y.; Yang, X. *Biosens. Bioelectron.* **2015,** *74,* 546–553. doi:10.1016/j.bios.2015.07.015
178. Mehta, V. N.; Jha, S.; Basu, H.; Singhal, R. K.; Kailasa, S. K. *Sens. Actuators, B* **2015,** *213,* 434–443. doi:10.1016/j.snb.2015.02.104
179. Li, H.; Huang, J.; Song, Y.; Zhang, M.; Wang, H.; Lu, F.; Huang, H.; Liu, Y.; Dai, X.; Gu, Z.; Yang, Z.; Zhou, R.; Kang, Z. *ACS Appl. Mater. Interfaces* **2018,** *10,* 26936–26946. doi:10.1021/acsami.8b08832
180. Yang, J.; Gao, G.; Zhang, X.; Ma, Y.-H.; Chen, X.; Wu, F.-G. *Carbon* **2019,** *146,* 827–839. doi:10.1016/j.carbon.2019.02.040
181. Travlou, N. A.; Algarra, M.; Alcoholado, C.; Cifuentes-Rueda, M.; Labella, A. M.; Lázaro-Martínez, J. M.; Rodríguez-Castellón, E.; Bandosz, T. J. *ACS Appl. Bio Mater.* **2018,** *1,* 693–707. doi:10.1021/acsabm.8b00166
182. Ting, D.; Dong, N.; Fang, L.; Lu, J.; Bi, J.; Xiao, S.; Han, H. *ACS Appl. Nano Mater.* **2018,** *1,* 5451–5459. doi:10.1021/acsanm.8b00779
183. Shivaji, K.; Mani, S.; Ponmurugan, P.; De Castro, C. S.; Lloyd Davies, M.; Balasubramanian, M. G.; Pitchaimuthu, S. *ACS Appl. Nano Mater.* **2018,** *1,* 1683–1693. doi:10.1021/acsanm.8b00147
184. Shahshahanipour, M.; Rezaei, B.; Ensafi, A. A.; Etemadifar, Z. *Mater. Sci. Eng., C* **2019,** *98,* 826–833. doi:10.1016/j.msec.2019.01.041
185. Yallappa, S.; Deepthi, D. R.; Yashaswini, S.; Hamsanandini, R.; Chandraprasad, M.; Ashok Kumar, S.; Hegde, G. *Nano-Struct. Nano-Objects* **2017,** *12,* 84–90. doi:10.1016/j.nanoso.2017.09.009
186. Pandiyan, S.; Arumugam, L.; Srirengan, S. P.; Pitchan, R.; Sevugan, P.; Kannan, K.; Pitchan, G.; Hegde, T. A.; Gandhirajan, V. *ACS Omega* **2020,** *5,* 30363–30372. doi:10.1021/acsomega.0c03290
187. Wang, H.; Zhang, M.; Ma, Y.; Wang, B.; Shao, M.; Huang, H.; Liu, Y.; Kang, Z. *J. Mater. Chem. B* **2020,** *8,* 2666–2672. doi:10.1039/c9tb02735a
188. Muktha, H.; Sharath, R.; Kottam, N.; Smrithi, S. P.; Samrat, K.; Ankitha, P. *Bionanosci.* **2020,** *10,* 731–744. doi:10.1007/s12668-020-00741-1
189. Wang, Z.; Liu, Q.; Leng, J.; Liu, H.; Zhang, Y.; Wang, C.; An, W.; Bao, C.; Lei, H. *J. Saudi Chem. Soc.* **2021,** *25,* 101373. doi:10.1016/j.jscs.2021.101373
190. Meela, M. M.; Mdee, L. K.; Masoko, P.; Eloff, J. N. *S. Afr. J. Bot.* **2019,** *121,* 442–446. doi:10.1016/j.sajb.2018.12.007
191. Abdel-Rahman, F. A.; Rashid, I. A. S.; Shoala, T. *J. Plant Prot. Res.* **2020,** *60,* 150–160. doi:10.24425/jppr.2020.133309
192. Khayal, A.; Dawane, V.; Amin, M. A.; Tirth, V.; Yadav, V. K.; Algahtani, A.; Khan, S. H.; Islam, S.; Yadav, K. K.; Jeon, B.-H. *Polymers (Basel, Switz.)* **2021,** *13,* 3190. doi:10.3390/polym13183190
193. Li, H.; Huang, J.; Lu, F.; Liu, Y.; Song, Y.; Sun, Y.; Zhong, J.; Huang, H.; Wang, Y.; Li, S.; Lifshitz, Y.; Lee, S.-T.; Kang, Z. *ACS Appl. Bio Mater.* **2018,** *1,* 663–672. doi:10.1021/acsabm.8b00345
194. Lahiani, M. H.; Dervishi, E.; Ivanov, I.; Chen, J.; Khodakovskaya, M. *Nanotechnology* **2016,** *27,* 265102. doi:10.1088/0957-4484/27/26/265102
195. Tripathi, S.; Sarkar, S. *Appl. Nanosci.* **2015,** *5,* 609–616. doi:10.1007/s13204-014-0355-9
196. Zheng, Y.; Xie, G.; Zhang, X.; Chen, Z.; Cai, Y.; Yu, W.; Liu, H.; Shan, J.; Li, R.; Liu, Y.; Lei, B. *ACS Omega* **2017,** *2,* 3958–3965. doi:10.1021/acsomega.7b00657
197. Waghmare, R. D.; Gore, A. H.; Anbhule, P. V.; Sohn, D.; Kolekar, G. B. *Data Brief* **2020,** *29,* 105345. doi:10.1016/j.dib.2020.105345
198. Qin, K.; Zhang, D.; Ding, Y.; Zheng, X.; Xiang, Y.; Hua, J.; Zhang, Q.; Ji, X.; Li, B.; Wei, Y. *Analyst* **2020,** *145,* 177–183. doi:10.1039/c9an01753d
199. Raina, S.; Thakur, A.; Sharma, A.; Pooja, D.; Minhas, A. P. *Mater. Lett.* **2020,** *262,* 127122. doi:10.1016/j.matlet.2019.127122
200. Yuan, M.; Zhong, R.; Gao, H.; Li, W.; Yun, X.; Liu, J.; Zhao, X.; Zhao, G.; Zhang, F. *Appl. Surf. Sci.* **2015,** *355,* 1136–1144. doi:10.1016/j.apsusc.2015.07.095
201. Zheng, M.; Wang, C.; Wang, Y.; Wei, W.; Ma, S.; Sun, X.; He, J. *Talanta* **2018,** *185,* 309–315. doi:10.1016/j.talanta.2018.03.066
202. Jhonsi, M. A.; Ananth, D. A.; Nambirajan, G.; Sivasudha, T.; Yamini, R.; Bera, S.; Kathiravan, A. *Spectrochim. Acta, Part A* **2018,** *196,* 295–302. doi:10.1016/j.saa.2018.02.030
203. Wang, H.; Li, H.; Zhang, M.; Song, Y.; Huang, J.; Huang, H.; Shao, M.; Liu, Y.; Kang, Z. *ACS Appl. Mater. Interfaces* **2018,** *10,* 16308–16314. doi:10.1021/acsami.8b03758
204. Arul, V.; Sethuraman, M. G. *Opt. Mater. (Amsterdam, Neth.)* **2018,** *78,* 181–190. doi:10.1016/j.optmat.2018.02.029

License and Terms

This is an open access article licensed under the terms of the Beilstein-Institut Open Access License Agreement (https://www.beilstein-journals.org/bjnano/terms), which is identical to the Creative Commons Attribution 4.0 International License (https://creativecommons.org/licenses/by/4.0). The reuse of material under this license requires that the author(s), source and license are credited. Third-party material in this article could be subject to other licenses (typically indicated in the credit line), and in this case, users are required to obtain permission from the license holder to reuse the material.

The definitive version of this article is the electronic one which can be found at:
https://doi.org/10.3762/bjnano.13.93